THE · UNIVERSITY · OF

WARWICK

A Multi-Analytical Investigation Into Glass Dopant Incorporation

by

Donna L. Carroll
(MPhys, PGCE:PCE)

0108220

Thesis

Submitted to the University of Warwick for the degree of

Doctor of Philosophy (PhD)

Department of Physics

April 2008

ALL MISSING PAGES ARE BLANK IN ORIGINAL

To my parents...

...and with many thanks to A. P. Howes and M. E. Smith.

---M M V I I I---

Contents

List Of Tables

List Of Figures

Declaration

The work for this thesis was carried out as a combination of full time and part time study at the Department of Physics of the University of Warwick from October 2005 to April 2008. It is the result of my own independent research except where it has been specifically referenced in the text, or in the case where the work has been based upon collaborative projects acknowledged in the relevant sections.

This thesis has been prepared in accordance with the University of Warwick's guidelines on the presentation of a research thesis and has not been previously submitted for any other awarded degree.

It has been agreed that this thesis may be photocopied for study purposes only and may be made available to the British Library under the condition that the relevant copyright regulations are upheld.

D. L. Carroll

Acknowledgements

I wish to thank the EPSRC for their funding as well as the Department of Physics for providing the facilities for this research. My samples were all manufactured and provided by external collaborators including the silver- and copper-doped phosphate glasses from the Eastman Dental Institute, University College London in collaboration with the University of Kent and Imperial College London, the yttrium- and lanthanum-doped glasses were provided by the Department of Physics at the University of Bath and finally the sulphur-doped aluminosilicates were manufactured at the Department of Earth Sciences, the University of Bristol.

I would like to express my appreciation for the help received from I. Ahmed and S. P. Valappil of the Eastman Dental Institute for their efforts in the antimicrobial studies, sample manufacture, dissolution and degradation investigations and thermal analysis of the silver and copper phosphates, D. M. Pickup of the University of Kent for his neutron diffraction and X-ray absorption spectroscopy work and M. R. Lees of the University of Warwick for his advice and guidance with the magnetic susceptibility studies as well as for his help running the VSM spectrometer. I would

also like to acknowledge the efforts of R. M. Kowalczyk of the University of Warwick, in completing the EPR measurements and simulations, M. E. Newton from the University of Warwick for his EPR, FTIR and Raman spectroscopy advice, S. J. York of the University of Warwick for the TEM images taken, R. A. Martin from the University of Bath for the production of the yttrium- and lanthanum-doped samples, microanalysis and thermal analysis and K. Klimm of the University of Bristol for providing the sulphur-doped samples along with their microanalysis.

I also wish to thank M. E Smith for his guidance and unwavering support which made this work possible.

List Of Publications

Publications resulting from various work within this thesis

R. A. Martin, P. S. Salmon, D. L. Carroll, M. E. Smith and A. C. Hannon, *Structure and thermal properties of yttrium alumino-phosphate glasses*, Journal of Physics: Condensed Matter, **20** (2008), 115204.

S. P. Valappil, D. M. Pickup, D. L. Carroll, C. K. Hope, J. Pratten, R.J. Newport, M. E. Smith, M. Wilson and J. C. Knowles, *Effect of silver content on the structure and antibacterial activity of silver-doped phosphate-based glasses*, Antimicrobial Agents and Chemotherapy, **51**:12 (2007), 4453–4461.

I. Ahmed, E. A. Abou Neel, S. N. Nazhat, J. R. Jones, D. M. Pickup, D. Carta, B. Newport, D. L. Carroll, M. E. Smith and J.C. Knowles, *The structure and properties of silver-doped phosphate based glasses*, Journal of Materials Science, **42** (2007), 9827-9835.

P. Guerry, D. L. Carroll, P. N. Gunawidjaja, P. Bhattacharya, D. Carta, D. M. Pickup, I. Ahmed, E. Abouneel, P. A. Thomas, J. C. Knowles, R. J. Newport and M. E. Smith, *Solid state NMR as a probe of inorganic materials: Examples from glasses and sol-gels*, Magnetic Resonance in Material Science, edited by J. Herberg, Y. Wu, P. Grandinetti, S. Hayes, I. Farnan, Materials Research Society Symposium Proceedings, **984E** (2007), Warrendale, PA, 0984-MM12-01.

Other published work

Y-T. Su, D. L. Carroll and G. R. Bell, *Vacuum deposition of palladium acetate films on S-GaAs substrates*, Research Communication submitted to Materials Chemistry and Physics.

S. Dixon, B. L. Cann, D. L. Carroll, Y. Fan and R. S. Edwards, *Non-linear enhancement of laser generated ultrasonic Rayleigh waves by cracks*, Nondestructive Testing and Evaluation, **23**:1 (2008), 25-34.

D. L. Carroll, T. F. Kemp, T. J. Bastow, and M. E. Smith, *Solid-state NMR characterisation of the thermal transformation of a Hungarian white illite*, Solid State Nuclear Magnetic Resonance, **28**:1 (2005), 31-43.

M. Schmucker, H. Schneider, K. J. D. MacKenzie, M. E. Smith, D. L. Carroll, *AlO_4/SiO_4 Distribution in tetrahedral double chains of mullite*, Journal of the American Ceramics Society, **88**:10 (2005), 2935-2937.

S. J. Charles, J. E. Butler, B. N. Feygelson, M. Newton, D. L. Carroll, J. W. Steeds, H. Darwsh, C. S. Yan, and R. J. Hemley, *Characterization of nitrogen-doped, chemical vapor deposited single crystal diamond before and after high temperature, high-pressure annealing*, Physica Status Solidi A: Applied Research, **242** (2004), 2473-2485.

Abstract

Several types of glass structure and the changes caused by dopant incorporation have been investigated. The glasses supplied have a range of uses in different areas of research and industry including rare-earth ion hosts for solid-state lasers, antibacterial ion hosts for prosthesis coatings and model magmas synthesised in an attempt to better understand the formation conditions within the upper mantle. The influence of various dopants on the properties and local structure of the samples was explored and a quantitative determination of the structural changes in the network as the dopant concentration was varied was achieved using ^{27}Al, ^{29}Si, ^{31}P and ^{33}S MAS NMR. Changes in Q species were identified for each sample by integrating the NMR spectra using a fitting program. Some dopants were found to create diverse changes in the connectivity of the glass networks and as such the coordination and other properties of some dopants within the samples were also identified using a range of analytical techniques including NMR, EPR, optical studies, X-ray absorption spectroscopy and neutron diffraction to determine explanations for the behaviour of different cation species within the glass.

Findings showed that silver- and copper-doping of phosphate based glass gave rise to unexpected connectivity between the phosphate units most likely due to some phase separation creating a different composition to that intended in the majority glass. This emphasises the importance of a careful and systematic approach to sample manufacture in achieving high sample stabilities, leading to a good degree of predictability in both structure and properties.

Lanthanum and yttrium ions, despite their huge difference in ionic size, showed very little difference in their effect upon the phosphate coordination in the glass samples as they remain outside the phosphate network, cross-linking between the terminal oxygen atoms. The aluminium ions however, showed evidence of behaving in both a cross-linking manner and in a network forming, tetrahedral role and it appears energetically favourable for them to avoid any Al-O-Al linkage, hence resulting in the formation of AlO_4 rather than exceeding the AlO_5 or AlO_6 quantities that would lead to this.

The sulphur NMR showed some preliminary hint at being a successful method for distinguishing between the sulphur speciation for samples formed under oxidising and reducing conditions and also gave rise to different numbers of ^{33}S sites depending upon the cations incorporated. This looks to be a very promising method for future use in understanding sulphur speciation in glasses.

Chapter 1

INTRODUCTION

1.1 Introduction

Nuclear magnetic resonance (NMR) evolved from the observation of radio frequency (r.f.) signals generated by atomic nuclei in 1945 by two groups of physicists independently (Purcell, Torry and Pound at Harvard University and Bloch, Hansen and Packard at Stanford University) [1]. The NMR technique has since been significantly enhanced and is now a powerful and popular method of determining the local surroundings of a nucleus. It has a vast range of applications in medicine, chemistry, engineering and physics.

This investigation is a study into several types of glass structure. The glasses studied have been supplied from several institutions and have a range of uses in different areas of research, but all have in common the incorporation of various dopants. It is the influence of these dopants on the properties and local structure of the samples that will be explored primarily using the NMR technique, but also employing a range of other analytical methods outlined in later chapters.

1.2 Phosphate glasses

Phosphate glasses have a wide range of uses including rare-earth ion hosts for solid-state lasers, forming bone china, nuclear waste hosts and surgical applications such as antibacterial ion hosts for prosthesis coatings.

Phosphate glasses consist of phosphate (P-) tetrahedral, PO_4, which are linked via covalent bonds with bridging oxygen atoms to form various phosphate anions [2]. The phosphate tetrahedra are characterised by the number of these bridging oxygen atoms that they are connected to, which is denoted by the Q^n species, where Q^n describes phosphorus atoms linked with n bridging oxygen atoms per phosphate tetrahedron. When ^{31}P NMR is performed on phosphate glass samples, the various phosphate units present in the sample give rise to spectral lines at distinctly different isotropic chemical shifts. There can be up to four of these distinct Q^n units (Q^0 to Q^3), as illustrated in figure 1.1. The ^{31}P chemical shift anisotropies (CSA) for

these Q^n species are relatively large [3] and can result in prominent spinning sidebands in a typical ^{31}P magic angle spinning (MAS) NMR spectrum of powdered phosphate glass samples, thus the requirement for faster spinning rates in order to improve the spectral resolution and reduce any overlap in these spinning sidebands. MAS NMR theory will be covered in more detail in section 2.5. By fitting Gaussian lineshapes to the resolved spectroscopic peaks, the relative abundance of each Q^n species can be easily quantified [4].

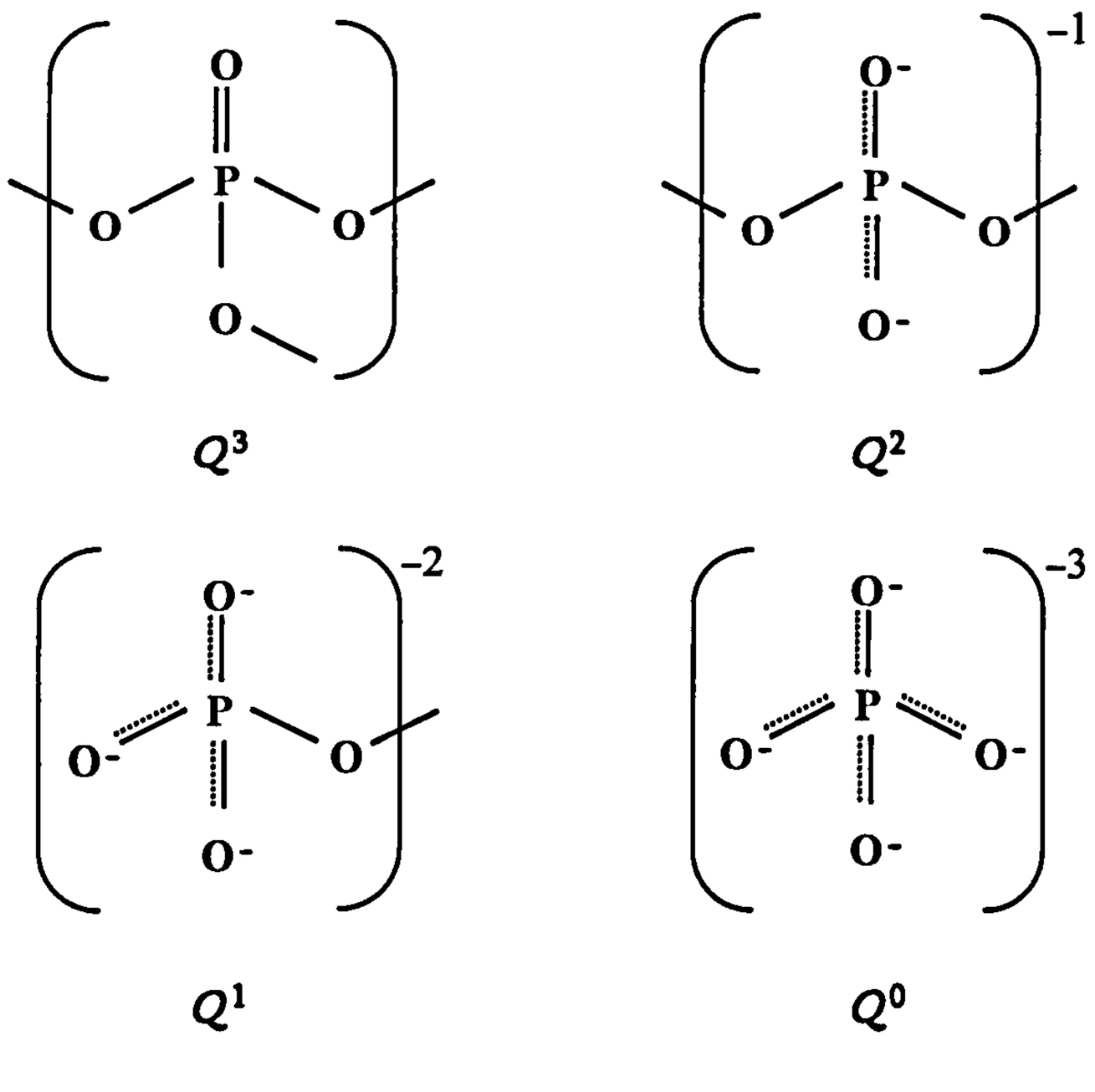

Figure 1.1: The four possible Q^n species of PO_4 phosphate tetrahedral units based upon those shown in work by Brow [2].

The phosphate glass structure can be described by a binary model or a random model where the former case is a more ordered arrangement with only two or fewer Q^n species present at one time. The actual model followed by the structure of a

particular glass is a subtle balance between various thermodynamic variables and this is still far from fully understood.

Pure phosphorus pentoxide, P_2O_5, in glassy form is extremely difficult to synthesise [3], so in order to aid the glass formation process sodium, calcium and sometimes aluminium may be incorporated into the structure, as in the samples used in this study.

One-dimensional (1D) ^{31}P NMR can only provide information about the local structure of phosphate glasses. To gain further insight into the connectivity between different Q^n species present (so-called medium-range order) two-dimensional (2D) MAS NMR could be used. Furthermore a double-resonance probe could be used to gain information about the connectivity between two entirely different nuclear species simultaneously.

Phosphate glasses of various compositions can be formed by incorporating different amounts of modifying oxide compounds into the phosphate network which for example, could be introduced in the form R_2O or RO (where R may be any alkali or alkali earth metal cation, R^+ or R^{2+}, respectively). For the case of monovalent R^+ cations, the glass can be described by $x\ R_2O + (1-x)\ P_2O_5$ with x as the molar fraction of oxide. Ultraphosphates are glasses where the molar percentage of P_2O_5 in the sample is greater than 50 mol. %, i.e. $0.0 < x < 0.5$. Metaphosphate glasses have

50 mol. % P_2O_5 ($x = 0.5$) and polyphosphate glasses have less than 50 mol. % P_2O_5 content ($1.0 > x > 0.5$). There are also more specific, intermediate regimes such as pyrophosphates where $P_2O_5 = 33$ mol. % ($x = \frac{2}{3}$), and orthophosphates, $P_2O_5 = 25$ mol. % ($x = \frac{3}{4}$) [2]. For each of these examples there is a specific formula to determine the fraction of each Q^n species present due to the depolymerising effect of the modifying oxide replacing the P_2O_5 in the phosphate network. Our samples are more complicated than this model as they contain more than one type of modifying oxide and we aim to discover any additional effects presented by the substitution of the copper, silver, aluminium, yttrium and lanthanum oxides into the various batches of samples supplied.

To a first approximation, the addition of an alkali oxide R_2O (or alkali earth metal oxide RO) has been shown in previous work in this area by Brow [2] and Van Wazer [5] to have the effect shown in equation 1.1 referred to as depolymerisation:

$$2Q^n + R_2O \rightarrow 2Q^{n-1} \tag{1.1}$$

The modifying oxide (R_2O) when added to the system rearranges such that the oxygen atoms become part of the glass network and a uniform structure is achieved. However, due to the presence of the metal ions, R^+, there are positive charges remaining which must be balanced. This has the effect of breaking the network structure by removing the oxygen bridges and thus forming more non-bridging

oxygen (NBO) atoms[i] as the modifying metal ion becomes part of the glass, but not part of the glass *network*, as depicted in figure 1.2. Thus, the higher the percentage of R_2O, the fewer bridging oxygen atoms predicted in a particular sample hence reducing the speciation number, n[ii].

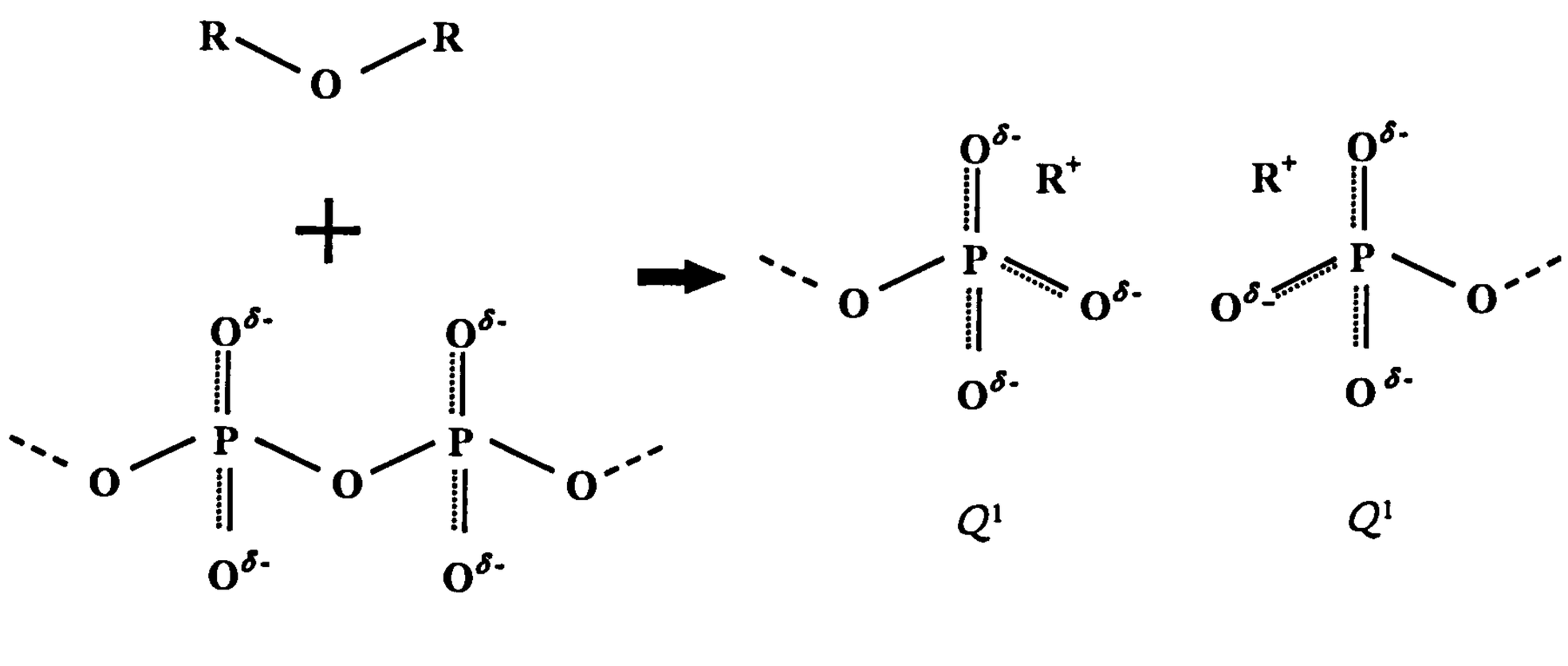

Figure 1.2: An example of the depolymerisation process acting upon Q^2 metaphosphate units as modifying oxides in the form of R_2O are added to a system, where R^+ is referred to as a modifying cation.

In the binary model for an ultraphosphate glass where $0.0 < x < 0.5$, theoretically only Q^2 and Q^3 tetrahedra are present and the fraction of Q^2 and Q^3 tetrahedra are given by equations 1.2 and 1.3, where x is the molar fraction of the modifying oxide present [5].

---

[i] Sometimes also referred to as terminal oxygen atoms.
[ii] It should be noted that the addition of a bivalent alkali earth metal modifying oxide in the form of RO (for example, CaO) would result in the same depolymerisation as the modifying cation now carries double the charge, R^{2+}.

$$f(Q^2) = \frac{x}{1-x} \tag{1.2}$$

$$f(Q^3) = \frac{1-2x}{1-x} \tag{1.3}$$

Metaphosphate glasses where $x = 0.5$, have networks consisting of purely Q^2 tetrahedra that form chains and rings, while polyphosphate glasses have networks based on Q^2 chains terminated by Q^1 tetrahedra (one bridging and three non-bridging oxygen atoms per tetrahedron) or by Q^1 dimers and individual Q^0 phosphate units [2]. When there is up to 67 % of modifying oxide present, the fractions of Q^1 and Q^2 tetrahedra are given by:

$$f(Q^1) = \frac{2x-1}{1-x} \tag{1.4}$$

$$f(Q^2) = \frac{2-3x}{1-x} \tag{1.5}$$

Then between 67 % and 75 %, the fractions of Q^1 and Q^0 tetrahedra are given by:

$$f(Q^0) = \frac{3x-2}{1-x} \tag{1.6}$$

$$f(Q^1) = \frac{3-4x}{1-x} \tag{1.7}$$

The various transitions between the Q species predicted by the Brow [2] model with changing composition are depicted in figure 1.3, although variations from this can arise from the occurrence of disproportionation in the form of $2Q^2 \leftrightarrow Q^3 + Q^1$ or $2Q^1 \leftrightarrow Q^0 + Q^2$ conversions to various extents within some samples.

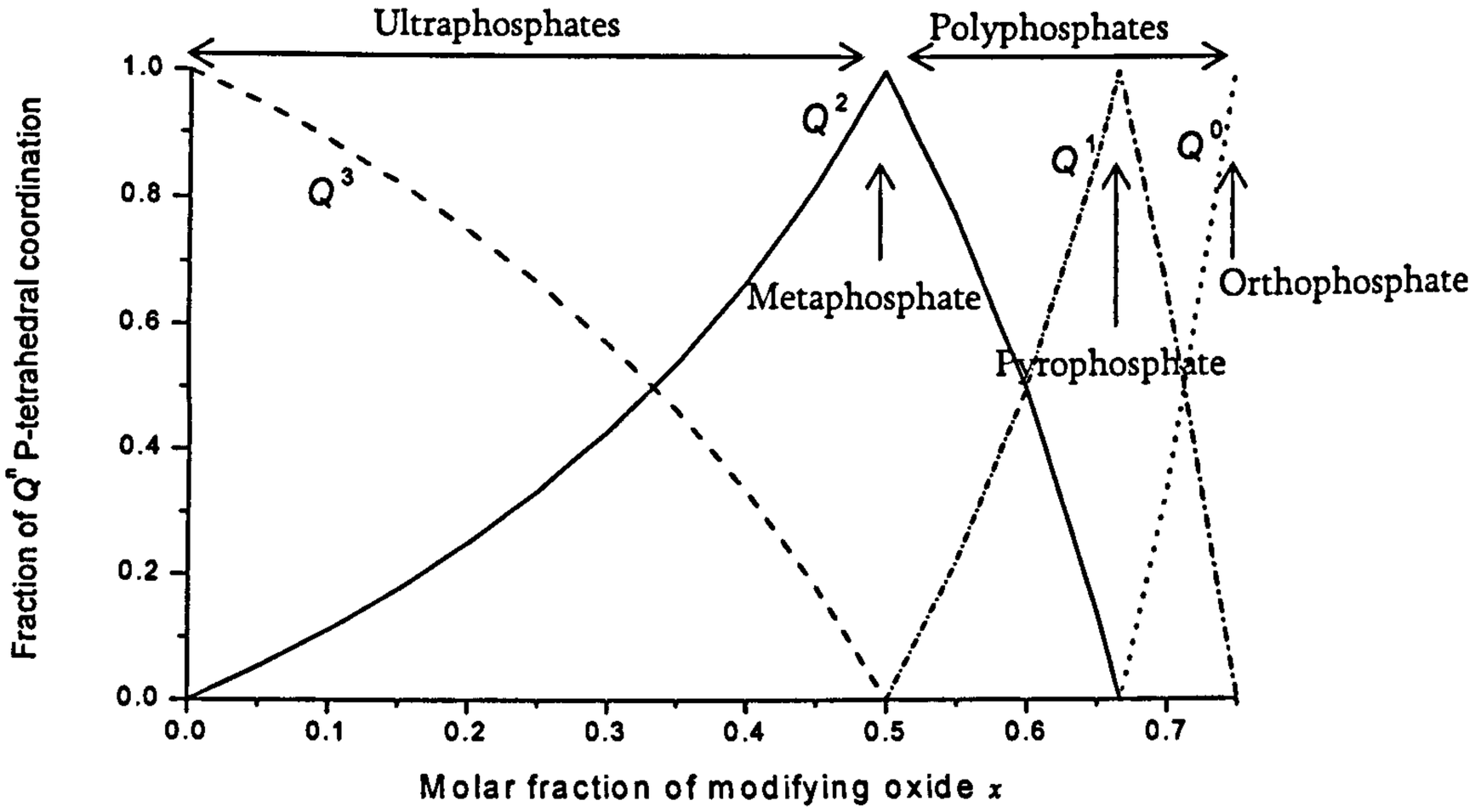

Figure 1.3: The predicted Q^n species transitions of PO_4 phosphate tetrahedral units based upon work by Brow [2].

It should also be noted that the sample formation conditions could make a significant difference as to whether the samples produced are hydrous or anhydrous, which is important as any water present may also act as a modifying oxide hence increasing the value of x which emphasises the importance of accurate determination of the sample composition inferred from chemical analysis studies.

1.2.1 Doping for the prevention of orthopaedic infections

Joint replacement operations are frequently used in orthopaedic surgery with more than 100,000 being performed in England and Wales each year [6] of which hip, knee, shoulder and elbow joint replacement are the most common. During surgery, damaged joints can be removed and replaced with an artificial prosthetic device.

Biomaterials research has developed a number of materials for hard and soft tissue replacement. Implants can consist of metal and plastic surfaces accurately shaped to restore the movement and function of the joint. Several metals are used, including stainless steel, alloys of cobalt and chromium, and titanium. Polyethylene is usually used for the plastic section. Plastic bone cement may also be used to anchor the prosthesis into the bone [7].

Like any surgical procedure, biomedical implant surgery can create certain life-threatening risks, such as material-related infections. These infections are caused by organisms which form a biofilm consisting of bacteria and their products, which attach to the surrounding host tissue [8]. The biofilm protects the organisms, reducing the effectiveness of any antibiotics and antiseptics used [9]. These infections can then spread throughout the body causing further complications, and must therefore be prevented. The current approach being investigated involves incorporating antimicrobial agents into host materials such as glass, which can then be used to coat the prosthesis. Both silver and copper ions have been found to exhibit antibacterial properties and silver has been found to work especially well against a broad range of microbes [9]. The glass used must therefore release these ions at a controlled rate either by allowing the ions to leach out or by breaking down and liberating the ions from the glass structure. Soluble phosphate glasses have thus far shown the most promising results for this behaviour as they have a predictable degradation rate. The samples used in this investigation involve silver-

and copper-doped phosphate glasses formed by melt-quenching. It is intended that by using solid-state MAS NMR the connectivity of the phosphorus and the environment of the sodium atoms are identified at the atomic level, as the dopant concentration is increased to ascertain the structure of these bioactive materials and how this relates to their antimicrobial properties so that they can be optimised. In light of the information obtained from the NMR studies, further analytical techniques can be employed in some cases to provide additional insight. The atomic structure of the samples is also known to affect the degradation rate of the glass [10] so NMR experiments will lead to information about the structural changes with doping concentration which could be used to make predictions of degradation by comparing results to previous work done in this area [10-12].

1.2.1.1 Sample background

The composition of the samples provided by the Division of Biomaterials and Tissue Engineering at University College London, Eastman Dental Institute can be described as follows:

- Silver-doped, mixed alkali metaphosphate glasses:

$$50\ \%\ P_2O_5 + 30\ \%\ CaO + (20 - x)\ \%\ Na_2O + x\ \%\ \delta$$

Where $\delta = Ag_2SO_4$.

- Copper-doped, mixed alkali polyphosphate glasses:

$$45\ \%\ P_2O_5 + 30\ \%\ CaO + (25 - x)\ \%\ Na_2O + x\ \%\ \delta$$

Where $\delta = CuO, Cu_2O, CuO_{0.5}$.

These are soluble samples with a chemically similar composition to bone material and will be studied initially using 1D MAS NMR experiments, observing both ^{31}P and ^{23}Na, to provide information about the network connectivity. Both sodium and calcium have been incorporated into the structure of these phosphate glasses in order to aid the glass formation process and to increase the strength of the material. These ions are routinely found in the human body, so are biocompatible [13]. The added antimicrobial agents are substituted for the Na_2O. The glasses were formed by melt-quenching using a starting mixture of NaH_2PO_4, $CaCO_3$, P_2O_5 and Ag_2SO_4 powders which were placed into a silica (SiO_2) crucible and inserted into a furnace at a temperature of 1100 °C for 1 hour and subsequently poured into a graphite mould to cool to room temperature. Further information about the glass manufacture can be found in references [10-12]. It can be seen that there is more than one type of modifying oxide incorporated into these samples and these should give rise to interesting results which can be compared to those in which only one type of modifying oxide is present in work by Brow [2]. The silver-doped phosphate glass compositions used in this study have previously been evaluated for antibacterial and antimicrobial activity against numerous types of bacterial organism including *Staphylococcus aureus* and *Escherichia coli* [10 & 11], during which it was

found that incorporation of ≥ 3 mol. % silver can produce an observable long-term antimicrobial effect against these organisms.

It should be noted that this investigation involves the substitution of one type of modifying cation for another to observe the effects of different modifier species upon the phosphate structure as it has been suggested that different cations may be incorporated in different ways [14] and do not always lead to depolymerisation. Some studies [14] have implied that certain cation species may leave the phosphate network coordination unchanged or may even be incorporated such that they become covalently bonded to the phosphate tetrahedra therefore increasing the number of bridging oxygen atoms which is described as network forming. The samples in this study contain a constant amount of P_2O_5 and the Brow model [2] can be used to predict the Q^n speciation depending upon the modifier present. Any deviations from the model with the cation substitution taking place may give rise to more specific information regarding the type of modifying oxide used in glass formation rather than a merely general case. Some of these samples were also heated to their crystallisation temperatures to observe which crystalline phases emerge as it is possible that these temperatures could be reached or exceeded during the prosthesis coating process and the effects of this should therefore also be understood.

1.2.2 Doping of phosphate glasses for use as solid-state laser media

All lasers contain an active medium exhibiting optical gain over a selected range of wavelengths [15]. In doped insulator lasers the lasing medium consists of impurity ions sitting in substitutional sites within a host material. The energy levels of these impurity ions are those involved in the laser transitions and can be modified by the type of host used, such that the same ions in different hosts produce different wavelengths. Furthermore, the thermal conductivity and expansivity of the host lattice has an effect on the operating power levels of the laser [15].

A lasing medium must achieve gain, population inversion and no additional absorption in the medium due to transitions other than those desired as most laser media have additional energy levels to those involved in the actual laser action. In addition to this, it is also important that there be no optical inhomogeneities in the material.

Phosphate glasses have attractive optoelectronic properties as they allow extremely high doping concentrations and doping effects are known to induce intriguing changes to their structure and properties [16], consequently they are being increasingly used as ion hosts for solid-state laser media [17]. For this reason there is growing interest in characterising and optimising the structure and ion implantation effects.

Previous studies by Hong [18] using single-crystal X-ray diffraction analysis have shown that the atomic scale network structure of phosphate glasses changes depending upon the rare-earth ion size. Different rare-earth ions bring varying properties to the solid-state laser gain media by influencing the fluorescence lifetime of the laser and the packing densities of the material [14]. This means that there are different advantages to the ions used, the most common of which include neodymium, erbium, lanthanum and yttrium. Neodymium has a large atomic size in comparison to erbium, both of which are frequently used in phosphate glass media, but are however unsuitable for NMR experiments at relatively high concentrations because of their paramagnetic effects. For this reason lanthanum and yttrium have been used in their place as they have comparable atomic sizes to neodymium and erbium respectively, where lanthanum is at the large cation radius end of the rare-earth series relative to yttrium [17]. How these ions affect the network structure and properties are of interest as these appear to be promising materials for efficient lasing media [18] and as these glasses contain rare-earth ions as a minor dopant only, the structural details can be difficult to obtain using diffraction methods such as X-ray diffraction (XRD) and neutron diffraction (ND) alone [14, 19 & 20], thus NMR techniques should bring an innovative perspective on the structure.

1.2.2.1 Sample background

The following samples pictured in figure 1.4 have been provided by the Department of Physics at the University of Bath and have the following composition:

- (25 – x) % (Al_2O_3) + x % (Y_2O_3) + 75 % (P_2O_5)
- 2 % (La_2O_3) + 5 % (Al_2O_3) + 22 % (Y_2O_3) + 71 % (P_2O_5)
- 15 % (La_2O_3) + 15 % (Al_2O_3) + 2 % (Y_2O_3) + 68 % (P_2O_5)
- 15 % (La_2O_3) + 35 % (Al_2O_3) + 50 % (SiO_2)
- 16 % (Y_2O_3) + 33 % (Al_2O_3) + 51 % (SiO_2)

The host material for the first three series of samples listed above is made up from the aluminophosphate component, where the lanthanum and yttrium both act as the substitutional ions. In the case of the latter two samples, the host material is the aluminosilicate glass and the lanthanum and yttrium have been added independently as a comparison. Aluminium is commonly incorporated into rare-earth phosphate and silicate glasses such as these to increase the strength and durability of the samples and further details regarding aluminosilicate glasses can be found in section 1.3.

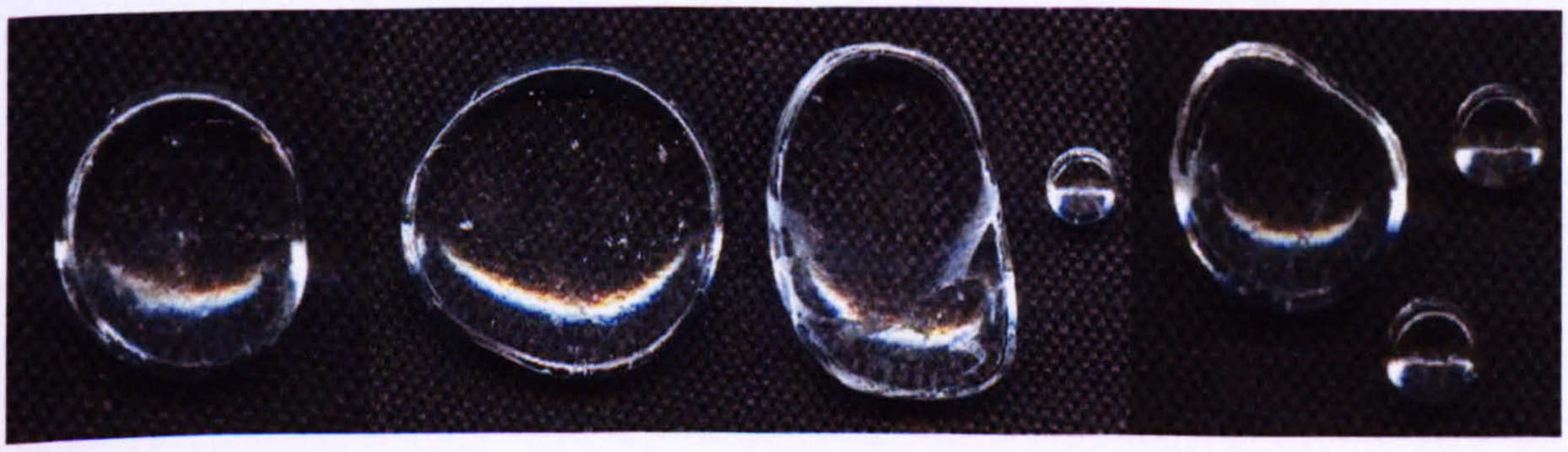

Figure 1.4: Yttrium-doped aluminophosphate glass samples before grinding. Photograph provided by Martin [21].

These samples were formed by fusing the initial dry oxide powders in alumina (Al_2O_3) crucibles in air which inevitably allowed the absorption of atmospheric water at room temperature before being placed into a preheated oven. The samples were heated in this oven at 500 °C for 1 hour, then heated further at 1000 °C for 30 minutes and lastly at 1620 °C for 30 minutes in separate preheated ovens [21 & 22]. Once removed the samples were poured into graphite moulds and annealed at 500 °C for 24 hours. The use of alumina crucibles at the start of this processes led to the incorporation of uncontrolled amounts of aluminium into the glass matrix [21 & 22] and this, along with other influences such as the moisture content of the oxide powder components and the atmosphere, all contribute to the overall composition achieved by the glass formation process. As the structure of the manufactured glasses is the focus of our investigation it was important to adopt a meticulous and systematic approach to the glass manufacture so that each sample was consistently created. Atmospheric water was allowed to be incorporated into the glass since attempts to form the glasses in a sealed environment excluding the presence of water were unsuccessful. This was interesting as it appears that the small quantities of atmospheric water possibly act as a catalyst and form phosphoric acid which helps to initiate the chemical processes involved in the formation before any heating occurs [22].

The glasses produced were initially assigned by the concentration of modifying oxide x R_2O_3 (aluminium and yttrium oxide) and phosphate content $(1 - x)$ (P_2O_5)

used in the starting compounds before formation. However, when electron probe microanalysis[iii] (EPMA) was employed by Martin [21 & 22], using a JEOL JXA 8600M EPMA to confirm these compositions post-manufacture, the glasses were found to contain higher levels of aluminium than expected which arose from the uncontrolled contamination from the alumina crucibles. These additional quantities of aluminium are enough to modify the phosphate network further as they change the ratio of modifier oxide (R_2O_3) to P_2O_5 predicted which can have subsequent effects on the structure and lasing properties of the glass as a lasing medium.

The EPMA results were therefore used in the calculations of network structure from the Brow model [2] and are described below in table 1.1 where the modifying oxide component of the glass consists of the combination of aluminium and yttrium oxide. As well as the incorporation of more than one type of modifying oxide during the formation process which may have an effect upon the network modifying process, the initial absorption of atmospheric water may also give rise to different results to those predicted by Brow [2] since water also acts as a network modifier. The EPMA was also performed at several points throughout various cross-sections of the samples to confirm the glass homogeneity.

[iii] This elemental analysis technique involves the wave dispersive detection of the characteristic X-rays emitted from the flat, polished specimen probed by a high energy electron beam.

Sample Constituents	Sample Label					
	A	B	C	D	E	F
Al_2O_3 / mol.%	34.3	23.4	18.9	12.4	8.3	2.6
Y_2O_3 / mol. %	0	6.6	11.6	16.7	24.2	26.3
P_2O_5 / mol. %	65.7	70.0	69.4	70.9	67.4	71.1
x	0.343	0.300	0.305	0.291	0.325	0.289

Table 1.1: Yttrium-doped aluminophosphate glass sample compositions, where x is the molar fraction of total modifying oxide (Al_2O_3 and Y_2O_3) within the samples, by Martin [21 & 22].

When incorporating trivalent cations R^{3+}, in the form of Al^{3+}, Y^{3+} or La^{3+}, or a mixture of these, into the phosphate glass network, as in the case of these samples, the system is described by $x\,R_2O_3 + (1-x)\,P_2O_5$ and equations 1.2 and 1.7 are transformed into equations 1.8 to 1.13 below.

In ultraphosphate glasses, where $0.00 \leq x < 0.25$:

$$f(Q^2) = \frac{3x}{1-x} \tag{1.8}$$

$$f(Q^3) = \frac{1-4x}{1-x} \tag{1.9}$$

For $x = 0.25$ the system becomes a metaphosphate glass consisting entirely of Q^2 tetrahedral chains and rings.

When $0.25 < x < 0.40$:

$$f(Q^1) = \frac{4x-1}{1-x} \tag{1.10}$$

$$f(Q^2) = \frac{2-5x}{1-x} \tag{1.11}$$

For $0.4 < x < 0.5$:

$$f(Q^0) = \frac{5x-2}{1-x} \tag{1.12}$$

$$f(Q^1) = \frac{3-6x}{1-x} \tag{1.13}$$

When $x = 0.4$ the glass is a pyrophosphate consisting only of Q^1 phosphate species, and when $x = 0.5$ they are orthophosphate glasses of individual Q^0 tetrahedral units. The transitions between the various phosphate network coordinations with increasing R_2O_3 modifier content are illustrated below in figure 1.5.

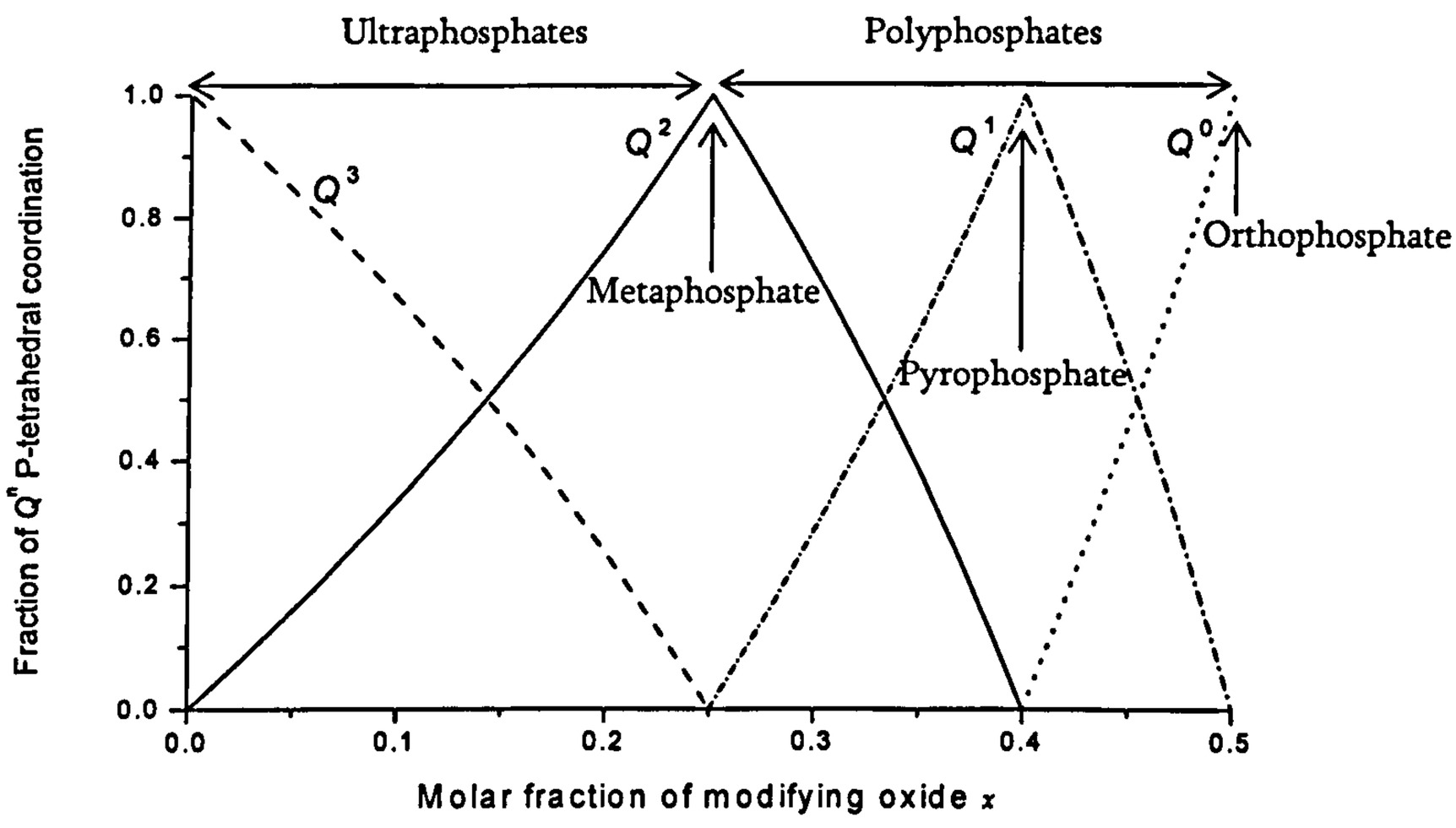

Figure 1.5: The predicted Q^n phosphate coordination transitions for phosphate based glass samples incorporating modifying oxides of the form R_2O_3.

As in the previous set of samples, this series of glasses display the effects of substituting one type of modifying oxide (yttrium) for another (aluminium oxide) whilst keeping the quantity of P_2O_5 approximately constant. This should give rise to

information regarding the different incorporation mechanisms involved for different modifier species since previous work by Hoppe [14] has discussed the possibility of some cation species behaving in other than just a depolymerising manner within a phosphate based glass.

Some aluminosilicate glasses containing exclusively yttrium or lanthanum were also prepared to observe the consequences of these various cations upon the glass networks and ^{27}Al, ^{29}Si and ^{31}P MAS NMR were performed on all of the samples where appropriate, as well as investigating changes in some of the sample durability properties.

1.3 Aluminosilicate glasses

Most naturally occurring silicate melts contain aluminium and both ^{27}Al and ^{29}Si NMR experiments have been widely performed in the history of the technique. For this reason there is a large ^{27}Al and ^{29}Si NMR database in which the chemical shifts are related to their corresponding structural unit, thus any new spectra can be compared to this standard data [23]. It is therefore straightforward to discover if the aluminium present in the sample is 4-, 5- or 6-fold coordinated and similarly the coordination of the silicon can be deduced. NMR studies of aluminosilicate glasses are popular as they can give an insight into the major processes occurring within the Earth, for example mantle melting and volcanic characterisation [24].

When performing NMR experiments on silicate samples, the dominant effect determining the chemical shift of the spectral lines is that of the atomic coordination number [4]. The second most noticeable influence on chemical shift is that of the nearest neighbour cation type and number. Bridging oxygen atoms are those shared between tetrahedral silicon or aluminium neighbours and substitution of tetrahedral aluminium in place of tetrahedral silicon neighbours causes a distinctive shift in the peak positions of the silicon [4]. For this reason ^{27}Al and ^{29}Si spectra of aluminosilicates often have multiple partially overlapping peaks which can cause peak fitting to become more complicated [4].

1.3.1 Sulphur-doping of aluminosilicate glasses for the investigation of sulphur speciation in model magma

^{33}S solid-state NMR has been used to study sulphur-bearing silicate and aluminosilicate glasses in order to gain an understanding of the sulphur speciation in synthesised model magmas. A greater understanding of volcanic eruptions, their predictions, effects on climate and emissions is being sought as they are currently poorly understood and reports of ^{33}S NMR experiments are rare due to the very low natural abundance of ^{33}S of 0.76 % [23].

The composition of volcanic gases has huge environmental and climatic impacts on a global scale, thus for geologists and volcanologists it is very important to attempt an

understanding of the effects of volcanic compounds released into the atmosphere when a volcano erupts or when non-eruptive degassing occurs. The acidic gases released can cause significant long-term damage to the surrounding environment and atmosphere in areas around the volcano.

The most common components of volcanic gases are water vapour, carbon dioxide (CO_2), sulphur dioxide (SO_2) in high temperature conditions or hydrogen sulphide (H_2S) in lower temperature conditions, nitrogen, helium, neon and argon. The quantities of volatile components emitted such as carbon dioxide, sulphur dioxide and hydrogen sulphide are fundamental in the understanding of the damage the gases can cause as they are acidic and can form acid rain, they are greenhouse gases and it is quite common for sulphur dioxide, for example, to be converted to sulphuric acid aerosol which has a distinct influence on the properties of ozone [25].

The specific compounds released during volcanic out-gassing processes depend primarily upon which elements are incorporated into the magma as it forms in the upper mantle. The conditions that define the compound incorporation are the temperature, pressure, composition of volatile elements present and their solubility within the magma, and most importantly, the amount of available oxygen, known as the oxygen fugacity, which is the tendency for oxygen to expand from one environmental compartment to another [26]. The specific value of the oxygen

fugacity is important as it affects which compounds become chemically stable during the formation process.

Earlier investigations into silicate glasses have been performed [27] and ^{33}S NMR has been shown as a practical method of probing the sulphur local environment even when the weight percentage is as low as 0.5 to 2.0 %. These previous experiments on crystalline compounds have shown that static spectra were chemical shift anisotropy dominated with chemical shift dispersion causing spectral broadening [28]. MAS narrows the spectral lines by up to a factor of 10 [27] and it is preferable to use high magnetic fields (i.e. 14.1 T) as it aids in increasing the signal-to-noise ratio and the Larmor frequency which in turn reduces probe ringing[iv] and second-order quadrupolar broadening.

The key parameters explored in these previous experiments were the solubility of sulphur species in silicate melts and the use of calcium as a controlling cation. It was shown that in hydrous glasses, sulphur was present in the form of sulphate (SO_4^{2-}) rather than as sulphide (S^{2-}) or sulphite (SO_3^{2-}). In the dry glasses there were two resonances present and the second was nanocrystalline potassium thiosulphate [27].

[iv] When an r.f. pulse is applied to the system, the current caused by the pulse can exert a small force upon the coil via its interaction with the magnetic field, which moves in response. This brief movement of the coil within the magnetic field is enough to induce a small, additional current in the coil which is then detected at the very start of the acquisition as part of the signal even though it is not a 'real' signal from the sample. This is known as ringing and this part of the detected signal must first be removed before undergoing any processing.

The experiments previously performed provide a foundation to the work to be completed as part of this project, although hypotheses of results from the new samples are limited due to the general lack of previous work involving ^{33}S solid-state NMR. Here, a wider range of improved model magmas will be studied to provide further information on the role of sulphur in aluminosilicate glasses with changing composition and formation conditions.

1.3.1.1 Sample background

These samples were provided by the Department of Earth Sciences at the University of Bristol and their compositions determined by Klimm[v] using EPMA can be found in table 1.2. The aluminosilicate glasses have been doped with small amounts (between 0.05 and 2.42 wt. %) of sulphur in order to synthesise model magmas in an attempt to gain an understanding of the sulphur coordination. If this technique proves successful then there is the possibility of attempting this on real magma samples in the not too distant future. It should however be noted that the weight percentages of sulphur incorporated in these samples are of a factor of ≥ 10 times greater than those that would be found in naturally formed magma samples. This was done in order to achieve a more easily observable NMR signal and this would therefore make NMR experiments on natural magma much harder to achieve in comparison. It is also important to note that unlike natural magma these

[v] Obtained through private correspondence.

synthesised samples contain no iron which, due to its paramagnetic properties would limit the use of the NMR technique.

Sample Constituents	*Sample Number*					
	1	*2*	*3*	*4*	*5*	*6*
SiO_2 / wt. %	72.62	69.36	72.54	75.07	73.98	68.57
TiO_2 / wt. %	0.33	0.00	0.31	0.00	0.00	0.00
Al_2O_3 / wt. %	15.73	18.90	15.79	0.00	0.00	0.00
CaO / wt. %	0.91	0.00	0.81	0.00	0.00	6.48
Na_2O / wt. %	8.99	11.69	9.28	23.42	0.00	22.53
K_2O / wt. %	1.18	0.00	1.15	0.00	24.56	0.00
SO_2 / wt. %	0.25	0.05	0.12	1.50	1.46	2.42

Table 1.2: Compositions of the sulphur-doped aluminosilicate glass samples by Klimm[vi].

The aluminosilicate based glasses were formed by weighing the corresponding amounts of each compound (given in table 1.2) and adding these constituents together in dry oxide powder form[vii] into platinum crucibles along with the carbonates $CaCO_3$, Na_2CO_3, K_2CO_3. These were then heated in a furnace to temperatures ranging between 700 to 1000 °C at a ramp rate of 50 °C hr^{-1} to remove the carbonate component. This left a pure oxide powder which was melted into a glass at 1400 °C for 1 hour at 1 atm in a platinum crucible and then cooled. It was ground into a powder and the melting process was repeated to achieve a more homogeneous glass which was then ground manually in an agate mortar to grain sizes of ~100 to 200 mm. This was then added into a gold[viii] crucible with a measured amount of sulphur and water, which was then welded closed and heated

---

[vi] Obtained through private correspondence.

[vii] The Al_2O_3 was first dried at 1000 °C for 24 hours as it is hygroscopic and contains a quantity of water and the other oxides were dried at 200 °C for 2 hours.

[viii] Gold crucibles were required due to the sulphur being highly reactive with other materials commonly used such as platinum.

using either an end-load piston cylinder, inner heated pressure vessel (IHPV) or coldseal pressure vessel (CSPV) under a controlled pressure and specific atmospheric conditions. The samples were heated to temperatures between 850 and 1000 °C using a high ramp rate of approximately 70 °C min^{-1} and left for between one and five days, depending upon the specific composition to be achieved, in order to force the speciation into certain sulphur states. The oxygen fugacity is a critical parameter to control and this was done so by using a sample holder in the furnace, known as a solid-state buffer, constructed from a material which allows the desired amount of oxygen to pass through into the crucible during heating. For example, for high oxygen fugacity conditions to obtain a highly oxidised sulphur state a sample holder of nickel-nickel oxide (NNO) was used, and conversely to create a reducing environment for the glass formation, a holder of quartz-fayalite-magnetite (QFM) was used to diminish the amount of oxygen from diffusing into the sample, therefore giving a lower oxygen partial pressure. In doing this the numerous samples had distinct formation conditions and the affects of this upon the sulphur structure could be compared.

As out-gassing of volatile chemicals from the exposed volcanic mantle and any flowing magma can lead to severe changes in the local atmospheric conditions this is of great interest for geologists and environmental scientists. These samples were investigated to better understand how the oxygen fugacity and volatile solubles affect the dissolution of the volatiles within the glass structure so as to predict

out-gassing behaviour. In nature it is not only which of the volatiles are present that affect the intake into the magma, but also the specific conditions in the upper mantle when the magma is formed and later expelled from the volcano. These important conditions such as the pressure, temperature, volatiles present, the other oxides incorporated, and the oxygen fugacity can be reproduced when making model magma samples. All of these factors contribute to changes in atomic structure observed and which state the sulphur may be found in, i.e. sulphate, sulphide or sulphite. By performing NMR on the samples provided it is hoped to compare the effects of changing the incorporated cations and oxygen fugacity on the sulphur sites.

References

[1] M. H. Levitt, *Spin dynamics: Basics of nuclear magnetic resonance*, John Wiley & Sons Ltd., Chichester, UK (2001).

[2] R. K. Brow, *Review: the structure of simple phosphate glasses*, Journal of Non-Crystalline Solids, **263** & **264** (2000), 1-28.

[3] H. Eckert, *Structural characterisation of noncrystalline solids and glasses using solid state NMR*, Progress in Nuclear Magnetic Resonance Spectroscopy, **24**:3 (1992), 187-194 & 223-230.

[4] J. F. Stebbins, *Nuclear magnetic resonance spectroscopy of silicates and oxides in geochemistry and geophysics*, Mineral Physics and Crystallography: A Handbook of Physical Constants, American Geophysical Union (1995), 303-331.

[5] J. R. Van Wazer, *Phosphorus and its compounds: Volume 1*, Interscience Publishers, New York, USA (1958).

[6] National Joint Registry for England and Wales, *Summary report to 2nd annual report*, (2005).

[7] L. Bren, *Joint replacement: An inside look*, FDA Consumer Magazine, **38**:2 (2004).

[8] J. P. O'Gara and H. Humphreys, *Staphylococcus epidermidis biofilms: importance and implications*, Journal of Medical Microbiology, **50** (2001), 582-587.

[9] D. J. Stickler, N. S. Morris and T. J. Williams, *An assessment of the ability of a silver-releasing device to prevent bacterial contamination of urethral catheter drainage systems*, British Journal of Urology, **78** (1996), 579-588.

[10] I. Ahmed, E. A. Abou Neel, S. N. Nazhat, J. R. Jones, D. M. Pickup, D. Carta, B. Newport, D. L. Carroll, M. E. Smith and J.C. Knowles, *The structure and properties of silver-doped phosphate based glasses*, submitted for the Journal of Materials Science, **42** (2007), 9827-9835.

[11] I. Ahmed, D. Ready, M. Wilson, and J. C. Knowles, A*ntimicrobial effect of silver-doped phosphate-based glasses*, Journal of Biomedical Materials Research Part A, **79**:3 (2006), 618-626.

[12] I. Ahmed, M. Lewis, I. Olsen and J. C. Knowles, *Phosphate glasses for tissue engineering: Part 1. Processing and characterisation of a ternary-based P_2O_5-CaO-Na_2O glass system*, Biomaterials, **25** (2004), 491-499.

[13] R. M. Moss, D. M. Pickup, I. Ahmed, J. C. Knowles, M. E. Smith and R. J. Newport, *Structural characteristics of antibacterial bioresorbable phosphate glass*, Advanced Functional Materials, (2008), 1-7.

[14] U. Hoppe, *A structural model for phosphate glasses*, Journal of Non-Crystalline Solids, **195** (1996), 138-147.

[15] J. Wilson and J. F. B. Hawkes, *Lasers: Principles and applications*, Prentice Hall International, London, UK (1987), 35-39.

[16] H. Zeng, Z. Sun, Y. Segawa, F. Lin, S. Mao and Z. Xu, *Photoluminescence and its temperature dependence of phosphate and fluorophophate optical glasses doped with fullerenes*, Journal of Physics D: Applied Physics, **34** (2001), 1044-1047.

[17] R. A. Martin, P. S. Salmon, C. J. Benmore, H. E. Fischer and G. J. Cuello, *Structure of lanthanum and cerium phosphate glasses by the method of isomorphic substitution in neutron diffraction*, Physical Review B, **68** (2003), 054203.

[18] H. Y-P. Hong, *The crystal structure of ytterbium metaphosphate, YbP_3O_9*, Acta Crystallographica B, **30** (1974), 1857.

[19] U. Hoppe, R. Kranold, D. Stachel, A. Barz and A. C. Hannon, *A neutron and X-ray diffraction stuffy of the structure of the LaP_3O_9 glass*, Journal of Non-Crystalline Solids, **232** & **234** (1998), 44-50.

[20] U. Hoppe, G. Walter, R. Kranold and D. Stachel, *Structural specifics of phosphate glasses probed by diffraction methods: a review*, Journal of Non-Crystalline Solids, **263** & **264** (2000), 29-47.

[21] R. A. Martin, P. S. Salmon, D. L. Carroll, M. E. Smith and A. C. Hannon, *Structure and thermal properties of yttrium alumino-phosphate glasses*, Journal Of Physics: Condensed Matter, **20** (2008), 115204.

[22] R. A. Martin, *Properties of rare earth phosphate glasses and rare earth halide liquids*, PhD Thesis, University of Bath, UK (2002).

[23] K. J. D. MacKenzie and M. E. Smith, *Multinuclear solid state NMR of inorganic materials*, Pergamon, London, UK (2002).

[24] A. Beran and E. Libowtzky, *Spectroscopic methods in mineralogy*, Eötvös University Press, Budapest, Hungary (2004), 408-415.

[25] D. Loyola, J. van Geffen, P. Valks, T. Erbertseder, M. Van Roozendael, W. Thomas, W. Zimmer and K. Wibkirchen, *Satellite-based detection of volcanic sulphur dioxide from recent eruptions in Central and South America*, Advances in Geosciences, **14** (2008), 35-40.

[26] *Comprehensive dictionary of physical chemistry*, Eds: L. Ulický and T. J. Kemp, Ellis Horwood Ltd. and PTR Prentice Hall, London, UK (1992).

[27] S. Couch, A. P. Howes, S. C. Kohn and M. E. Smith, *^{33}S solid state NMR of sulphur speciation in silicate glasses*, Solid State NMR, **26** (2004), 203-208.

[28] T. A. Wagler, W. A. Daunch, P. L. Rinaldi, A. R. Palmer, *Solid state ^{33}S NMR of inorganic sulfides*, Journal of Magnetic Resonance, **161** (2003), 191-197.

Chapter 2

THEORETICAL BACKGROUND TO NMR

2.1 Introduction

NMR is an experimental method used to provide structural information regarding the local environmental configuration of nuclei. The NMR technique exploits the magnetic properties of the atomic nuclei within the sample, which have an intrinsic nuclear spin contributing to an angular momentum. For a nucleus to be NMR-active it must have a non-zero spin *I*, where *I* is the spin quantum number, as this means that the nucleus has an intrinsic permanent magnetism. The spin contributes to the angular momentum of the nucleus as well as providing the

magnetic moment. The spin angular momentum $\underline{s}$ is given by $|\underline{s}| = \hbar\sqrt{I(I+1)}$, where in the z-direction it is reduced to $s_z = m\hbar$ using $m = I, I-1, \ldots, -I$. It is how the nuclear magnetic moments interact with the external magnetic field $\underline{B}_0$ applied by the NMR magnet, and how they are affected by the application of an r.f. pulse, that leads to information about the structure of the sample.

An NMR signal is detected for specific nuclei resulting in a spectrum of frequencies containing peaks in intensity (spectral lines) at specific frequencies. The spectral frequency is usually reduced to a scale δ, in parts per million, sometimes referred to as the chemical shift scale (see section 2.4.2), which is calculated using the following equation:

$$\delta = \frac{\nu - \nu_{ref}}{\nu_{ref}} \tag{2.1}$$

ν is the experimentally measured frequency and ν_{ref} is the frequency of the reference compound. The spectra are given in this form rather than in Hz because in this way the spectra are normalised to be independent of the magnetic field used by the spectrometer. This makes it easy for experimentalists to compare data from their different magnetic fields.

The peaks in intensity arise due to the absorption of energy at a frequency specific to a nucleus. This is because, when placed in a magnetic field the nuclear spins undergo the Zeeman interaction and the nuclear energy levels split, removing the

degeneracy. It is the difference in these energies that is measured by the NMR experiment[i]. The factors determining the peak positions of the signals present in the NMR spectra are discussed in further detail in section 2.4.2 regarding the chemical shift interaction.

The area under a spectral peak is directly proportional to the number of nuclei giving rise to the signal [1] and can be determined by integration. This makes the technique valuable for revealing the relative abundance of the different sites for a specific nucleus within each sample.

The nuclear spins can also undergo numerous interactions which affect the signal received due to interactions with other nuclei (dipole-dipole coupling) [1], their environments (chemical shift interaction) and bonding connectivities (spin-spin (J-) coupling) which each have distinct effects on the spectra collected. The value of the nuclear spin and the element itself determine which of these interactions are significant and many deductions about the samples can be made from these spectra which is what makes NMR so beneficial and broad ranging. The symmetry of the charge distribution of the nucleus is also a significant factor in determining the spectral lineshape via the key interactions present. If a nucleus has a spin angular momentum number of $I = ½$ then it has a spherical electric charge distribution (like a 1s hydrogen orbital), examples are ^{1}H, ^{29}Si, and ^{31}P. NMR experiments are

---

[i] This will be covered in greater depth in section 2.4.

relatively simple for these nuclei and the lineshapes of the peaks present tend to be Gaussian in solids which undergo magic angle spinning (MAS). Nuclei which have higher spin numbers have a non-spherical electrical charge distribution and this complicates the spectra due to the additional interactions that these nuclei experience [2], termed the quadrupole interaction.

Sensitivity (i.e. the signal-to-noise ratio) is a critical parameter in collecting NMR data. A strong signal is required from relatively few nuclei and the volume of sample is directly related to the strength of the signal (proportional to $N\gamma^3 B_0^2/T$, where N is the number of spins per unit volume, γ is the gyromagnetic ratio and T is the temperature of the sample in Kelvin). NMR is a relatively insensitive spectroscopic method as it requires between 10^{14} and 10^{23} spins in a sample to produce sufficient signal, even when the signal is strongly amplified. The signal-to-noise ratio is also dependent on the quality of the electronics of the equipment used [3].

The natural abundance of some NMR active nuclei is very low (for example ^2H is 0.02 % naturally abundant in comparison with ^1H at 99.98 % abundance [4]) and thus in these experiments sufficient signal can be difficult to achieve, to the extent that with some rarely occurring nuclei such as ^{17}O (0.04 % naturally abundant [4]), isotopic enrichment methods must be used.

Another key challenge in the experiments is the resolution of spectral lines which can be improved by MAS NMR which narrows the lines and is covered in section 2.5 in more detail.

Despite these difficulties, NMR is an important spectroscopic technique especially when the information obtainable from other methods such as diffraction, is limited by the absence of any long-range order in certain samples [5].

2.2 Basic principles of NMR

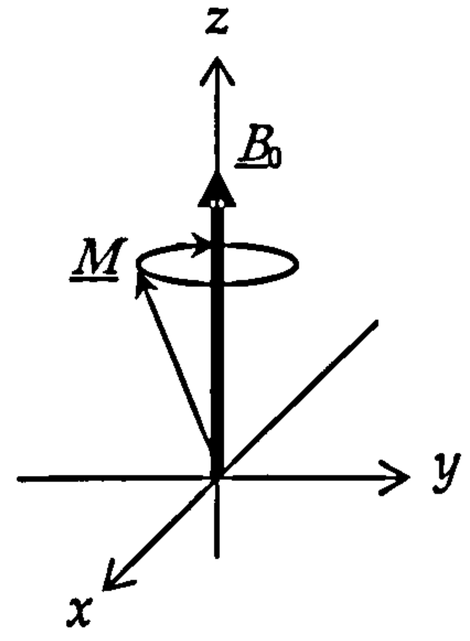

Figure 2.1: Precession of the net magnetisation M of nuclear spins in a B_0 field.

A magnetic field B_0 in the z-direction, provided by a superconducting magnet, is depicted in figure 2.1. The nuclear spins of the atoms in a sample when placed into this magnetic field precess about the B_0 (z) direction at a frequency specific to that nucleus, which is determined by the gyromagnetic ratio (gamma, γ) and the magnetic field strength. The precession frequency of the spins, known as the

Larmor frequency, is given by equation 2.2 in Hz, and the angular frequency is given by equation 2.3 in rad s^{-1} [6].

$$\underline{\upsilon} = \gamma \underline{B}_0 / 2\pi \tag{2.2}$$

$$\underline{\omega} = 2\pi \underline{\nu} = \gamma \underline{B}_0 \tag{2.3}$$

The nuclear magnetic moment for a single nucleus is given in equation 2.4 [6]. The nuclear spins in the sample have the same frequency and angle to the magnetic field but, due to their quantum nature, they have an almost equal probability of being either spin-up or spin-down relative to the $\underline{B}_0$ direction[ii], thus at any given time the total magnetisation vector reduces to nearly zero. However, the population of the states is determined by a Boltzmann distribution of energies so there will always be slightly more spin-up nuclei (for positive gamma[iii] nuclei), or slightly more spin-down nuclei (for negative gamma nuclei), giving rise to a small net magnetisation vector, $\underline{M}$, given by equation 2.5 [6].

$$\underline{\mu} = \gamma \underline{s} \tag{2.4}$$

$$\underline{M} = \sum_i \underline{\mu}_i = \sum_i \gamma \underline{s}_i \tag{2.5}$$

[ii] This is in the case of spin $I = ½$ nuclei as the nuclear spins can align with an external magnetic field $\underline{B}_0$ in only $2I + 1$ ways, either reinforcing or opposing $\underline{B}_0$.

[iii] Where gamma (γ) is the gyromagnetic ratio for these nuclei and is a constant for each specific isotope. It relates the magnetic moment μ and the spin number I for any specific nucleus $\gamma = \mu / \hbar I$.

In order to detect a signal, a small, additional oscillating magnetic field $\underline{B}_1$ must be applied perpendicular to the original static magnetic field direction by introducing an r.f. pulse generated by the same coil that is used to receive the NMR signal. The effect of this $\underline{B}_1$ field is best explained in the rotating frame [6] where from this perspective the frame itself rotates at the same rate as the oscillating $\underline{B}_1$ field which therefore appears stationary. However, in this frame there is a fictitious magnetic field of $-\underline{\omega}/\gamma$ introduced along the z-direction, hence the net field in this frame is the vector sum of $\underline{B}_1$ and $\underline{B}_0 - \underline{\omega}/\gamma$. Thus at resonance, $|\underline{B}_0| = |\underline{\omega}/\gamma|$, only $\underline{B}_1$ remains and in this frame the consequence of $\underline{B}_1$ is to tip the initially longitudinal magnetisation towards the xy plane. This results in the net magnetisation eventually lying wholly within the xy plane, after a so-called 90 ° pulse, and this is now termed the transverse magnetisation. The above is a classical explanation of the formation of the transverse magnetisation which in the quantum picture is equivalent to the population of the energy levels being equalised and is described in more detail later. The precession of this magnetisation in the xy plane (in the laboratory frame) induces an electromotive force (EMF) in the surrounding coil. It is this induced EMF that is measured by the NMR spectrometer. However, the net magnetisation vector does not stay in the xy plane indefinitely as the spins undergo relaxation processes which diminishes the signal received, this is described in the following section.

2.3 Relaxation

There are two types of relaxation mechanism that affect the net magnetisation vector, the first being the spin-spin (transverse) relaxation and the second, the spin-lattice (longitudinal) relaxation. The former is loss of signal due to the loss of coherence between the precessions of individual nuclear spins. The spins exchange energy amongst themselves and in doing so, lose coherence. The latter mechanism involves the individual nuclear spins returning to their equilibrium net magnetisation along the z-axis, and during this process the spins exchange energy with the lattice, for example via energy exchange with electrons or phonons.

Each of these relaxation processes has a characteristic relaxation time determined by the local environment of the nucleus. The spin-lattice relaxation time is denoted T_1 and the spin-spin relaxation time is denoted by T_2, where $T_1 \geq T_2$.

Due to this relaxation process, the signal induced in the coil decays away and hence the signal received is known as a free induction decay (FID). It is this FID that is Fourier transformed to give spectroscopic information in the frequency domain.

2.4 Interactions

The nuclear spin Hamiltonian overleaf describes the sum of the types of interactions experienced by the nuclei at a given time t.

$$\mathcal{H}_{total} = \mathcal{H}_Z + \mathcal{H}_{CS} + \mathcal{H}_D + \mathcal{H}_Q^{(1)} + \mathcal{H}_Q^{(2)} \quad (2.6)$$

$\mathcal{H}_Z$ describes the Zeeman interaction, $\mathcal{H}_{CS}$ the chemical shift, $\mathcal{H}_D$ the dipole-dipole coupling and $\mathcal{H}_Q^{(1)}$ and $\mathcal{H}_Q^{(2)}$ the first-order and second-order quadrupolar coupling for nuclei of $I > ½$. All of these interactions have both an isotropic and an anisotropic component, for example $\mathcal{H}_{CS} = \mathcal{H}_{CS}^{(iso)} + \mathcal{H}_{CS}^{(aniso)}$. The anisotropic component gives rise to an angular dependence with respect to the externally applied magnetic field, which results in a broad lineshape for solid-state powdered samples known as a powder pattern. The interactions are each individually explained in this section. There are also other possible interactions, for example J-coupling, however these other interactions are small enough, and the spectral techniques used here are such that they can be neglected in the samples investigated in this study and are not discussed further.

2.4.1 Zeeman splitting

Quantum mechanics dictates that a nucleus of spin I has $2I + 1$ energy levels which in the absence of a magnetic field are degenerate. Under the application of a magnetic field this degeneracy is removed by Zeeman splitting as illustrated in figure 2.2.

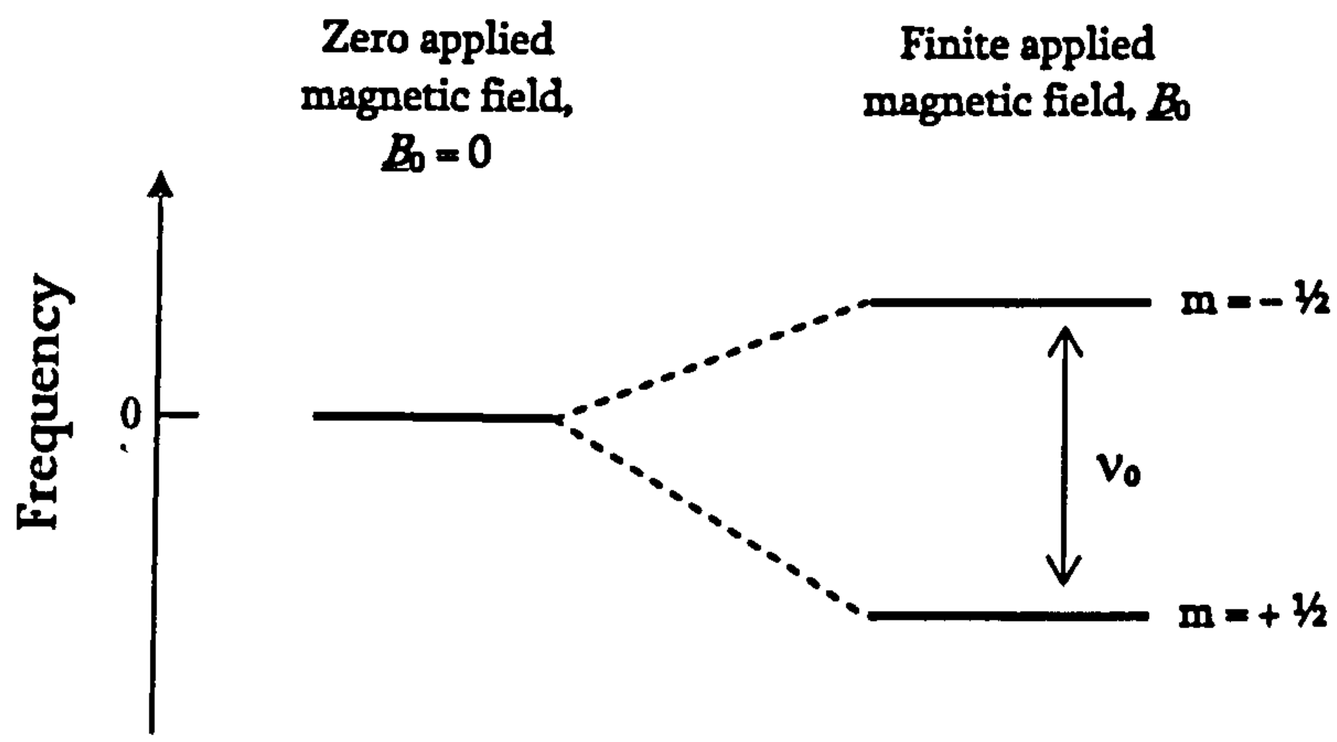

Figure 2.2: Zeeman splitting of the nuclear energy levels within an applied magnetic field.

For nuclei with $I = ½$ such as ^{31}P as in the example shown in figure 2.2, there are two distinct energy levels known as Zeeman states each described by a magnetic quantum number m, where $m = I, I - 1, \ldots, -I$, in this case $m = \pm ½$ [6]. The Hamiltonian representing this interaction in general is $\mathcal{H}_z = -\underline{\mu}\cdot\underline{B_0} = -\mu_z B_0 = -\hbar\omega_0 I_z = -m\gamma\hbar B_0$ which gives a difference in energy between the levels in this example of $\Delta E = \gamma\hbar B_0$ [7]. The energy levels are directly related to the nuclear structure and the effects of the chemical environment [6].

As $\Delta E = h\nu$ the difference in energy between the energy levels has a corresponding frequency given by equation 2.7, which is the same as that derived classically in equation 2.2 showing that the splitting frequency due to the Zeeman interaction and the Larmor frequency are the same. It is this energy transition that is measured by the NMR technique.

$$\underline{\upsilon} = \gamma\underline{B}_0/2\pi \qquad (2.7)$$

2.4.2 Chemical shift

A chemical shift interaction resulting in a shift in the spectral frequencies of the peaks present in a particular NMR spectrum is caused by interactions between the electrons and the nuclei which affect the overall local magnetic field experienced by the nuclei through shielding and deshielding effects. The Hamiltonian for the chemical shielding is given by $\mathcal{H}_{CS} = -\gamma h \underline{I} \cdot \underline{\sigma} \cdot \underline{B}_0$, where $\underline{\sigma}$ is the chemical shielding tensor. Hence with $\underline{B}_0$ along the z-axis, $\mathcal{H}_{CS} = -\gamma h I_z \sigma_{zz} B_0$, where σ_{zz} is described by equation 2.8 in spherical coordinates, and the anisotropy, $\Delta\sigma$, and asymmetry, η_{CS}, are given in 2.9 and 2.10.

$$\sigma_{zz} = \sigma_{iso} + \frac{\Delta\sigma}{2}\left[(3\cos^2\theta - 1) + \eta_{cs}\sin^2\theta\cos 2\phi\right] \tag{2.8}$$

$$\Delta\sigma = \sigma_{zz} - \sigma_{iso} \tag{2.9}$$

$$\eta_{cs} = \frac{\sigma_{xx} - \sigma_{yy}}{\sigma_{zz}} \tag{2.10}$$

In practical terms the factors determining the peak positions (chemical shift/shielding) are due to atoms residing in different chemical environments, for instance:

- coordination number;
- nearest neighbour type;
- next nearest neighbour type;
- and crystallographic inequivalence.

A change in any of these environmental and chemical factors would result in a change in the electron density, thus modifying the shielding effect of the electrons and creating an alteration in chemical shift.

2.4.3 Dipole-dipole interaction

The local magnetic fields associated with the magnetic moments of surrounding nuclei can interact with each other and this so-called dipole-dipole interaction is dependent upon the magnetic moments ($\underline{\mu} = \gamma\underline{s}$) and the internuclear separation, $\underline{r}$ [6]. The magnetic field due to the intrinsic permanent magnetism from one nucleus is experienced by its neighbouring nuclei and vice versa. For the case of dipole-dipole coupling, the isotropic term of the Hamiltonian describing the interaction is zero and the anisotropic term for a pair of isolated interacting spins gives rise to an NMR powder pattern spectrum with angular dependence, in the form of what is known as a Pake doublet, as shown in figure 2.3. This spectral pattern arises from the signal from nuclei with a distribution of angles between the internuclear vectors connecting the interacting nuclei (denoted by j and k) and the magnetic field $\underline{B}_0$. This angular dependence is directly proportional to $\frac{1}{2}(3\cos^2\theta - 1)$ where θ is the angle between the internuclear vector $\underline{r}_{jk}$ and the $\underline{B}_0$ field. The powder pattern also has a dependence on the internuclear distance, r_{jk}, proportional to $1/r_{jk}^3$ and the Hamiltonian describing this dipole interaction is given in

equation 2.11, which in the truncated, energy conserving case reduces to equation 2.12 for heteronuclear (unalike) adjacent nuclei j and k [8].

$$\mathcal{H}_D^{jk} = \frac{\mu_0}{4\pi}\frac{\gamma_j\gamma_k\hbar^2}{r_{jk}^3}\left(\underline{I}_j\cdot\underline{I}_k - \frac{3(\underline{I}_j\cdot\underline{r}_{jk})(\underline{I}_j\cdot\underline{r}_{jk})}{r^2}\right) \tag{2.11}$$

$$\mathcal{H}_D^{jk} = \frac{\mu_0}{4\pi}\frac{\gamma_j\gamma_k\hbar^2}{r_{jk}^3} I_z^j I_z^k\left(3\cos^2\theta - 1\right) \tag{2.12}$$

In the samples studied in this investigation the dipole-dipole coupling is small in relation to the other interactions present.

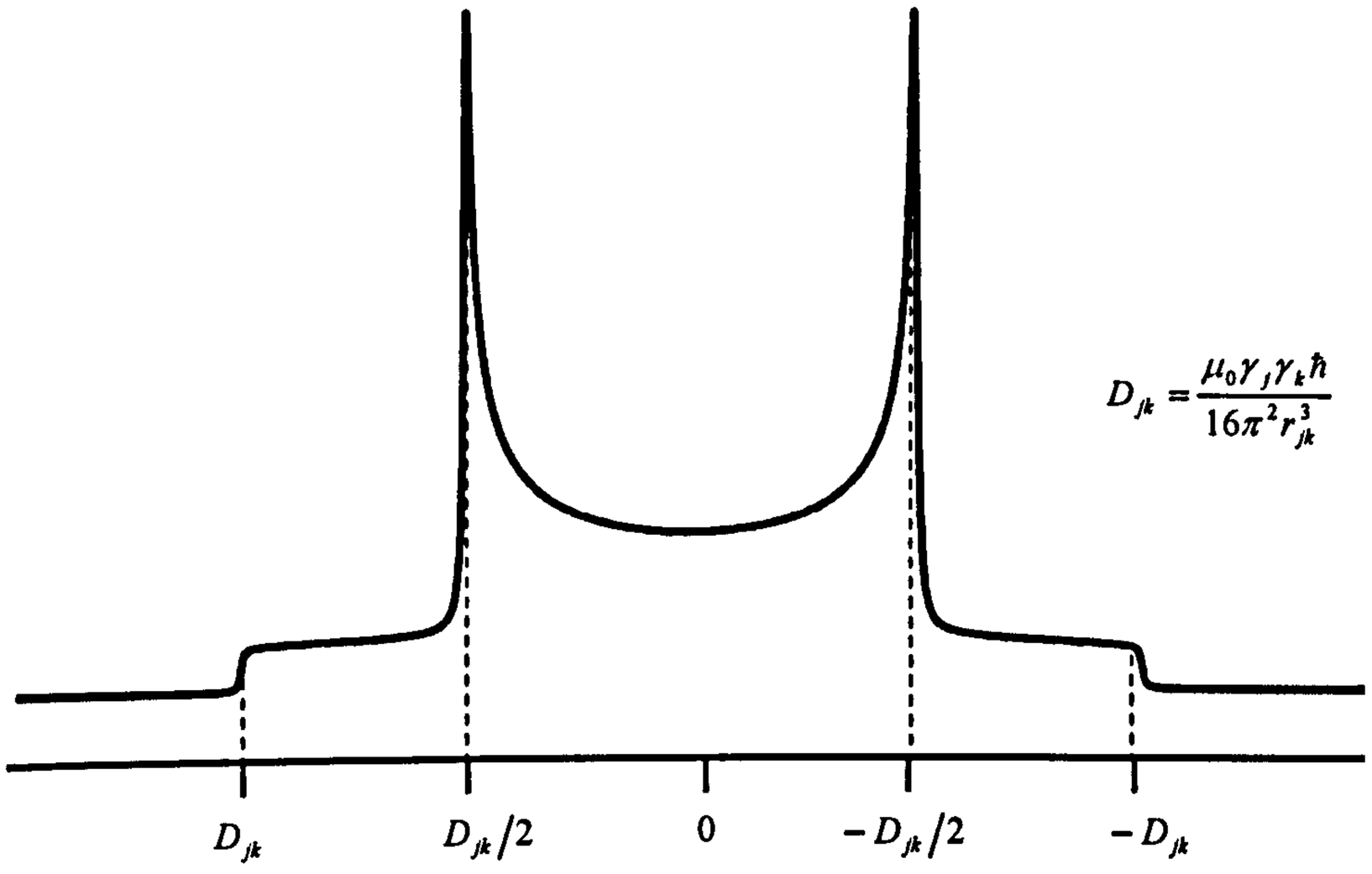

Figure 2.3: An example of the Pake doublet NMR powder pattern where D_{jk} is the dipole frequency for the interaction between two nuclei of different nuclear species. If the two species were identical (i.e. homonuclear) the dipole frequency D_{jj} would be a factor of $\sqrt{2}$ larger.

2.4.4 Electric quadrupole coupling

As explained in section 2.4.1 a nucleus of spin I has $2I+1$ possible orientations, thus for a nucleus such as sodium which is spin $I = 3/2$, it has four energy levels which in the absence of a magnetic field are degenerate.

For nuclei such as sodium with a nuclear spin, $I > 1/2$, the nuclear electrical charge distribution is ellipsoidal rather than spherical with excess positive charge at the poles and a depletion of charge towards the centre of the nucleus [2]. This means that the nucleus possesses an electric quadrupole moment in addition to its magnetic dipole moment [9]. The non-spherically symmetric nuclear electric charge distribution interacts with any electric field gradients present, perturbing the otherwise equally split Zeeman energy levels and the quadrupole Hamiltonian describing this interaction is outlined below in equation 2.13 [7]. χ_Q is the quadrupolar coupling constant given by equation 2.14 and the quadrupolar interaction is also affected by the asymmetry parameter, η_Q, described in equation 2.15, which relates to the asymmetry of the electric field gradient. eQ is the nuclear quadrupole moment and eq is the principal component of the electric field gradient tensor ($\underline{\underline{V}}$) at the specific site [5 & 7].

$$\mathcal{H}_Q = \frac{h\chi_Q}{4I(2I-1)}\left[(3\cos^2\theta-1)(3I_z-I(I+1))+3\sin\theta\cos\theta(I_z(I_++I_-)+(I_++I_-)I_z)+\frac{3}{2}\sin^2\theta(I_+^2+I_-^2)\right] \quad (2.13)$$

$$\chi_Q = \frac{e^2qQ}{h} \quad (2.14)$$

$$\eta_Q = \frac{V_{xx}-V_{yy}}{V_{zz}} \quad (2.15)$$

Taking sodium as an example due to the fact it has been thoroughly investigated during this study; under the application of a magnetic field the degeneracy of the four energy eigenstates is lifted due to the Zeeman effect as shown in figure 2.4. They become distinct energy levels each described by a magnetic quantum number, *m*.

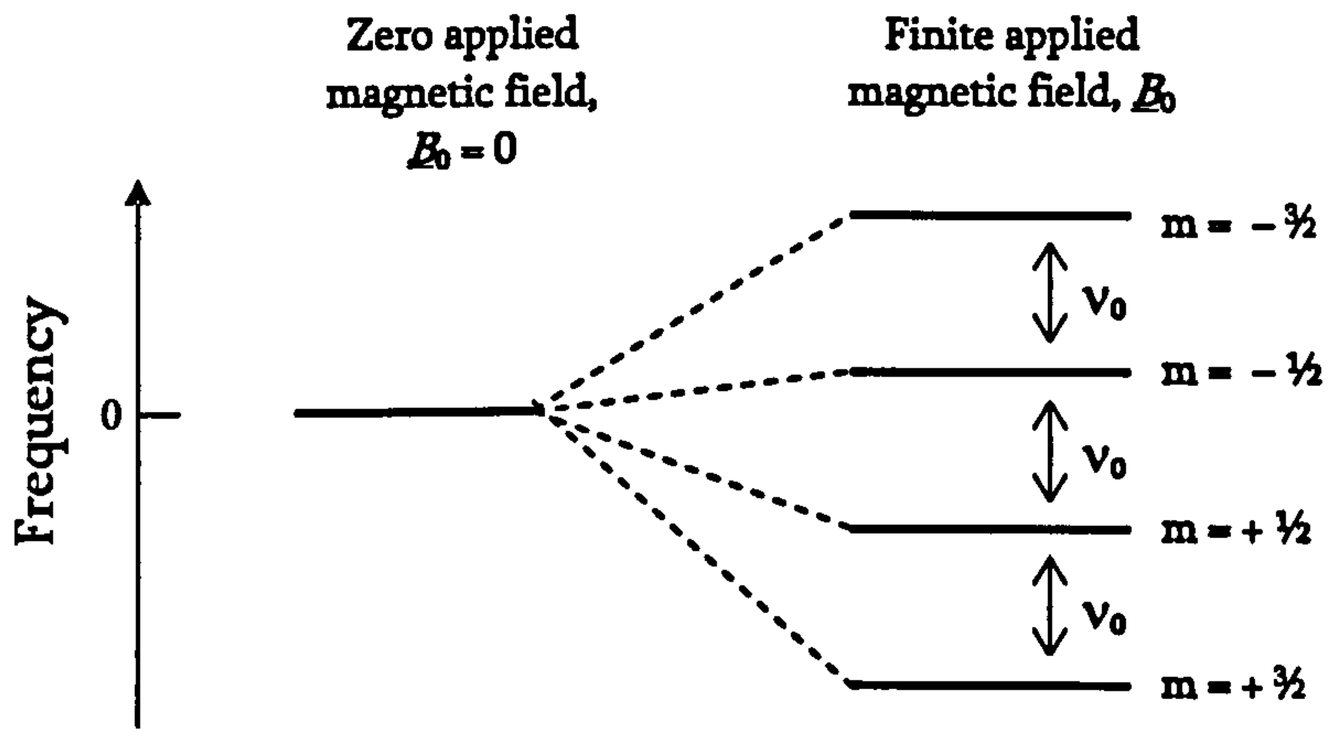

Figure 2.4: Zeeman splitting of the nuclear energy levels of a positive gamma, spin $I = ½$ nucleus within an applied magnetic field.

The separation between each successive energy level under Zeeman splitting is the same and it is this energy transition that is measured by the NMR technique as the corresponding frequency, ν_0. Transitions between other energy levels (for example between $m = +3/2$ and $m = -1/2$) are not observable in NMR as they do not induce transverse magnetisation under the application of an r.f. pulse. As in the $I = ½$ case, the position of the peak in the NMR spectrum at the spectral frequency ν_0, given by equation 2.7, is dependent upon the nuclear structure and chemical environment and is determined by the chemical shift described in section 2.4.2. This peak frequency is also affected by interactions such as dipole-dipole and spin-spin

coupling which may correspond to further shifts in peak position and broadening of the signal observed, discussed in 2.4.3.

The first-order effect of the quadrupolar interaction with the electric field gradient is to perturb each of the nuclear energy levels by a small frequency $\nu_Q^{(1)}$ described in equation 2.16 [7], where $\nu_Q^{(1)} << \nu_0$.

$$\nu_Q^{(1)} = \left(\frac{3\chi_Q}{4I(2I-1)}\right)\left(3\cos^2\theta - 1\right)\left(m - \tfrac{1}{2}\right) \qquad (2.16)$$

This perturbation causes the non-central transitions (where $m \neq \frac{1}{2}$) to be shifted sufficiently far from the Larmor frequency that they are not usually obsevered using conventional pulsed NMR techniques [7]. However, the central transition where $m = \frac{1}{2}$ is unaffected, unless the interaction is strong enough for the second-order effects to be noticeable. The first-order perturbation of the energy levels is illustrated in figure 2.5, which is not to scale.

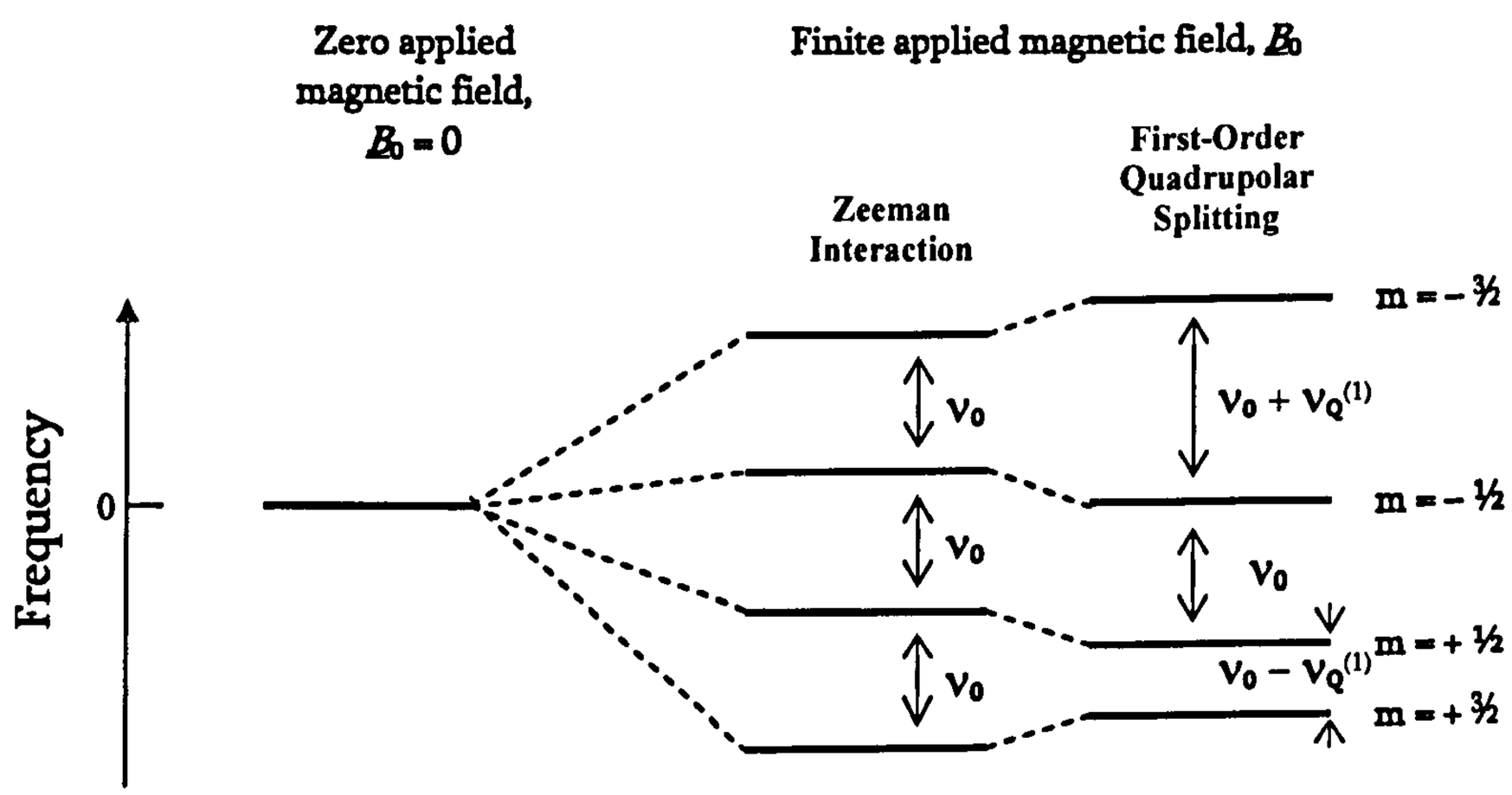

Figure 2.5: Quadrupolar splitting of the nuclear energy levels within an applied magnetic field.

As can be seen from the energy level diagram, the $m = +3/2$ to $m = +1/2$ transition has become smaller in energy since $(1/2 - m) = -1$, whereas the $m = +1/2$ to $m = -1/2$ transition has remained the same because $(1/2 - m) = 0$ and for the $m = -1/2$ to $m = -3/2$ transition, the transition frequency has become larger due to the addition of a factor of $(1/2 - m) = +1$ [6].

NMR experiments performed on static powdered samples such as this would now have the following appearance:

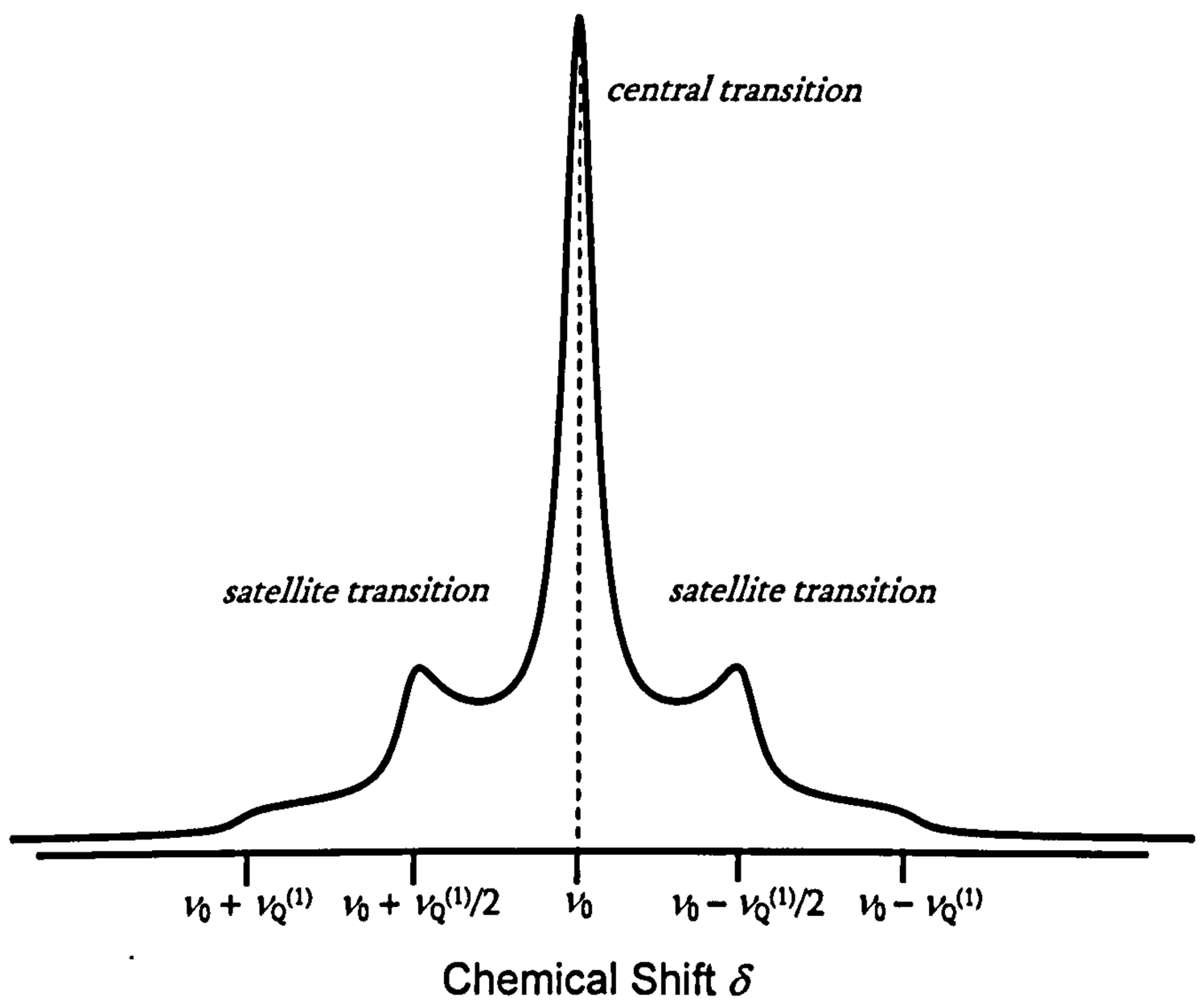

Figure 2.6: An example of a static NMR spectrum showing the expected signal from a spin $I = 3/2$ nucleus such as ^{23}Na, due to the quadrupolar effect.

This lineshape is similar to a Pake doublet which was discussed in section 2.4.3 and the points at $\nu_0 \pm \nu_Q^{(1)}/2$ are known as singularities. The central line is due to the

$m = \pm\frac{1}{2}$ transition which would be the same as that observed with no quadrupolar interaction present only lower in intensity, as the intensity is now divided between the central and satellite transitions in the ratio 3:4:3 [3].

The satellite transitions are dependent upon the crystallographic orientation of the sample and as such have a spatial dependence upon the second-order Legendre polynomial $\frac{1}{2}(3\cos^2\theta - 1)$ due to the perturbation term. This overall lineshape in figure 2.6 is not normally observed since $\nu_Q^{(1)}$ is of the order of MHz and the spectral widths of the NMR lines are typically only between 200 and 400 kHz so these singularities would be out of the observed frequency range for most χ_Q.

If the quadrupolar coupling is sufficiently strong this gives rise to an observable second-order perturbation of the energy states in addition to the first-order effect so that the energy bands are once again shifted, this time by an amount $\nu_Q^{(2)}$ described below in equation 2.17 for the central transition when $\eta_Q = 0$ [7].

$$\nu_Q^{(2)} = \left(-\frac{9\chi_Q^2}{64\nu_0 I^2(2I-1)^2}\right)\left(I(I+1)-\tfrac{3}{4}\right)\left(1-3\cos^2\theta\right)\left(9\cos^2\theta-1\right) \qquad (2.17)$$

The shift caused by this effect is proportional to χ_Q^2/ν_0 and changes the isotropic shift to lower values [5]. In addition to this the signal becomes broadened due to this anisotropy arising from the orientation dependence which is a function of the fourth-order Legendre polynomial:

$$P_4(\theta) = \frac{1}{8}\left(35\cos^4\theta - 30\cos^2\theta + 3\right) \qquad (2.18)$$

This causes the central transition lineshape to undergo yet another anisotropic broadening which is depicted in figure 2.7.

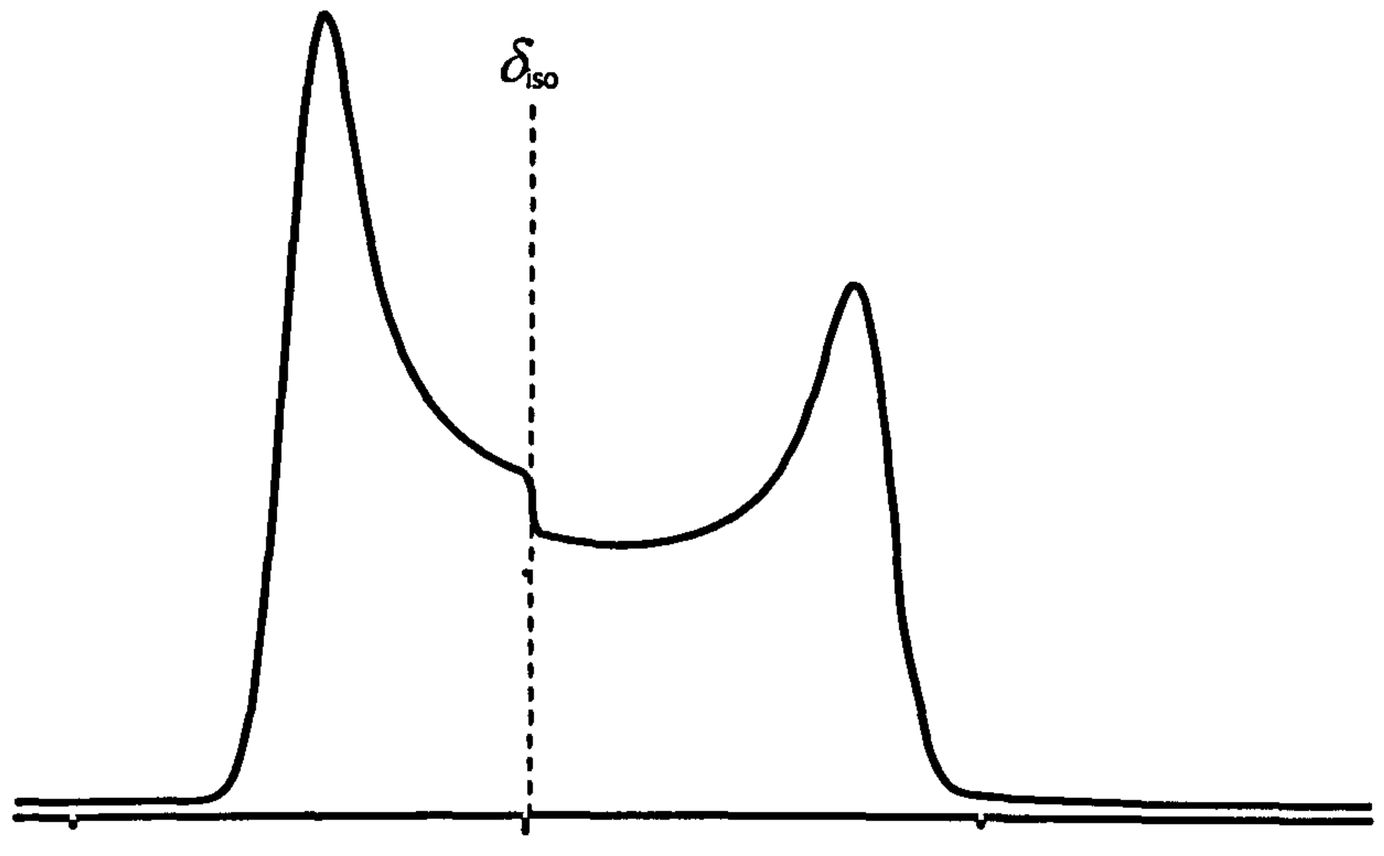

Figure 2.7: An example of an ideal, static NMR spectrum of a quadrupolar nucleus with sufficiently strong second-order quadrupole interaction.

It is now important to note that the isotropic chemical shift, δ_{iso}, in figure 2.7 is no longer in the centre of the spectral feature equal to the frequency ν_o it is instead near the left-hand shoulder of the peak as shown [6].

2.5 Magic angle spinning

In liquid NMR the rapid, isotropic tumbling of the molecules within the sample averages all of the orientations so the peaks observed in the NMR spectra are only due to the isotropic chemical shift term and very narrow lines are obtained. The magic angle spinning method aims to achieve a similar result for solid-state samples.

The magic angle spinning technique is the process in which a powdered sample loaded into a rotor is physically rotated about an axis at $\theta = 54.74°$ to $\underline{B_0}$ in order to average the anisotropic NMR interactions [6] due to their dependence upon the second- and fourth-order Legendre polynomials, $P_2(\theta)$ and $P_4(\theta)$ respectively. This specific angular dependence arises as a function of the spatial dependence of each interaction and the actual 'magic' angle is derived from the second-order Legendre polynomial shown in equation 2.19, the function of which is shown later in figure 2.10.

$$P_2(\theta) = \frac{1}{2}\left(3\cos^2\theta - 1\right) \tag{2.19}$$

Under magic angle spinning, although there is still a distribution of orientations for the nuclei in the powdered sample, a modulation term of the interaction in the form of the second-order Legendre polynomial as shown in equation 2.19 arises. This can be set to zero and thus removes the effect of the anisotropic broadening interactions such as CSA and dipole-dipole coupling [6], hence improving the resolution between neighbouring spectral lines. It also acts to remove spinning side bands from the central peak which become separated by an amount equal to the spinning frequency.

Using ^{23}Na NMR as an example, where I = ³⁄₂, this would have the effect of narrowing the satellite transitions into spinning sidebands with the separation

between the sidebands being equivalent to the spinning speed, as shown in figure 2.8 which compares the static and MAS NMR spectra.

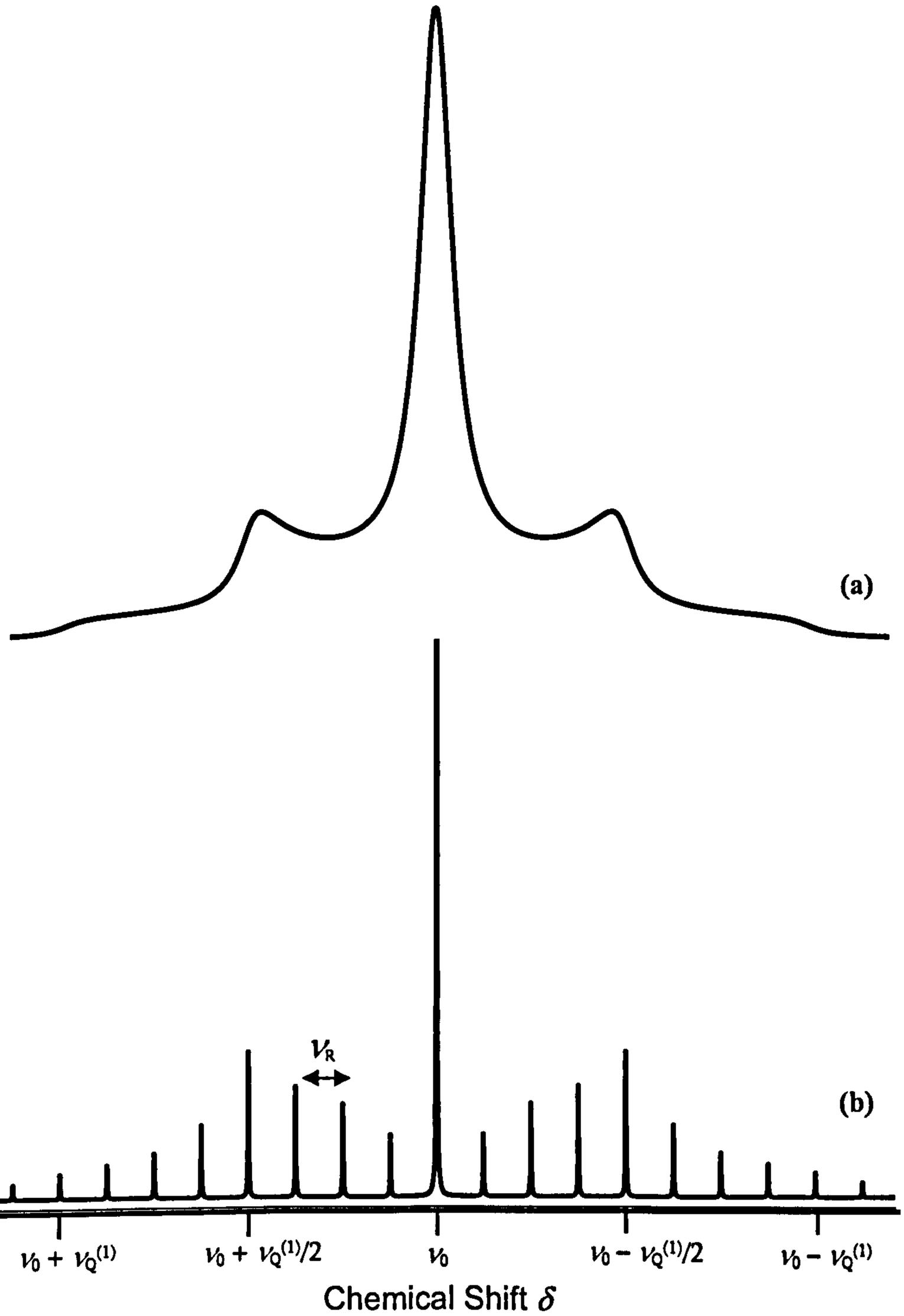

Figure 2.8: An example of the NMR spectrum of a spin $I = 3/2$ nucleus such as ^{23}Na where (a) shows the static NMR signal and (b) shows the MAS case using a spinning frequency of ν_R.

Since there is no first-order quadrupolar broadening of the central transition, under MAS the other effects (e.g. chemical shielding or dipolar interactions) will be

narrowed as discussed above. If, however, the second-order quadrupolar perturbation of the energy states is strong enough to be observable, the effect of sufficiently rapid rotation would be to greatly reduce but not completely remove the anisotropic second-order quadrupolar interaction. Consequently the residual width of the signal is reduced usually by a factor close to 3.5 times [5] although this depends weakly on η_Q, discussed previously [10]. The effect of MAS on the second-order quadruploar broadened NMR lineshape is shown in figure 2.9.

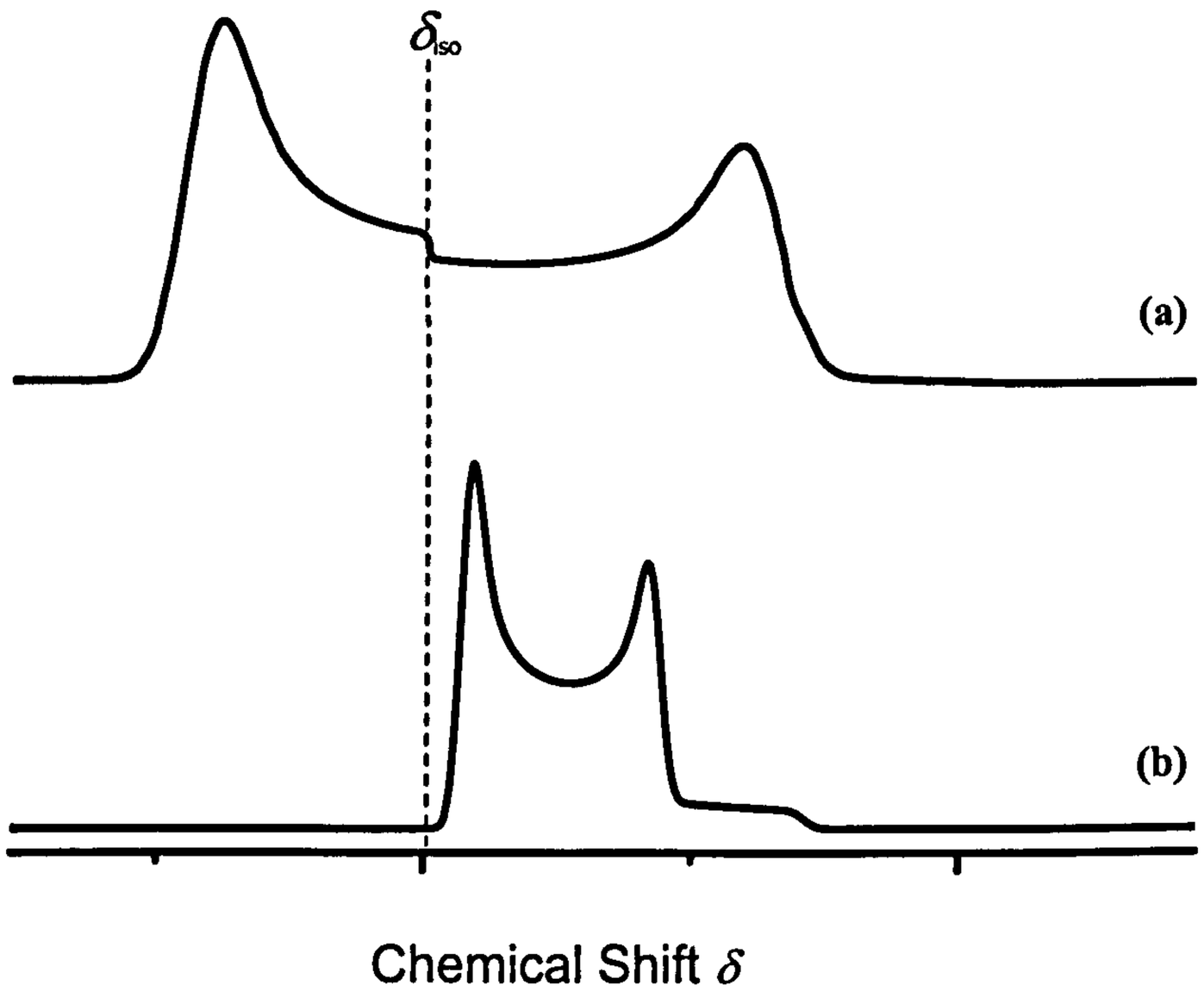

Figure 2.9: (a) An example of an ideal, static NMR spectrum of a quadrupolar nucleus with sufficiently strong second-order quadrupole interaction. (b) The effects of MAS upon the NMR signal.

If $P_2(\theta)$ and $P_4(\theta)$ are plotted against θ as shown in figure 2.10, it can be seen that $P_2(\theta)$ passes through zero when $\theta = 54.74°$ so any interactions dependent on $P_2(\theta)$

will reduce to zero when spun at this angle to the applied external magnetic field, however $P_4(\theta)$ passes through zero when $\theta = 30.56\,°$ and $\theta = 70.12\,°$.

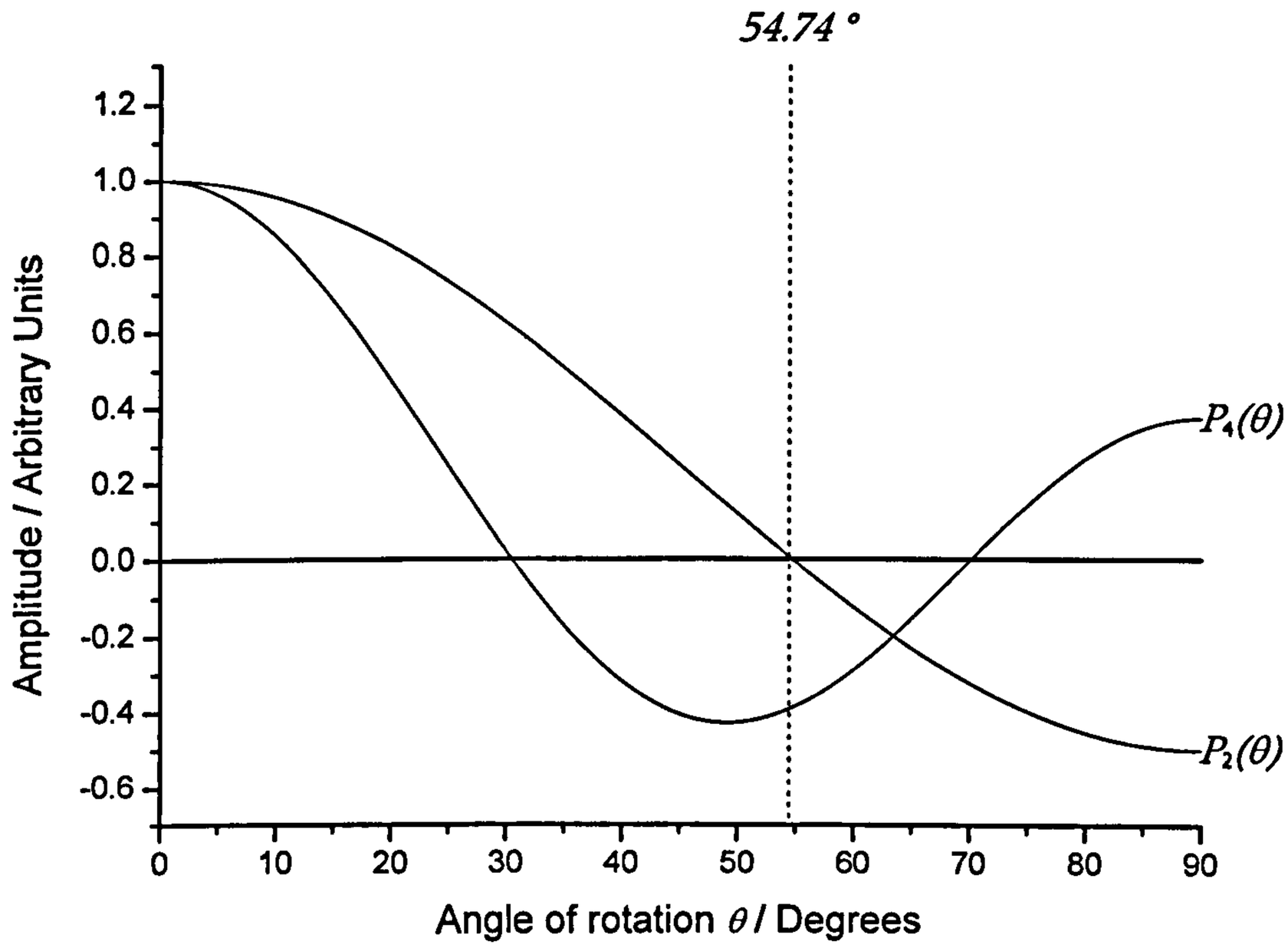

Figure 2.10: The second- and fourth-order Legendre polynomials as functions of angle to the applied magnetic field B_0.

Although spinning the sample at the magic angle of 54.74 ° does not reduce the fourth-order Legendre polynomial to zero, it does now have a smaller magnitude than it did at $\theta = 0\,°$, hence reducing the second-order interaction effect present by approximately 60 %.

The rotation frequency of the sample is also a factor that influences the narrowing of the spectral lines via MAS since a certain, specific rotational frequency must be surpassed for narrowing to be clearly observable i.e. the Gaussian FWHM linewidth

if $I = ½$ and CSA dominated, or the residual second-order quadrupolar width if $I > ½$ [10]. For a quadrupolar nucleus, the frequency that this occurs at is dependent upon the strength of the quadrupolar interaction and is usually of the order of a few kHz. The larger the quadrupolar interaction of a particular site, the higher this value must be. Below this specific frequency, no real narrowing effect can be observed although some modulation of the signal will occur.

In the case of a sample containing a distribution of sites with varying strengths of quadrupolar interaction, then in order to reduce the linewidth of the spectroscopic signal using MAS, the sample must be rotated sufficiently fast to narrow the signal arising from the site with the weakest quadrupolar interaction. Further increase in the rotational speed will now reduce the linewidth of sites in the distribution with larger quadrupolar interactions and this continues up to the point where the speed exceeds that necessary to narrow the strongest interaction. Above this speed, any additional benefits from increasing the speed will be negligible. The effect of the distribution is that, perhaps counter intuitively, the spectral lines become broader as the spinning speed increases [8].

When fitting spectra of this type the fits must include the parameters of peak position in ppm, amplitude in arbitrary units, Gaussian broadening in Hz, centre of the quadrupolar distribution, χ_Q, in MHz and the width of the quadrupolar distribution, $\Delta\chi_Q$, also measured in MHz.

References

[1] H. Günther, *NMR spectroscopy - An introduction*, John Wiley & Sons Ltd., Chichester, UK (1980).

[2] P. J. Hore, *Nuclear magnetic resonance*, Oxford University Press, New York, USA (1995).

[3] E. Fukushima and S. B. W. Roeder, *Experimental pulse NMR: A nuts and bolts approach*, Perseus, Reading, UK (1981).

[4] R. K. Harris, *Nuclear magnetic resonance spectroscopy: A physicochemical view*, Pitman Books Ltd, London, UK (1983), 230-232.

[5] J. F. Stebbins, *Nuclear Magnetic Resonance Spectroscopy of Silicates and Oxides in Geochemistry and Geophysics*, Mineral Physics and Crystallography: A Handbook of Physical Constants, American Geophysical Union (1995), 303-331.

[6] M. H. Levitt, *Spin Dynamics: Basics of Nuclear Magnetic Resonance*, John Wiley & Sons Ltd., Chichester, UK (2001).

[7] M. E. Smith and E. R. H. van Eck, *Recent advances in experimental solid state NMR methodology for half-integer spin quadrupolar nuclei*, Progress in Nuclear Magnetic Resonance Spectroscopy, **34** (1999), 159-201.

[8] K. J. D. MacKenzie and M. E. Smith, *Multinuclear solid state NMR of inorganic materials*, Pergamon, London, UK (2002).

[9] J. K. M. Sanders and B. K. Hunter, *Modern NMR Spectroscopy; A guide for chemists*, Oxford University Press, New York, USA (1988).

[10] H. -J. Behrens and B. Schnabel, *The second order influence of the nuclear quadrupole interaction on the central line in the NMR of quadrupolar nuclei using rapid sample spinning*, Physica B, **114** (1982), 185-190.

Chapter 3

NMR Experimental Methodology

3.1 Introduction

In order to successfully perform an NMR experiment the sample must contain NMR-active nuclei of non-zero spin *I*. The sample is then packed into a ceramic rotor in powdered form to ensure that there is a random distribution of crystallographic orientations to the direction of the magnetic field. The rotors used are available in a variety of materials and diameters depending upon the type and volume of material being investigated, the spinning speeds required and the temperature of the experiment. The rotor is placed into a probe which in turn is

inserted into the bore of a superconducting magnet such that the sample sits at the centre of the magnetic field.

The probe is attached to a dry, filtered gas supply, the airflow of which is used to physically rotate the rotor at various spin rates which can be controlled down to an accuracy of approximately ±1 Hz. This spinning frequency can be precisely measured using a fibre optics spin rate detector fitted within the probe, which may be monitored using an oscilloscope or frequency counter. The probe contains the relevant electronics required for the coil used to generate the electromagnetic field of the r.f. pulse, to detect the NMR signal and be resonant at the correct NMR frequency. Once placed within the bore of the magnet the probe is connected via a preamplifier and receiver, to the computer console and must be tuned to the desired frequency which is dependent upon the magnetic field strength of the magnet and the type of nucleus studied. This tuning is achieved by varying the capacitors and inductors contained within the probe. The magic angle can also be adjusted to ensure that it is at 54.74 ° to the applied magnetic field $\underline{B}_0$.

The magnetic field required for an NMR experiment must be stable and have a high level of homogeneity, it is therefore supplied by a superconducting magnet consisting of a niobium-based superconducting alloy solenoid [1] maintained at an operating temperature between 2.2 K and 4.3 K achieved by immersion in liquid

helium [2]. This is surrounded by a vacuum chamber to reduce any thermal conductivity, which is then encased in liquid nitrogen at a temperature of 77 K [3].

The samples researched in this study have been supplied from various academic institutions and arrived in bulk, grain or powdered form. None of these samples were made in-house and the relevant institutions involved in their manufacture have all been identified in this section[i]. Information about the exact sample formation process has been included in section 1 of this report but additional details may be found in the references.

3.2 The NMR spectrometer

The spectrometers used for the various nuclei are listed below in table 3.1:

Spectrometer Details	*Nuclei*
Varian Infinity-Plus 300 MHz spectrometer equipped with a 7.1 T superconducting magnet.	^{31}P, ^{65}Cu
Varian-Chemagnetics CMX 360 MHz Infinity spectrometer equipped with an 8.45 T magnet.	^{29}Si, ^{23}Na, ^{31}P
Varian-Chemagnetics CMX 600 MHz Infinity spectrometer equipped with a 14.1 T magnet.	^{23}Na, ^{27}Al, ^{33}S
Varian-Chemagnetics CMX 800 MHz Infinity spectrometer equipped with an 18.8 T magnet.	^{23}Na, ^{27}Al

Table 3.1: Spectrometer allocation for each nucleus studied.

[i] I would like to acknowledge the various teams who have provided me with samples upon which to base this work, see section 1 and the formal acknowledgements for further details.

The nuclei investigated require different spectrometers that can operate over a large frequency range enabling the study of a variety of nuclei using the optimum magnetic field [4]. For a specific nucleus the highest frequency, corresponding to the highest magnetic field should be used to maximise sensitivity, as the signal is proportional to B_0^2. Choosing higher fields also reduces the deadtime[ii] associated with each pulse, which is inversely proportional to the operation frequency [4]. The disadvantage however, is that if there exists a contribution to a particular spectral line via an interaction which scales proportionally with field, then going to higher fields may cause the effect to swamp the signal, so this must also be considered. For example, the quadrupolar interaction scales as $1/B_0^2$ and as such becomes less significant at high fields, whereas CSA is directly proportional to B_0 thus giving a broader linewidth at high fields (in Hz). Therefore, if a sample has a large CSA (for example samples with high ^{31}P content [1]) then increasing the operating field can have detrimental effects on the signal received by creating more spinning sidebands.

It is also important to choose a suitable probe for each sample, for example, one which does not contain the same material as that being studied or consisting of a material with an NMR frequency close to that being investigated. If a probe contains copper whilst running ^{23}Na experiments on the 8.45 T spectrometer, the frequencies are close enough that a Cu peak is observed in the Na spectra.

[ii] The deadtime is the finite time between the NMR coil switching between applying the r.f. pulse to the system and receiving the NMR signal. During this time no signal can be detected.

Furthermore, in some samples a large quantity of material is a virtue if the signal is weak, but there arises a trade off between sample volume (directly related to the rotor size) and spinning speed, as smaller rotor diameters increase the possible spin rate leading to better resolution by removing the sidebands.

3. 3 Pulse sequences

3.3.1 Single-pulse NMR experiments

The most basic NMR experiment is that using a single r.f. pulse. The pulse sequence can be best described visually and the diagram for this is illustrated in figure 3.1.

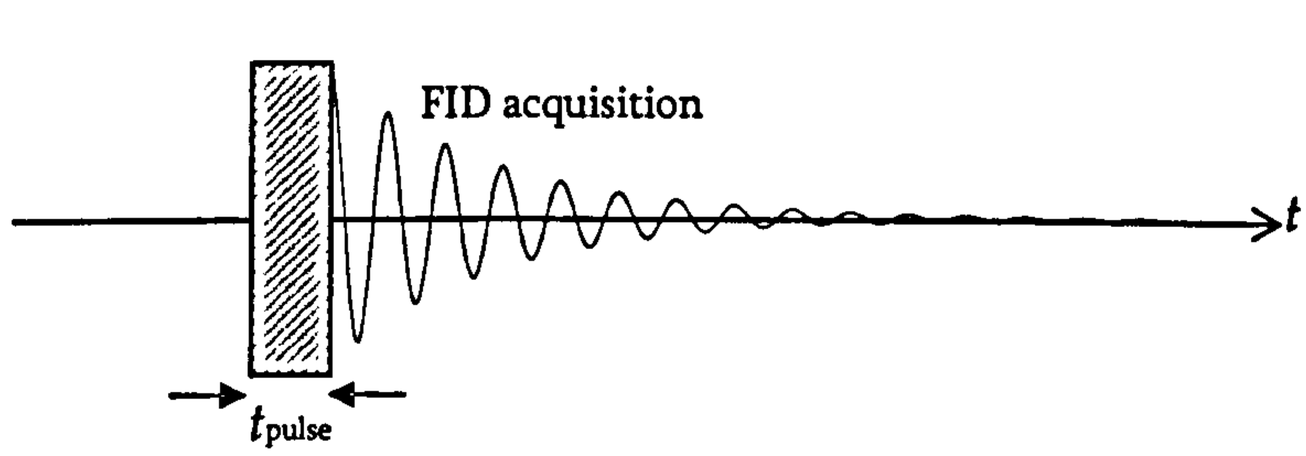

Figure 3.1: A representation of a one-pulse NMR experimental sequence.

The figure shown represents the timing sequence of the one-pulse NMR experiment. The time axis runs horizontally from left to right to demonstrate the timing of the applied pulse and the received FID. Note that this has not been drawn to scale [3] as

the r.f. pulse is usually of the order of microseconds whilst the acquisition is of the order of milliseconds[iii].

The applied r.f. pulse acts to tip the net magnetisation vector such that it is directed along the *xy* plane to allow a signal to be detected using the surrounding inducting coil. The longer the time duration of the r.f. pulse, the larger the flip angle applied. Ideally the applied pulse should flip the net magnetisation vector by 90 ° directly from the *z*-axis into the *xy* plane in order to obtain a stronger signal as it is only the precession of the magnetisation in this plane which contributes towards the signal. However, for samples that require a very long r.f. pulse to achieve this 90 ° flip angle due to the value of their gyromagnetic ratio, or for samples with a long T_1 spin-lattice relaxation time, it can sometimes be more effective to use a shorter tip angle and instead pulse faster and take a larger number of data acquisitions in order to increase the signal-to-noise ratio and to compensate for the smaller component of magnetisation in the *xy* plane [3 & 4].

As considered in chapter 2, the NMR signal is weak and the acquired data can contain high noise levels. In order to increase the signal-to-noise ratio the experiment is repeated numerous times and the signals are added, which is referred to as signal averaging [3]. Signal averaging works due to the random nature of the

---

[iii] The deadtime occurs immediately after the r.f. pulse has ended and delays the commencement of the acquisition for a finite time so the observed data collected has the start of the FID missing. As this deadtime is so short in comparison to the r.f. pulse and FID duration, it has been omitted from figure 3.1.

noise contribution which therefore does not sum in a linearly accumulative fashion whereas the signal does. The signal-to-noise ratio increases by a factor of $\sqrt{n}$ for n acquisitions summed. However, it must be noted that due to the finite spin-lattice relaxation time, T_1, taken for all of the nuclear spins in the sample to have returned to their equilibrium positions, there must be a sufficient delay, greater than five times the duration of T_1, in between each pulse applied to obtain a quantitatively relaxed spectrum.

3.3.2 Spin-echo pulse sequence experiments

In the case of the sulphur-doped aluminosilicate glass samples, a more complicated pulse sequence must be used as ^{33}S has a low gyromagnetic ratio ($\gamma = 2.055 \times 10^7$ rad T^{-1} s^{-1} which is less than 20 % of the gyromagnetic ratio for ^{31}P of 10.8394×10^7 rad T^{-1} s^{-1}). As the Larmor frequency for sulphur is low (46.07 MHz using a 14.1 T magnet) any corruption of the start of the data acquisition can be detrimental to the Fourier transformed frequency spectrum, because of effects such as probe ringing can last for longer at lower frequencies such that more of the FID is lost. To avoid these effects a pulse sequence known as a spin-echo experiment is used which consists of two r.f. pulses where the second pulse is 180° with a separation time of $\tau/2$, see figure 3.2.

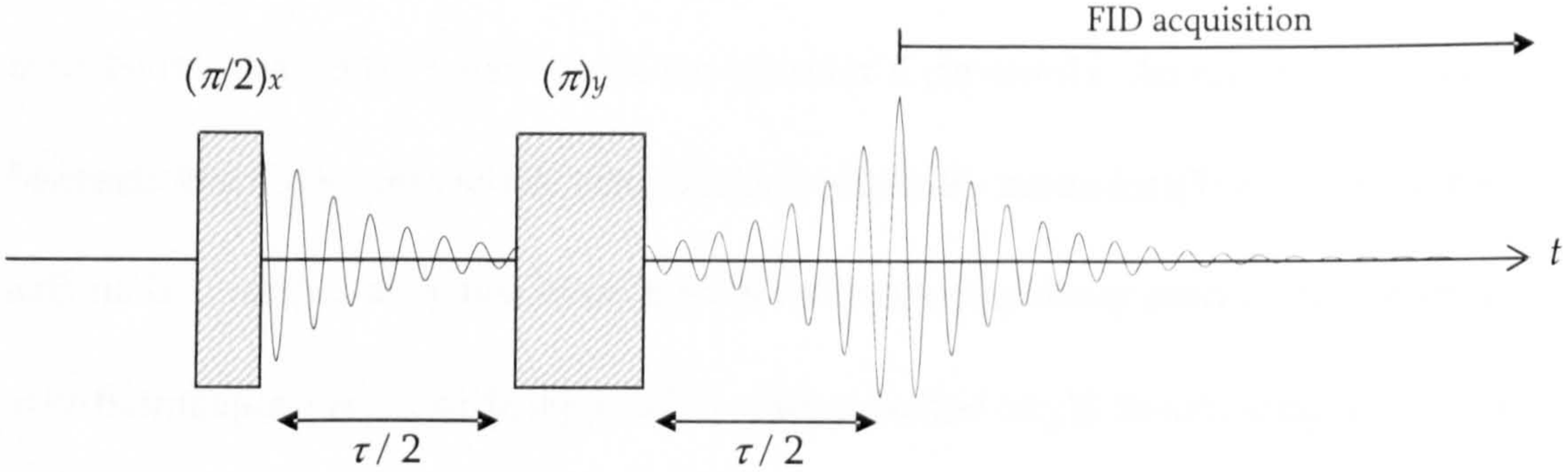

Figure 3.2: A representation of a two-pulse spin echo NMR experiment.

The first pulse applied is a 90° ($\pi/2$) pulse (in this case along the x-axis of the rotating frame [3]) which flips the net magnetisation into the xy plane as in the single-pulse experiment. During the time $\tau/2$ a certain amount of dephasing of the spins will have occurred due to the individual nuclear spins experiencing slightly different local magnetic fields. Their magnetisation vectors therefore begin to spread out in a fan-like manner in the xy plane as the group of spins lose coherence. At time $\tau/2$ the second 180° (π) pulse is applied in the rotating frame about the y-axis (denoted by the subscripts in figure 3.2), so that the magnetisation vectors are rotated about the y axis where they refocus after a time $\tau/2$ forming the spin-echo signal [3]. This means that the FID when acquired is now a time $\tau/2$ away from the pulse which removes any of the corrupting effects from the beginning of the acquisition leaving a cleaner and more easily processed signal.

3.4 Sample preparation

Regardless of the form in which NMR samples are received (i.e. in bulk form, shards, grains or powders) the samples must all be finely ground powders in order to pack them into the NMR rotors such that they can be spun in a stable way within the probe and also to give an isotropic sample to achieve a spatial averaging as some samples may have a preferred crystallographic orientation. Once tightly packed into the rotor the magic angle may be checked using yttrium aluminium garnet (YAG) as a reference sample for ^{27}Al NMR. The probe can then be tuned for the relevant nucleus.

3.5 Specific experimental details for the samples studied

3.5.1 Copper- and silver-doped phosphate glasses

The silver- and copper-doped phosphate glass samples were supplied by the Eastman Dental Institute at University College London. The initial ^{31}P NMR experiments were performed using a Varian-Chemagnetics CMX 360 MHz Infinity spectrometer equipped with an 8.45 T magnet operating at a frequency of 145.85 MHz. A Varian 4 mm probe was used and the samples were spun at ~12 kHz. A standard one pulse experimental procedure was used. The spectra for the purely glassy samples were accumulated with a single pulse of 2 μs (corresponding to a tip angle of 90 °) and a recycle delay of 3 s. For the partially crystalline samples a single pulse of 1.4 μs (corresponding to a tip angle of 30 °) and a recycle delay of 450 s were used as they

were found to have an extremely long T_1 relaxation time of 360 s so to compensate for this long T_1 a smaller tip angle was used thus allowing a shorter recycle delay. The spectra were referenced against a secondary reference of $NH_4H_2PO_4$ at a shift of +0.9 ppm such that the spectrum is reported on a shift scale relative to the primary shift reference of 85 % H_3PO_4. These experiments were later repeated using a Varian Infinity-Plus 300 MHz spectrometer equipped with a 7.1 T superconducting magnet.

^{23}Na NMR experiments were performed on both sets of samples using a Varian–Chemagnetics CMX 360 MHz Infinity spectrometer equipped with an 8.45 T magnet operating at a frequency of 95.43 MHz using a Bruker 4 mm probe with the sample spinning at ~12 kHz, as well as a Varian-Chemagnetics CMX 600 MHz Infinity spectrometer equipped with a 14.1 T magnet operating at a frequency of 159.03 MHz, using a 3.2 mm probe with the sample spinning at ~16 kHz. The experiment was performed at two fields because ^{23}Na has spin $I = 3/2$ and therefore has asymmetric peaks due to the non-spherical electric charge distribution giving rise to the quadrupolar interaction. The quadrupolar coupling constant, χ_Q, that describes this interaction can be found from collecting spectra at multiple fields and peak fitting. A selection of the samples were also recorded using a Varian–Chemagnetics CMX 800 MHz Infinity spectrometer equipped with a 18.8 T magnet operating at a frequency of 211.73 MHz in order to constrain the fitting parameters further.

Additional experimentation completed is outlined in chapter 4.

3.5.2 Yttrium- and lanthanum-doped phosphate glasses

The samples supplied from the University of Bath were a mixture of aluminophosphate and aluminosilicate glasses. They were firstly ground into a fine powder and ^{31}P, ^{27}Al and ^{29}Si NMR experiments were all performed.

Aluminium NMR is a commonly used technique as the natural abundance of ^{27}Al is 100 % so there is no need to enrich the samples. ^{27}Al is a spin ½ nucleus and thus has a quadrupole moment arising from a non-spherical charge distribution which interacts with the electric field gradient. One effect of having a quadrupole interaction is that it broadens peaks and the peaks also become asymmetric, thus it is advantageous to run these experiments at two fields so that the quadrupolar coupling constant can be determined more accurately by fitting the quadrupolar lineshape [5]. Another advantage of running experiments at higher fields is that the resolution is much improved and peaks can therefore be more easily distinguished. The two-field data was collected using one-pulse experiments using both a Varian-Chemagnetics CMX 600 MHz Infinity spectrometer with a 14.1 T magnet operating at a frequency of 156.33 MHz with a Varian 3.2 mm probe at a spin rate of ~20 kHz, and a Varian-Chemagnetics CMX 800 MHz Infinity spectrometer along

with a 18.8 T magnet operating at a frequency of 208.57 MHz using a Varian 3.2 mm probe and a spin rate of ~16 kHz.

^{31}P and ^{29}Si experiments are considered simple in comparison as they are spin $I = ½$ nuclei and as such have spherical charge distributions. ^{31}P is also a 100 % naturally abundant nucleus with a large magnetic moment and thus high sensitivity. ^{29}Si has a natural abundance of 4.7 % and usually has a high spectral resolution due to narrow spectral lines. Both the ^{31}P and ^{29}Si NMR experiments were performed using a Varian-Chemagnetics CMX 360 MHz Infinity spectrometer together with an 8.45 T magnet. The operating frequency for the ^{31}P experiments was 145.85 MHz and a Varian 4 mm probe was used and the samples were spun at ~12 kHz. 71.23 MHz was the operation frequency used for the ^{29}Si NMR using a Chemagnetics Apex 6 mm probe and a spinning frequency of ~4 kHz.

3.5.3 Sulphur-doped aluminosilicate glasses

The sulphur-doped aluminosilicate glasses were supplied from the University of Bristol and were ground into fine powders before ^{33}S NMR experiments were completed. These studies were carried out using a Varian Chemagnetics CMX 600 MHz Infinity spectrometer equipped with a 14.1 T magnet operating at 46.07 MHz. Spectra were collected using a Varian 4 mm T3 probe and the samples were spun at ~15 kHz. A spin-echo sequence with a 90 ° pulse followed by a 180 °

pulse and extended (16 pulse) phase cycling to perform the usual phase cycle whilst removing any artefacts produced by the direct magnetisation from the second pulse, was used [6]. The delay between these two pulses was set as the inverse of the MAS spinning frequency (66.7 μs) such that the echo formed by the spin-echo and the echo formed by the MAS rotation are in phase, and a recycle delay of 1 s was used. The spectra were referenced against a secondary reference of CaS at a shift of –28.5 ppm, such that the spectrum is reported on a shift scale relative to the primary shift reference of CS_2.

^{33}S is a quadrupolar nucleus ($I = 3/2$) with a low abundance and a small gyromagnetic ratio (therefore known as a low gamma nucleus) making these experiments highly insensitive especially considering the extremely low molar percentages of ^{33}S present in the samples. The experiments thereby needed long averaging times and numerous experimental difficulties arose whilst setting up the equipment. Only one published study [6] has thus far applied this technique as it is still considered as a scientific experiment in its infancy [7].

^{27}Al NMR was also performed on the samples containing aluminium. This was achieved using a Varian-Chemagnetics CMX 600MHz Infinity spectrometer with a 14.1 T magnet operating at a frequency of 156.33 MHz with a Varian 3.2 mm probe at a spin rate of ~20 kHz

3.6 Data processing

The data retrieved from an NMR experiment is the superposition of a large number of data acquisitions, the more of which are collected, the better the signal-to-noise ratio obtained. The raw data collected is in the form of an FID as discussed in section 2.4, which shows a spectrum of signal points in the time domain. As there are various effects such as probe ringing as mentioned in section 1.3.1 which occur prior to the start of the data acquisition, so that the first few points of the acquired data can sometimes be corrupted and thus need removing from the FID. This can be achieved using Varian-Chemagnetics Spinsight acquisition and processing software version 4.3.2 and a backwards extrapolation can then be inserted in order to return the same number of points, otherwise the removal of points from the start of the FID would introduce a shift in the timescale, creating a phase shift of the frequency domain data. A DC offset correction must then be performed which ensures that the FID is centred along the $y = 0$ baseline such that no artificial frequencies will be observed once the Fourier transform of the data is performed.

To improve the signal-to-noise ratio and to give a smoother output signal, the raw data can be smoothed by both or either, removing the end points of the FID where the signal has decayed sufficiently for this data to be unimportant to the spectrum and by multiplying the signal by a mathematical function [1] which enhances the beginning of the FID where the signal is at its strongest.

Once these functions have been successfully performed the fast Fourier transform (FFT) can be used to give an output spectrum of intensity versus frequency, which in turn is scaled to give the spectrum in terms of chemical shift, δ, in ppm.

3.7 Data fitting

In order to obtain any quantitative information from the spectroscopic data, often the spectral lines must be fitted using a specially designed fitting program to give values such as the relative abundance of the different site occupancies for a specific nucleus within each sample and for $I > ½$ nuclei, the values describing their quadrupolar interactions.

The two main fitting programs used are DMFit [8] and QuadFit [9]. DMFit has the advantage of being simple and fast to use for simplistic systems as the Gaussian peaks added can be easily manipulated and provides an immediate read out of chemical shift position in ppm, full width at half maximum height (FWHM) in ppm, and the intensity as a percentage of all of the peaks present. The fitting can however become more complicated in cases where there are a large number of overlapping spectral lines present in a spectrum, for example in partially crystallised glass samples that are hugely disordered. The program is nonetheless sufficient for spectra of nuclei that are spin $I = ½$ as the peaks present are assumed to be purely Gaussian.

For systems where $I > ½$, DMFit is sometimes not adequate as it cannot readily take into account distributions of the quadrupolar interaction for example, and in this case QuadFit was used. This fitting process here is more complex as the fits are achieved by a very much 'trial and error' approach and there are many more parameters that can be manipulated, giving rise to extra uncertainties in the fits. However, collecting spectra at multiple fields constrains these parameters and leads to a more accurate overall fit from which the data obtained includes the peak position in ppm, intensity as a percentage of the total intensity of the peaks present, Gaussian broadening in Hz, quadrupolar coupling constant, χ_Q, in MHz and the quadrupolar distribution, $\Delta\chi_Q$, also measured in MHz.

References

[1] K. J. D. MacKenzie and M. E. Smith, *Multinuclear solid state NMR of inorganic materials*, Pergamon, London, UK (2002).

[2] A. Street, *Superconducting magnets: at the heart of NMR*, NMR Spectroscopy, Spectroscopy Europe, **15**:1 (2003), 10-13.

[3] M. H. Levitt, *Spin dynamics: Basics of nuclear magnetic resonance*, John Wiley & Sons Ltd., Chichester, UK (2001).

[4] E. Fukushima and S. B. W. Roeder, *Experimental pulse NMR: A nuts and bolts approach*, Perseus, Reading, UK (1981).

[5] J. F. Stebbins, *Nuclear magnetic resonance spectroscopy of silicates and oxides in geochemistry and geophysics*, Mineral Physics and Crystallography: A Handbook of Physical Constants, American Geophysical Union (1995), 303-331.

[6] S. Couch, A. P. Howes, S. C. Kohn and M. E. Smith, *^{33}S solid state NMR of sulphur speciation in silicate glasses*, Solid State NMR, **26** (2004), 203-208.

[7] J-B. d'Espinose de Lacaillerie, F. Barberon, B. Bresson, P. Fonollosa, H. Zanni, V. E. Fedorov, N. G. Naumov and Z. Gan, *Applicability of natural abundance ^{33}S solid-state NMR to cement chemistry*, Cement and Concrete Research, **36**:9 (2006), 1781-1783.

[8] D. Massiot, F. Fayon, M. Capron, I. King, B. Alonso, J-O. Durand, B. Bujoli, Z. Gan and G. Hoatson, *Modelling one- and two-dimensional solid-state NMR spectra*, Magnetic Resonance in Chemistry, **40** (2002), 70-76.

[9] T. F. Kemp, *High field solid state ^{27}Al NMR of ceramics and glasses*, Masters Thesis, University of Warwick, UK (2004).

Chapter 4

Other Experimental Techniques

4.1 Introduction

In addition to NMR numerous other experimental techniques have been employed in this study to gain a further understanding of the glass coordination, molecular bonding, dopant site occupancy and valences, magnetic and thermal properties, degradation rates and antibacterial effects, to name but a few. What follows in this chapter is a description of the theoretical background and experimental methodology for the main analytical techniques performed by the author, whilst supplementary experiments conducted on the samples in this study by collaborators

including antibacterial studies, differential thermal analysis (DTA), neutron diffraction (ND) and X-ray absorption near edge structure (XANES) for example, have been briefly described along with their findings in the relevant results sections and the appropriate acknowledgements for all external collaborative work can be found within this information.

4.2 Electron paramagnetic resonance

The physical principles of the electron paramagnetic resonance (EPR) technique are comparable to those applicable to NMR, the critical difference being that whereas NMR probes the structural atomic environments via manipulation of the magnetic properties of nuclear spins, EPR exploits the spins of unpaired electrons to ascertain similar information.

4.2.1 Background theory

Electrons have a magnetic moment μ arising from their spin[i] ($S = ½$) and orbital angular momentum, which in the presence of an external magnetic field $\underline{B}_0$ aligns either parallel or antiparallel with the field ($m_S = \mp ½$, respectively), analogous to the spin $I = ½$ nuclei in an NMR $\underline{B}_0$ field. The energy for the $m_S = +½$ level relating to the electron spin aligning against the magnetic field, is greater than that of the $m_S = -½$ state and is linearly dependent upon the magnetic field strength applied.

[i] Equivalent to I for nuclear spins.

This phenomenon is known as the electronic Zeeman effect and the difference in energy between the two states arising is given by $\Delta E = g_e \mu_B B_0$ where g_e is the Landé g-factor (or Zeeman splitting constant) for a free electron equal to 2.002319304386 [1] and μ_B is the Bohr magneton ($\mu_B = e\hbar/2m_e$). With the application of a magnetic field, magnetic dipole transitions can be induced between the two electron states if photons of the correct energy, $h\nu$, are applied to the system, as this is known as the resonance condition.

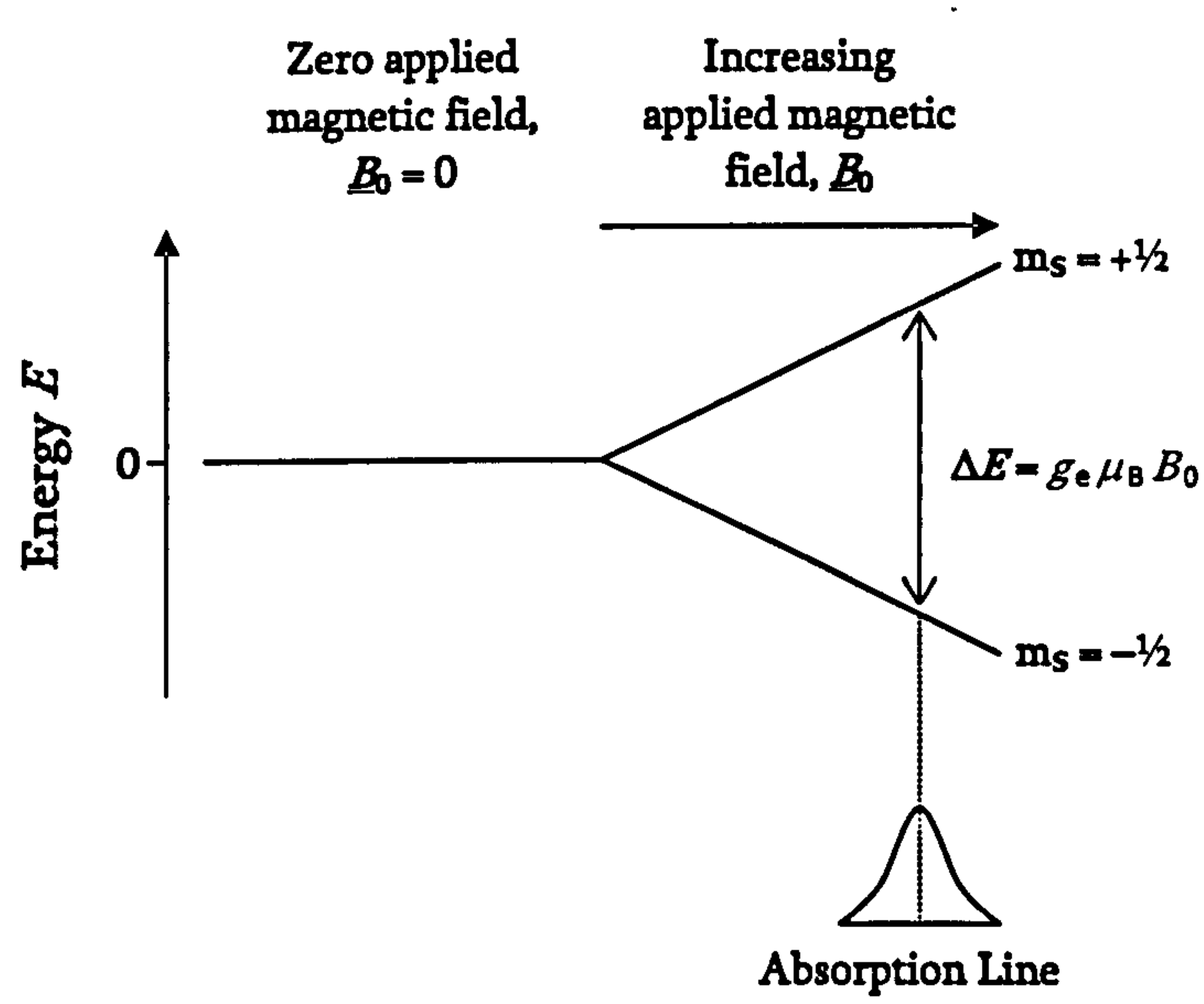

Figure 4.1: Electronic Zeeman energy level splitting for an electron in an applied magnetic field B_0. Transitions between the two levels are permitted when the incoming microwave energy is equal to that of the energy level difference and an absorption line such as the one shown is achieved.

Unlike the NMR method, the EPR technique implemented uses a fixed frequency of microwaves and an external magnetic field provided by an electromagnet that is swept until it matches the energy of the microwaves $h\nu = \Delta E = g_e \mu_B B_0$, see figure 4.1. Microwaves are used rather than the radio frequency wavelengths in NMR as the magnetic moment of an electron is far greater than that of a nucleus

which means that a higher frequency is required for similar magnetic field strengths although typically a smaller magnetic field (~0.35 T) is used in EPR. When the swept field matches the microwave frequency, transitions between the unpaired electrons in the two energy levels (spins states) are created. Due to a Maxwell-Boltzmann population distribution there are slightly more electrons in the lower state resulting in a net absorption of energy at this field as the lower level electrons are excited into the higher level population. The electrons from the higher state undergo spin-lattice (longitudinal) relaxation via phonon emission and re-enter the lower state maintaining the population difference and leading to a constant absorption of microwaves. This absorption is observed with respect to the swept field by the detection of differences in the impedance of the sample cavity (explained in more detail in the following section 4.2.2) and a lock-in detector is used to minimise noise, resulting in the spectra being displayed as the first derivative of the absorbance as a function of field in Gauss.

In addition to the spin-lattice relaxation, as in NMR there is a spin-spin (transverse) relaxation process due to loss of coherence between the electron spins and these mechanisms contribute to the Lorentzian absorption line achieved from the absorption of microwave radiation. Anisotropic effects discussed below give rise to additional broadening of this linewidth causing the absorption line to become more Gaussian in appearance [2], although the spectrometer output is the first derivative of this signal.

When the unpaired electrons undergoing the dipole transitions are associated with atoms in a material such as the solid glass powders examined in this study, the electrons can experience variations in the overall magnetic field as a result of the local magnetic fields in the surrounding environment. Thereby the total effective magnetic field experienced by the electrons can be described by $B_{eff} = B_0(1-\sigma)$ where σ accounts for all of the effects of local magnetic field variations. The difference in energy between the states therefore becomes $\Delta E = g_e \mu_B B_{eff} = g_e \mu_B B_0(1-\sigma) = g\mu_B B_0$, where $g = g_e(1-\sigma)$ and is known as the g-factor [1]. This g-factor value can be determined in an EPR experiment by measuring the field and frequency at which resonance occurs. Variations of g away from g_e describe the differences between the electrons in the material and free electrons, giving rise to information about the nature of the electronic structure and atomic orbital containing the unpaired electron which in turn aids in describing their chemical environment. As the spin-orbit coupling of the electrons influences their effective magnetic moment, the splitting of the electron energy levels and consequently the measured g-factor can also indicate the extent of this coupling. Environmental characteristics can also influence the shape of EPR spectral lines as well as their spectral linewidth values, ΔB, achieved from an experiment. As the magnetic field variations are not necessarily isotropic this leads to an anisotropic Zeeman interaction, thus different values of g can be obtained along different axes which can cause splittings in the EPR lines observed, leading to information about any symmetry in the environment [1].

Other interactions within the material which contribute to the changes in local magnetic environment of the unpaired electrons are described by the effective spin Hamiltonian in a very similar way to NMR and this is outlined below:

$$\mathcal{H}_{\text{total}} = \mathcal{H}_{\text{ElectronicZeeman}} + \mathcal{H}_{\text{ZeroField}} + \mathcal{H}_{\text{Hyperfine}} + \mathcal{H}_{\text{Quadrupole}} + \mathcal{H}_{\text{NuclearZeeman}} \qquad (4.1)$$

The electronic Zeeman interaction can be determined by the g-values arising and has been described above which also takes spin-orbit coupling into consideration. Electrons can also interact with each other giving rise to exchange and zero-field interactions [1], which as the name suggests, are present in the absence of an external field. A system of two coupled, unpaired electrons leads to four energy levels [3] and the exchange interaction arising from the Coulomb interacting electron wavefunctions lifts some of the degeneracy of these electron spin states leading to a triplet and a singlet state separated in energy [1] without the need for a magnetic field. In addition to this exchange interaction, dipole-dipole interactions cause the three-fold degeneracy of the triplet state to be removed in the absence of a magnetic field [1] as shown in figure 4.2. This dipole-dipole interaction between the electrons is analogous to that between the nuclei in NMR, where the local magnetic fields associated with the magnetic moments of neighbouring unpaired electrons are experienced by each other and the strength of interaction is dependent upon their interspatial separation. A distribution of these interactions means that this effect can create strong broadening of the spectral features present in the EPR spectra [2]. In these experiments there was no evidence for the exchange interaction in our

samples, but the dipole-dipole interaction is most likely responsible for broadening the signals observed.

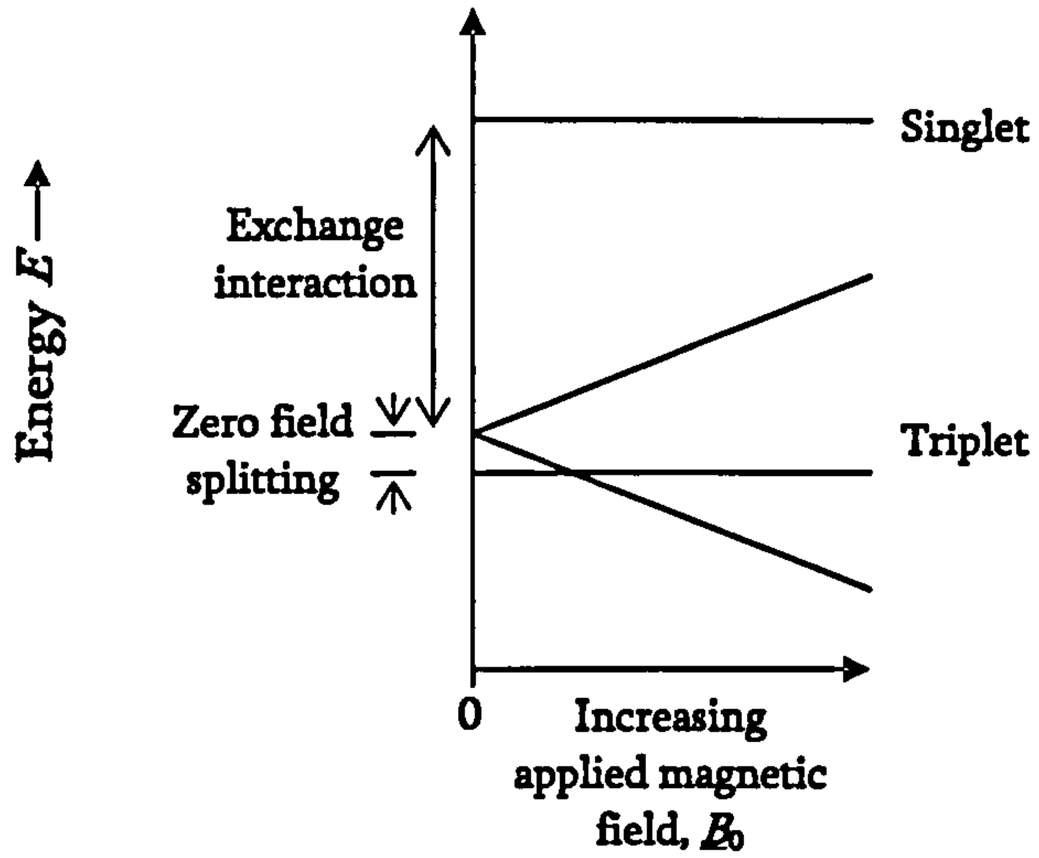

Figure 4.2: Effects of the exchange interaction and zero field splitting on the energy levels for two coupled electrons in an increasing applied magnetic field B_0.

The hyperfine interaction is a measure of the coupling between the magnetic moments of the unpaired electrons and nuclei with spin $I > 0$ such as spin $I = ½$ copper nuclei, creating further energy level perturbations which produces additional lines in the EPR spectrum [1]. The number of additional lines is indicative of the nuclear spin, I, involved and the magnitude of the splitting between the lines indicates the degree of interaction or coupling between electronic and nuclear magnetic moments which can reveal the probability density of the unpaired electron distribution at the nucleus [1].

The quadrupole interaction is the effect that a nucleus of spin $I > ½$ has upon the environment of the unpaired electrons due to their asymmetric charge distributions as discussed in the NMR section (2.4.4). These nuclei have a characteristic quadrupolar moment which is a measure of the anisotropy or departure of the nuclear electrical charge distribution from spherical symmetry. The charge interacts with any electron field gradients due to surrounding electron charges, further perturbing the energy states of the unpaired electrons. This has only a very small effect on the spectra producing at most a slight asymmetric shift in the lines present.

Finally the nuclear Zeeman effect is the same as that in NMR where the externally applied magnetic B_0 field interacts with the magnetic moments of nuclei with spin $I > 0$. However to a first-order approximation this has no effect on the EPR spectrum since we are observing only the transitions governed by the selection rules $\Delta m_S = \pm 1$ and $\Delta m_I = 0$ [2], see figure 4.3.

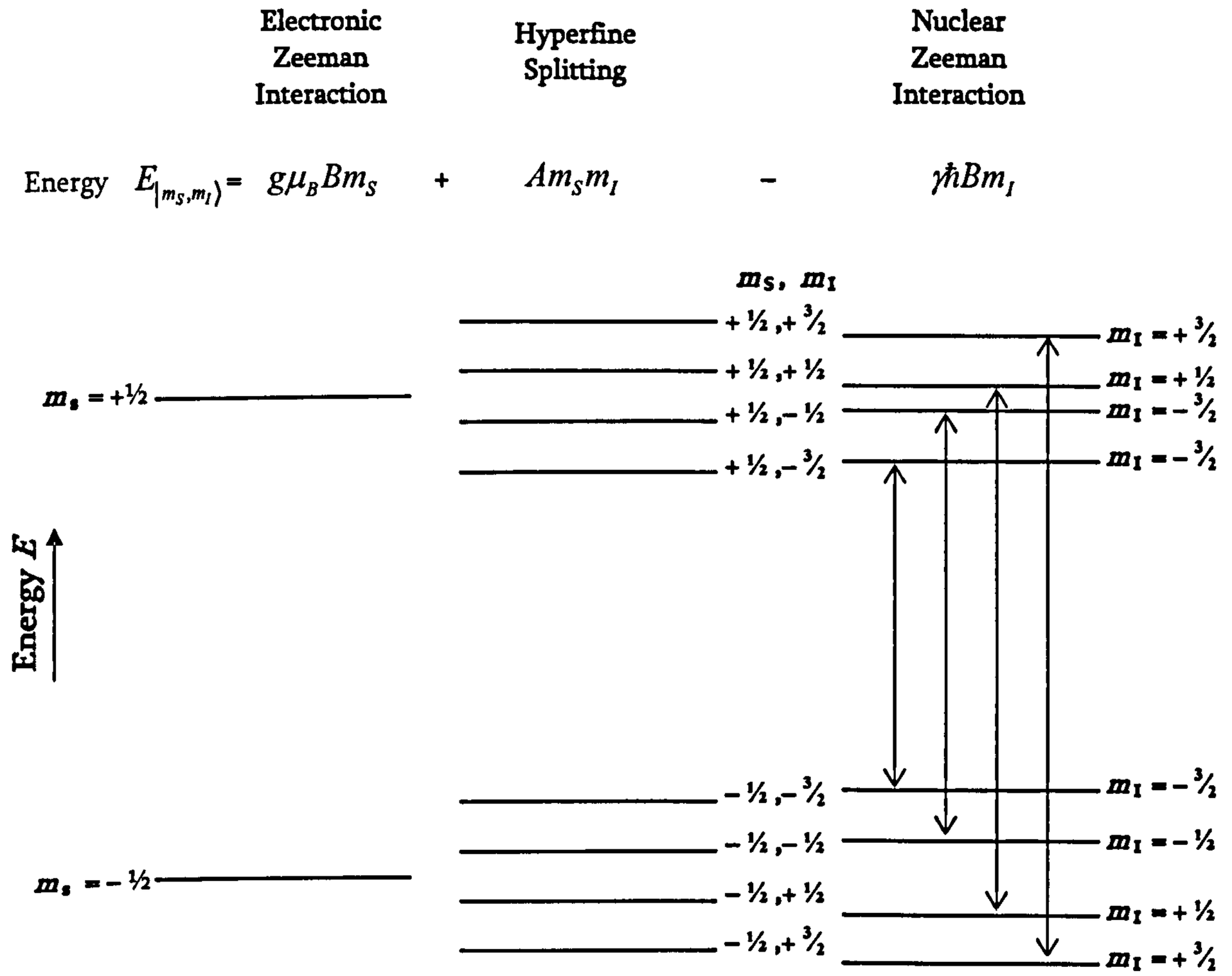

Figure 4.3: The energy level splitting for an $S = ½$ unpaired electron in a finite magnetic field B_0 undergoing the electronic Zeeman interaction, hyperfine splitting due to the presence of copper nuclei and the nuclear Zeeman interaction. The energies associated with each contribution are stated where A is the hyperfine structure term and the nuclear Zeeman interaction illustrates the energy perturbations involved. The $\Delta m_S = \pm 1$ and $\Delta m_I = 0$ allowed transitions are also displayed.

4.2.2 Experimental details

The EPR measurements were completed using a continuous wave (CW) Bruker EMX X-band (8 to 12 GHz) spectrometer with an operation frequency between 9.5 to 9.8 GHz. The microwave source and the EPR detector are housed within a microwave bridge. The microwaves are produced by a Gunn diode source of 200 mW power which is used as an oscillator coupled to a waveguide resonator that

channels the waves into the sample cavity. An automatic frequency controller (AFC) ensures that the output frequency is equal to that of the sample cavity by detecting any difference between the actual oscillator frequency and the target frequency and producing a voltage proportional to the difference arising. This is fed back into the tuning circuit which changes the oscillator to the correct frequency at the beginning of each experimental scan thereby minimising any drift. As it is difficult to linearly vary the power of the Gunn diode itself an attenuator controls the power of the microwaves entering the sample cavity. This was set at 44 dB for each of the experiments and is equivalent to a power of 8 μW incident upon the cavity, thus ensuring no microwave power saturation occurred.

The spectrometer was equipped with a Bruker ER4119HS transverse electrical (TE) 011 cavity into which the powdered samples were loaded using cylindrical quartz sample tubes. The waveguide channels the microwaves into this cavity via an aperture called the iris which controls the amount of microwaves entering and reflecting from the cavity by way of a screw adjustment altering the impedance between the cavity and waveguide [1]. These refinements are achieved via the manipulation of running parameters by adjusting the options on the computer-based interface console managing the signal processing and control electronics. The loaded cavity is matched such that reflection of microwaves is a minimum, meaning that almost all of the microwave energy is stored in the cavity. The efficiency of the cavity at storing this energy is dependent upon the properties of the sample cavity

and is measured by the quality-, or Q-factor. This Q-value is calculated by the ratio of energy stored to the energy dissipated within the cavity [1], such as through absorption from electrons in the cavity walls, sample holder and sample. When energy is lost in the cavity walls, the microwaves generate electrical currents in these side walls and this generates heat. When the magnetic field provided by a Bruker ER070 electromagnet, supplying a maximum field of 0.6 T (6000 G), is varied (in the case of these experiments, through a sweep width of 0.3 T (3000 G)), the resonant frequency of the paramagnetic centres in the sample is reached such that absorption of the microwaves takes place. The absorption of microwaves causes the Q-factor to decrease due to losses in energy and this changes the coupling and impedance between the cavity and the waveguide so that they are no longer critically coupled and microwave power is reflected [1]. This reflected microwave power passes through a circulator which redirects it to a detector. The absorption of the microwaves is measured with respect to the swept B_0 field and as such this field must be accurately measured using a Hall probe. As the Hall probe does not sit exactly in the same position as the sample, there can be a small difference between the B_0 field detected and that experienced by the sample. By running a reference sample at the beginning of each experimental session which has a known g-factor and resonance field frequency, any adjustments can be made if there is a slight experimental shift in the expected value.

The sensitivity of the EPR technique is dependent upon the instrument parameters such as the microwave frequency, ν, and the volume of sample present [1]. Influences on the spin environment such as temperature have a strong effect upon the linewidth of the spectrum [1] and the overall characteristics of the spectra such as their linewidth affect the ease with which the spectra can be clearly detected. The properties of the sample cavity also highly influence the sensitivity of the experiments, typically in the instrument used the unloaded cavity has a Q-factor of ~15000 which dropped to between 3000 and 8000 when our samples were inserted.

Phase sensitive detection is used in EPR to enhance the signal-to-noise ratios of the signals observed. This is achieved by using a lock-in detector which functions by sinusoidally varying the B_0 magnetic field over a small range with a given frequency (known as the modulation frequency). This means that the EPR signal over this magnetic field range gives rise to a sinusoidal signal of the same frequency, but with an amplitude proportional to that of the first harmonic of the EPR signal intensity. By comparing this signal to a reference frequency equal to that of the modulation frequency, the lock-in detector produces a DC output signal proportional to the derivative EPR amplitude. As only the signal with exactly the correct frequency and phase as the modulation is picked out by the detector, noise and interference are eliminated from the spectra leading to increased sensitivity [1].

As the aim of the EPR experiments was to provide an indication of the amount of paramagnetic Cu^{2+} centres in the samples compared to the total quantity of copper, it was critical that the integrated intensity of the EPR spectrum be determined accurately as the concentration of paramagnetic ions within the sample is directly proportional to integrated intensity of the EPR spectrum. The intensity of each spectrum was determined using the Bruker WinEPR interactive control system software version 2.11b for data processing by first performing a baseline correction of the integrated signal to correct for any misalignment in the critical coupling, and following this with a double integration as the spectra are recorded as the first derivative of absorbance. This gives a relative integrated intensity that can be compared for all samples after normalising for the sample masses, to give an indication of the change in paramagnetic ion concentration. It is however important to note that the intensities measured must be normalised for the gain used, the number of acquisitions taken and the acquisition time for each scan if these differ for each experiment, although this is now achieved automatically by the spectrometer when collecting the data. The gain used varied between 1×10^3 and 1×10^5 depending upon the strength of the signal received and four scans were taken for each spectrum to achieve better signal-to-noise ratios.

In order to calculate the total number of paramagnetic centres in the samples rather than simply an idea of the general changes as copper-doping levels are varied, the spectra from all samples were compared to a reference sample of anhydrous copper

(II) sulphate powder ($CuSO_4$) (Fisons Scientific) where it is known that for each mole of copper (II) sulphate powder, there is one mole of Cu^{2+}. This means that knowing the mass of each sample and the molecular weights of these, the integrated intensities could be converted to a concentration of Cu^{2+} ions.

Typical associated errors arise from baseline corrections, sample positioning and sample tube variations, leading to uncertainties of up to 40 % [4]. Other factors which can affect the intensities measured are the spectrometer running parameters, therefore highlighting the importance of keeping variables such as the microwave power constant for each experiment or scale accordingly as the integrated intensity is proportional to this [1]. Sample temperature affects the EPR linewidth and intensity as the signal measured is inversely proportional to the temperature since paramagnetism is governed by Curie's law [5]. All spectra were collected at room temperature and experiments on each set of samples were completed on as few separate occasions as possible for consistency. The *Q*-factor of the sample cavity was found to vary greatly with sample position as it is important for the sample to sit where the magnetic field and microwave field are at a maximum as these are the driving mechanisms for the electron transitions. Keeping the sample where the electric field is a minimum means that dielectric losses contributing to poor signal-to-noise can be avoided [1 & 4]. A polytetrafluorethylene (PTFE) Teflon pedestal was used to support the sample holders and minimise any differences in position between each of the samples. The *Q*-factor can also be affected by water

content and variations in the quality of the quartz sample tubes used as the electrons in these materials can absorb the microwaves hence reducing the quality of the critical-coupling bringing about discrepancies in the measured intensities [1]. This has been discussed in greater detail in the results section 6.2.6.

As well as calculating the intensities of the EPR signals received, some simulations were completed using the Bruker BioSpin SimFonia CW processing and simulation package version 1.26 for the PC in which the experimental spectra could be loaded. The fields and splitting of the EPR signals received provide information about the environment of the unpaired electrons, therefore simulating the spectra leads to an indication of the *g*-factors, environmental symmetry, site coordination, distribution and occurrence of hyperfine splitting affecting the electrons.

4.3 Magnetic susceptibility studies

4.3.1 Background theory

The paramagnetic character of an atom arises from its possession of an unpaired electron within its orbitals since electrons have a magnetic moment, μ, originating from their angular momentum, J, consisting of an orbital, L, and spin, S, component[ii]. The magnetic susceptibility χ of a material is a measure of the magnetic response of its magnetic moment to the presence of an external magnetic field of flux B where $\chi = \mu_0 M/B = M/H$ [5]. M is the net magnetisation of the

[ii] $S = ½$ for Cu^{2+} ions [6].

material, μ_0 is the magnetic constant also known as the permeability of free space and H is the magnetic field strength. If χ is small and negative then the material is referred to as diamagnetic where there are no unpaired electrons and thus no contributions from the electron magnetic moments. However, the orbital electrons act as current loops and according to Faraday and Lenz's laws, create a net magnetisation opposing the applied field B. In paramagnetic materials $\chi > 0$ and the magnetic moments of unpaired electrons align such that there is a net magnetisation in the direction of the magnetic field, thereby enhancing it [5]. However, in general, paramagnetic materials also exhibit a diamagnetic contribution, however these effects are far weaker [7].

The paramagnetic susceptibility per mole is given by Curie's law, $\chi = C/T$, where C is the Curie constant and T is the temperature [5]. At sufficiently low external magnetic fields ($\mu_0 H << k_B T$, where k_B is Boltzmann's constant) and relatively high temperatures (higher than the interaction strengths that can give rise to ordering) the Curie constant is given by equation 4.2 [5], below:

$$C = \frac{n\mu_B^2 \mu_{eff}^2}{3k_B} \tag{4.2}$$

n is the molar fraction of paramagnetic centres in the material, μ_B is the Bohr magneton and μ_{eff} is the effective magnetic moment or effective magneton of each paramagnetic ion and can be described by equation 4.3 where g is the Landé g-factor.

$$\mu_{eff} = g\left[J(J+1)\right]^{1/2} \tag{4.3}$$

To investigate the paramagnetism of a material one can therefore apply a constant B field and vary the temperature whilst measuring the net magnetisation M using a magnetometer, discussed in more detail in the following section 4.3.2. This technique is known as thermomagnetic analysis (TMA) and gives a measure of χ versus T from which the Curie constant can be obtained giving a value for n so long as the value for μ_{eff} is known. Conversely it can also be used to estimate μ_{eff} if the value for n is known.

It is important to also mention that some materials can exhibit magnetic ordering in the absence of an applied field due to interactions between the magnetic moments of the atoms. This ordering can be ferromagnetic (FM), antiferromagnetic (AFM) or some other more complicated correlations [5]. In a FM material the magnetic moments of the atoms all align parallel to each other displaying a finite magnetisation in absence of field. In AFM materials the magnetic moments align antiparallel to their neighbouring atoms, i.e. they counter align, leading to zero net magnetisation.

This magnetic ordering is present only below a certain temperature and the type of ordering present can be identified using a magnetometer by applying the Curie-Weiss law shown below (equation 4.4) [5 & 7]. The Weiss constant, θ, gives rise to information about the interactions between the magnetic ions in the sample

where $\theta > 0$ suggests FM behaviour and $\theta < 0$ for AFM interactions within a material.

$$\chi = \frac{C}{T - \theta} \tag{4.4}$$

A vibrating sample magnetometer (VSM) can also be used to detect the net magnetisation of a sample and its operational procedure is outlined in the experimental details section (4.3.2.2). The VSM was operated in the low temperature and high field regime whilst the sample magnetisation was recorded as it saturated with increasing magnetic field *B*. If the magnetic moment of the system arises only from the spin angular momentum contribution as predicted for the copper ions of interest in our samples [5], the system is referred to as quenched. In this case $J = S = ½$ and as the applied magnetic field is increased the magnetisation per mol is given by equation 4.5 using $J = ½$ and $g \approx 2$ [5].

$$M = ngJ\mu_B B_J(x) \approx n\mu_B B_J(x) \tag{4.5}$$

In this equation n is the molar fraction of paramagnetic ions and $B_J(x)$ is the Brillouin function shown in equation 4.6 with variable x given in equation 4.7 [5].

$$B_J(x) = \frac{2J+1}{2J}\coth\left(\frac{(2J+1)x}{2J}\right) - \frac{1}{2J}\coth\left(\frac{x}{2J}\right) \approx 2\coth(2x) - \coth(x) \tag{4.6}$$

$$x = \frac{gJ\mu_B B}{k_B T} \approx \frac{\mu_B B}{k_B T} \tag{4.7}$$

Therefore by experimentally detecting the saturated magnetisation per Bohr magneton (the magnetic moment on each paramagnetic site) per mol and plotting against x from equation 4.7, the molar fraction of paramagnetic centres can be calculated.

4.3.2 Experimental details

It was only possible to implement the SQuID and VSM magnetic susceptibility techniques in this study as the Cu^{2+} ions are the only potentially occurring paramagnetic ions present within our samples. If this were not the case we would not be able to differentiate between these and any other paramagnetic species.

4.3.2.1 SQuID magnetometer measurements

The powdered samples were carefully weighed and loaded into small gel capsules which were in turn fixed to the sample rod arm that could be inserted into the length of the airlocked superconducting quantum interference device (SQuID) magnetometer cavity held at vacuum pressures of the order of a few mbar.

A Quantum Design magnetic property measurement system (MPMS) magnetometer (version 5S) with a SQuID detection system was used to collect the magnetic susceptibility data with respect to changing temperature. The SQuID magnetometer

consists of a cylindrical bore superconducting magnet maintained at liquid helium temperature (4.2 K) in a liquid helium dewar surrounded by a liquid nitrogen chamber (77 K). This provides an axially symmetric variable magnetic field encompassing a sample channel containing superconducting pick-up detection coils, also known as gradiometers, which inductively couple to the sample. These detection coils surrounding the sample sit in the uniform magnetic field region of the magnetic bore and measure the changes in magnetic flux of the sample as it is step-scanned through the channel within the coils [8]. In the presence of a magnetic field the magnetic moments of any paramagnetic material within the specimen align with the field producing a net magnetisation. As the sample is scanned vertically through the pick-up coils the movement of the magnetisation causes a change in magnetic flux which induces a current into the coils according to Faraday's law of electromagnetic induction [9]. The coils of the gradiometer are coupled to a SQuID which is isolated from any magnetic fields by magnetic shielding. The SQuID consists of superconducting rings joined via very thin insulating layers known as Josephson junctions whose high sensitivity means that extremely weak signals deriving from the changes in current through the pick-up coils can be measured [8]. This is because the currents induced in the pick-up coils create a change in resistance over the Josephson junctions leading to an output voltage from the SQuID that is proportional to the magnetic moment of the sample. The output voltage of the SQuID detector varies as the sample is moved upwards from the initialisation position and through the pick-up coils performing a vertical

scan. The plot of voltage response with displacement through the coils is characteristic of the geometry of the pick-up coil windings and the response leads to an indication of the magnetic moment of the sample for each scan by implementing a regression algorithm which calculates the magnetic moment by mathematically fitting an analytical curve to the response data [8]. There are two types of algorithm available using the MPMS MultiVu application software for post operation analysis, which is also used for controlling and monitoring the hardware. The first algorithm is known as an iterative regression which can accommodate for variations in the sample's position within the pick-up coils due to any thermal expansion of the sample rod as the temperature is ramped up [8]. However, if the signal is very small, a linear regression is required that assumes a constant central scan position of the sample within the pick-up coils as the signal is no longer strong enough for the central position to be accurately detected [8].

As the voltage response has been calibrated to a palladium standard of known mass and magnetic susceptibility over a range of magnetic fields this allows the magnetic moment from other samples to be measured. From these measurements the magnetisation and magnetic susceptibility can be calculated to give their change as a function of temperature which can in turn be used to calculate the Curie and Weiss constants of the material in question.

These measurements of SQuID output voltage were taken as the temperature was swept from 5 to 400 K in 1 K increments. A fixed magnetic field of 1000 G (0.1 T) was employed and a ramp rate of 2 K min^{-1} was used with two measurements taken at each temperature (thus a total of 792 points were obtained). In some samples the readings were repeated as temperature was decreased from 400 to 5 K in order to check for variations in magnetic susceptibility due to possible phase transitions occurring, however, none were observed. For the samples of higher copper-doping (≥ 5 %) the iterative regression was used as it was observed to give a more accurate mathematical fit to the voltage response data, however the linear regression algorithm was required for the 1 % doped samples due to the small voltage signals arising. The values for the magnetic moment calculated from the algorithms were converted to magnetic susceptibility values by dividing through by the field and scaling by the mass of the sample and the molecular weights. This was then plotted against T and fitted to give a value for the Curie constant, see section 6.2.6.

4.3.2.2 VSM measurements

An Oxford Instruments superconducting MagLab VSM system was employed to measure the magnetisation of our copper phosphate powdered glass samples as the externally applied magnetic field was increased. To prepare the samples for these measurements the glass powders were first pressed at approximately 0.8 GPa for two minutes to form cylindrical pellets of approximately 1 mm thickness. These were

then cut into smaller sections of measured mass to allow easier placement onto the polyaryletheretherketone (PEEK) sample holder where they were fixed into position using polytetrafluorethylene (PTFE) tape. This holder is attached to the end of a sample rod which can be mounted into the VSM sample chamber where it sits in a uniform magnetic field provided by a liquid nitrogen- and liquid helium-cooled superconducting solenoid whose current and consequent magnetic field are controlled by an Oxford ObjectBench computer operation system [10]. The sample resides equidistant between two pick-up coils wound in opposite senses and the end of the sample rod possesses a vibration exciter in the form of a loudspeaker-type electromagnetic velocity transducer [10] which provides sinusoidal vertical vibrations (~1.5 mm peak to peak) in the sample channel with a fixed frequency of 55 Hz. When the experiment is run the magnetic field magnetises the sample forcing the alignment of the magnetic moments with the field producing a net magnetisation. The magnetic field of the sample causes a change in magnetic flux as the sample oscillates which induces an electric field resulting in an AC current proportional to the magnetisation in the pick-up coils as described by Faraday's law. This signal is detected utilising a unity gain buffer and lock-in amplifier. A description of a general lock-in amplifier has been given in the EPR experimental details and as such section 4.2.2 should be referred to for further details.

The amplitude of the signal measured is proportional to the magnetic moment of the sample and as the voltages have been calibrated to a standard sample of known

magnetic moment, they can give a value for the molar magnetisation (magnetic moment per unit mol) of the samples under study to a high degree of accuracy when the mass and molar weight of the sample are known [10]. The magnetic field sweeps up to its set maximum value using computer interface software to automate this process and for data collection. A plot of magnetisation with respect to the magnetic field, *B*, can therefore be generated and in these experiments a set temperature of 1.5 K was achieved using a pumped liquid helium cryostat, while the magnetic field was swept through 0 to 10^5 G (0 to 10 T).

This technique as well as the SQuID method, is highly sensitive to mechanical vibrations especially as the VSM implements a vibrating transducer [7] thus a heavy frame is used to ensure that this transducer and the pick-up coils are vibrationally isolated from each other and the whole system is mounted on a 400 kg concrete plinth supported by four airpads at each corner to strongly damp any external vibrations that may travel through the laboratory floor.

Although the VSM technique is sensitive to small magnetic moments it is not as sensitive as the SQuID magnetometer technique as the inherent nature of the SQuID device makes it more sensitive to smaller changes in magnetic moment. Problems with the VSM measurements were also encountered as the powdered pellets on some occasions broke up as some of the powder moved in the sample holder as the ions attempted to align with the magnetic field since these powdered samples were

not ideal for pellet formation. This movement of the sample during measurements caused changes in the detected signal as the sample geometry is altered and as such measurements would have to be rerun after the sample pellets were prepared again. Despite these minor difficulties the VSM technique provided good quality complementary data to compare with the Cu^{2+}/Cu_{Total} percentages obtained from the SQuID measurements.

4.4 Fourier transform infrared spectroscopy

4.4.1 Background theory

Infrared (IR) spectroscopy can be used to investigate the sample composition and structure of a wide range of materials and has commonly been implemented in studying the bonding mechanisms in glass structures such as the phosphate based glass samples being investigated here [11-15]. The IR spectroscopic procedure can lead to an indication of changes in the arrangement of molecules, bond type and force constants with variation in sample composition [16].

Previous work has specifically employed Fourier transform infrared (FTIR) spectroscopy in the study of the bonding modes in copper-doped phosphate glasses as this infrared spectroscopic technique has the advantages of being quick and efficient with fast scan rates, high levels of optical throughput (Jacquinot advantage) and no need for optical focussing [17 & 18].

The information revealed using this technique describes some of the vibrational modes of the molecules present within the sample. The spectrum obtained provides an infrared 'fingerprint' which can be compared to known vibrational frequencies. Each molecule has $3n - 6$ vibrational modes ($3n - 5$ for linear molecules) where n is the number of atoms within the molecule, and these modes can include symmetric and antisymmetric stretching, bending, rocking, wagging and twisting [16]. Each of these modes occurs at a specific frequency equivalent to a discrete energy level determined by the type of mode, mass of atoms and strength of covalent bond between them [16]. When the infrared radiation has a frequency equal to that of the vibrational mode, the radiation is absorbed, giving rise to absorption lines in the spectrum of frequencies observed in an FTIR spectrum subject to that mode being active. There are however selection rules associated with this process and vibrational modes will only be present in FTIR if the absorption of energy gives rise to a change in the net dipole moment of the molecule, so a homonuclear diatomic molecule for example, would show no active vibrational modes in the spectrum [19-21]. For this reason Raman spectroscopy can be a very useful complementary technique as it conforms to different selection rules [21] (see section 4.5.1), although molecules with little symmetry such as those occuring in glass samples are likely to be active in both infrared and Raman spectroscopy.

4.4.2 Experimental details

The FTIR spectrometer used for these experiments was a Perkin Elmer Spectrum-GX with a total operation range between 30 and 15000 cm^{-1} (0.0037 to 1.8600 eV). All experiments performed here made use of the mid-infrared region 370 to 4000 cm^{-1} (30 to 1.4 μm) using a deuterated triglycine sulphate (DTGS) infrared detector with a KBr beamsplitter and glowbar source to provide the necessary electromagnetic radiation. The schematic diagram in figure 4.4 illustrates the Michelson interferometer-type setup of the spectrometer with the beamsplitter providing the two beam paths to each of the mirrors, one fixed and the other sweeping a distance, d, with time. The two beams reflect and return to the beamsplitter where they recombine with a phase difference, ϕ, and pass through the sample before reaching the detector.

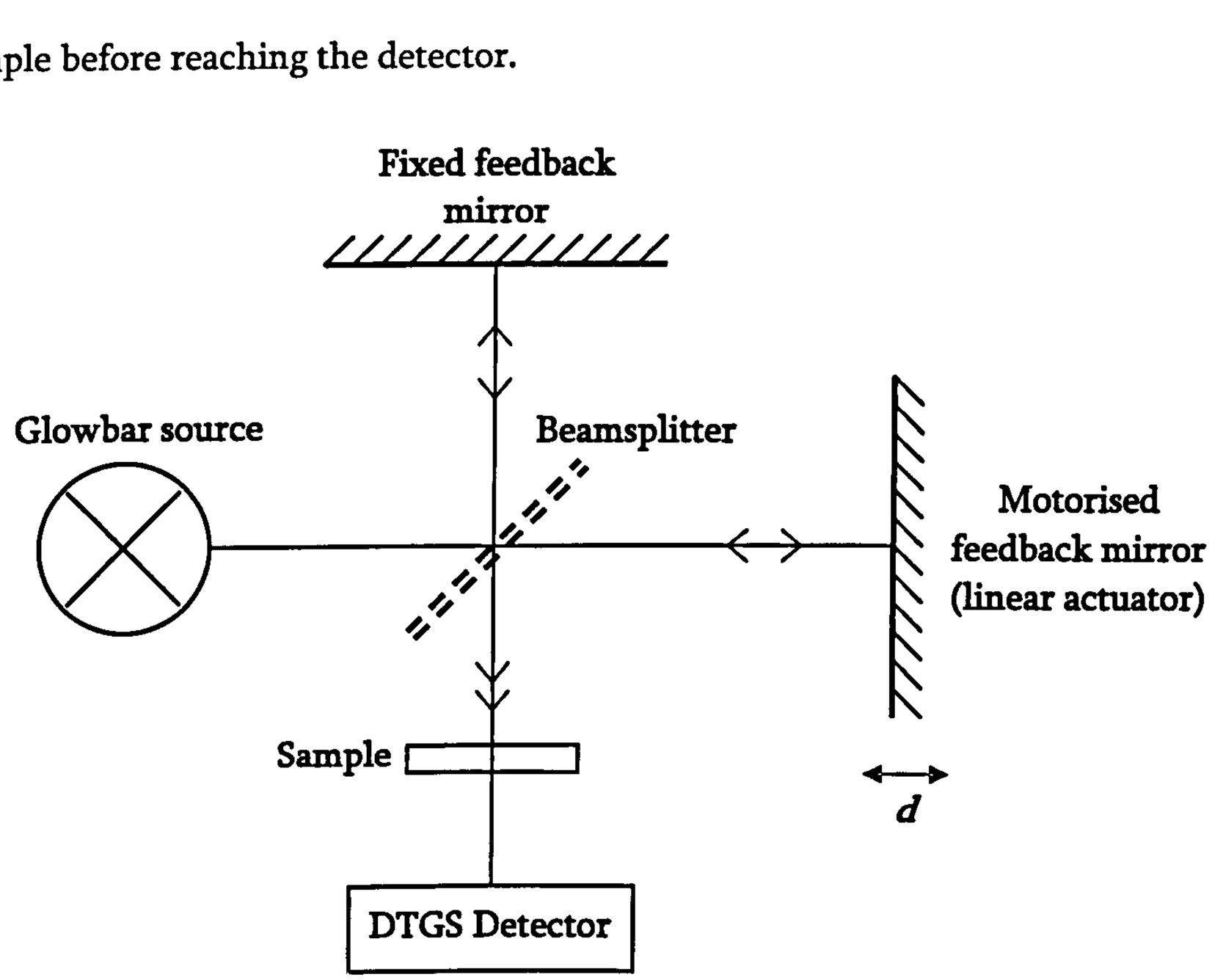

Figure 4.4: Schematic diagram of the Michelson interferometer-type setup of the FTIR spectrometer.

The DTGS detector monitors the total intensity received in the time-domain (which can be related to the path difference Δ between the two beams which is internally monitored by a helium-neon (HeNe) laser which calibrates this for each scan made) for all of the wavelengths present in the beam simultaneously known as the Felgett or multiplex advantage [18], hence the high data acquisition rates achievable. The computer running the Perkin Elmer Spectrum version 5.0.1 data collection server digitises the output signal measured and performs a fast Fourier transform to convert the information into the frequency domain. A direct comparison between the Fourier transformed experimental signal received at the detector after passing through a sample and the direct Fourier transformed signal from the source give a ratio showing any absorption occurring at the frequencies observed by giving an output of absorbance plotted against frequency in the units of wavenumber (cm^{-1}), common for most optical spectrometry measurements. The absorption coefficient μ can be determined using Lambert-Bouguer's law (sometimes referred to as the Beer-Lambert law [21]) in equation 4.8 [20] which can be rearranged to give equation 4.9.

$$I_t = I_0 \exp(-\mu t) \tag{4.8}$$

$$\mu = \frac{2.3}{t} \log_{10}\left(\frac{I_0}{I_t}\right) \tag{4.9}$$

I_0 is the intensity incident upon the sample and I_t is the intensity transmitted through it, where I_0/I_t is referred to as the transmittance, T_μ. This first expression (equation 4.8) should also take into consideration any reflected light, but since this is

allowed for in the experiments by using a background sample this can be neglected. The term $\log_{10}(I_0/I_t)$ is equal to the absorbance and t is the thickness of the sample in cm and as such, each spectrum taken must be scaled by the thickness of the sample to give a plot of absorption coefficient (cm^{-1}) versus wavenumber, in order to make a direct comparison between them. The absorption coefficient is directly proportional to the number of absorbing centres in the medium.

It is also important to note that a background spectrum must be acquired prior to any experiments as atmospheric carbon dioxide and water vapour within the sample chamber contribute to the absorption of infrared radiation within this frequency range. The experimental spectrum acquired can then be adjusted to account for this background at the end of each experiment.

4.4.3 Sample preparation

The copper-doped glass samples in glass disc form were ground and polished to give thin discs (~ 1.5 to 4.5 mm) with parallel faces to minimise any potential scattering of light from the faces of the sample. After attempting the FTIR measurements on these samples it was found that all of the copper phosphate glasses were too highly absorbing within the infrared region ($\mu_{max} \approx 50\ cm^{-1}$). As the samples had not been annealed it was not possible to polish and grind them to thinner dimensions without causing multiple fractures from the stresses that this process applies. Thus the

standard approach to dilute the samples was taken [19] where 6 mg of powdered sample for each glass was ground in a clean mortar and mixed with 150 mg of FTIR spectroscopic grade KBr powder (Sigma-Aldrich) which is transparent in the mid-infrared region. This mixture was then compressed at approximately 0.8 MPa for two minutes to form pellets of approximately 0.4 mm thickness. A background spectrum was first recorded using a pure spectroscopic grade KBr pellet to account for any additional absorption from the chamber atmosphere or from reflections of light from the KBr pellet that could be removed from subsequent spectra. All measurements were taken at room temperature using 40 scans and collecting data points every 0.2 cm^{-1} which resulted in a resolution of 2 cm^{-1}.

4.5 Raman spectroscopy

4.5.1 Background theory

Raman spectroscopy is an experimental technique that exploits the Raman effect which is the inelastic scattering of photons by molecules (or atoms). The photons incident upon a sample interact with the lattice and scattering can occur from the vibrational modes present within the sample as the electromagnetic radiation interferes with the molecule's polarisability and induces a dipole moment causing a phonon to be emitted or absorbed by the incident photon [21]. This gives rise to two types of inelastic scattering, Stokes scattering which involves the emission of a phonon, thus the incident photons lose energy, or anti-Stokes scattering where a

phonon is absorbed leading to an increase in photon energy [22]. For anti-Stokes scattering to be possible there must already be phonons present in the material before any light is incident upon it and hence is dependent upon temperature which influences the phonon population. The difference in energy between the incident and scattered light in terms of frequency is known as the Raman shift and it is this shift away from the original incident photon frequency that is measured in Raman spectroscopy. Like the absorption bands observed in FTIR, the discrete Raman shift values detected are indicative of the various vibrational modes present within the sample and can be sensitive to any changes in phosphate chain lengths due to the presence of network modifier species in glass samples such as ours, thus leading to information about the interactions between the network atoms with the cations in the local environment.

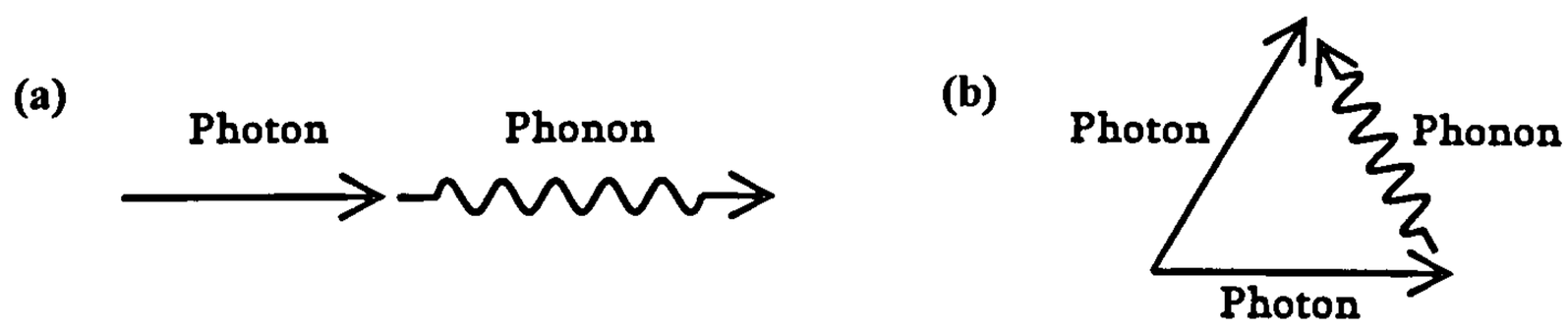

Figure 4.5: (a) The Feynman diagram for the IR absorption process and (b) the Feynman diagram for Raman scattering.

Unlike the IR spectroscopy employed in the study of these glasses, the Raman technique is not a linear process as it involves two photons of differing energy as well as a phonon, see figure 4.5. For this reason the data observed using this method cannot be directly compared in terms of the absorption peak intensities as the intensity is not simply proportional to the number of vibrational modes giving rise

to it as it is a function of its Raman cross-section (its probability of interaction) which is different for each vibrational mode. This is one of the main limitations of the method when compared to FTIR and results in a purely qualitative analysis only. It was however beneficial to employ Raman spectrometry due to its different selection rules to IR spectroscopy. As discussed previously in section 4.4.1, a vibrational mode is only IR active if the absorption of electromagnetic radiation leads to a change in the dipole moment of the molecule, whereas for a vibrational mode to be Raman active, there must be a change of polarisability arising from the inelastic photon scattering process where the incident radiation (electromagnetic field) interacts with the molecules inducing an electric dipole which changes with respect to time as the atoms vibrate [21]. This means that, for example, in IR spectroscopy homonuclear diatomic molecules would have no IR absorption as they have no dipole moment, but they would however have a Raman spectrum as the vibration of their bonds would modify the interactions between the electrons and nuclei thereby changing the polarisability. It is this important difference between the selection rules of these two spectroscopic methods that consequently highlights the virtue of their complementary analysis.

4.5.2 Experimental details

The copper-doped phosphate based glass discs were polished and analysed as flat bulk sections using a Renishaw inVia Raman Microscope system using a Reliant

series argon laser source at 514.5 nm laser excitation with an incident power of 20 mW. The experimental setup of the instrument is shown in figure 4.6 and depicts the laser light passing through a number of lenses, focussing mirrors and a beamsplitter before reaching the Leica DM IRB optical microscope using a ×50 objective where it is focussed to a small (~1 to 5 μm) spot. The anti-Stokes Raman shift is analysed in this microscopy by operating in a 180 ° backscatter geometry as this measures the scattered photons which have received the largest possible change in frequency which is important as the Raman shift is a small one (of the order of a few percent of the incident frequency only) [21]. The collected backscattered light returns through the microscope optics and beamsplitter which is coupled to a Raman spectrometer. As most of the scattered light has undergone Rayleigh scattering and is therefore the same frequency as the laser, the signal from the weak Raman shift must be resolved and this can be a difficult task as it is so close in wavelength to the elastically scattered light from the laser (since the phonon frequencies emitted are so very small). For this reason holographic (or notch) filters are used to remove the reflected light which has undergone no frequency change so that it is only the photons with a shift away from the original lasing frequency that are measured. The spectrometer incorporates a collection of optics including a double monochromator (of focal length 0.25 m) with pre-slit focusing lenses, a slit of width 20 μm and a grating of 1800 lines mm^{-1} before reaching the detector. Raman spectroscopy is a rather insensitive technique as the number of photons that are Raman scattered compared to those elastically (or Rayleigh) scattered is of the order

of > 10^5 times smaller [21], thus the detectors used must be highly sensitive even when an intense laser is used for the excitation source hence the use of a high sensitivity ultra-low noise Renishaw RenCam deep depletion charge-coupled device (CCD) array. The spectrometer variable parameters and data acquisition settings are controlled by a computer with WIRE 2.0 service pack 9 management software.

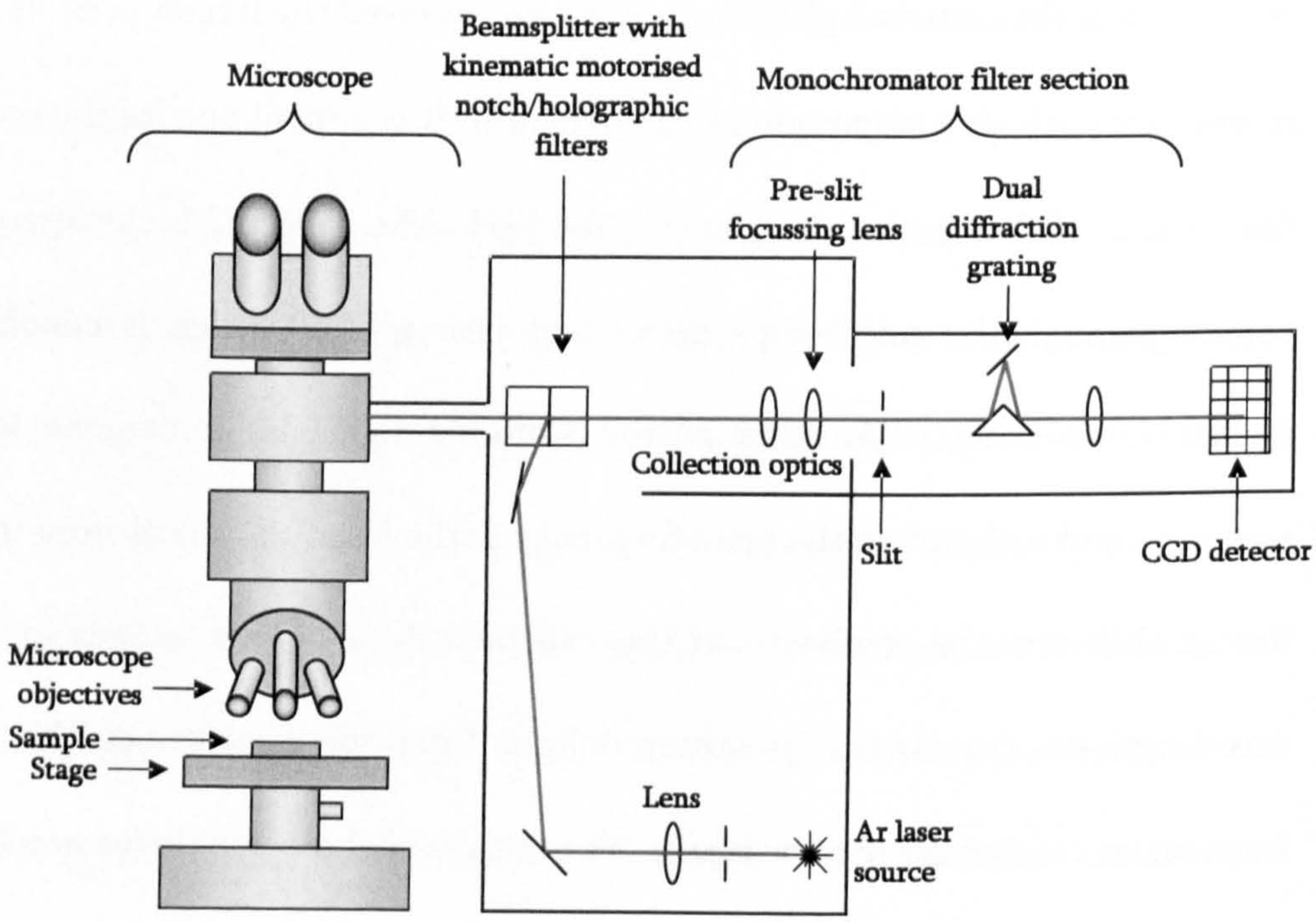

Figure 4.6: Schematic of the experimental setup and laser beam path of the Raman spectrometer.

Before the acquisition of any glass sample data from the instrument, the wavenumber axis of the spectrometer was first calibrated by loading a silicon (111) wafer onto the sample stage and focussing the incident beam upon it using the Leica microscope to optimise the signal to the maximum number of counts. A static mode Raman spectrum centred at 520 cm^{-1} was recorded using one accumulation and an

exposure time of 1 s to ensure that the position of the silicon band was at 520 cm^{-1} [23].

All Raman measurements were taken at room temperature within a frequency range between 400 and 1300 cm^{-1}, centred on 850 cm^{-1}, averaging ten sequential accumulations per sample and a detector acquisition time of 1 s for each accumulation. The resolution of the spectra obtained is in the region of 4 cm^{-1}. These parameters were found sufficient to give a good signal to noise ratio and the spectra displayed are the average of these accumulations.

4.6 Chemical analysis using SEM-EDX

The Brow model [24] as outlined in chapter 1, depends upon sample composition and was used to predict the phosphate tetrahedral connectivities expected in our glass samples. The phosphate and modifier quantities used in the calculations were those given by the compositions of the starting mixtures. Since the predicted Q speciation values obtained were compared with all experimental data throughout this study it was critical that the molar fractions used in calculation were accurate and correct. As such, the glass sample compositions were checked by chemical analysis.

4.6.1 Background theory and experimental details

A Zeiss Supra 55-VP scanning electron microscopy (SEM) system coupled with an energy dispersive X-ray detector (EDX) were used for the analysis of sample composition. The SEM works by firing a finely focussed electron beam with energies between 0.1 to 30.0 keV (where accelerating voltages of 25.0 kV were implemented in these experiments in order to excite the copper X-ray lines), onto a sample using a thermal field emission gun (FEG) and condenser focussing lenses in an ultra-high vacuum (UHV) environment of ~10^{-6} mbar vacuum pressure [25]. The electrons interact with the specimen generating a range of radiation and scattered electrons. To view the samples a secondary electron scintillation-photomultiplier detector was used, known as an Everhart-Thornley detector [25] which attracts secondary electrons via the application of a bias voltage. Secondary electrons are those liberated from the sample with energies < 50 eV gained predominantly from the incoming primary electron beam. These strike the scintillator, emitting light that is transmitted through a light-guide to a photomultiplier where a pulse of electrons is produced in response to the photons which may then be amplified. As the digitally controlled primary electron beam is raster-scanned across the sample surface the resulting image is displayed on a computer monitor and as the yield of secondary electrons is high and since they originate from a small sampling volume they give good image resolution ideally of ~1.5 nm.

To perform the chemical microanalysis the emission of X-rays is detected in EDX as the sample is bombarded with the electron beam. Localised electrons can be liberated from an atom as the primary electrons interact with them leaving the atoms in an excited state. When the empty state becomes filled by another electron the atom relaxes releasing the excess energy. This energy is released either in the form of a lower energy, visible wavelength photon (known as cathodoluminescence) if the vacancy is in one of the outer electronic orbitals, otherwise energy is released in the form of an X-ray photon or Auger electron [25]. As the X-ray energy is characteristic of the atomic species and selection rules prohibit certain electron transitions, it is possible to use these X-ray energies to determine the atoms present within a sample [25]. The spectra collected consist of these X-rays as well as background radiation from Bremsstrahlung (braking) radiation emitted to conserve energy as primary electrons lose kinetic energy in passing through the electric field of the atoms in the sample. This is not characteristic of the atoms and must be subtracted from the spectra. The backgrounds were fitted and removed after each measurement and this was completed a number of times for the same set of data to give an estimate of the error that this background subtraction contributes to the quantitative results.

The solid-state detector used in EDX fixed at a working distance (WD) of 15 mm, consists of a semiconducting p-n junction with applied bias voltage so that any X-ray radiation incident upon it creates electron and hole charge carrying pairs providing

a current pulse lasting < 1 μs and proportional to the X-ray energy [25]. Each pulse is amplified and the signal passes to a computer operating as a multichannel analyser (MCA) where the X-ray energy is registered in its characteristic channel so that a graph of the detected energies and the number of counts is obtained. This pulse processing time is finite and during which the next pulse cannot be collected and is rejected until the system is ready. This period is known as the deadtime and if too high can give rise to artefacts in the elemental analysis as the MCA struggles to decipher between multiple pulses received [25]. It is therefore important to control the number of pulses reaching the detector by varying the aperture size of the electron gun collimation (set at 60 μm in our experiments) and there arises a trade off between having a large number of pulses for strong signal-to-noise and having a small deadtime.

Qualitative analysis is efficient as the computer identifies the elements present from their line positions in the spectra. However, resolution can be poor as the lines are broad and this can make it difficult to resolve between closely spaced elements. To quantitatively estimate the relative amount of elements present within the sample the peaks present are fitted using the EDAX Genesis Spectrum Quant ZAF version 3.60 analysis software. This compares the number of characteristic X-rays from the specimen in a fixed time (200 s in these experiments) to the number arising from the calibration standards of known composition that had previously been calibrated to when first setup. As the compositions of the sample and standards are not the same

a ZAF correction is completed which considers the differences in average atomic number (Z) which can effect the efficiencies of X-ray generation since it effects electron penetration into the sample and electrons backscattered without emitting any X-rays [25]. Difference in absorption (A) of X-rays during exit from the sample is accounted for, as this depends on the elements present. X-rays can also sometimes excite lower energy fluorescence radiation (F) in samples containing several elements giving rise to more lower energy X-rays than expected and this is also computed [25].

In completing these experiments it is important that the sample must be conducting, otherwise as electrons bombard the material charge builds up and repels the electron beam. Non-conducting samples are therefore usually coated in a conducting layer, however as these samples were powders (the glass disc samples were not obtained until later in this study) the variable-pressure (VP) method was employed where the EDX experiments were performed at lower vacuum, therefore higher pressures (15 and 30 Pa) so that any charging on the sample was removed by the presence of air molecules and by doing this at two pressures the computer reads both of the spectra collected and extrapolates back, predicting the spectral results at lower pressures in the absence of any signal that may arise from the higher pressure atmosphere. To select the experimental region from each sample (usually an area of the order of 30 by 30 μm to 150 by 150 μm depending upon the grain sizes) a solid-state electron backscatter detector must be used as the secondary electrons are not energetic

enough to reach the detector at these higher variable pressures. Backscattered electrons are generally of much higher energies (~50 eV) as these are primary electrons which scatter and then depart from the sample while maintaining a large fraction (~80 %) of their initial energy. They are however not as numerous as secondary electrons, have a greater range of energies and originate from a larger sample volume therefore reducing the image resolution achieved from 10 to 15 nm [25].

Problems encountered using the EDX technique include that the background of the carbon sample stub used for mounting the sample gives rise to a strong signal which must be neglected from the overall elemental quantification. The EDX detector has thin polymer windows preventing contaminants from the specimen chamber from condensing onto the detector surface and absorbing X-rays but the window itself absorbs low energy X-rays making the detection and quantification of light elements (lighter than boron) with energies < 1 keV unreliable in the absence of chemically similar standards at the time of experimentation [25]. Topographical effects can also give discrepancies in results as the X-rays can only be detected in the line of sight of the detector and the ZAF correction is a function of angle, thus it is preferential to have flat polished samples rather than powders with grains of varying topography [25]. However, experiments were repeated on some glass disc samples when a selection of these later became available, and no significant differences in the average sample compositions were found within the usual experimental error.

References

[1] J. A. Weil, J. R. Bolton and J. E. Wertz, *Electron Paramagnetic Resonance: Elementary theory and practical applications*, John Wiley & Sons Inc., New York, USA (1994).

[2] W. Gordy, *Theory and applications of electron spin resonance*, John Wiley & Sons Inc., New York, USA (1980).

[3] T. F. Prisner, *Pulse high-frequency / high-field EPR*, Advances in Magnetic and Optical Resonance, **18-20** (1997), 245-299.

[4] M. Mazúr and M. Valko, *Error sources in quantitative EPR spectroscopy*, EPR newsletter, **13**:1-2 (2003), 27.

[5] C. Kittel, *Introduction to solid state physics*, 7th Ed., John Wiley and Sons Inc., New York, USA (1996).

[6] G. W. C. Kaye and T. H. Laby, *Tables of physical and chemical constants*, 86th Ed., Longman, Harlow, UK (1995).

[7] J. Crangle, *The magnetic properties of solids*, Edward Arnold Publishers Ltd., London, UK (1977).

[8] *Quantum Design MPMS MultiVu Application User's Manual*, Quantum Design, San Diego, USA (2000).

[9] W. J. Duffin, *Electricity and magnetism*, 4th Ed., McGraw-Hill, London, UK (1990).

[10] *Operating manual for oxford instruments superconducting vibrating sample magnetometer system*, Manual 1: Version 3, Oxford Instruments Ltd., Oxon, UK (1995).

[11] A. Chahine, M. Et-tabirou and J. L. Pascal, *FTIR and Raman spectra of the Na_2O-CuO-Bi_2O_3-P_2O_5 glasses*, Materials Letters, **58** (2004), 2776-2780.

[12] P. Y. Shih, J. Y. Ding and S. Y. Lee, *^{31}P MAS-NMR and FTIR analyses on the structure of CuO-containing sodium poly- and meta-phosphate glasses*, Materials Chemistry and Physics, **80** (2003), 391-396.

[13] M. Gabelica-Robert and P. Tarte, *Infrared spectrum of crystalline and glassy phosphates: preservation of the pyrophosphate group in the glassy structure*, Journal of Molecular Structure, **79** (1982), 251-254.

[14] C. Ananthamohan, C. A. Hogarth, C. R. Theocharis and D. Yeates, *Investigation of infrared absorption spectra of copper phosphate glasses containing some rare earth oxides*, Journal of Materials Science, **25** (1990), 3956-3959.

[15] C. A. Hogarth and G. R. Moridi, *Infrared spectra of copper-calcium-phosphate glasses*, Journal of Materials Science Letters, **3** (1984), 481-483.

[16] A. D. Cross and R. A. Jones, *An introduction to practical infra-red spectroscopy*, 3rd Ed., Butterworth & Co. Publishers Ltd., London, UK (1969).

[17] D. A. C. Compton, J. Drab and H. S. Barr, *Accurate infrared transmittance measurements on optical filters using an FT-IR spectrometer*, Applied Optics, **29**:19 (1990), 2908-2912.

[18] S. Wartewig, *IR and Raman spectroscopy: Fundamental processing*, Wiley-VCH, Weinheim, Germany (2005).

[19] W. Brügel, *An introduction to infrared spectroscopy*, Methuen & Co. Ltd., London, UK (1962).

[20] I. Simon, *Infrared radiation*, Van Nostrand Company Inc., New Jersey, USA (1966).

[21] J. R. Ferraro and K. Nakamoto, *Introductory Raman spectroscopy*, Academic Press Inc., London, UK (1994).

[22] H. A. Szymanski, *Raman spectroscopy: Theory and practice*, Plenum Press, New York, USA (1967).

[23] *Renishaw inVia Raman microscope methods for users document*, Renishaw, Gloucestershire, UK (2006).

[24] R. K. Brow, *Review: the structure of simple phosphate glasses*, Journal of Non-Crystalline Solids, **263** & **264** (2000), 1-28.

[25] P. J. Goodhew, J. Humphreys and R. Beanland, *Electron microscopy and analysis*, 3rd Ed., Taylor and Francis, London, UK (2001).

Chapter 5

SILVER PHOSPHATE GLASS

5.1 Introduction

The antibacterial properties of silver have been rigorously studied in past decades and silver-based material devices now are more commonly being used in surgical procedures and other medical treatments to prevent the development and spread of infections [1]. As newer applications are currently being developed in order to incorporate these antibacterial ions into medical prosthetics for example, an understanding of the glass hosts used to contain these dopants is therefore

important. In this study a series of mixed alkali metaphosphate glass samples were provided for investigation with silver-doping levels of up to 20 %.

5.2 Results and discussion

5.2.1 Silver antibacterial properties

In investigations into these glass samples by Ahmed et al. [1] and Valappil et al. [2], analysis of the antimicrobial effectiveness of silver-doped phosphate based glasses was performed against a range of organisms commonly associated with infections, such as *Staphylococcus aureus,* methicillin-resistant *Staphylococcus aureus* (MRSA) and *Escherichia coli.* Viability studies on the growth of these organisms were also conducted and showed significant antibacterial effects even at low (3 %) silver-doping [1]. The experiments confirmed the antimicrobial properties expected of these glasses and for further information regarding their bactericidal activity see [1] and [2], appendix A.

5.2.2 Durability investigations

As the function of these glasses is to deliver a long term, controlled rate of antibacterial silver ions into solution, it is highly desirable for the degradation and ion release rates of the samples to be tailored accordingly. The dissolution rates were obtained by monitoring the surface area and weight of the samples in disc form

whilst being agitated in deionised water in an incubator at 37 °C to give a measure of the weight loss per unit area, over time [2 & 3]. The degradation profiles collected (refer to references [2 & 3] and appendices A and B) show that the dissolution rates decrease as doping levels increase, with a larger change in dissolution rate observed as the doping increases from 3 to 5 mol. %, than from 0 to 3 mol. %. The reduction in dissolution continues with additional doping but becomes less prominent as doping levels exceed 10 %, see appendix B. This effect was expected as it has previously been suggested [3] that the addition of silver increases the ionic cross-linking between the phosphate tetrahedra thus strengthening the nature the overall glass structure. These experiments are therefore consistent with silver ions entering the glass and taking up a similar but stronger, charge balancing role as the sodium ions. As sample degradation decreases with substitution for silver this is highly supportive of claims that the ionic cross-linking nature of the silver ions is greater than that of the sodium [3]. The sample degradation experiments were also performed on the 0, 3 and 5 % doped samples in a nutrient broth at 37 °C to simulate the more realistic environment in which mircoorganisms may grow and these results were entirely consistent with those taken using deionised water [1].

Correspondingly, both the sodium and calcium ion release results [2 & 3] are in general agreement with the dissolution data, with the ion release rates diminishing with rising silver-doping concentration, see appendices A and B (references [2 & 3]). The ion release studies on the calcium, sodium and phosphate anions were

simultaneously conducted by analysing the deionised water medium used for the degradation studies at various intervals using ion chromatography (Dionex) [2]. The silver ion release experiments were measured using a commercial silver testing kit (1.14831.0001; Merck) [2 & 3] and showed that although the silver-doping levels did alter the release rates, there was no systematic correlation between the doping quantity and overall release rates. This may be due to the silver ions on one hand strengthening the material as they are added, but also providing more ions in the sample to be released as doping is increased.

The phosphate anion release rates were performed to give an indication of the dissolution mechanism for these glasses, see references [2 & 3] and appendices A and B. The release of PO_4^{3-} (Q^0 units) and $P_2O_7^{4-}$ (Q^1 dimers) were investigated but these were found to be released only in very small quantities of < 6 ppm and < 1 ppm after 120 hours, respectively, and showed no change with silver-doping which is consistent with a metaphosphate glass such as this, which should consist of only Q^2 metaphosphate chains and rings [4]. The small quantities of these anions released can be accounted for by disproportionation (section 1.2). The release of $P_3O_{10}^{5-}$, corresponding to a Q^2 unit terminated by two Q^1 end units, was also released in very small quantities in each of the samples (< 2 ppm after 120 hours) and it was noted that the quantities released were even smaller for samples containing more silver. From theses studies the anion released at the greatest rate was found to be $P_3O_9^{3-}$ (Q^2 ring of three phosphate units). This anion is not only predicted to be the

most commonly (or only) occurring Q^n species within metaphosphate glasses but in investigations by Chahine et al. [5], glass dissolution was suggested to preferentially involve the release of metaphosphate P-O chains into the solution through the breaking of the cross-linking bonds of the cations between them [5]. The release rates of this anion was highest for the base glass sample containing no silver which is therefore consistent with claims that silver has stronger ionic cross-links than sodium ions, although the rate of release changed negligibly as doping increased any further [5].

An example of the differential thermal analysis (DTA) performed on the 17.5 mol. % doped phosphate glass sample is shown in figure 5.1, with the glass transition temperature, T_g, crystallisation temperature, T_c, and melting temperatures, T_m, clearly labelled. This technique measures the temperature difference arising between a specimen and reference compound (in this case powdered quartz) as they undergo the same heating rates and can therefore give an indication of any endothermic or exothermic events due to changes in the specimen relative to the inert reference sample. These measurements were completed using a Setaram differential thermal analyser under an inert nitrogen atmosphere with an applied heating rate of 20 °C min^{-1} up to a maximum temperature of 1000 °C. The data was baseline corrected by performing a blank run and subtracting this from the original plots. No systematic relationship between these temperatures and the doping concentrations of each sample was found and this is shown in table 5.1. This was

somewhat unexpected as the addition of silver ions has shown a significant increase in chemical durability demonstrated by the reduced glass dissolution rates observed and it is common that greater chemical durability in turn results in higher glass transition temperatures. The lack of correlation between the glass dissolution trends and the DTA features is most likely due to the differences in the mechanisms involved during each process. As mentioned above, work by Chahine et al. [5] reports that the dissolution process of these glasses involves the hydration of the glass surface during which the cross-linking bonds of the cations are broken, releasing the metaphosphate P-O chains into the solution. This implies that replacing the sodium cations with supposedly stronger cross-linking silver ions can reduce dissolution rates as this only affects the type of modifier in the glass, not the quantity, so the phosphate chains present should remain the same. Gao et al. [6 & 7] also describe reduction in glass dissolution by forming stronger cross-links as these not only strengthen the glass structure but also decrease the diffusion rate of water molecules within the glass which may act to depolymerise the network and increase dissolution. In contrast, the glass transition and crystallisation processes involve an overall reordering of the glass network which may not necessarily involve the breaking or forming of bonds, only the movement of constituent phosphate units and cations to a lower energy system. We cannot therefore, easily determine what effect the replacement of sodium for silver ions would have on these processes although it is thought that increased strength of cross-linking would increase the complexity of the structure reducing the ease of movement and rearrangement of

the glass network constituents during these processes. FTIR could possibly be employed in an attempt to observe the subtle changes in bonding involved in these various transitions. The melting process involves the breaking of more bonds than dissolution as such high temperatures and therefore energies are involved. This means that the weaker ionic cross-links become less critical in holding the structure together as the temperature increases because even the stronger P-O covalent bonding can be broken when the system melts leading to a less prominent effect of the cation replacement upon the melting temperature. A change in the amount of modifying oxide within the sample would affect the connectivity between phosphate units which would result in more distinct changes in T_g, T_c and T_m, but in these samples there is only a change in modifier species, not its total quantity. The concentration of phosphorus (50 % P_2O_5) is not changed, thus the phosphate tetrahedral units should remain unaltered producing a system consisting purely of Q^2 metaphosphate chains and rings [4].

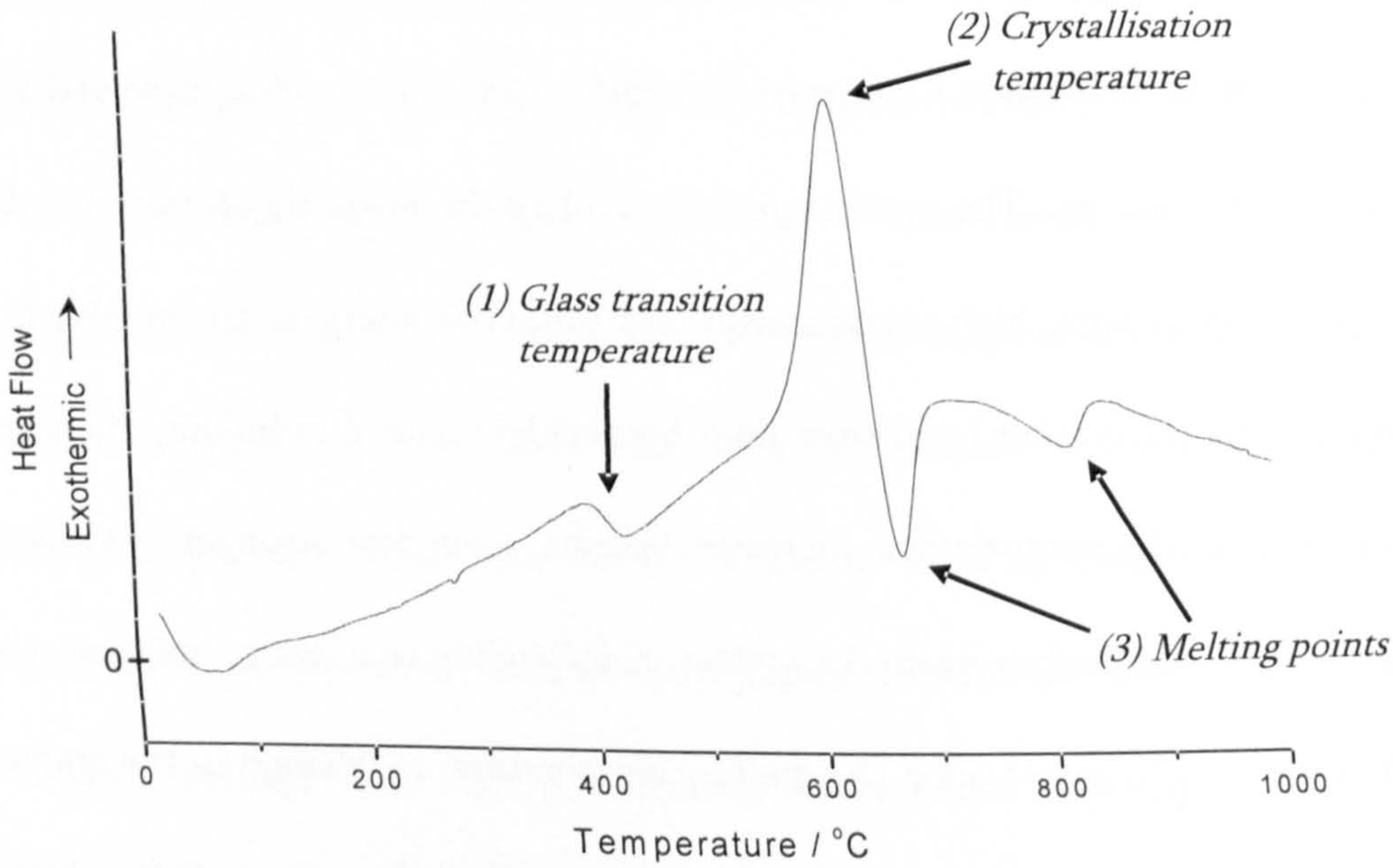

Figure 5.1: Differential thermal analysis (DTA) for the 17.5 mol. % silver-doped phosphate glass sample, against a reference sample of alumina, by Ahmed [3].

Silver-doping / mol. %	T_g */°C ± 1 °C*	T_c */°C ± 1 °C*		T_m */°C ± 1 °C*	
		Peak 1	*Peak 2*[i]	*Peak 1*	*Peak 2*
0.0	378	523	590		743
1.0	394	520	554	716	748
2.0	399	520	541	712	752
3.0	392	523	559		746
4.0	401	532	556		748
5.0	396	549			751
10.0	393	570		726	793
12.5	407	564	611	716	803
17.5	410		616	673	820
20.0	409		601		830

Table 5.1: DTA measurements by Ahmed [3] for the silver-doped glass samples showing no distinctive correlation between doping and temperature of significant events.

[i] Where some DTA traces show more than one crystallisation and melting peak.

5.2.3 Structural investigations

^{31}P MAS NMR was used to investigate the changes in glass structure occurring as the silver-dopant concentration was increased. It is hoped that this structural information will help to explain the changes observed in glass properties. In the ^{31}P NMR spectra for the silver-doped phosphate glasses, the single most prominent isotropic peak observed in figures 5.2 and 5.3, occurs at a chemical shift of -25 ± 1 ppm which has a series of accompanying spinning sidebands. This central peak corresponds to metaphosphate Q^2 phosphate units [8] in which each phosphorus atom is linked with two bridging oxygen atoms per tetrahedron. From work by Brow [4] and Van Wazer [9] to a first approximation this phosphate coordination was expected to dominate the structure as metaphosphate glasses with 50 % P_2O_5 should consist entirely of Q^2 chains and rings within the model used [4 & 9]. With $\leq$ 10 mol. % Ag_2SO_4 doping, the relative intensity of Q^2 speciation present is between 95 and 99 ± 2 % with no direct correlation with the doping concentration, see table 5.2.

Ag-doping / mol. %	Q^1 peak			Q^2 peak			Q^3 peak			Unidentified peak		
	δ_{iso} / ppm ± 1 ppm	Δ / ppm ± 1 ppm	I / % ± 2 %	δ_{iso} / ppm ± 1 ppm	Δ / ppm ± 1 ppm	I / % ± 2 %	δ_{iso} / ppm ± 1 ppm	Δ / ppm ± 1 ppm	I / % ± 2 %	δ_{iso} / ppm ± 1 ppm	Δ / ppm ± 1 ppm	
0.0	–9	7	1	–25	11	96	–35	7	2	0	6	
1.0	–8	8	2	–24	10	97	–35	5	1			
2.0	–9	5	1	–24	10	98	–35	6	1			
3.0				–25	11	99	–35	6	1			
4.0				–25	12	95	–35	8	5			
5.0				–25	12	99	–39	6	1			
10.0	–8	9	1	–26	13	96	–40	10	2	0	3	1
12.5				–24	14	86	–36	16	14			
15.0	–7	7	1	–26	14	88	–39	13	11			
17.5				–26	14	86	–39	14	14			
20.0	–7	11	4	–24	14	79	–37	15	15	3	8	2

Table 5.2: Chemical shift, FWHM and integrated intensity values for the fits of the ^{31}P NMR spectra from the silver-doped samples.

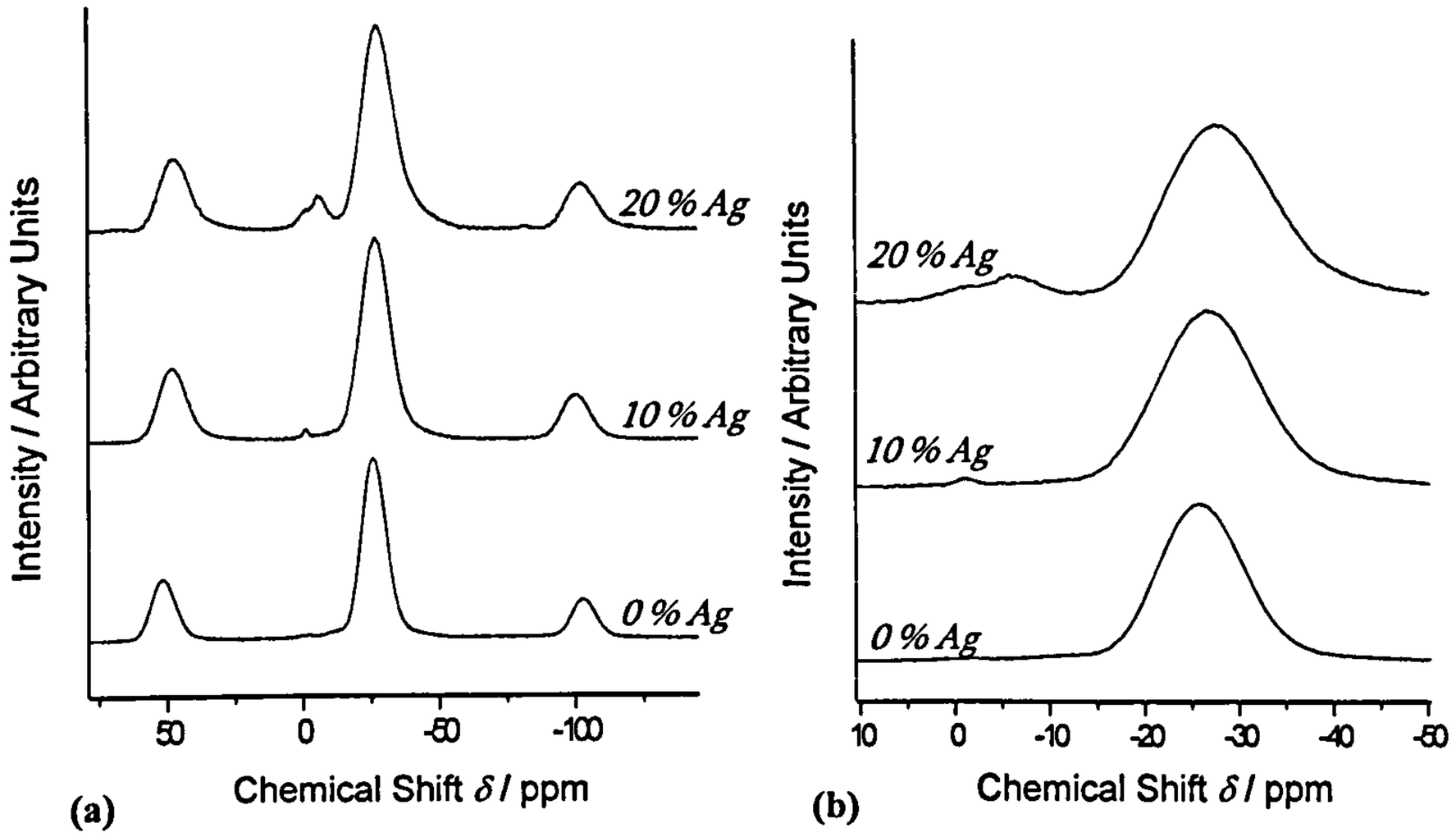

Figures 5.2 (a) and (b): ^{31}P MAS NMR spectra for the silver-doped samples 50 % P_2O_5 + 30 % CaO + (20 – x) % Na_2O + x % Ag_2SO_4, showing the distinct presence of the Q^2 peak with Q^1 forming at higher doping at two different scales for clarity of the centrebands.

The remaining structural composition at doping levels of ≤ 10 % consists of a very small fraction (up to 5 ± 1 %) of both Q^1 and Q^3 tetrahedral speciation at –9 and –36 ± 1 ppm, respectively, as can be seen from the fit in figure 5.3, and these are also present in the ternary base glass. There is also an unidentified peak arising in the ^{31}P NMR spectra between 0 and 3 ± 1 ppm for samples of 0, 10 and 20 % doping. These measurements were repeated to check for consistency and the results remain unchanged. This peak between 0 and 3 ± 1 ppm has not been identified and has yet to be explained.

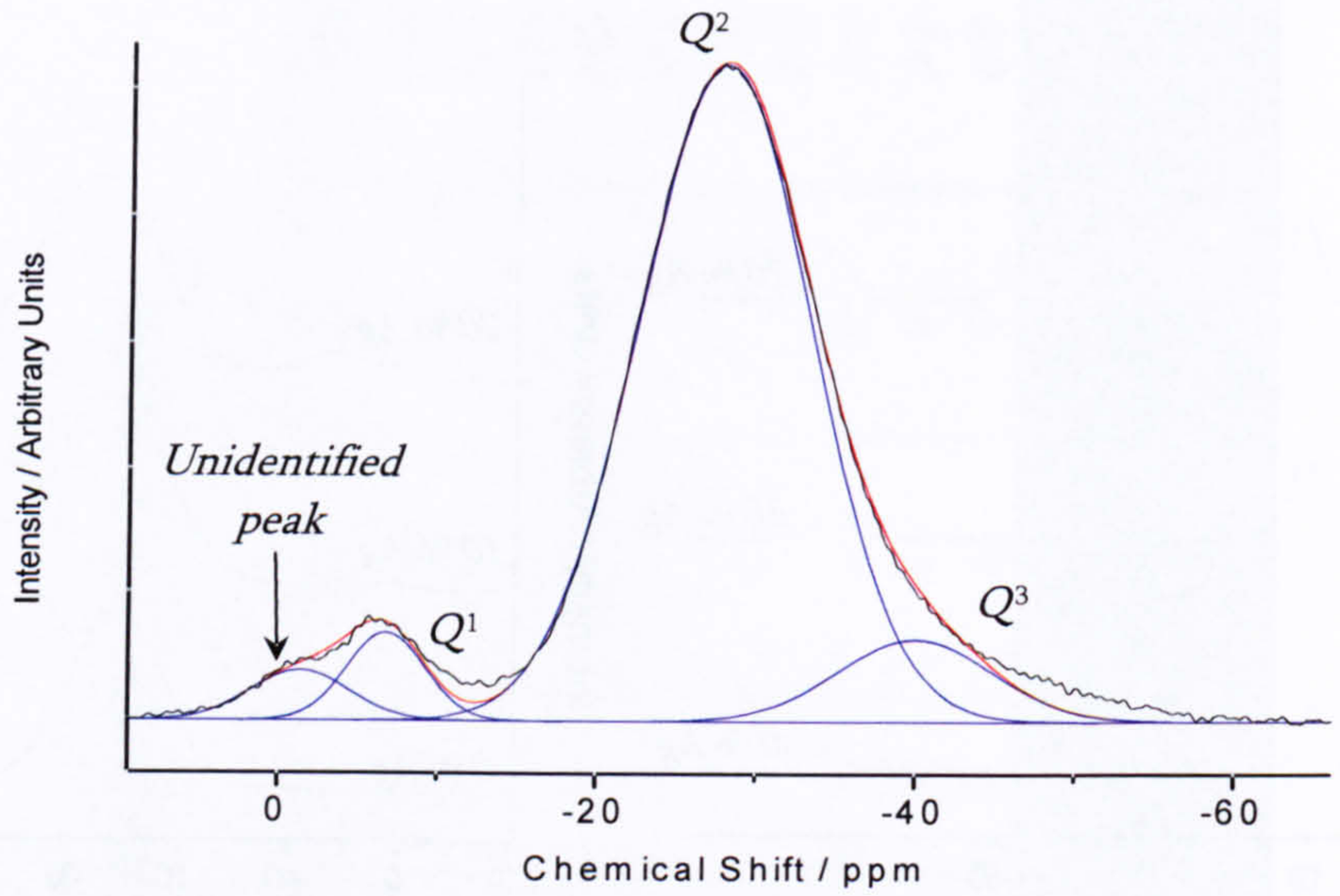

Figure 5.3: The deconvolution of the peaks present in the ^{31}P MAS NMR spectrum for the 20 mol. % silver-doped sample. The blue lines show the peaks fitted, the black line is the original spectrum and the red line shows the overall convoluted fit.

Although a small percentage of Q^1 and Q^3 tetrahedra were detected at ≤ 10 % doping, this is still consistent with the predicted binary model proposed by Brow [4] and Van Wazer [9] which suggests that a non-crystalline metaphosphate glass such as this consisting of 50 mol. % P_2O_5 should consist exclusively of Q^2 units forming chains and rings [4]. The presence of both Q^1 and Q^3 species is most likely explained by the occurrence of disproportionation (see section 1.2) since glasses do not always perfectly conform to the proposed model. Although a glass of this composition should be accurately described by the binary model [4] certain glass compositions are more closely described by this model than others, for example, glasses containing sodium or potassium cations are generally more accurately related to this model than those in which lithium is the dominant cation present [4]. This is due to the process known as disproportionation that occurs to varying extents in

different glass structures in which a number of phosphate tetrahedra may convert into other Q species. For our metaphosphate glass which is predicted to consist of Q^2 tetrahedra, disproportionation can be described by $2Q^2 \leftrightarrow Q^3 + Q^1$. Glasses can be modelled as binary or random systems where these cases are the two extremes and there is a continuum of possible states between them due to the disproportionation process. As the relative percentages of Q^1 and Q^3 tetrahedra observed in these samples are so small and are approximately equal to each other with doping concentrations of ≤ 10 %, then it is possible to make the assumption that these results are almost consistent with the binary model with a small amount of disproportionation occurring.

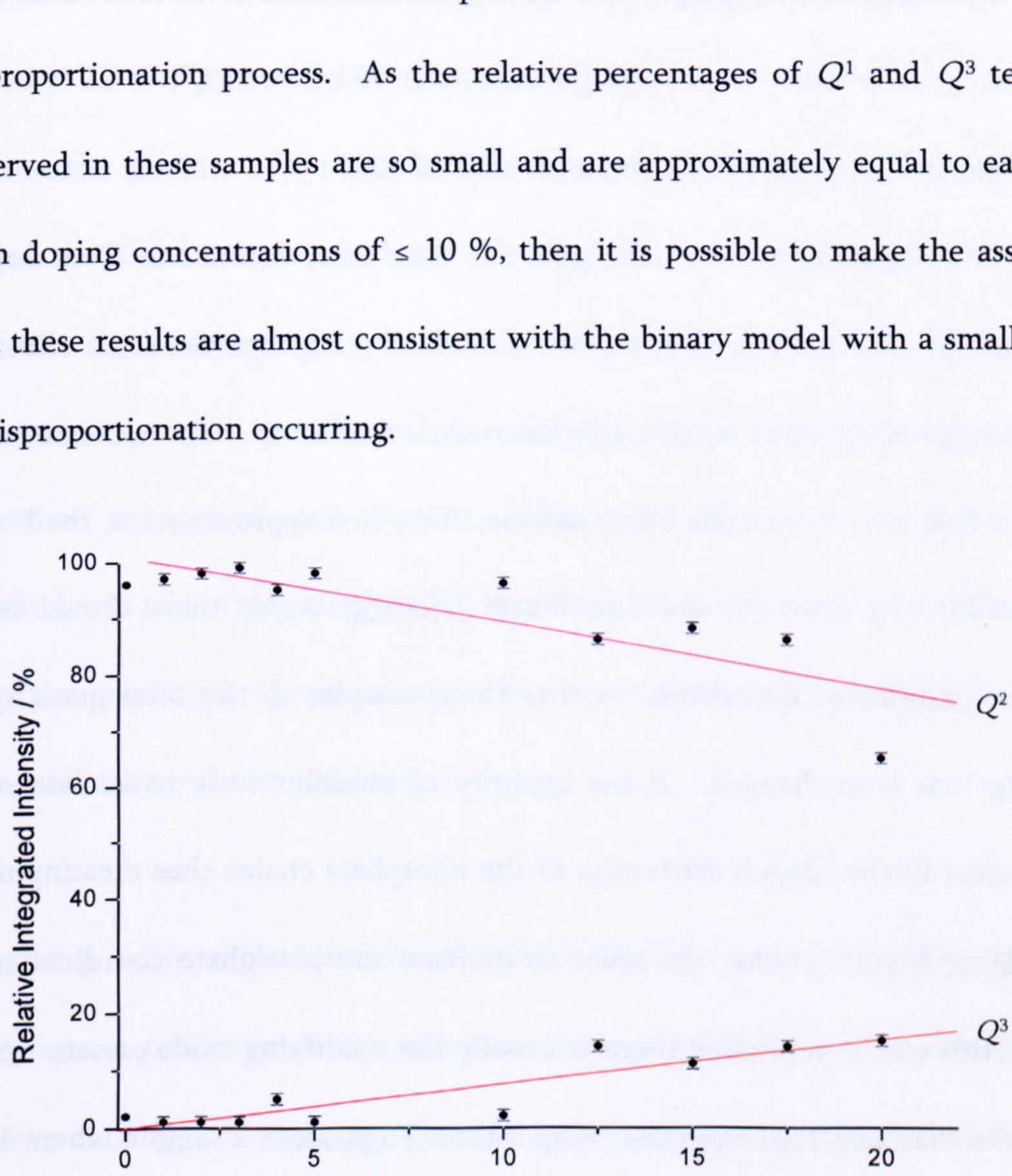

Figure 5.4: Change in Q^2 and Q^3 speciation with increasing Ag_2SO_4 doping concentration.

With silver-doping concentrations in excess of 10 mol. % the percentage of Q^2 drops significantly whilst that of Q^3 increases to between 11 to 15 ± 2 %, shown in table 5.2 and in figure 5.4. There is a rapid increase in Q^3 speciation (by 12 ± 2 %) as doping increases from 10.0 to 12.5 % doping, which then remains approximately constant with additional doping. At a doping concentration of 20 mol. % there is 4 ± 2 % of Q^1 (most likely from disporportionation), 79 ± 2 % of Q^2, 15 ± 2 % of Q^3, and an unidentified peak with a chemical shift of +3 ± 1 ppm with an intensity of 2 ± 2 %, the fit of which is shown in figure 5.3. This sharp increase in Q^3 as doping concentrations exceed 10 % cannot now be caused by disproportionation effects as the percentage of Q^3 units significantly outweighs that of Q^1. The increase in Q^3 must therefore arise from some other process. To a first approximation, the binary model outlined by Brow [4] and Van Wazer [9] suggests that there should be no change in phosphate coordination within these samples as the total quantity of modifying ions is unchanged. If the quantity of modifier were to increase, one would expect further depolymerisation of the phosphate chains thus creating more non-bridging oxygen atoms. In order to increase the phosphate coordination as observed, this would imply that there is actually less modifying oxide present within the samples than expected from the composition. To produce a sample where 15 % of the phosphate units have Q^3 connectivity as measured for the 20 % silver-doped case, this implies that instead of a metaphosphate glass, the glass would have to be an ultraphophate of 54 % P_2O_5 and 46 % of modifying oxide only. As 4 % is not a high deviation from the predicted 50 % P_2O_5 composition it was important to perform

some chemical analysis in order to check the sample constituents [10]. Inductively Coupled Plasma Mass Spectroscopy (ICP-MS) was used to achieve this [10] and as the name implies this technique employs a combination of an inductively coupled plasma with a mass spectrometer. A sample was dissolved in diluted hydrochloric acid (HCl) containing deionised water (with a resistivity of 18 MΩ cm) and pumped into the ICP-MS system where it emerges as an aerosol which is introduced into base of the plasma. The high temperature plasma ionises the elemental species within the liquid sample which are then directed to the mass spectrometer, which separates the ions according to their mass-to-charge ratio. Ions of the selected mass-to-charge ratio are directed to a detector which determines the number of individual isotopes of each element. This found the sample composition to be within < 1 % of the target value [10] showing that it is unlikely that any deviation from the predicted Q speciation is due to unaccounted for differences in the elemental chemical compositions.

Another possible explanation for the unexpected Q^3 percentages measured could arise from a tendency of the silver to phase separate from the glass producing silver-containing colloidal aggregates or nanoparticle clusters and evidence of this occurring has been found in many other studies on similar glass samples [11-13]. If phase separation of all of the silver ions at 20 % doping occurred, this would leave only 37.5 % of modifying oxide (calcium) remaining in the overall network resulting in 40 % of Q^3 units which is far greater than that observed. To give a Q^3 percentage

of 15 % as the ^{31}P NMR implies, 7.4 % of the total silver content would have had to phase separate, leaving 54 % P_2O_5 and 46 % of modifying oxide remaining. As this suggests that not all of the silver would phase separate to produce a Q^3 peak with an intensity equal to that observed, this is consistent with the Q^3 peak only becoming prominent after 10 % of silver-doping is exceeded. It could be that phase separation only occurs after a certain amount of silver has been introduced to the system, consistent with the dramatic 12 ± 2 % increase in the Q^3 peak observed as the silver changes from 10.0 to 12.5 % of the sample. If the phase separation results in the formation of silver metal nanoparticles this would be detectable using room temperature spectrophotometry experiments in the ultraviolet (UV) to visible region (300 to 800 nm). This technique detects the absorption of light through a sample due to the electronic transitions of the charge carriers between various states within the electronic bands of the material [14] and the samples were analysed on a Cary 400 Scan UV-visible spectrophotometer. The spectra recorded in figure 5.5 however, displayed no evidence for the existence of silver metal nanoparticles which should give rise to an absorption band peaking around ~400 nm [10-13, 15, 16]. The absorption edge appearing as the spectra approach 300 nm is characteristic of the undoped sodium metaphosphate glasses [15].

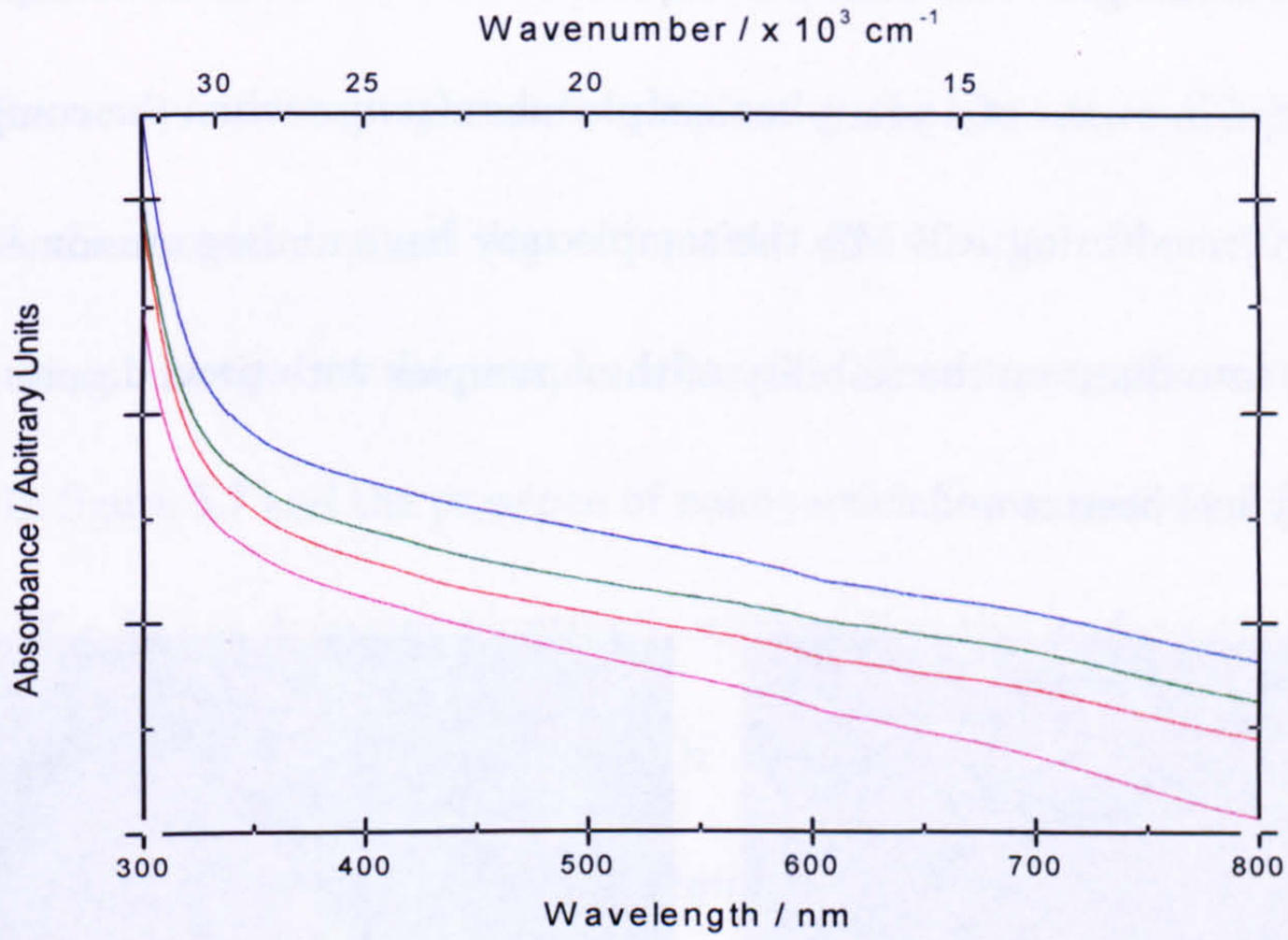

Figure 5.5: The UV-visible spectrophotometry measurements for the 5 % (purple), 10 % (red), 15 % (green) and 20 % (blue) silver-doped samples. Measurements taken by Pickup [10].

SEM imaging coupled with EDX was also conducted to see whether any possibly non-metallic silver clusters were visible as the spectrophotometry would not detect these. Figure 5.6 displays some SEM images for the silver-doped powdered samples and although these clearly display powdered grains of a variety of sizes, any prominent silver nanoparticles or clusters could not be successfully identified. This suggests that if any nanoparticles are present then they must be below the detectable limit which is less than a few tens of nanometers for powders since any compositional contrast is combined with topographical variations, making small clusters more challenging to distinguish [17]. The EDX analysis did however, show variations in the elemental composition when analysing different regions of the glass network. Due to the limitations in accuracy of the EDX technique it was not possible to verify the extent of the inhomogeneity other than to say that the samples

appear a little heterogeneous. It is also important to note that as these experiments were completed in excess of a year after sample manufacture when the compositions had been confirmed using ICP-MS, the sample may have undergone some changes which brings into question the stability of these samples with time, despite the care in which they had been stored.

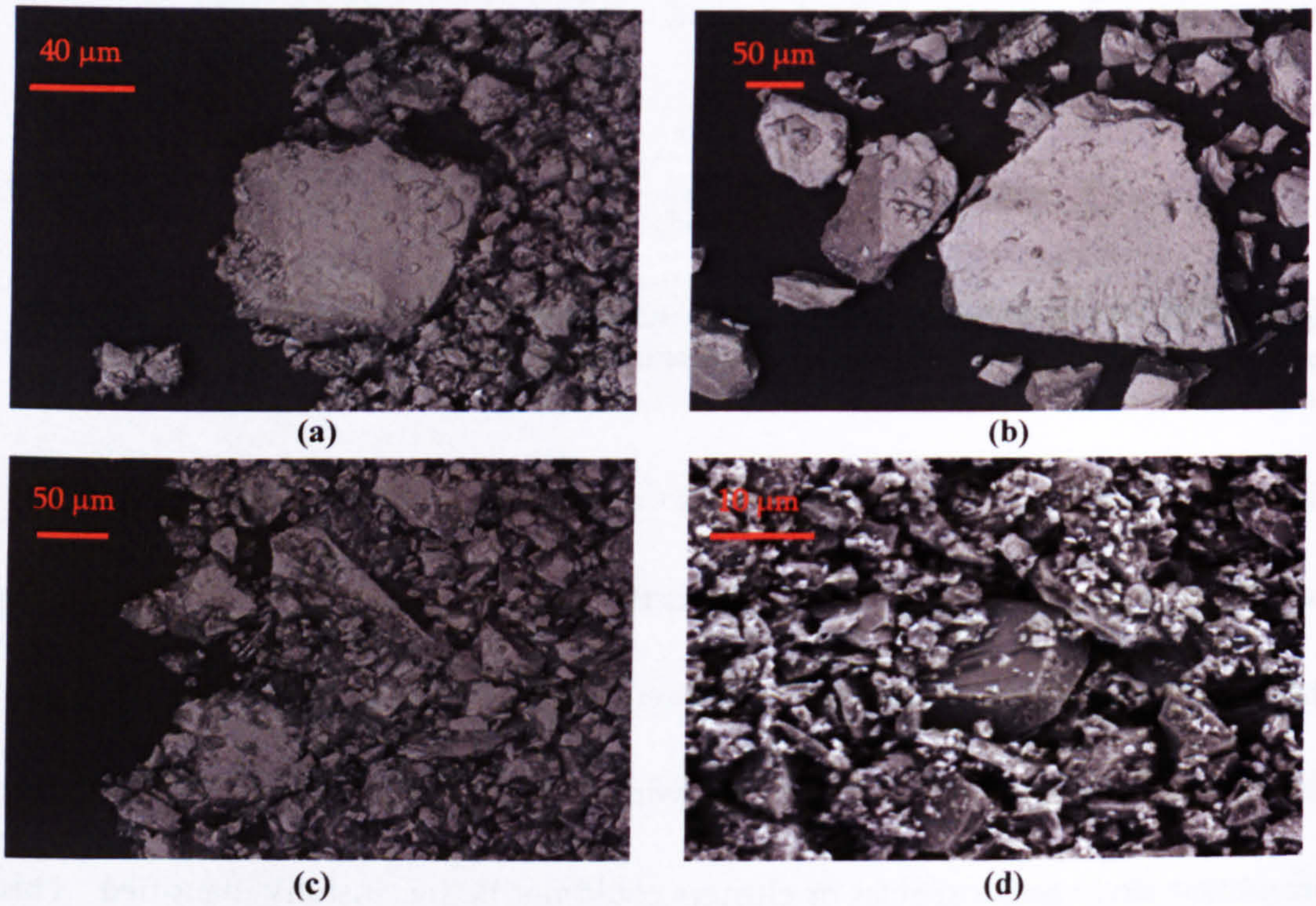

Figure 5.6: The SEM images taken from the (a) 0, (b) 5, (c) 10 and (d) 20 % silver-doped powdered phosphate glass samples.

Images of the 20 % silver-doped powdered sample were also collected with a JEOL 2000fx transmission electron microscope (TEM) system using a 200 kV electron beam, which although similar in experimental setup to the SEM, views the unscattered electrons passing directly through the sample as they impact upon a phosphor screen beneath the sample [17]. This technique gives an indication of

mass-thickness contrast with much better magnification and resolution than SEM [17]. The sample was prepared by dispersing the powder in isopropanol and methanol, then sonicating and depositing this onto a carbon film with copper grid before drying. Images of the sample taken at different magnifications are shown overleaf in figure 5.7 and the presence of nanoparticles was confirmed from the dark particles of < 40 nm diameter identified, surrounding the surface of the powdered phosphate glass grains, consistent with the occurrence of phase separation. Although these nanoparticles were chemically analysed using the EDX system coupled to the TEM, it was not possible to accurately determine their composition other than to say that they are silver-containing. The composition of the bulk of the material could also not be confirmed meaning that our predictions for the phosphate speciation may no longer be valid.

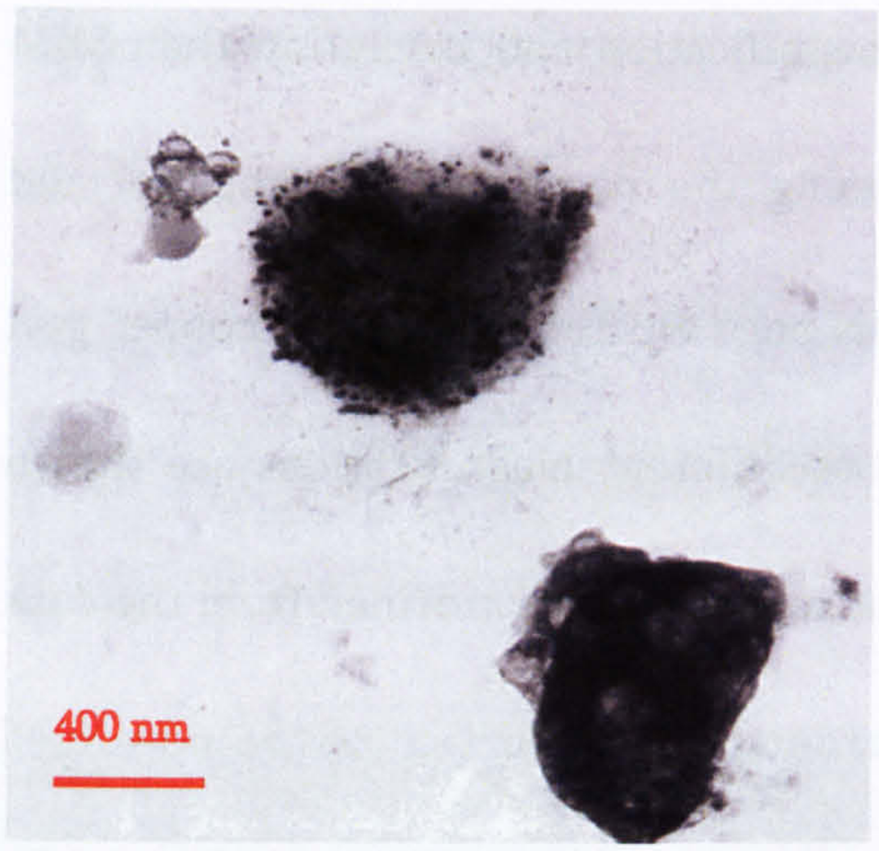

(a)

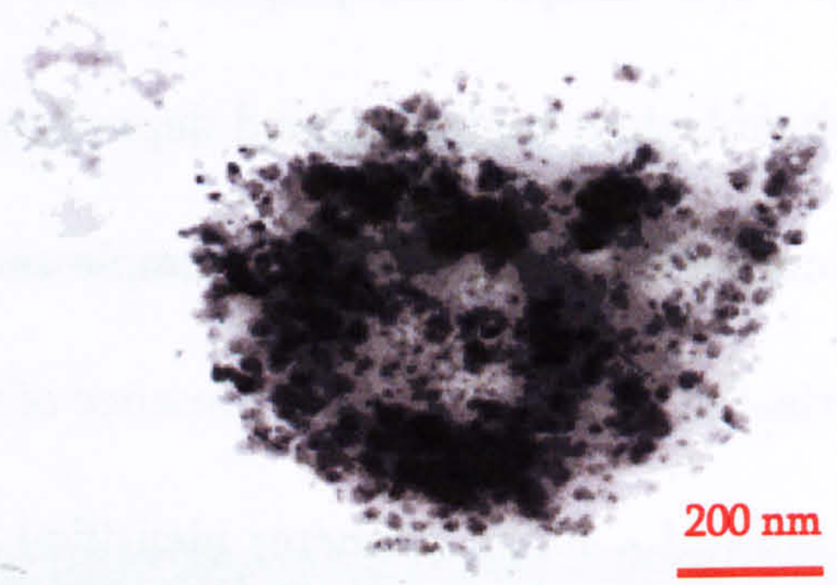

(b)

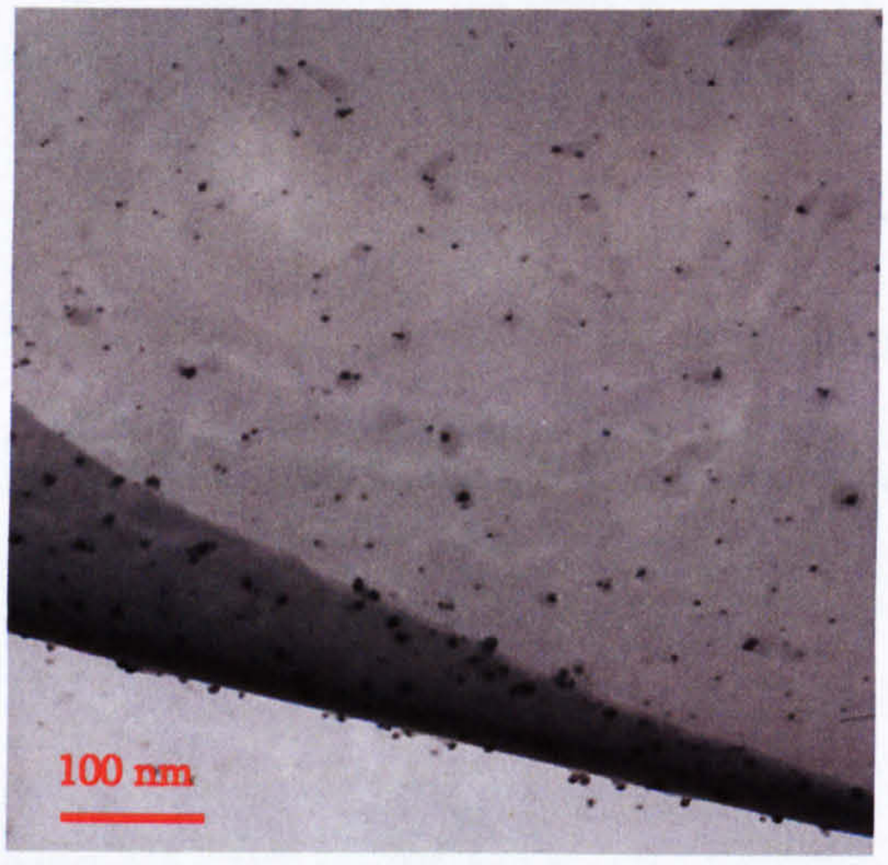

(c)

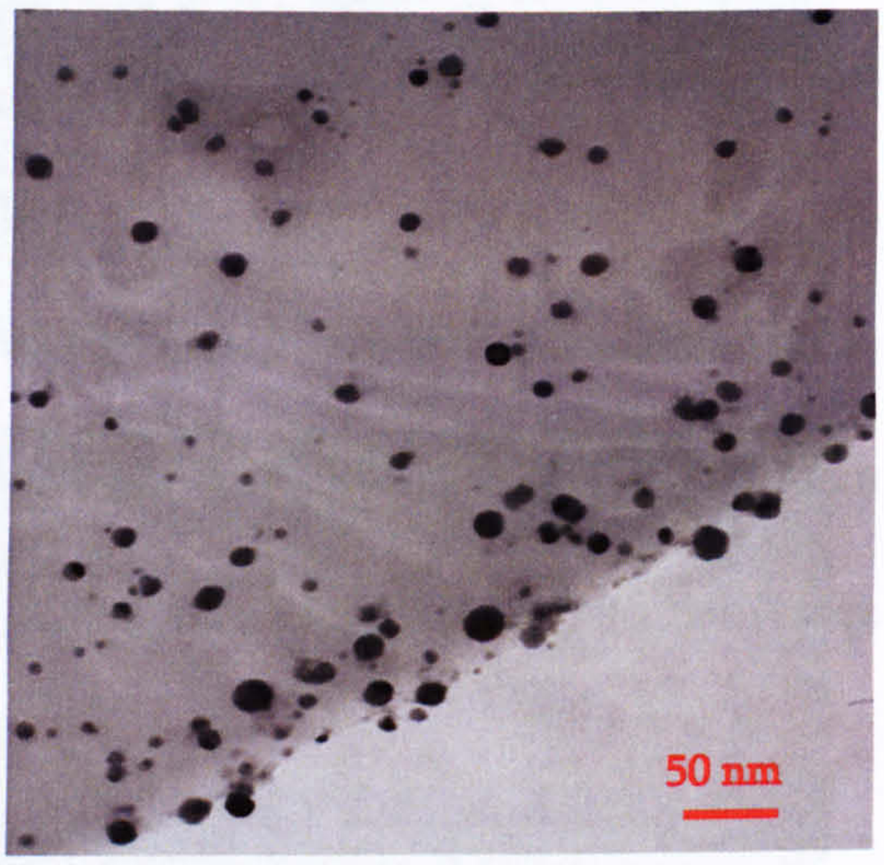

(d)

Figure 5.7 (a) to (d): TEM images by York, of the 20 % silver-doped powdered glass samples at various magnifications as indicated on each image. (a) Shows a number of powdered grains whilst (b) is a magnified image of the top grain from (a). (c) and (d) both show a magnified view of the nanoparticles observed.

Again the critical caveat to note in these results is that these measurements were conducted in excess of one year after the other experiments were completed and although kept in silica-containing desiccators and away from light, silver is known to tarnish due to its reactivity with air and its possible contaminants [18]. This was especially suspected as the powdered samples which had originally appeared white in colour, changed to a brown-tinted, off-white appearance as they aged. Any

changes in the sample with time could have given rise to these nanoparticle formations after the NMR and other measurements had been completed meaning that these TEM results are somewhat inconclusive.

Although we were able to detect some sort of phase separation which may well explain the presence of Q^3 phosphate units since if the majority of silver separates into these clusters then the remaining glass network would consist of a higher percentage of phosphorus pentoxide and a smaller amount of network modifier, we cannot however confirm whether this phase separation was actually present at the time when the NMR investigation took place. We also do not know to what extent the silver has phase separated since we cannot accurately determine either the bulk sample or nanoparticle composition. It is therefore still important to explore other possibilities to explain the presence of the Q^3 phosphate units present. In previous studies [19] discussion has arisen regarding possible network forming behaviour of cations such as zinc and magnesium which could lead to an increase in phosphate coordination via repolymerisation. This so-called network forming behaviour means that some cations could potentially increase the connectivity between phosphate units which may account for greater percentages of higher Q^n species. However, unlike the ions listed above, there has been no evidence in the literature reviewed of network forming silver as this would involve the ions becoming tetrahedrally coordinated and becoming part of the phosphate tetrahedral network. This behaviour is not thought possible since there is no tendency for silver to reside

in tetrahedrally coordinated sites due to its electronic configuration and network modifying nature. To determine the silver oxidation state occurring within these glasses silver X-ray absorption near edge structure (XANES) spectroscopy was performed.

XANES is a spectroscopic technique that explores the atomic absorption of X-rays produced by a synchrotron radiation source which can sweep the photon energies such that they are just great enough to excite core level electrons into a higher, unoccupied state. Below these energies the photons cannot excite any electrons, thus absorption is low but when the energy is sufficient, a large increase in X-ray absorption is observed known as the absorption edge. The X-ray energies used in XANES are typically swept to ~100 eV above the absorption edge which also gives an indication of absorption taking place by the photoelectrons emitted from the atom with low kinetic energies that consequently undergo multiple scattering from surrounding atoms [20]. The energy and intensity of the absorption edge observed contains information regarding the oxidation state of the absorbing atom, and the higher energy region extracts chemical information such as the coordination environment, geometrical distortions and configuration of the atomic species within its surrounding network [20]. This technique allowed us to not only obtain an idea of the silver coordination within the glass sample, but also enabled us to determine its oxidation state. This is important as the silver in these samples is added in the form of Ag^+ in the compound Ag_2SO_4 but the silver was expected to oxidise at the

high glass forming temperatures (1100 °C) to form Ag^{2+} within the glass [1]. However, only Ag^{+} has been found to be an effective antibacterial agent and as these glasses have shown success in their antibacterial capabilities, there must be some Ag^{+} within the samples, and it is possible that the silver is therefore occurring in mixed valences. For this reason it is important to determine the redox state of the silver to aid explanations of the sample properties and it is also possible that the two oxidation states may have different effects upon the chemical structure.

The Ag K-edge XANES measurements taken on these samples were made at ~77 K on Station 16.5 of Synchrotron Radiation Source (SRS), Daresbury Laboratory, UK, using a ring energy of 2 GeV and stored current of 150 to 250 mA. The finely ground samples were diluted in spectroscopic grade polyethylene (Aldrich) and pressed into pellets ready for experimentation. Further information regarding the experimental details are outlined in references [2] and [3], included in appendices A and B.

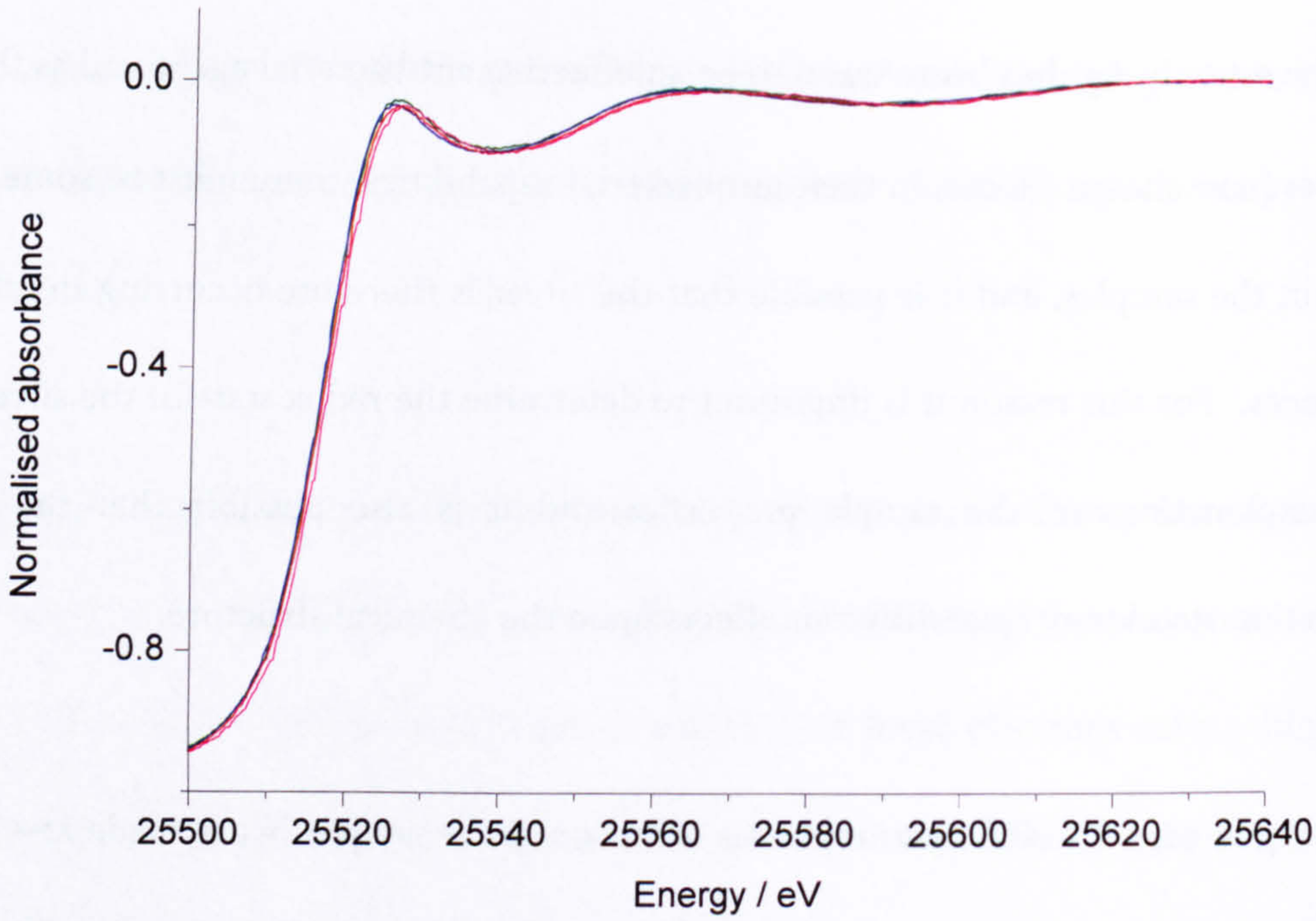

Figure 5.8: Ag K-edge XANES for the 5 (pink), 10 (red), 15 (green) and 20 % (blue) silver-doped samples by Pickup [10] and adapted from [2 & 3].

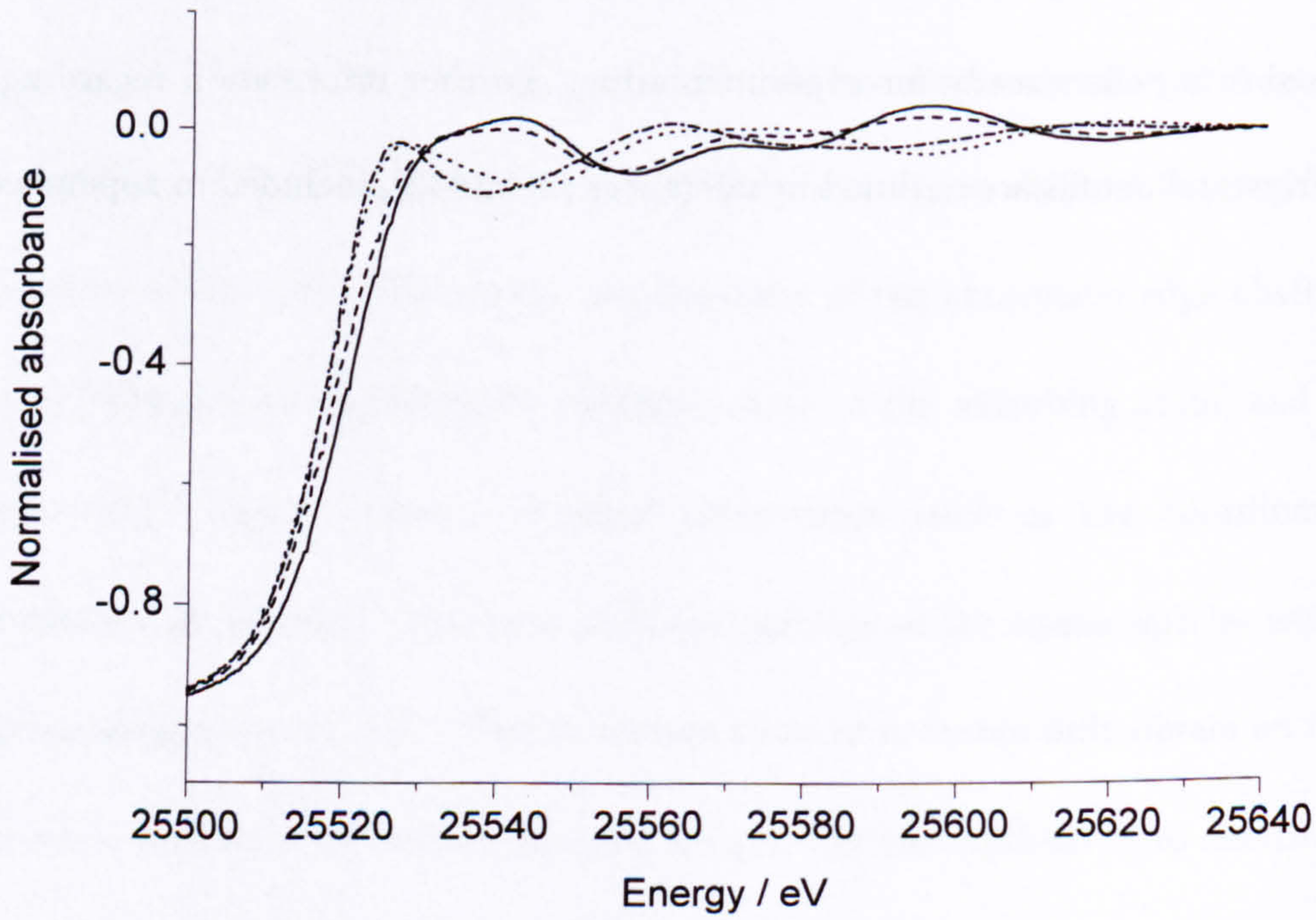

Figure 5.9: Ag K-edge XANES spectra for the AgO (——), Ag_2O (- - - -), Ag_3PO_4 (.....) and Ag_2SO_4 (- · - · -) reference compounds by Pickup [10], adapted from [2 & 3] .

The Ag K-edge XANES results gave rise to identical spectra for the 5, 10, 15 and 20 % silver-doped phosphate glass samples as can be seen in figure 5.8 [2 & 3]. This implies that the oxidation state and local environment of the silver ions is consistent for each of these glasses. The Ag K-edge XANES spectra for these samples were compared to four reference samples, AgO, Ag_2O, Ag_3PO_4 and Ag_2SO_4 (figure 5.9) and the glass sample spectra and the X-ray absorption edge positions were found to directly overlay that of the Ag_2SO_4 reference, see figure 5.10 comparing the 10 % silver-doped sample to this reference. This suggests that the silver is in the same oxidation state within these samples and the Ag_2SO_4 reference, which is an Ag^+ compound. This is a significant result as it is this silver oxidation state that is highly desirable for use in biomedical applications. The presence of Ag^+ also shows that the systematic replacement of Na_2O with Ag_2SO_4 in this sample series results in the direct substitution of one Na^+ ion for one Ag^+, thus confirming that there should be no further change in network connectivity with doping.

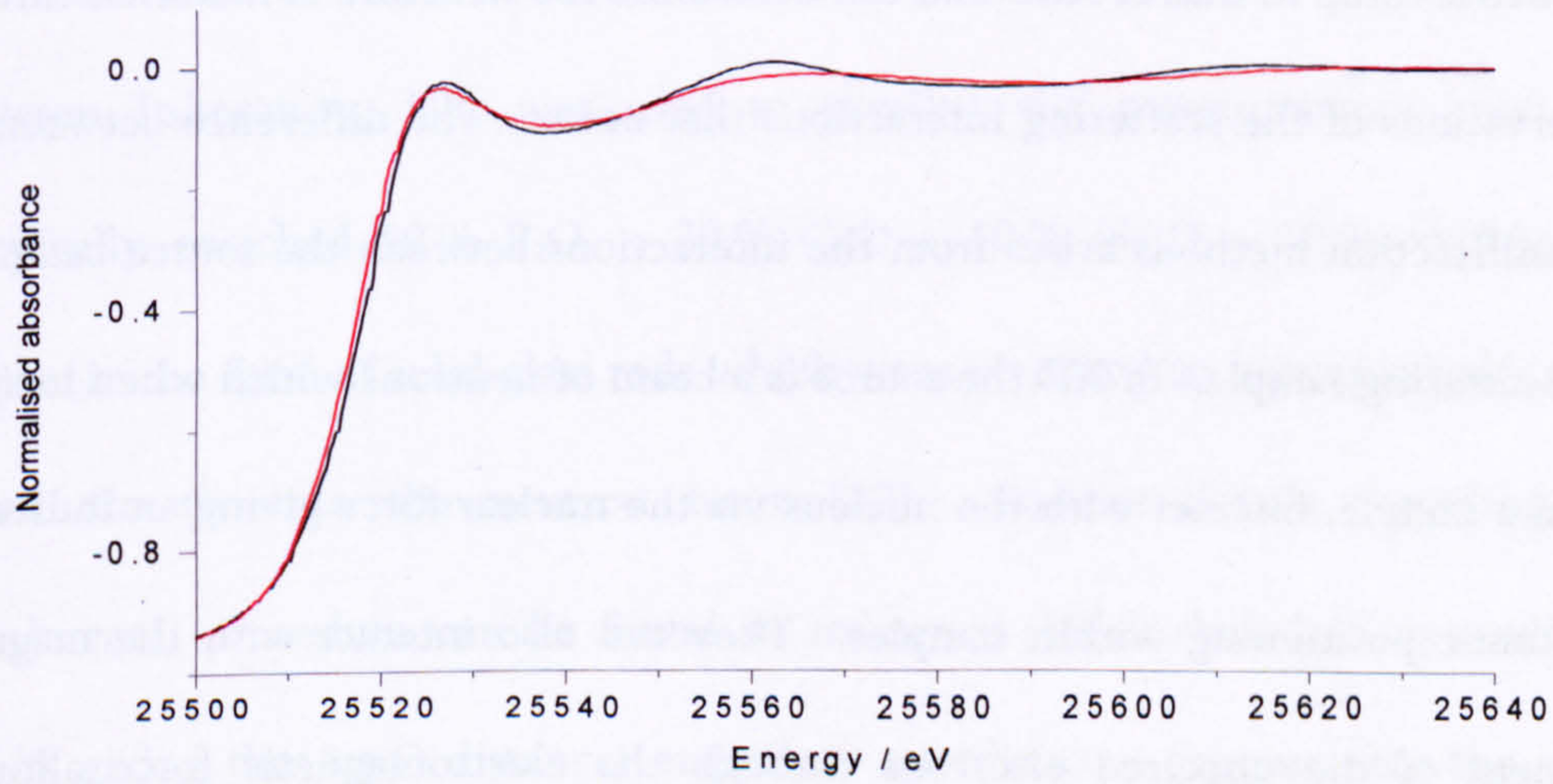

Figure 5.10: Ag K-edge XANES for the 5 % silver-doped phosphate based glass sample (red) compared to the Ag_2SO_4 reference compound (black) by Pickup [10] and adapted from [2 & 3] in appendices A and B.

The overall shape of the XANES spectra is affected by the surrounding environment and as the number of surrounding oxygen atoms increases, the absorption edge becomes sharper [21]. As the shape of the edge and the higher energy portions of the spectra for our samples is similar to that of the Ag_2SO_4 spectrum within which the silver is 6-fold coordinated, it is reasonable to assume that the silver in our glass samples also resides in an octahedron of oxygen atoms, therefore ruling out any network forming, tetrahedrally coordinated silver.

Although the Ag K-edge XANES results successfully determined the silver valence state and gave an indication of the silver octahedral coordination within the samples, this technique can be insensitive to the more subtle distortions of the local environment. Neutron diffraction with isotopic enrichment (NDIS) was therefore implemented to probe with significantly enhanced qualitative reliability, the local structural surroundings of the silver ions. ND is a diffraction technique similar in geometric setup to that of XRD and can determine the structure of materials through observations of the scattering interactions that occur. The difference between the two diffraction methods arises from the interactions between the source beam and the scattering sample. In ND the source is a beam of neutrons which when incident upon a sample, interact with the nucleus via the nuclear force giving an indication of atomic positioning within samples. They can also interact with the magnetic moment of the unpaired electrons through the electromagnetic force allowing magnetisation to be investigated, but as this glass system is purely diamagnetic, this

use of ND has been neglected here. XRD involves a beam of X-ray photons which diffract primarily from the electron cloud surrounding each atom in the sample and hence the diffracted X-ray intensities are larger for atoms of higher atomic numbers (Z). As the neutrons interact directly with the nucleus the contribution to the diffracted intensities does not have a systematic relationship with Z but is instead different for each isotope allowing isotopic substitution to be used in order to obtain information regarding the partial structure arising from one particular element of interest, which is especially desirable in disordered materials such as these [10]. Silver has two naturally occurring isotopes ^{107}Ag and ^{109}Ag, with roughly the same abundances (51.8 and 48.2 %, respectively). Atoms are described by their scattering lengths, the square of which is proportional to their scattering cross-section and the scattering lengths of ^{107}Ag and ^{109}Ag are 7.555 fm and 4.165 fm respectively [10], leading to very different diffraction intensities.

The GEM diffractometer at the ISIS pulse neutron source at the Rutherford Appleton Laboratory, UK, was used to conduct the measurements upon the isotopically enriched 50 % P_2O_5 + 30 % CaO + 10 % Na_2O + 10 % $^{107/109}Ag_2SO_4$ samples in the form of solid glass rods which were mounted on a sample holder and placed directly into the neutron beam [10]. Further details regarding the experimental procedure can be found in reference [10] included in appendix C. Results giving the Ag-O distances and silver coordination propose that the silver ions are surrounded by a highly distorted octahedron of oxygen ligands with the six

oxygen atoms residing at three distinct distances from the central silver ion. The Ag-O distances derived from the data were 0.228, 0.251 and 0.258 ± 0.003 nm with associated coordination numbers of 2.1, 2.7 and 1.1 ± 0.5, respectively. These results are consistent with those from the Ag K-edge absorption spectra which suggested that the silver ions in these samples resided in a similar coordination to those in Ag_2SO_4. In this reference sample the silver ions are surrounded by six oxygen atoms at three distinct distances (0.239, 0.244 and 0.266 nm), with a coordination of 2 each, and as such this shows good qualitative agreement of the two sets of experimental results. The other parameters gained from this NDIS investigation include the P-O, Na-O, Ca-O, O-O and P-P correlations and were typical of those expected for metaphosphate glasses showing two distinct P-O distances relating to the bridging and non-bridging oxygen atoms [10]. These results also confirmed the presence of Q^1, Q^2 and Q^3 speciation observed from the NMR measurements and can be found within the tables of data in reference [10], included in appendix C.

The ^{23}Na MAS NMR was performed to provide information regarding the local structural environment surrounding the sodium ions in the samples which charge balance the non-bridging oxygen present. Three fields were used to better constrain the fitting parameters. An example of the ^{23}Na NMR spectra for the 3 mol. % doped sample is given in figure 5.11 at these fields to show the improved resolution (narrower spectra) when performing at higher frequencies, and slight shift in peak

position due to the effect of the second-order quadrupole interaction with change in magnetic field [22].

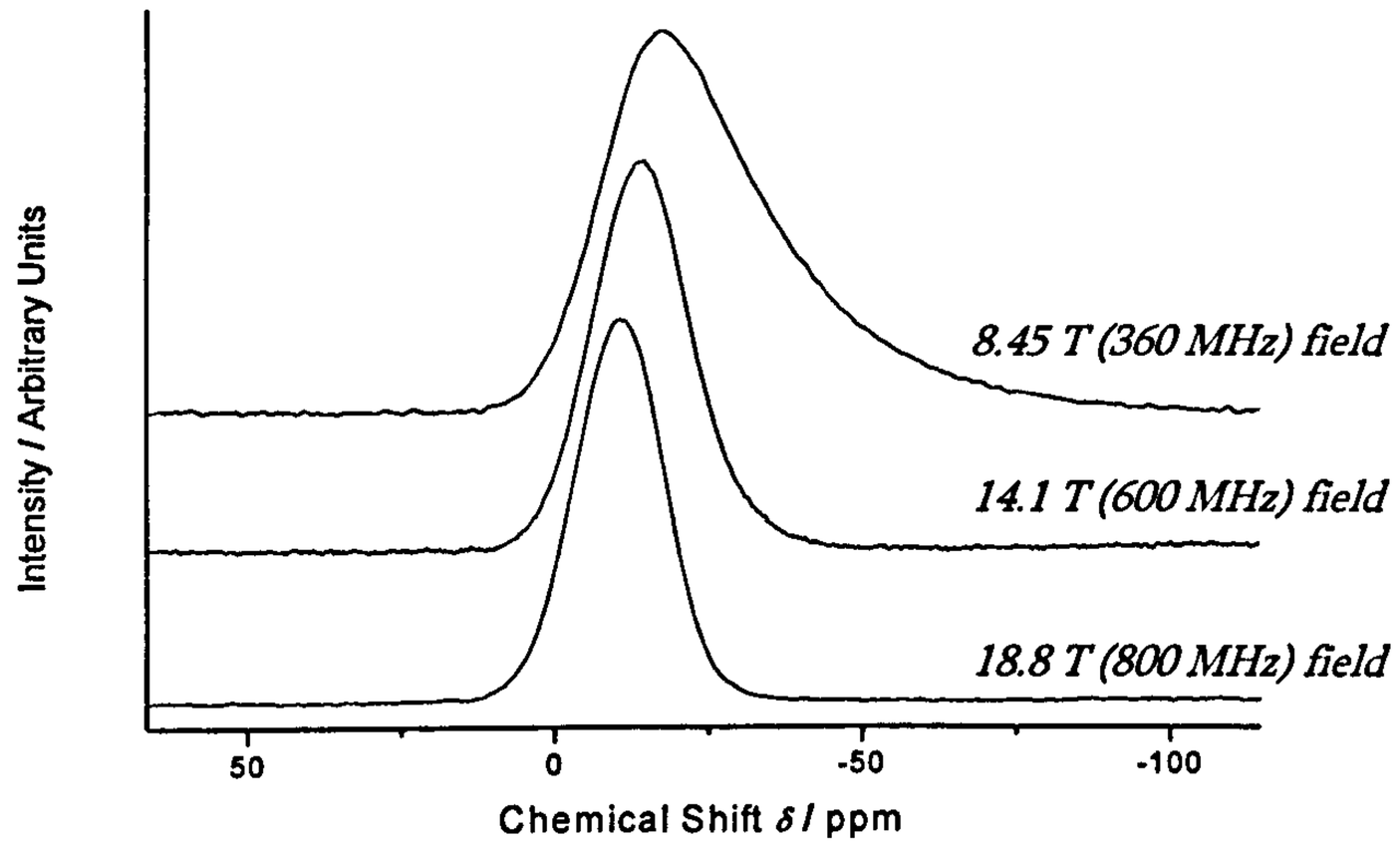

Figure 5.11: ^{23}Na spectra for the 3 mol. % silver-doped sample showing the improved resolution at higher field.

At low field the asymmetry of the peak is clearly evident and shows the presence of a distribution of quadrupolar interactions [8]. The parameters deduced from fitting these spectra gave values for the quadrupolar coupling constant, χ_Q, in MHz, which determines the amount of distortion surrounding the ^{23}Na sites within the glass, and the quadrupolar distribution, $\Delta\chi_Q$, in MHz, that leads to an idea of how broad the distributions present in the glass are and hence how disordered the sodium sites are. These silver-doped samples showed a general drop in both of these values, see table 5.3, however the associated errors are substantial (figure 5.12). When considering the uncertainties, no distinct change in ordering or distortion within the glass can be determined as larger quantities of silver are incorporated. To provide more conclusive information the data processing and fitting must be refined significantly

to produce more precise data. In cases such as this, unambiguous determination of the local coordination of sodium from the NMR data can be far from straight forward. It would therefore also be useful to perform Na K-edge XANES to give additional information regarding the coordination to allow better understanding of the cross-linking between the sodium and the surrounding non-bridging oxygen atoms. This would provide a more complete description of the glass system as the sodium environment and coordination is often highly complicated due to a lack of definite structure from the disorder arising in glasses [23]. This could also lead to more detailed comparisons between the sodium and silver cross-linking effects to understand the mechanisms for the silver ions providing stronger cross-links which strengthen the overall glass network and structure.

Silver-doping / mol. %	***δ_{iso} / ppm ± 2 ppm***	***χ_Q / MHz ± 0.3 MHz***	***$\Delta\chi_Q$ / MHz ± 0.2 MHz***
0.0	–7	2.7	1.8
1.0	–7	2.6	1.7
2.0	–8	2.5	1.7
3.0	–8	2.4	1.5
4.0	–8	2.5	1.8
5.0	–7	2.5	1.7
10.0	–8	2.5	1.7
12.5	–8	2.4	1.7
15.0	–8	2.3	1.3
17.5	–8	2.4	1.7

Table 5.3: ^{23}Na NMR data for the silver-doped phosphate glass samples.

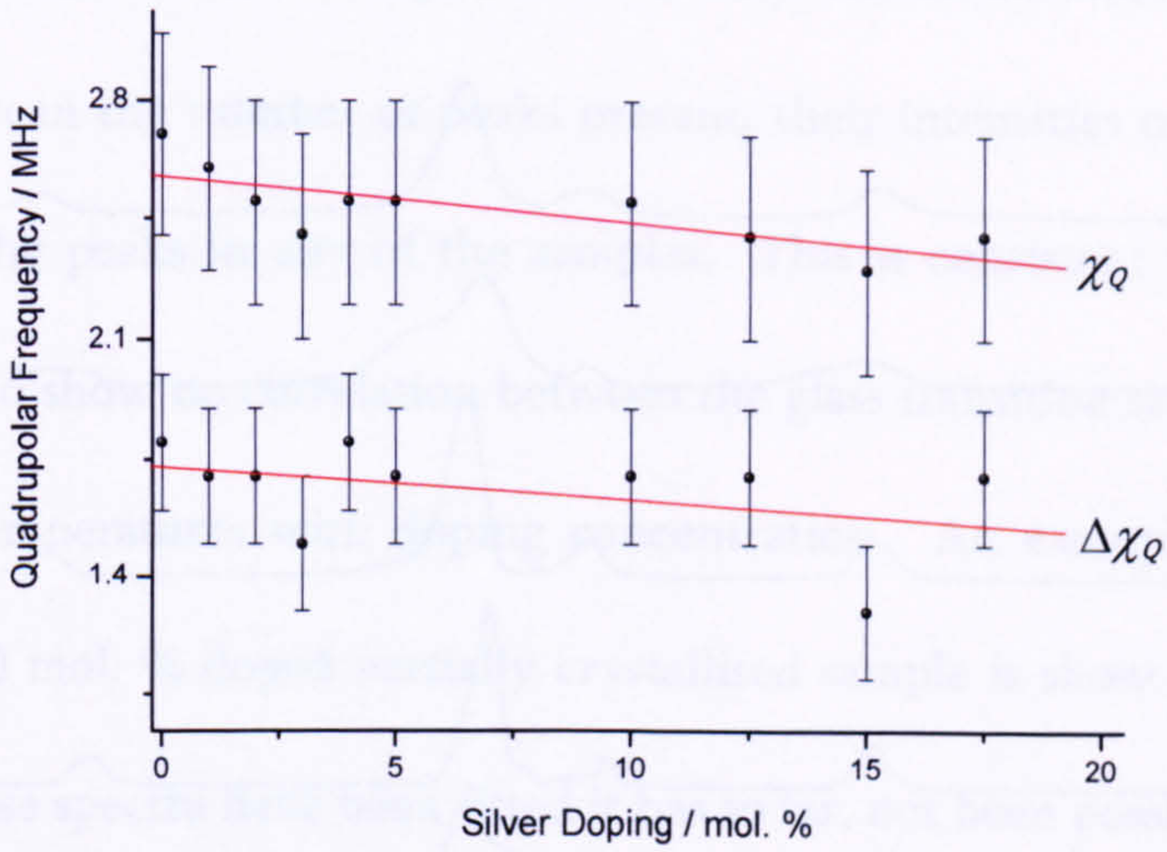

Figure 5.12: The ^{23}Na NMR quadrupolar coupling constant and quadrupolar distribution as a function of doping concentration for the Ag_2SO_4 doped glass samples, with lines of best fit.

5.2.4 Partially crystallised samples

After the crystallisation temperatures were measured from the DTA (see section 5.2.2), the melt-quenched glass samples were heated to this temperature for two hours to create crystallised samples. These crystallised samples were produced to provide information regarding any phases that become present once the crystallisation temperature for that particular sample has been surpassed. This was attempted as the crystalline phases could possibly affect the glass properties such as dissolution and degradation rates. The T_c of phosphate glasses can also be quite low therefore if any heat treatment methods are used during the prosthesis coating process it could possibly result in the crystallisation of the glass, so it is important to appreciate the effects that this may have on the properties of the samples and their bioactivity. The ^{31}P NMR spectra for these samples are given in figure 5.13.

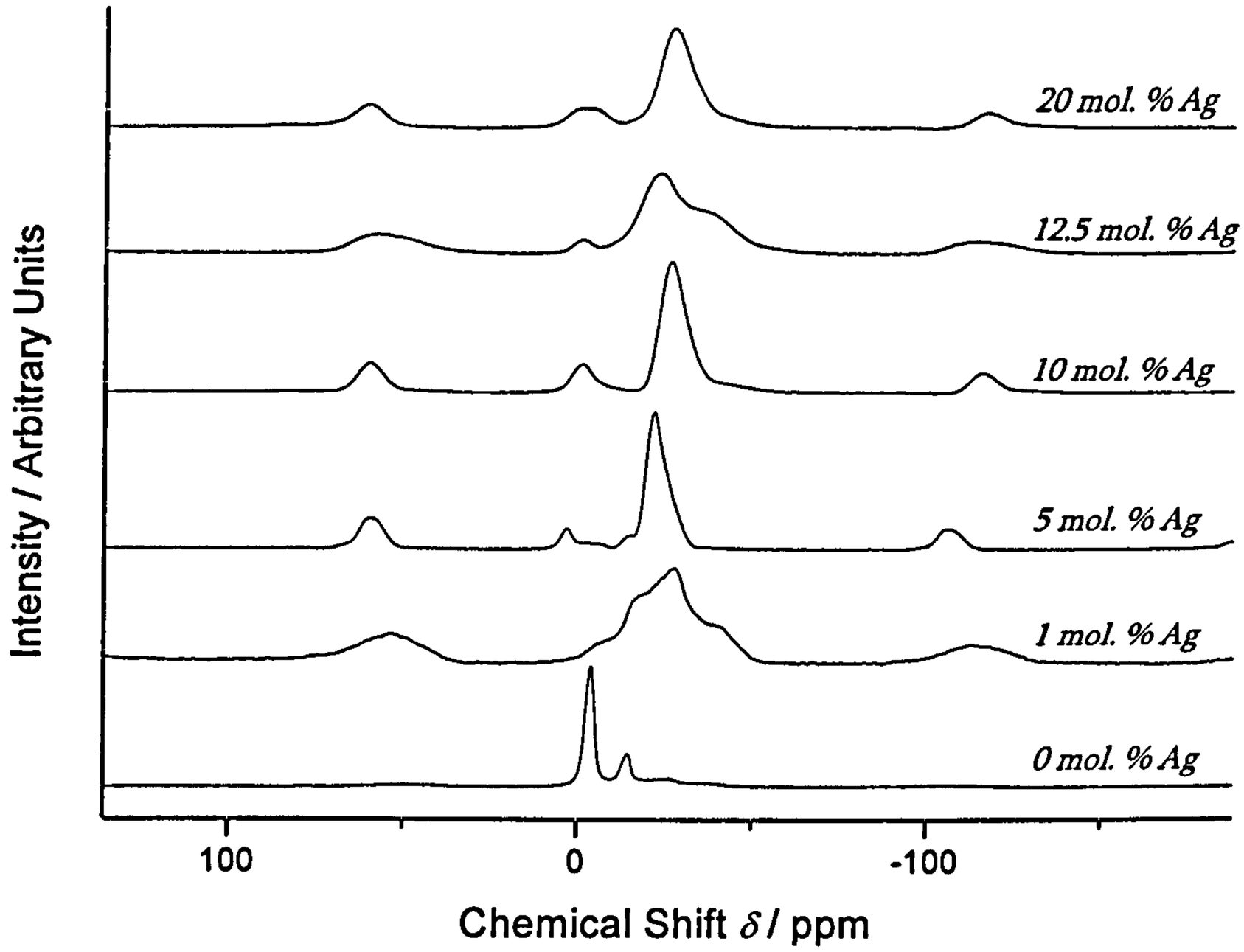

Figure 5.13: ^{31}P MAS NMR spectra of Ag_2SO_4 doped partially crystallised phosphate glass samples at a spin rate of ~12 kHz.

Difficulties arose in interpreting the NMR data from the crystallised phase glasses as they were found to contain both glassy and crystallised components. The glassy components could be identified as they gave rise to broad spinning sidebands. These partially crystallised samples show that the crystalline phase is both more ordered and less anisotropic than the glass phase, since it gives rise to narrower spectral peaks, no related sidebands and different T_1 relaxation times to the glass phase. The T_1 relaxation times were extremely long, approximately 360 s in these samples for the crystalline components, which made the experiments lengthy.

The results obtained for these samples show a very disordered state with no clear correlation between the number of peaks present, their intensities or the chemical shift values of the peaks in any of the samples. This is consistent with the DTA results which also show no correlation between the glass transition temperature and crystallisation temperatures with doping concentration. An example of the peak fitting for the 10 mol. % doped partially crystallised sample is show in figure 5.14, but although these spectra have been fitted it has so far, not been possible to identify the crystalline phases corresponding to the NMR peaks present via comparisons with work by Duncan [24] which reports on many crystalline phase ^{31}P chemical shift values.

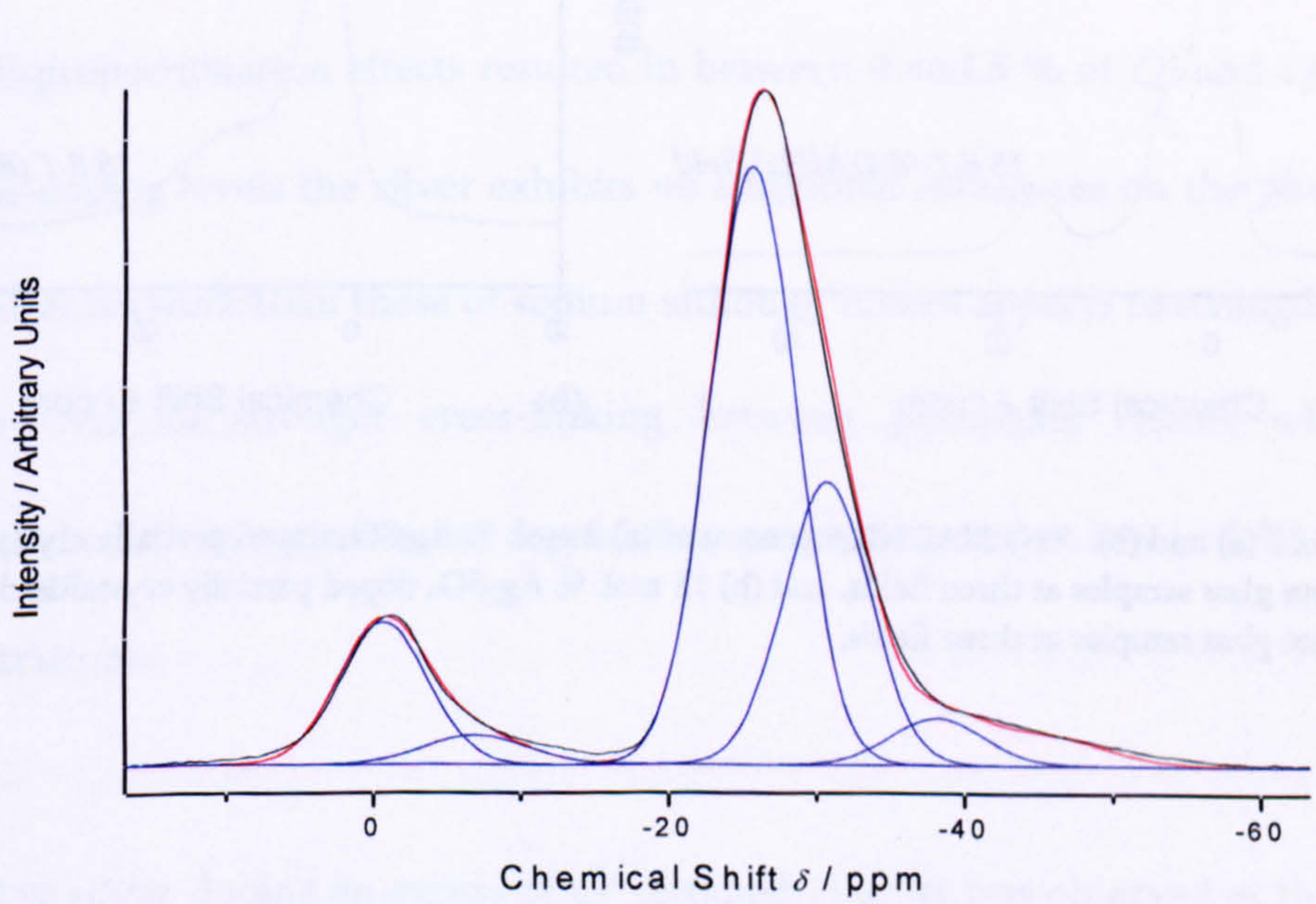

Figure 5.14: The deconvolution of the peaks present in the ^{31}P NMR spectrum for the 10 mol. % silver-doped partially crystallised sample. The peak fits are shown in blue, the red line shows the overall fit and the black line shows the original spectrum.

In addition to the ^{31}P NMR, ^{23}Na NMR experiments were also performed on these partially crystalline samples, although due to time constraints these have not yet been fitted. An example of the data collected at the three fields available for our experiments are shown in figures 5.15 (a) and (b).

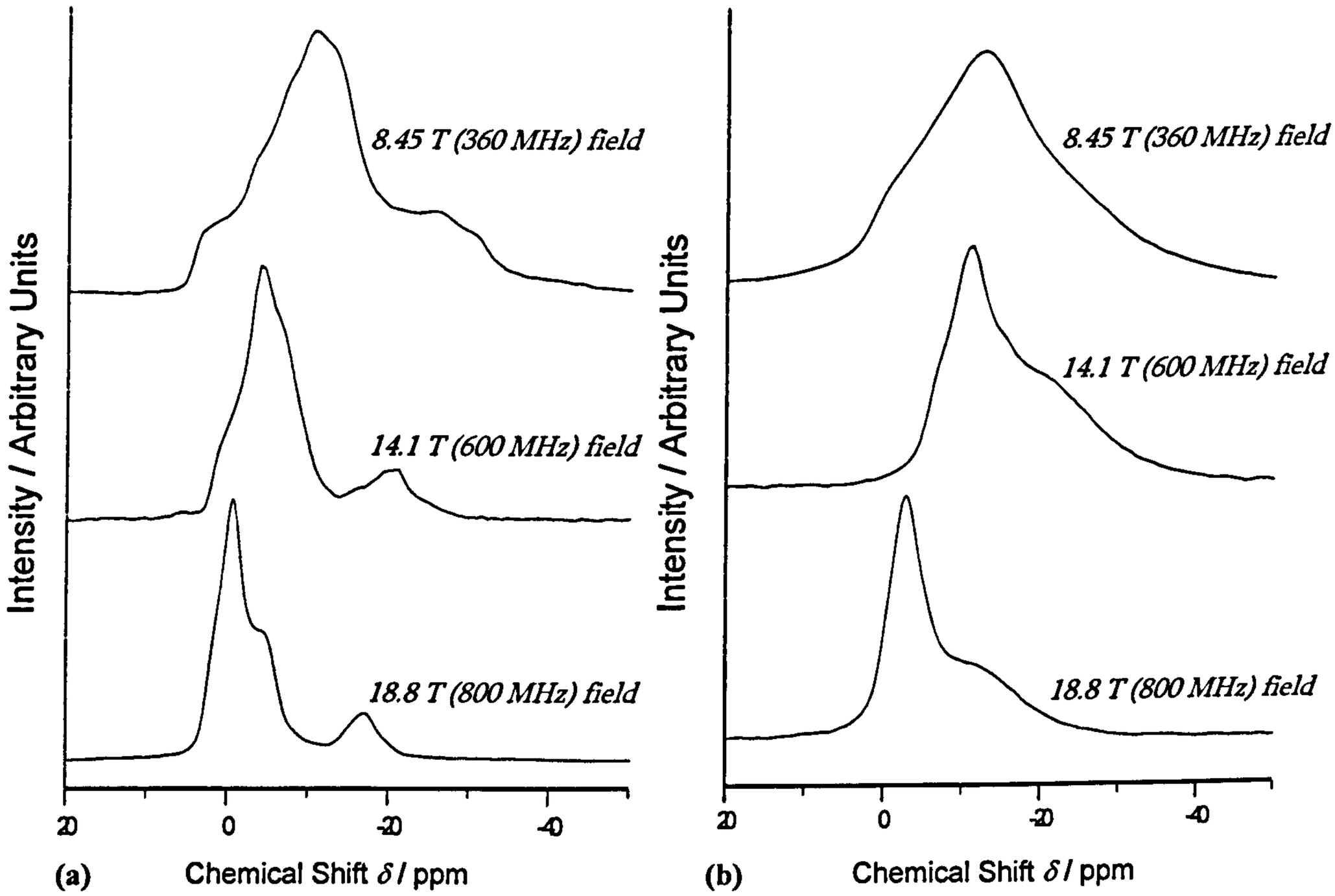

Figure 5.15 (a) and (b): ^{23}Na MAS NMR spectra of (a) 3 mol. % Ag_2SO_4 doped partially crystallised phosphate glass samples at three fields, and (b) 15 mol. % Ag_2SO_4 doped partially crystallised phosphate glass samples at three fields.

5.3 Conclusions and further work

From the exploration of the silver-doped phosphate glass structure and properties we have successfully verified the antibacterial nature of the glass which is associated with the presence of Ag^+ ions, confirmed as the only silver valence state within the

samples from XANES measurements. The release of these silver ions from the samples with time was also shown from the degradation studies which confirm that these samples have the desired properties for their role as antibacterial ion hosts. These degradation studies also confirm our ability to control the dissolution of these glasses by adjusting the dopant incorporation which can be important in their application.

The NMR technique proved invaluable in investigating the structural parameters of the samples and showed that for ≤ 10 % silver-doping the phosphate structure of the glasses closely follows that predicted from the binary model outlined by Brow [4] with Q^2 metaphosphate units comprising between 95 to 99 % of the structure. The slight disproportionation effects resulted in between 0 and 5 % of Q^1 and Q^3 units. At these doping levels the silver exhibits no additional influences on the phosphate tetrahedral network than those of sodium although it does appears to strengthen the structure via its stronger cross-linking between phosphate chains which is manifested as an alteration in the degradation properties even at low (≤ 5 %) doping concentrations.

At > 10 % silver-doping an excess of Q^3 tetrahedral units was observed as the silver now appears to have a very different influence on the phosphate network than sodium. The possible explanations for this include that the chemical composition was perhaps not correctly predicted and although the ICP-MS data showed

consistent elemental results, the EDX measurements highlighted the heterogeneity of the samples but could not confirm the elemental composition since the degree of accuracy of this technique is questionable at these levels and furthermore, changes in the sample may have occurred over time if the sample is in fact unstable. Network forming would result in repolymerisation of the phosphate network hence increasing the network coordination, but the silver was found to reside in an octahedrally coordinated environment charge balancing the terminal oxygen atoms present in the sample rather than becoming tetrahedrally incorporated as part of the phosphate units. Phase separation was suggested to create a deficit of modifying oxide within the remaining glass network but the spectrophotometry measurements performed could not detect any metallic nanoclusters within the samples. The TEM did however show observable silver-containing colloids within the 20 % doped sample although we cannot determine whether these originated in the samples upon formation or resulted from sample aging. These TEM results therefore do not provide conclusive evidence for a silver-containing phase separating out as a cause of the unexplained Q^n species observed. It would be highly desirable to conduct additional TEM measurements upon the lower doped (< 10 %) silver phosphates or some remade and newly manufactured samples in an attempt to determine the cause of the Q^3 species observed but any answers at present are elusive. The unidentified peak observed in some of the ^{31}P NMR spectra also remains unexplained.

Although some high quality NMR has been produced showing interesting effects of the silver-dopants on the phosphate tetrahedra, to further extend this work it would be valuable to implement ^{17}O multiple quantum NMR of ^{17}O enriched silver-doped glasses [25 & 26] to resolve the different oxygen bridges in the samples. Work is currently underway to construct an enrichment furnace which may be used to incorporate ^{17}O into the samples of interest. It would also be beneficial to run ^{109}Ag NMR experiments on the samples and to gain further insight into the connectivity between different Q species present 2D MAS NMR or double-resonance experiments could be used which should provide increased resolution and additional information. Developing a better understanding of the differences between the roles of sodium and silver cations in these glass systems would also be desirable and perhaps sodium K-edge XANES measurements would assist in describing the sodium environment.

The spectra obtained from the crystallised samples were complex and the crystalline components must be identified as any effects that these may have upon dissolution and degradation rates would be interesting in cases where the samples exceed their crystallisation temperatures during the prosthesis coating process.

References

[1] I. Ahmed, D. Ready, M. Wilson, and J. C. Knowles, *Antimicrobial effect of silver-doped phosphate-based glasses*, Journal of Biomedical Materials Research Part A, **79**:3 (2006), 618-626.

[2] S. P. Valappil, D. M. Pickup, D. L. Carroll, C. K. Hope, J. Pratten, R. J. Newport, M. E. Smith, M. Wilson and J. C. Knowles, *Effect of silver content on the structure and antibacterial activity of silver-doped phosphate-based glasses*, Antimicrobial Agents and Chemotherapy, **51**:12 (2007), 4453-4461.

[3] I. Ahmed, E. A. Abou Neel, S. N. Nazhat, J. R. Jones, D. M. Pickup, D. Carta, B. Newport, D. L. Carroll, M. E. Smith and J.C. Knowles, *The structure and properties of silver-doped phosphate based glasses*, submitted for the Journal of Materials Science, **42** (2007), 9827-9835.

[4] R. K. Brow, *Review: the structure of simple phosphate glasses*, Journal of Non-Crystalline Solids, **263** & **4** (2000), 1-28.

[5] A. Chahine, M. Et-Tabirou, M. Elbenaissi, M. Haddad and J. L. Pascal, *Effect of CuO on the structure and properties of* $(50 - x/2)Na_2O$-$x\,CuO$-$(50 - x/2)P_2O_5$ *glasses*, Materials Chemistry and Physics, **84** (2004), 341-347.

[6] H. S. Gao, T. E. Tan and D. Wang, *Effect of composition on the release kinetics of phosphate controlled release glasses in aqueous medium*, Journal of Controlled Release, **96** (2004) 21-28.

[7] H. S. Gao, T. E. Tan, D. Wang, *Dissolution mechanism and release kinetics of phosphate controlled release glasses in aqueous medium*, Journal of Controlled Release, **96** (2004) 29-36.

[8] K. J. D. MacKenzie and M. E. Smith, *Multinuclear solid state NMR of inorganic materials*, Pergamon Press, London, UK (2002).

[9] J. R. Van Wazer, *Phosphorus and its compounds: Volume 1*, Interscience Publishers, New York, USA (1958).

[10] R. M. Moss, D. M. Pickup, I. Ahmed, J. C. Knowles, M. E. Smith and R. J. Newport, *Structural characteristics of antibacterial bioresorbable phosphate glass*, Advanced Functional Materials, **18** (2008), 634-639.

[11] L. Baia, M. Baia, W. Kiefer, J. Popp and S. Simon, *Structural and morphological properties of silver Nan particles - phosphate glass composites*, Chemical Physics, **327** (2006), 63-69.

[12] K. Uchida, S. Kaneko, S. Omi, C. Hata, H. Tanji, Y. Asahara, A. J. Ikushima, T. Tokizaki and A. Nakamura, *Optical nonlinearities of a high concentration of small metal particles dispersed in glass: copper and silver particles*, Journal of the Optical Society of America B, **11**:7 (1994), 1236-1243.

[13] A. E. Hughes, and S. C. Jain, *Metal colloids in ionic crystals*, Advances in Physics, **28**:6 (1979), 717-828.

[14] R. C. Denny and R. Sinclair, *Visible and ultraviolet spectroscopy*, John Wiley and Sons Ltd., Chichester, UK (1987).

[15] R. F. Bartholomew, *Structure and properties of silver phosphate glasses - Infrared and visible spectra*, Journal of Non-Crystalline Solids, **7** (1972), 221-235.

[16] K. A. Bogle, S. D. Dhole and V. N. Bhoraskar, *Silver nanoparticles: synthesis and size control by electron radiation*, Nanotechnology, **17** (2006), 3204-3208.

[17] P. J. Goodhew, J. Humphreys and R. Beanland, *Electron microscopy and analysis*, 3rd Ed., Taylor and Francis, London, UK (2001).

[18] P. T. McTigue and D. J. Young, *Phototarnishing of silver and copper*, Australian Journal of Chemistry, **18** (1965), 1851-1853.

[19] U. Hoppe, *A structural model for phosphate glasses*, Journal of Non-Crystalline Solids, **195** (1996), 138-147.

[20] *Handbook of X-ray spectrometry (practical spectroscopy)*, Eds: R. E. Van Grieken and A. A. Markowicz, 2nd Ed., Marcel Dekker Inc., New York, USA (2002).

[21] D. A. McKeown, H. Gan and I. L. Pegg, *Silver valence and local environments in borosilicate and calcium aluminoborate waste glasses as determined from X-ray absorption spectroscopy*, Journal of Non-Crystalline Solids, **351** (2005), 3826-3833.

[22] M. H. Levitt, *Spin Dynamics: Basics of Nuclear Magnetic Resonance*, John Wiley & Sons Ltd., Chichester, UK (2001).

[23] L. Cormier and D. R. Neuville, *Ca and Na environments in Na_2O-CaO-Al_2O_3-SiO_2 glasses: influence of cation mixing and cation-network interactions*, Chemical Geology, **213** (2004), 103-113.

[24] T. M. Duncan, *A complication of chemical shift anisotropies*, Farragut Press, Chicago, USA (1990).

[25] A. Flambard, L. Montagne and L. Delevoye, *A new ^{17}O-isotopic enrichment method for the NMR characterisation of phosphate compounds*, Chemical Communications, **32** (2006), 3426-3428.

[26] C. Jäger, P. Hartmann, R. Witter and M. Braun, *New 2D NMR experiments for determining the structure of phosphate glasses: a review*, Journal of Non-Crystalline Solids, **263** & **4** (2000), 61-72.

Chapter 6

COPPER PHOSPHATE GLASS

6.1 Introduction

The mixed alkali base glass for the copper-doped samples was a ternary glass consisting of 45 % P_2O_5 + 30 % CaO + 25 % Na_2O. Copper in the form of copper (II) oxide (CuO) or copper (I) oxide (Cu_2O or $CuO_{0.5}$) has been substituted systematically in place of the Na_2O. Three starting compounds for the dopants were used to observe any differences arising due to the varying ratio of copper to oxygen content, or from differences in the copper oxidation states. Further studies were later conducted as it was necessary to confirm whether the initial copper valence states of

the starting compounds had any bearing on those existing within the glass once formed. The $CuO_{0.5}$ doped samples contain the same molar percentage of copper as the CuO doped samples only added in the form of Cu^{+} rather than Cu^{2+}. Consequently any differences between the results of these samples can be attributed to either the molar percentage of copper or the copper redox states. Two sets of powdered samples were available, chemically the same but one set manufactured a year prior to the second set. Experiments were initially completed on the first batch as they were newly manufactured and available from the start of this study, whereas both sets of samples were later explored. This not only allowed investigations to be performed regarding the stability of the glass structure over this time, but also allowed investigations into the robustness and reproducibility of the glass manufacturing technique. Towards the end of this study some samples in glass disc form, rather than powdered form, also became available.

6.2 Results and discussion

6.2.1 Antibacterial studies

The antibacterial properties of copper-doped phosphate based glasses have been demonstrated in previous studies by Mulligan et al. [1] whose results showed reductions in viable *Streptococcus sanguis* NCTC 10904 [1] biofilm activity after 24 hours growth on 5 % and 10 % copper-doped glass disc samples. Experiments were conducted on our copper-doped samples to check their antibacterial properties

by growing *Staphylococcus aureus* NCTC 6571 biofilm onto each of the 10 % copper-doped (CuO, Cu_2O and $CuO_{0.5}$) samples and comparing them to the growth on the control, base glass, using the method outlined by Valappil et al. [2]. However, in this case the antimicrobial effect was assessed only using confocal laser scanning microscopy (CLSM). CLSM is a widely used imaging technique especially in cell biology and employs a laser beam focussed onto a point on a fluorescent specimen. The fluorescence emission from the sample along with any reflected laser light, returns to the microscope which, by using an aperture to select only the fluorescent light from the focal point on the specimen, detects these photons using a photomultiplier tube [3]. The light signal is converted to an electrical one and computer processing software can be used to create a final image after the laser beam has been scanned across the area of interest resulting in high resolution imaging [3]. The glass disc samples with 48 hours of biofilm growth were covered in a viewing solution [2] which acts to stain the live and dead bacteria present so that they could be accounted for. These images could then be used to demonstrate the antibacterial effectiveness of the copper ions within the glass samples as shown in figure 6.1. The viable (green) and nonviable (red) bacteria were present on the glass disc surfaces after 48 hours of biofilm growth. Figure 6.1 (a) is the image taken of the biofilm growth on the base glass sample showing large regions dominated by live bacteria, whereas those for the other samples show far fewer regions of live bacteria and also show more clearly the presence of nonviable bacteria displaying evidence for the antimicrobial effects of the copper contained within the glass samples.

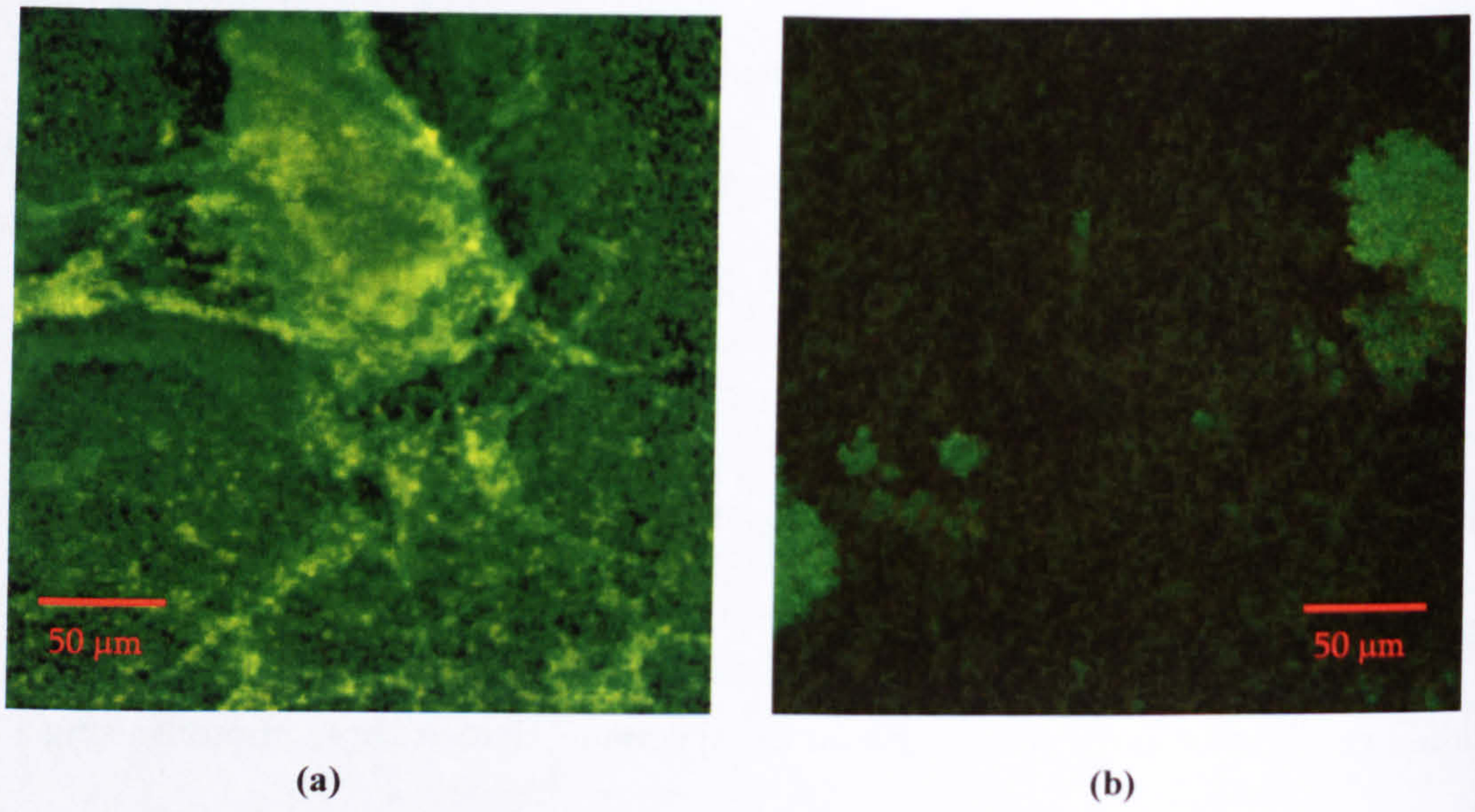

Figure 6.1: CLSM images by Valappil showing the live (green) and nonviable (red) bacteria from ***S. aureus*** biofilms after 48 hours of growth onto (a) the base glass and the 10 % doped (b) $CuO_{0.5}$, (c) CuO and (d) Cu_2O discs.

6.2.2 ^{31}P NMR experimentation

As only the earliest manufactured samples were available at the start of the investigation the ^{31}P NMR experiments were completed on these first, the spectra of which are shown in figures 6.2 to 6.4.

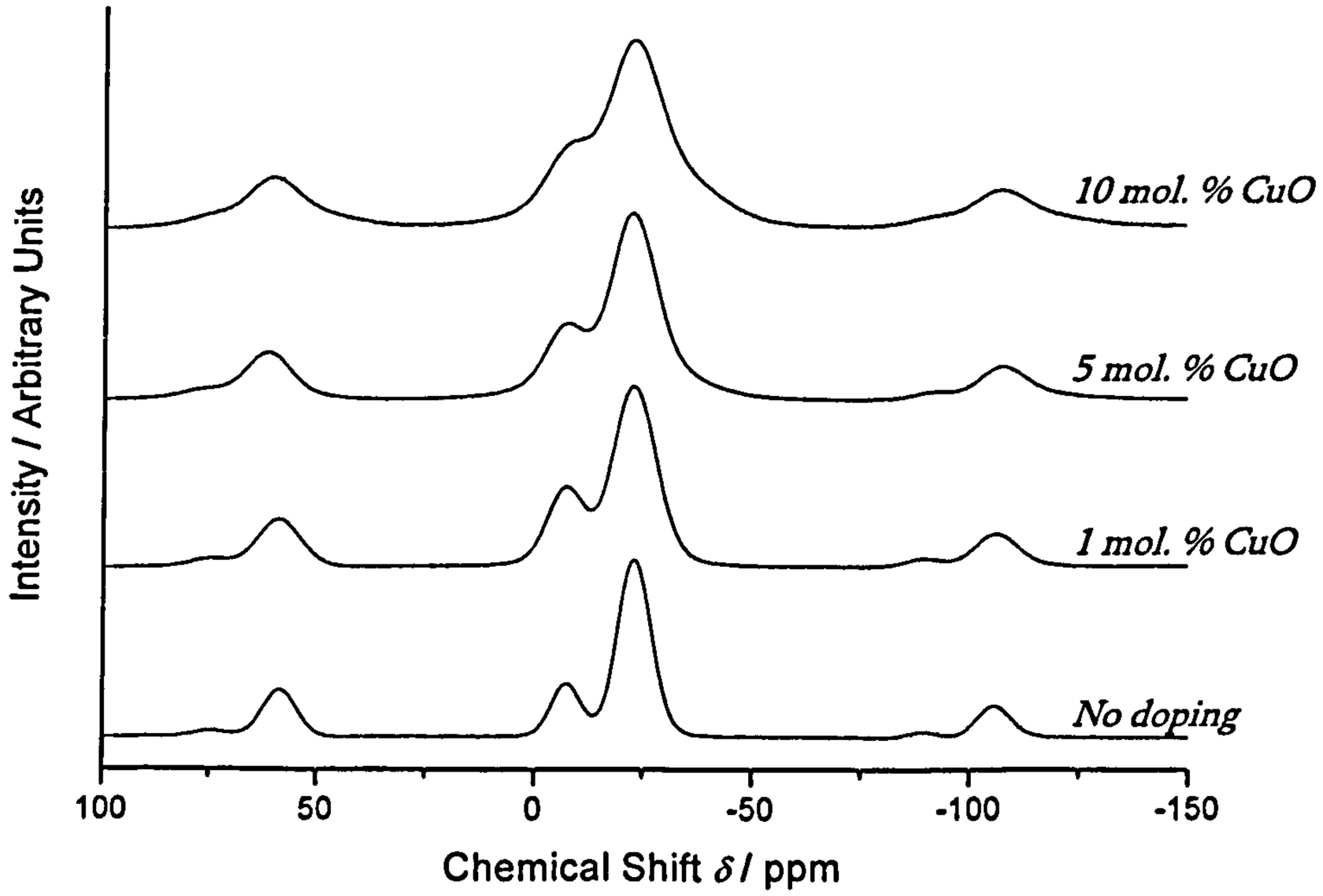

Figure 6.2: The ^{31}P MAS NMR spectra for the CuO doped glasses at a magnetic field of 8.45 T, spinning at ~12 kHz.

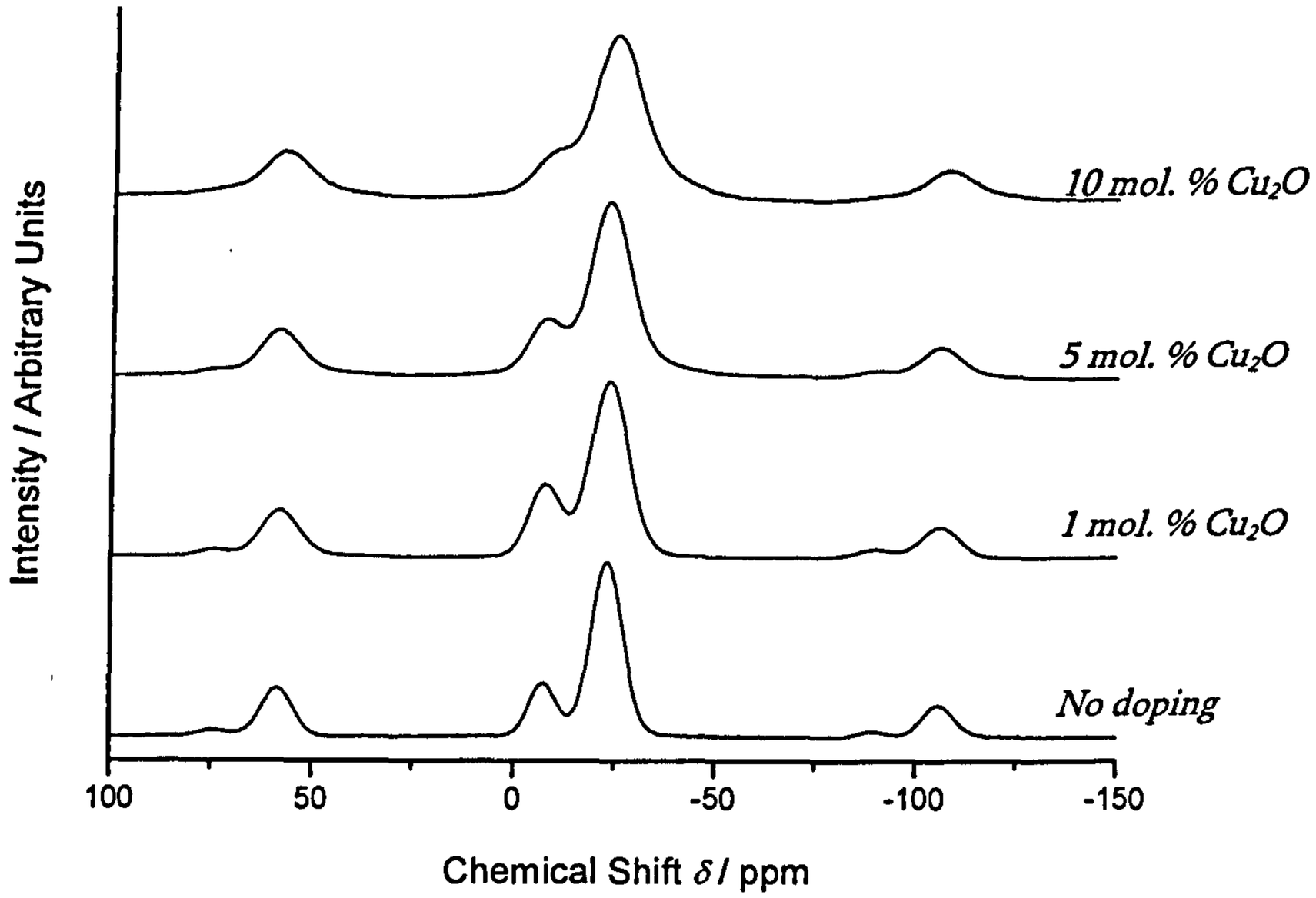

Figure 6.3: The ^{31}P MAS NMR spectra for the Cu_2O doped glasses at a magnetic field of 8.45 T, spinning at ~12 kHz.

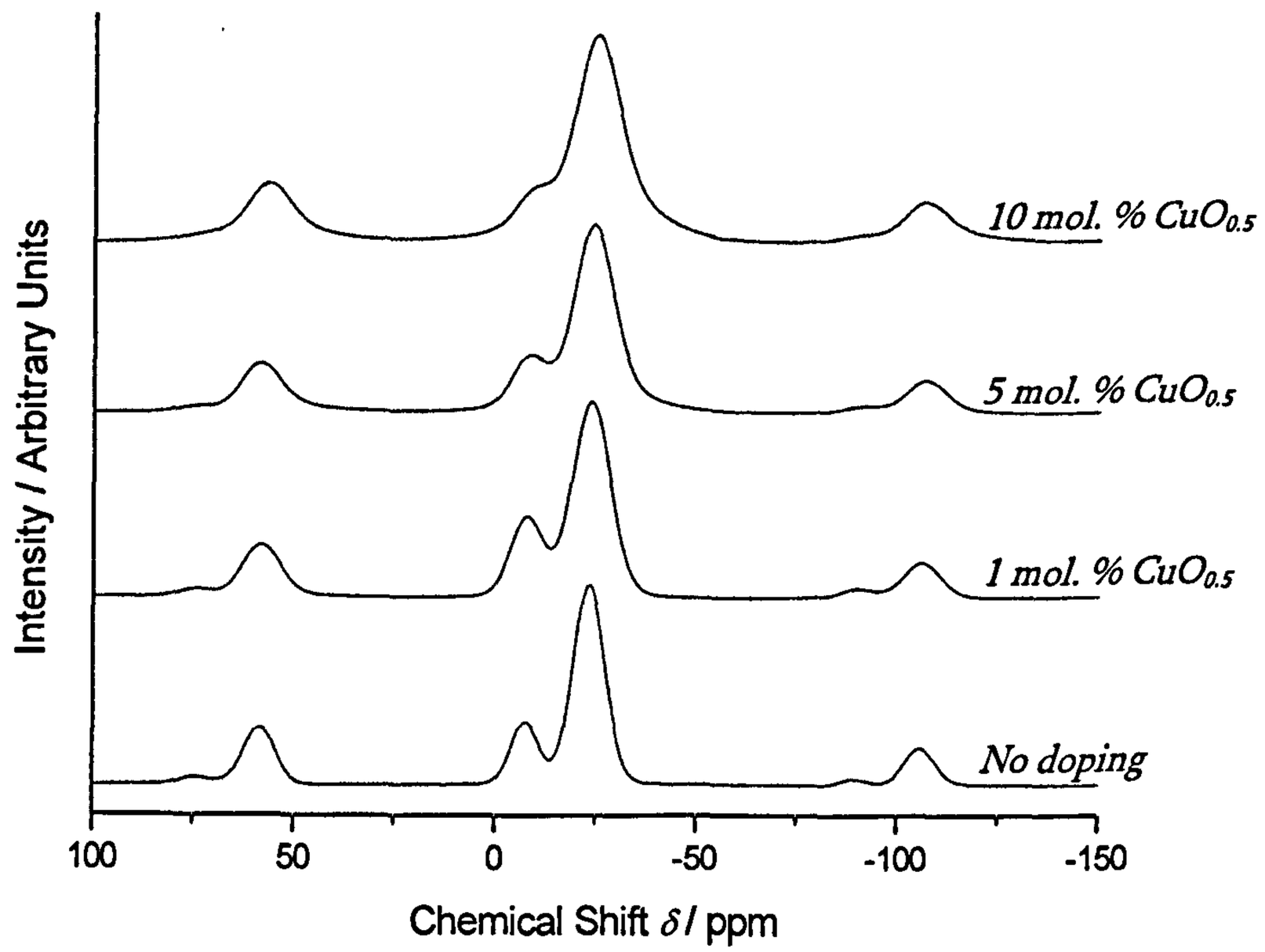

Figure 6.4: The ^{31}P MAS NMR spectra for the $CuO_{0.5}$ doped glasses at a magnetic field of 8.45 T, spinning at ~12 kHz.

Using the Brow model [4], these samples which are comprised of 45 % P_2O_5 and 55 % of mixed modifying oxide should give rise to a phosphate structure consisting of 22 % polyphosphate Q^1 phosphate tetrahedral units and 78 % of metaphosphate Q^2 units (see section 1.2). The NMR data from the base glass (table 6.1) clearly shows consistency with the theory as these predicted values were equivalent to those measured. This is reassuring as it shows that this ternary base glass containing two types of cation species, sodium (an alkali metal) and calcium (an alkaline earth metal), conforms exactly to the expectations of the model employed [4]. The NMR data from the copper-doped samples however, shows that as more copper is added to the system in place of sodium, the Q^n distributions begin to deviate from the expected model. At 1 % doping this deviation is minimal and the samples can still be considered to be governed by the Brow model [4]. However, as doping increases further, beyond 5 %, a significant change is detected via the appearance of unexpected Q^3 phosphate units. The NMR data collected for the CuO doped samples shows that as copper-doping increases, the relative percentage of Q^1 remains approximately constant whilst that of Q^2 decreases and the percentage of Q^3 increases, see figure 6.5. Thus it appears that some Q^2 units are changing to Q^3 units by the formation of more bridging oxygen atoms. For the Cu_2O and the $CuO_{0.5}$ doped samples, the relative percentages of both Q^1 and Q^2 units present within the samples drop with increasing doping concentration as the quantity of Q^3 units increases, although the drop in Q^1 is far more prominent (8 ± 1 % compared with 3 ± 1 % for the drop in Q^2 speciation), the data of which is given in table 6.1. It is

important to note that these results give only the relative integrated intensity for the various Q species present and a quantitative idea of the absolute changes occurring was investigated further in section 6.2.5.

Cu content / mol. %	*Peak 1 (Q^1)*			*Peak 2 (Q^2)*			*Peak 3 (Q^3)*		
	δ_{iso} / ppm ± 0.4 ppm	*Δ / ppm ± 0.7 ppm*	*I / % ± 1 %*	*δ_{iso} / ppm ± 0.4 ppm*	*Δ / ppm ± 0.7 ppm*	*I / % ± 1 %*	*δ_{iso} / ppm ± 0.4 ppm*	*Δ / ppm ± 0.7 ppm*	*I / % ± 1 %*
0 %	–6.5	8.0	22	–22.5	9.8	78			
1 % CuO	–6.1	10.1	23	–22.6	12.1	77			
5 % CuO	–6.6	12.1	23	–22.2	12.3	69	–34.8	12.8	8
10 % CuO	–7.3	13.9	22	–23.0	14.1	64	–38.0	14.6	14
1 % Cu_2O	–6.7	10.0	24	–22.5	10.8	76			
5 % Cu_2O	–6.7	10.9	18	–22.5	12.1	75	–35.9	14.3	7
10 % Cu_2O	–8.3	13.1	16	–23.9	13.3	73	–36.9	12.6	11
1 % $CuO_{0.5}$	–6.7	9.5	22	–22.6	11.2	78			
5 % $CuO_{0.5}$	–7.1	10.6	17	–22.8	11.8	77	–34.8	11.6	6
10 % $CuO_{0.5}$	–7.7	12.7	14	–23.5	13.3	75	–37.7	15.0	11

Table 6.1: The ^{31}P NMR data obtained for the copper-doped phosphate glass samples.

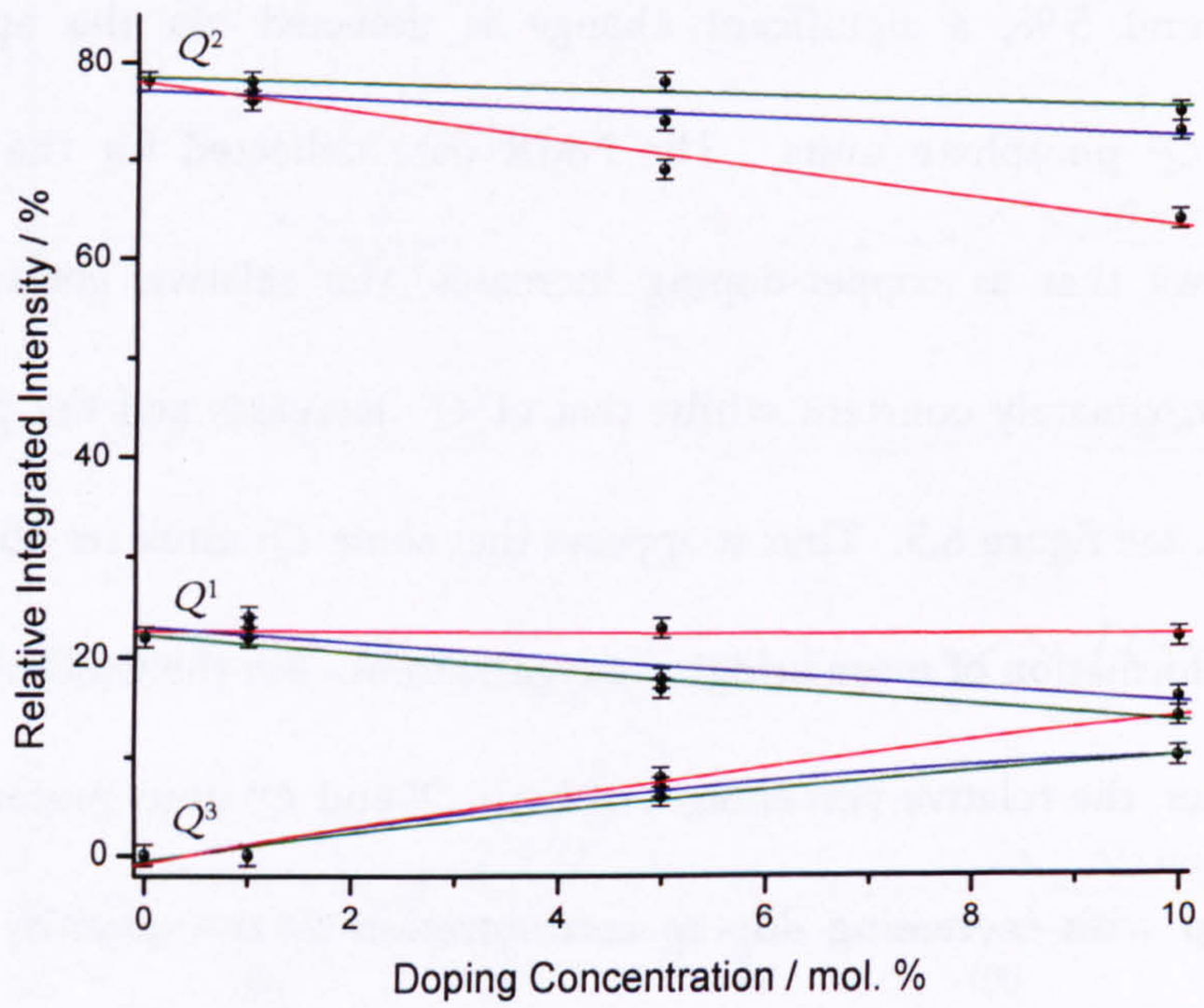

Figure 6.5: Change in Q^1, Q^2 and Q^3 speciation as copper-doping levels become more concentrated for the CuO doped samples (in red), the Cu_2O doped samples (blue), and the $CuO_{0.5}$ doped samples (shown in green). Note that the lines are merely guides to the eye.

The results from these samples imply that as the copper content in all of these samples increases beyond 5 %, more bridging oxygen atoms appear to form, hence changing the observed phosphate network coordination. This was somewhat unexpected as the conventional wisdom suggests that the initial introduction of the modifying cations into the system at a concentration of 55 % should produce depolymerisation of the phosphate network resulting in the breaking of bridging oxygen atoms between the various phosphate units producing the Q^1 and Q^2 observed for the base glass. The substitution of one type of cation for another (in this case copper in place of sodium) should theoretically produce no additional changes in the phosphate network connectivity so long as two Na^+ ions are replaced by either one Cu^{2+} or two Cu^+ ions. This therefore emphasises the importance of accurately determining the copper valences, which at this time had not yet been investigated, but is clearly a major influence on our expectations of the network. Nevertheless, if accurately governed by the Brow model [4] none of the copper-doped samples studied should have produced any Q^3 phosphate units at all as there is not enough phosphorus present within the samples. Despite this, up to 14 % of Q^3 units were measured while the Q^1 level was observed to drop to as low as 14 % (in the case of the 10 % Cu_2O doped sample) and Q^2 dropped to 64 % (for the 10 % CuO doped glass) as shown in table 6.1 and figures 6.2 to 6.5. An example of a fitted spectrum is also given in figure 6.6. This is an interesting result showing that the type of modifying cation incorporated can significantly change the phosphate speciation and in the case of copper, no longer appears to follow the Brow model [4].

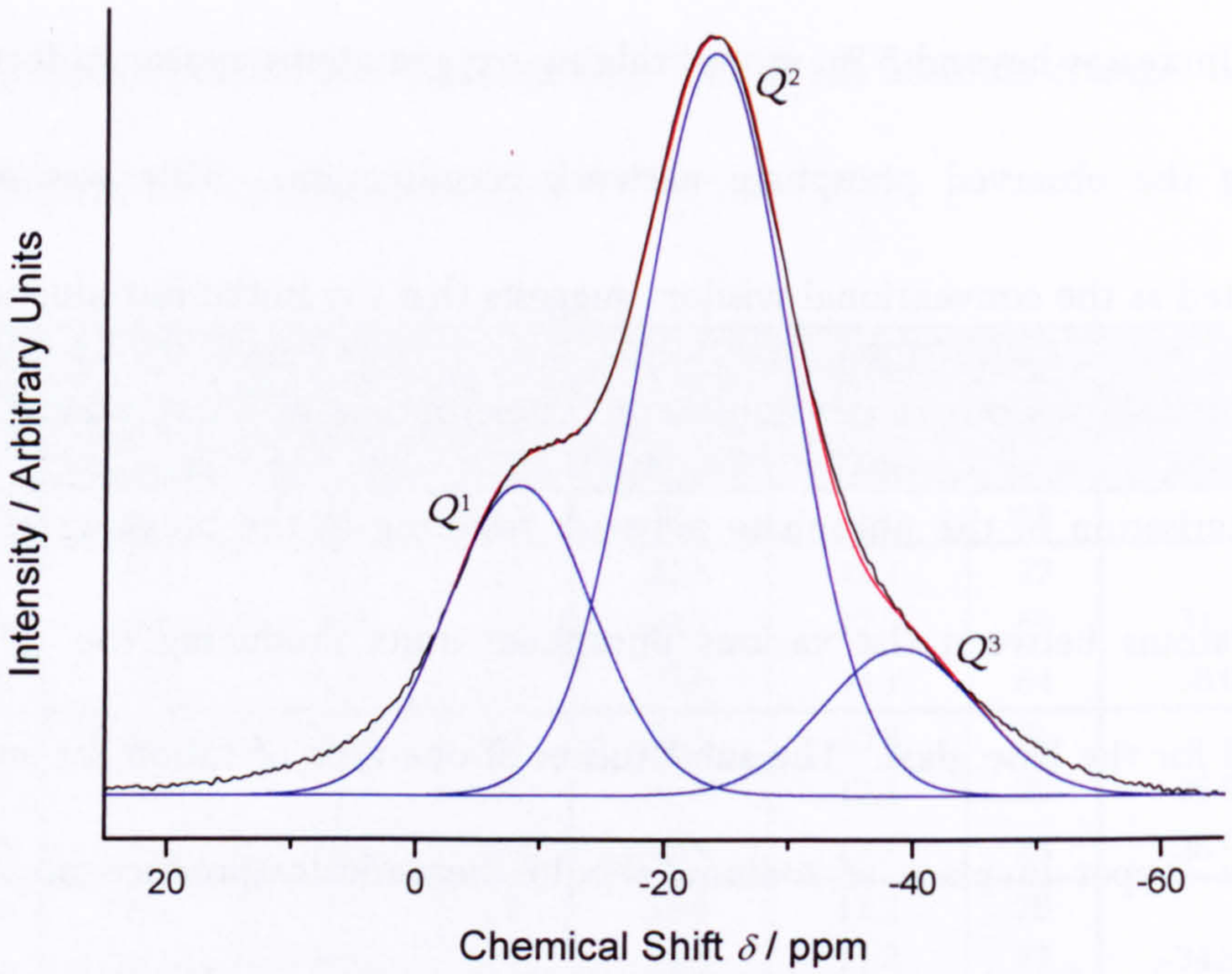

Figure 6.6: An example of the data fit for the 10 mol. % CuO doped sample, showing the Q^n species present. The blue lines show the peaks fitted, the black line is the original spectrum and the red line shows the overall summed fit.

Before these deviations from the suggested model could be confirmed for certain, it was first important to check that the sample compositions are the same as those used in the model calculations which were taken from the initial composition predicted from the powdered oxide starting components. The chemical analysis results are described in the following section (6.2.3) and these confirmed the values used in the model. Not only is the predicted phosphate coordination not what is observed, but the occurrence of three types of phosphate species simultaneously within the samples is highly suggestive of a deviation from the model used. This indicates that the differences arising in the phosphate networks as copper replaces the sodium must arise from disparities between the properties of sodium and copper ions.

Different influences of these two cation species upon the phosphate environment are expected to arise due to their different charge (depending upon the copper oxidation state since it is a transition metal element), ionic size and other properties that determine their most energetically favourable coordinations within the glass such as their electronic configurations. Brow [4] suggests that sodium ions charge balance the non-bridging oxygen atoms of the phosphate tetrahedra producing ionic cross-links. The copper ions were expected to be incorporated in a similar way and as such it is important to discover the redox states of the copper ions as the effects of Cu^{+} or Cu^{2+} replacing the Na^{+} ions may be different. The different forms of copper-doping mean that when CuO is introduced into the samples in place of Na_2O, two sodium ions are replaced by only one copper ion. If the copper remains as Cu^{2+} within the glass then this replacement should have no effect upon the Q^n species arising (see section 1.2). However, the Cu_2O doping provides a direct one-to-one substitution of sodium to copper, whereas both the CuO and the $CuO_{0.5}$ doped samples replace only half the number of modifying cations. Before we can comment on the potential effects of these substitutions, the copper oxidation state must first be identified and this was later investigated in detail (section 6.2.6).

Other potential explanations for the unexpected ^{31}P NMR results for the copper-doped samples that must be further investigated in this study include the possibility of copper phase separation, leaving a different percentage of modifying oxide remaining within the glass, the effect of any paramagnetic copper that may be

present within the samples, as well as the different effects of the two possible copper valence states, and finally the possibility of copper ions behaving as network formers as a recent study has described the possibility of this phenomenon [5].

6.2.3 Imaging and chemical analysis

As the Brow model [4] was used to estimate the expected phosphate tetrahedral connectivities in the samples calculated based upon the starting compositions which may not necessarily be the same for the final glass, scanning electron microscopy equipped with energy dispersive X-ray analysis (SEM-EDX) was used to chemically analyse the samples and also to provide an indication of the samples' chemical homogeneity.

The SEM-EDX experiments were performed at variable pressures (15 and 30 Pa) on three separate regions of each sample to obtain an average elemental composition for each. The errors involved in the experimental technique were estimated from the sampling of various regions in each sample and by repeating the fitting of the background subtraction. It should be noted that the dominant contribution to the errors arises from the poor estimation of oxygen levels in the sample since the X-rays produced from these are low in energy and often absorbed by the detector windows, see section 4.6. The ZAF correction of the EDAX system discussed in section 4.6.1, relies upon the oxygen content in its calculations and uncertainties in

the oxygen level estimation can therefore lead to errors in the quantification of other elements.

The measurements were performed on all of the copper-doped samples including those that were manufactured a year earlier and a few additional samples that had been remade again to check for consistency in the sample preparation technique. The target and achieved compositions are given in tables 6.2 to 6.4 and show that within the estimated uncertainty the achieved compositions are very close to those desired implying that the predictions made using the Brow model are reliable. No changes in sample composition with time could be determined and the glass formation technique appears consistent. Trace elements of silicon, magnesium and sometimes aluminium stated in the results tables 6.2 to 6.4 were also found, but at such small concentrations these have very little impact on the other experiments performed and have most likely been incorporated during the glass formation process where silica crucibles and other apparatus were employed. An example of a spectrum collected is shown in figure 6.7. Experiments were also performed on a selection of glass disc samples when they later became available. These were mechanically ground and polished to provide a flat surface for experimental exposure to show any discrepancies that may have arisen in the powdered sample analysis due to topographical variations, however, none were found. Overall these results show that the reproducibility of the glass manufacturing process is good and

that the glass constituents can be estimated to be consistently within 3 % of the target compositions.

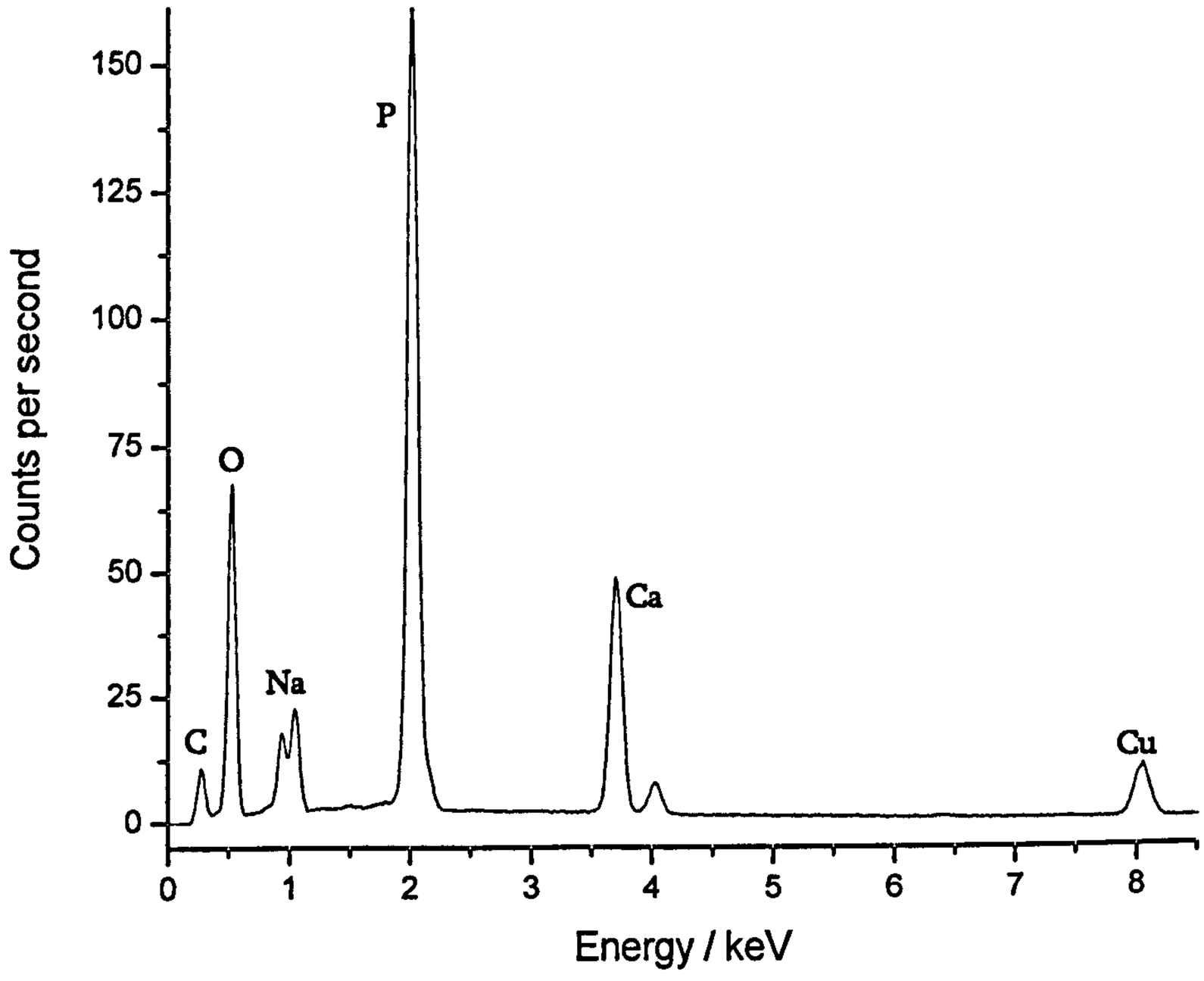

Figure 6.7: The SEM-EDX spectrum showing the energy of the detected X-rays versus number of counts for the most recently manufactured Cu_2O 10 % doped sample.

	Elemental composition / at. %					
	P **± 2**	***O*** **± 2**	***Ca*** **± 1**	***Na*** **± 0.5**	***Cu***	***Trace elements*** **± 0.05**
Base target composition	**20**	**62**	**7**	**11.1**	**0**	
Experimental (old sample)	20	60	6	12.5	0	Si = 0.12, Mg = 0.12
CuO 1 % target composition	**20**	**62**	**7**	**10.7**	**0.22**	
Experimental (old sample)	20	61	6	12.5	0.36 ± 0.05	Si = 0.11, Mg = 0.16
Experimental (new sample)	22	59	7	11.5	0.32 ± 0.05	Si = 0.13
Experimental (new sample in disc form)	23	57	7	12.8	0.24 ± 0.05	Si = 0.11, Mg = 0.1, Al = 0.1
CuO 5 % target composition	**20**	**63**	**7**	**9.0**	**1.1**	
Experimental (old sample)	22	60	6	10.5	1.8 ± 0.1	Si = 0.19, Mg = 0.12, Al = 0.12
Experimental (new sample)	23	57	8	9.2	1.7 ± 0.5	Si = 0.20, Mg = 0.1
CuO 10 % target composition	**20**	**64**	**7**	**6.8**	**2.3**	
Experimental (old sample)	21	60	6	8.0	3.6 ± 0.5	Si = 0.26, Mg = 0.14, Al = 0.11
Experimental (new sample)	21	62	6	8.2	2.1 ± 0.5	Si = 0.14, Mg = 0.12

Table 6.2: The EDX elemental analysis results for the CuO doped samples compared to the desired compositions, where other trace elements detected including nickel, were in total < 3 % of the overall signal and therefore regarded as negligible.

	Elemental composition / at. %					
	P **± 2**	***O*** **± 2**	***Ca*** **± 1**	***Na*** **± 0.5**	***Cu***	***Trace elements*** **± 0.05**
Cu_2O 1 % target composition	**20**	**62**	**7**	**10.7**	**0.44**	
Experimental (old sample)	22	58	7	11.3	0.31 ± 0.05	Si = 0.13, Mg = 0.14
Experimental (new sample)	22	58	7	11.7	0.43 ± 0.05	Si = 0.14, Mg = 0.10
Cu_2O 5 % target composition	**20**	**62**	**7**	**8.9**	**2.2**	
Experimental (old samples)	21	60	7	10.2	1.1 ± 0.1	Si = 0.14, Al = 0.10
Experimental (new sample)	21	60	6	10.5	1.9 ± 0.5	Si = 0.15, Al = 0.1
Cu_2O 10 % target composition	**20**	**62**	**7**	**6.7**	**4.4**	
Experimental (old sample)	22	61	7	8.2	2.11	Si = 0.13, Mg = 0.10
Experimental (new sample)	21	61	6	8.2	3.0 ± 0.5	Si = 0.16, Mg = 0.12, Al = 0.1
Experimental (new sample in disc form)	21	59	6	8.0	4.5 ± 0.5	Si = 0.16, Mg = 0.13, Al = 0.1

Table 6.3: The EDX elemental analysis results for the Cu_2O doped samples compared to the desired compositions, where other trace elements detected including nickel, were in total < 3 % of the overall signal and therefore regarded as negligible.

	Elemental composition / at. %					
	P **± 2**	***O*** **± 2**	***Ca*** **± 1**	***Na*** **± 0.5**	***Cu***	***Trace elements*** **± 0.05**
$CuO_{0.5}$ 1 % target composition	**20**	**62**	**7**	**10.9**	**0.22**	
Experimental (old sample)	21	59	6	12.5	0.24 ± 0.05	Si = 0.13, Mg = 0.14
Experimental (new sample)	23	58	7	11.9	0.28 ± 0.05	Si = 0.11
$CuO_{0.5}$ 5 % target composition	**20**	**62**	**7**	**10.1**	**1.1**	
Experimental (old sample)	23	58	7	10.1	1.2 ± 0.1	Si = 0.18, Al = 0.16
Experimental (old remade sample)	23	58	8	9.5	1.3 ± 0.1	Si = 0.14, Mg = 0.10
Experimental (new sample)	22	59	7	10.2	1.1 ± 0.1	Si = 0.13
$CuO_{0.5}$ 10 % target composition	**20**	**62**	**7**	**9.0**	**2.3**	
Experimental (old sample)	21	62	6	8.6	1.6 ± 0.1	Si = 0.15, Mg = 0.14
Experimental (old remade sample)	23	60	7	7.5	2.3 ± 0.5	Si = 0.13
Experimental (new sample)	22	61	7	7.9	2.1 ± 0.5	Si = 0.15, Al = 0.21

Table 6.4: The EDX elemental analysis results for the $CuO_{0.5}$ doped samples compared to the desired compositions, where other trace elements detected including nickel, were in total < 3 % of the overall signal and therefore regarded as negligible.

After confirming the sample constituents, it was thought that rather than the copper ions having significantly different effects on the phosphate network than the sodium ions, another possible explanation for the Q speciation observations could be that the atoms in the glass were perhaps not mixing homogeneously and that copper phase separation was occurring, especially as the samples appeared rather inhomogeneous in colour (see figures 6.8 and 6.9). Despite the elemental analysis from the EDX results suggesting that the samples were homogeneous, the EDX technique can sometimes not be accurate enough to detect small variations in heterogeneity.

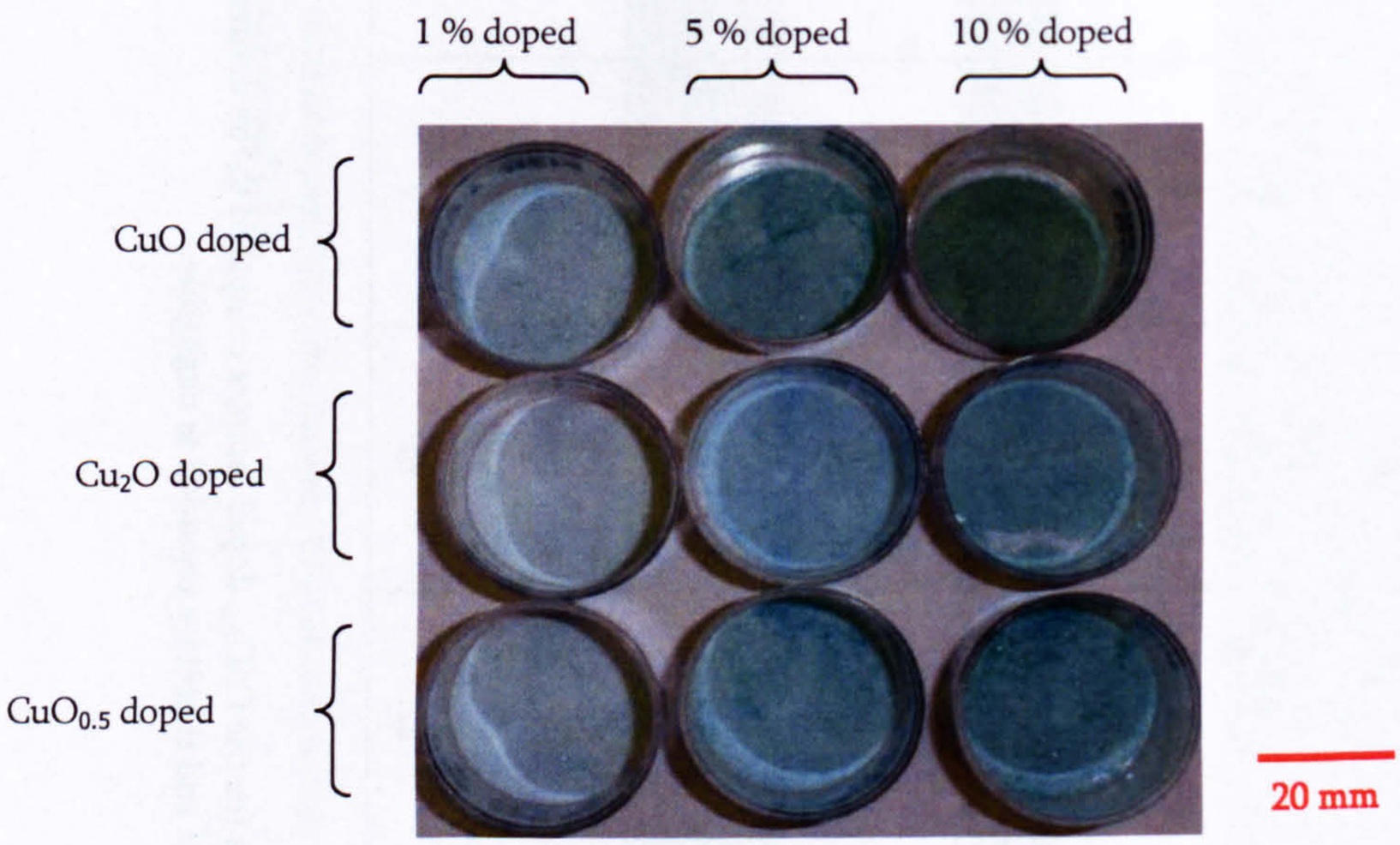

Figure 6.8: Photograph of the powdered copper phosphate glass samples.

If the copper has crystallised out of the network then the remainder of the glass would consist of a smaller percentage of modifying oxide therefore increasing the connectivity between the phosphate tetrahedra. However, an X-ray diffraction experiment performed on the CuO 10 % doped sample using a Bruker AXS D5005

X-ray diffractometer suggested that the sample was entirely amorphous with no crystalline phase observable.

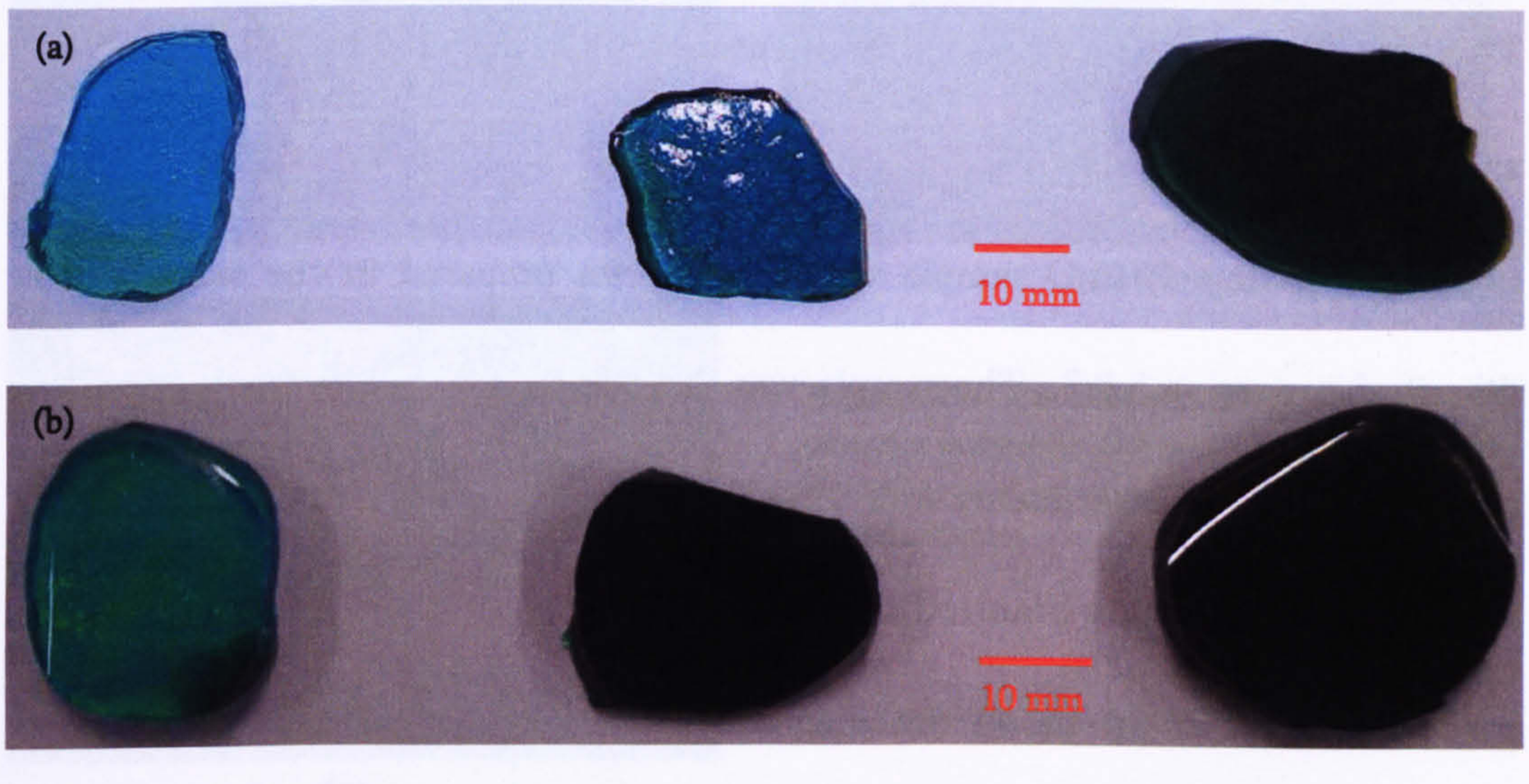

Figure 6.9: Photographs of the glass discs for the (a) CuO doped, (b) Cu_2O doped and (c) $CuO_{0.5}$ doped samples, with doping increasing from 1, 5 to 10 % from left to right.

Figure 6.10 shows the SEM images of some of the sample regions that were chemically analysed. When analysing different areas of each specimen, the samples looked as thought they were homogeneous and the images displayed no evidence for any nanoparticle clustering of copper resulting from phase separation. However the ability of the SEM to view nanoparticles is not as good as TEM, the details of which have been explained in section 5.2.3. The unscattered electrons detected give an

indication of mass-thickness contrast while the elastically scattered electrons can give rise to Bragg diffraction patterns if the sample has any crystalline order [6]. This latter method was therefore implemented using a JEOL 2000fx TEM system and applying a 200 kV electron beam to observe the presence of any crystalline ordering in the 10 % doped Cu_2O sample which had been prepared in the same way as described in section 5.2.3. The sample was then deposited on a carbon film with a gold grid ready for experimentation. However, no evidence of phase separation was found. As the detection limit to this technique allows the observation of crystalline particle clusters down to ~5 nm diameters (consistent with silver nanoparticle observations by Baia et al. [7]), this suggests that if nanoclusters really are forming in these samples then they must be smaller than this. Very small clusters ≤ 5nm may be highly problematic to detect as at this scale copper clusters would not necessarily consist of metallic copper (Cu^0) observable using optical spectroscopy and if the copper clustering was occurring without undergoing crystallisation, possible due to its amorphous glass interface surroundings, then detecting the clusters using TEM and XRD would also be unsuccessful. TEM-EDX was also used to confirm the composition of this sample and was entirely consistent with expectations, again giving rise to a composition within 3 % of the target quantities.

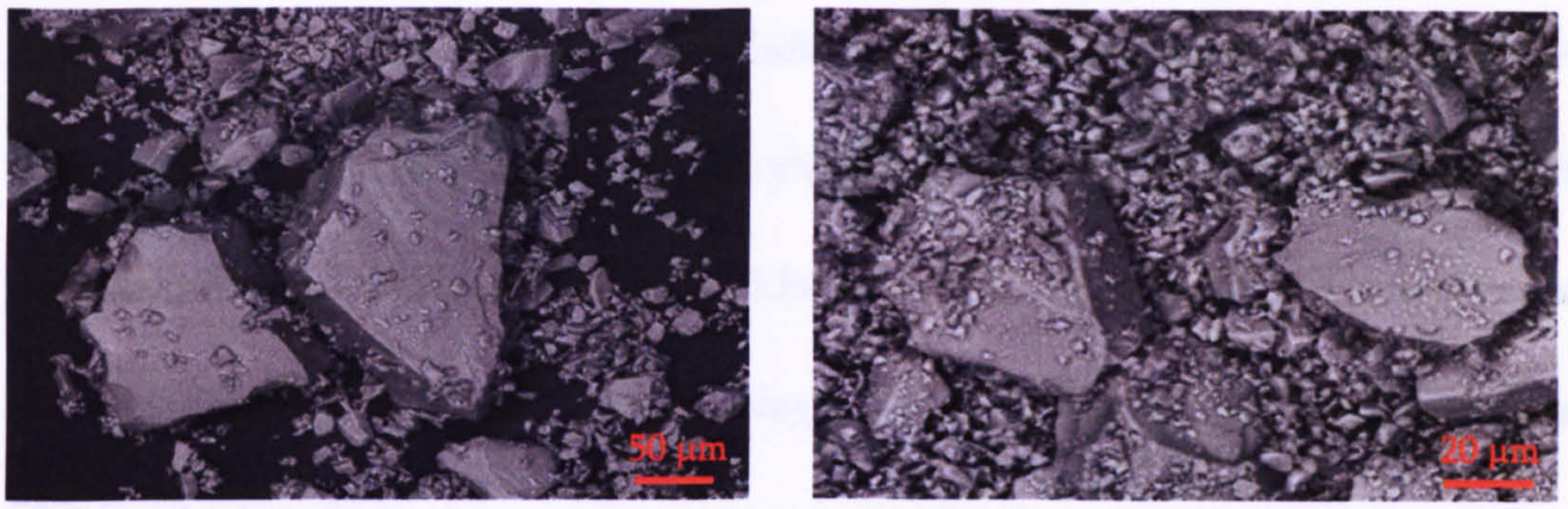

(a) (b)

(c)

Figure 6.10: The SEM secondary electron detector images for the (a) 1 % $CuO_{0.5}$, (b) 5 % $CuO_{0.5}$ and (c) year older 10 % $CuO_{0.5}$ doped samples.

6.2.4 Copper oxidation state investigations

Once the sample constituents had been confirmed as correct this meant that the unexpected Q^n distributions observed needed further investigation. A possibility was that the peak observed in the NMR spectra that had been assigned as Q^3, may not actually be from Q^3 but may be a Q^2 peak that had undergone a paramagnetic shift from interactions with copper. This would occur because any paramagnetic fields can interact with the applied magnetic fields, changing the effective magnetic field at the nuclei of interest. This would be true only if the copper was in the Cu^{2+} redox state which is paramagnetic and the copper in the samples may occur in both common oxidation states, Cu^{+} and Cu^{2+}. The blue-green appearance of the samples clearly shown in figures 6.8 and 6.9 suggests that there are some Cu^{2+} ions present in

the samples as this is a well known characteristic of Cu^{2+}. The presence of Cu^{2+} ions within the sample was confirmed by room temperature spectrophotometry experiments in the ultraviolet (UV) to visible region (300 to 1100 nm) as described in section 5.2.3, pages 134 to 135. This gave rise to the optical absorption spectra shown in figure 6.11.

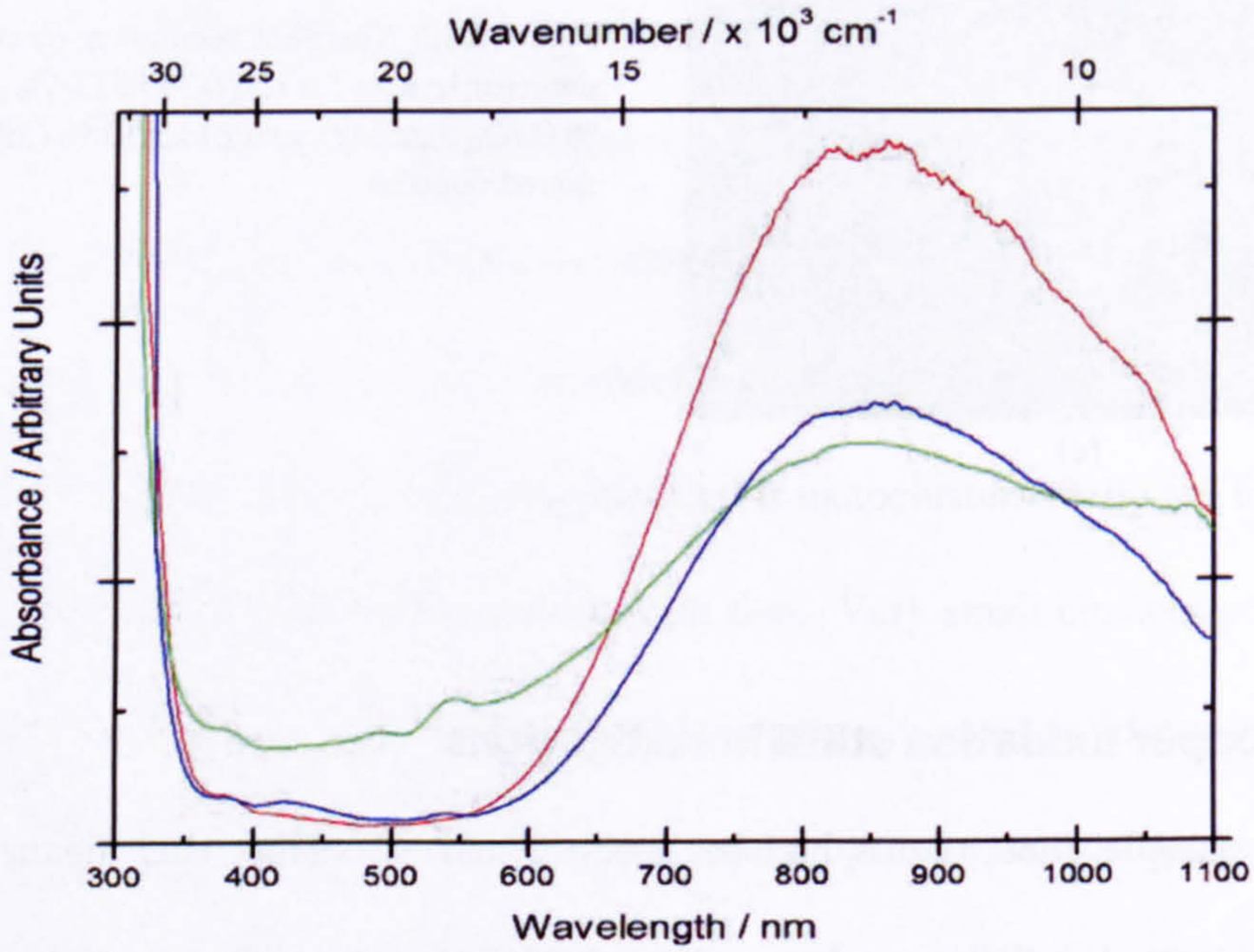

Figure 6.11: The UV-visible spectrophotometry absorption spectra for the CuO 1 % (green), Cu_2O 1 % (red) and $CuO_{0.5}$ 1 % (blue) glass disc samples.

This figure shows the absorption occurring as a function of wavelength (or wavenumber) for each of the 1 % copper-doped polished glass disc samples, each approximately 2 mm thick, where the spectra have been normalised by thickness. Due to the highly absorbing nature of the glasses (characteristic of Cu^{2+} doping) these experiments could not be successfully performed on samples of higher doping levels. The spectra in figure 6.11 show a strong absorption band at ~850 nm

(11000 cm^{-1}) which is characteristic of that arising from distorted octahedral Cu^{2+} incorporation into phosphate based glasses [8 & 9], therefore confirming the presence of Cu^{2+} ions in the glass even at low doping concentrations. The absorption band edge in the UV region arising as the wavelength drops to 300 nm is indicative of Cu^{+} which is known to create an absorption band in phosphate glasses peaking between 240 and 250 nm [9-11] thereby suggesting a mixed valence state within these samples.

It should also be noted here that this spectrophotometry experiment showed no evidence for any colloidal copper metal (Cu^{0}) particles which would have resulted in an absorption peak in the region of ~550 to 600 nm [12-14]. This rules out any copper phase separation that may result in the formation of metallic copper nanoclusters or colloidal aggregates, although this phase separation may not occur until greater levels of copper are added to the system as the ^{31}P NMR did not show any discrepancies in results until a doping level of 5 % was reached.

The confirmation of Cu^{2+} ions within the samples is important as it is the paramagnetic property of these Cu^{2+} ions that could cause a shift in the spectral lines observed implying that the peak at approximately –36 ppm, may in fact be a paramagnetically shifted Q^2 peak. To test this theory a ^{31}P NMR experiment was performed at two temperatures as the paramagnetic susceptibility, χ, is governed by Curie's law, $\chi = C/T$, as described in section 4.3.1, where C is the Curie constant

and T is the temperature. As the paramagnetic effect is therefore inversely proportional to temperature [15] it should be possible to observe a temperature dependent shift in the spectral lines due to these effects.

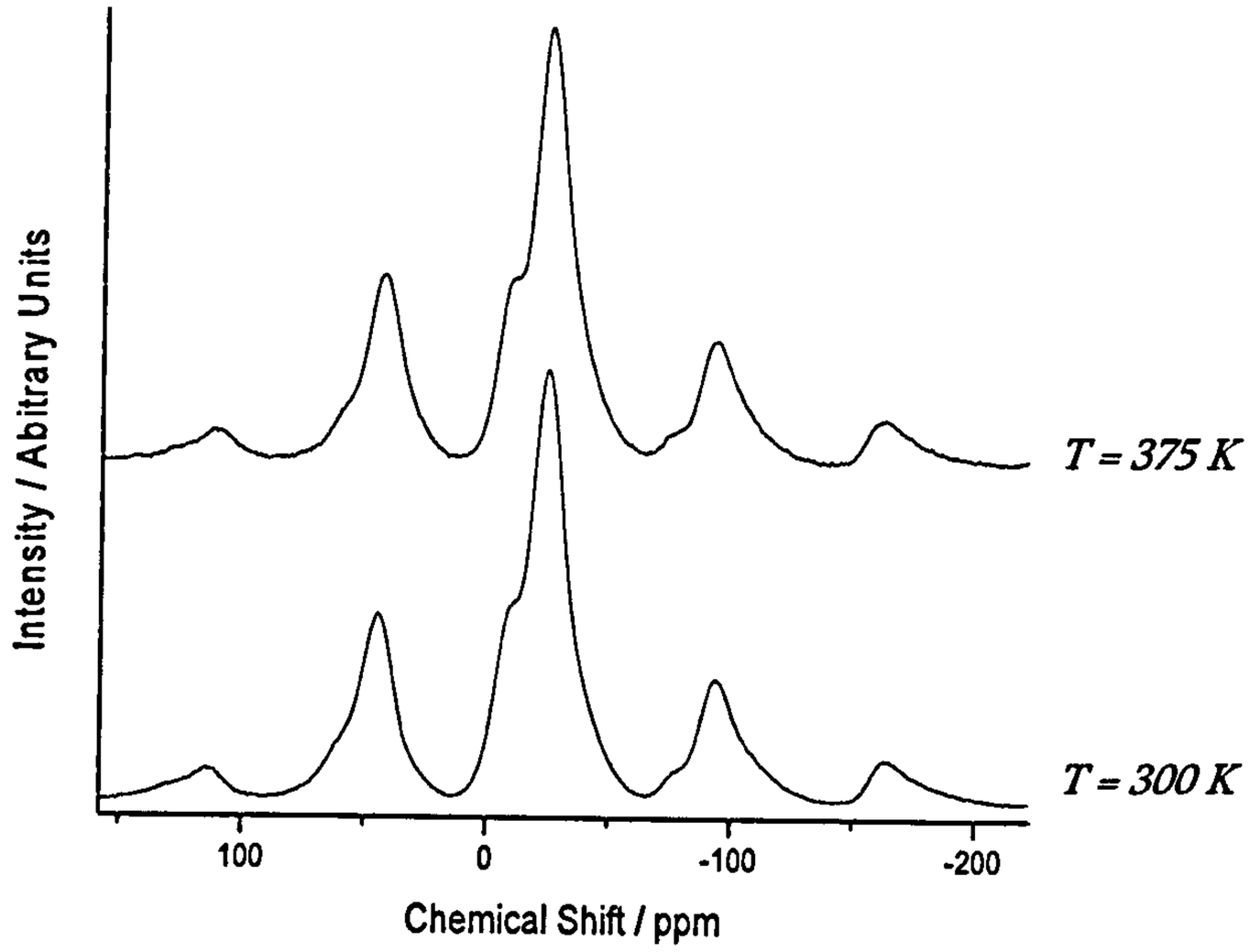

Figure 6.12: A comparison of the ^{31}P NMR spectra for the 10 mol. % CuO doped sample at two different temperatures using a magnetic field of 8.45 T, spinning at ~10 kHz.

The high temperature experiment[i] shown in figure 6.12, was performed in order to observe a peak shift due to the paramagnetic effect with the intention of observing the extent of the shift and extrapolating to infinite T to deduce the peak position without any paramagnetic influences. However, when the experiment was run at 300 and 375 K[ii] no shift in any of the peaks present was observed suggesting that any paramagnetic Cu^{2+} ions incorporated into the network are either too few to have a

[i] The high temperature experiments could only be performed at a maximum spinning frequency of 10 kHz, hence the difference between the high temperature spectra and those in figures 6.3 to 6.6.
[ii] This was the highest temperature achievable using the equipment available although it would be preferable to experiment at higher temperatures.

visible effect on the NMR spectra, are coordinated in such a way that they do not affect the ^{31}P NMR signal from the phosphate tetrahedra or that the phosphate tetrahedra they do effect, they do to such an extent that they diminish the signal entirely. In order to have no affect upon the ^{31}P NMR signal this would imply that if there were any Cu^{2+} ions present, they are not likely to be network forming and covalently bonding as part of the tetrahedra. Instead they may be sitting in sites within the sample, where they do not have a distinct chemical effect on the surrounding phosphate glass network, such as the ionically charge balancing sites similar to those occupied by the sodium, as predicted, thus producing no paramagnetic chemical shift.

The presence of paramagnetic ions such as Cu^{2+} in abundances of greater than a few tenths of a molar percent can broaden NMR spectra significantly [16], possibly to the extent that the signal arising from the phosphorus tetrahedra affected by any Cu^{2+} ions would no longer be observable in the NMR spectrum. If the Cu^{2+} ions do diminish the NMR signal completely for the phosphate tetrahedra associated with the paramagnetic ions, then what the NMR technique actually observes is only the signal from those unaffected phosphate tetrahedra. These unaffected tetrahedra may not be a true representation of all of the phosphate tetrahedra if Cu^{2+} ions have a preferential coordination or site occupancy within the glass and could offer an explanation for the resulting unexpected Q speciation. In fact it would be expected that any loss of ^{31}P NMR signal through paramagnetic affects would more strongly

affect the sites with lower connectivity as these phosphate tetrahedra have more non-bridging oxygen atoms to be charge balanced by the copper ions. This could lead to a greater relative percentage of Q^3 being observed as these phosphate sites could be the least affected by the Cu^{2+} ions.

6.2.5 Quantitative ^{31}P NMR

The NMR experiments were repeated on the original samples (now a year older) as well as the second batch of more recently manufactured samples containing the same amount of copper-doping. These experiments were conducted using a Varian Infinity-Plus 300 MHz spectrometer equipped with the 7.1 T superconducting magnet outlined in section 3.2 and the spectra were fitted using DMFit, see section 3.7. The samples were each weighed before experimentation in order to give quantitative information about the overall NMR signal intensities as a function of copper-doping.

Cu content / mol. %	Peak 1 (Q^1)			Peak 2 (Q^2)			Peak 3 (Q^3)		
	δ_{iso} / ppm ± 0.4 ppm	Δ / ppm ± 0.7 ppm	I / % ± 1 %	δ_{iso} / ppm ± 0.4 ppm	Δ / ppm ± 0.7 ppm	I / % ± 1 %	δ_{iso} / ppm ± 0.4 ppm	Δ / ppm ± 0.7 ppm	I / % ± 1 %
0 %	–6.2	8.2	25	–22.1	9.9	75			
1 % CuO	–6.4	9.9	24	–22.3	10.9	73	–33.9	8.7	3
5 % CuO	–7.0	12.6	23	–22.7	12.4	66	–34.9	12.3	11
10 % CuO	–6.7	12.8	15	–23.7	16.2	67	–40.8	17.0	18
1 % Cu_2O	–6.3	8.9	23	–22.3	10.6	75	–34.4	8.8	2
5 % Cu_2O	–7.0	11.2	20	–22.9	12.3	73	–36.4	13.5	7
10 % Cu_2O	–7.9	12.1	14	–23.9	13.8	72	–38.5	13.9	14
1 % $CuO_{0.5}$	–6.3	8.8	22	–22.1	10.8	77	–35.0	9	2
5 % $CuO_{0.5}$	–7.3	11.8	19	–22.4	11.5	68	–34.1	13.3	13
5 % $CuO_{0.5}$ (Remade)	–7.2	11.6	19	–23.0	11.8	73	–34.5	13.3	8
10 % $CuO_{0.5}$	–7.8	12.3	13	–23.9	13.4	73	–38.9	15.1	14
10 % $CuO_{0.5}$ (Remade)	–8.1	11.5	13	–24.1	13.5	74	–38.9	13.5	13

Table 6.5: ^{31}P NMR data from the original copper phosphate glass samples rerun using the Varian Infinity-Plus 300 MHz spectrometer equipped with a 7.1 T superconducting magnet.

Cu content / mol. %	Peak 1 (Q^1)			Peak 2 (Q^2)			Peak 3 (Q^3)		
	δ_{iso} / ppm ± 0.4 ppm	Δ / ppm ± 0.7 ppm	I / % ± 1 %	δ_{iso} / ppm ± 0.4 ppm	Δ / ppm ± 0.7 ppm	I / % ± 1 %	δ_{iso} / ppm ± 0.4 ppm	Δ / ppm ± 0.7 ppm	I / % ± 1 %
1 % CuO	–6.3	9.1	22	–22.3	10.5	76	–32.6	8.3	2
5 % CuO	–7.0	11.6	19	–22.8	12.1	73	–34.8	12.3	8
10 % CuO	–7.6	11.3	13	–24.0	14.1	74	–38.7	13.8	13
1 % Cu_2O	–6.3	9.7	25	–22.2	11.2	75			
5 % Cu_2O	–7.2	11.2	20	–22.9	12.2	75	–35.7	9.6	5
10 % Cu_2O	–7.6	10.8	15	–23.7	15.5	72	–38.7	11.8	13
1 % $CuO_{0.5}$	–6.2	8.9	25	–22.1	10.6	75			
5 % $CuO_{0.5}$	–7.0	11.4	20	–22.8	12.0	73	–34.7	11.7	7
10 % $CuO_{0.5}$	–7.8	12.0	13	–24.0	13.6	74	–38.6	14.8	13

Table 6.6: ^{31}P NMR data from the more recently manufactured copper phosphate glass samples using the Varian Infinity-Plus 300 MHz spectrometer equipped with a 7.1 T superconducting magnet.

The fit parameters from these experiments have been outlined in tables 6.5 and 6.6 above and show good consistency with the original samples run on the 360 MHz (8.45 T) spectrometer (section 6.2.2) as they show the same general trends with doping and fit parameters within ± 4 % of the original values. As such the spectra

have not been displayed again. Since the masses of the samples were also measured, this allowed us to plot the normalised signal intensity against doping (figure 6.13), whilst also observing any changes in the relative sideband intensity and FWHM values for the ^{31}P NMR peaks arising. Figure 6.13 shows that the normalised signal clearly reduces with increasing copper-doping. This signal reduction is more prominent for the Cu_2O doped samples providing strong evidence supporting the theory that the incorporation of paramagnetic copper (II) ions within the sample is responsible for the loss of signal generated from a significant number phosphate tetrahedra. The reduction in signal observed indicates that the Q speciation percentages obtained from ^{31}P NMR can no longer be used to give an absolute indication of the phosphate coordination within the glass network of the entire sample as the signal observed using NMR arises only from those phosphate tetrahedra unaffected by any paramagnetic broadening.

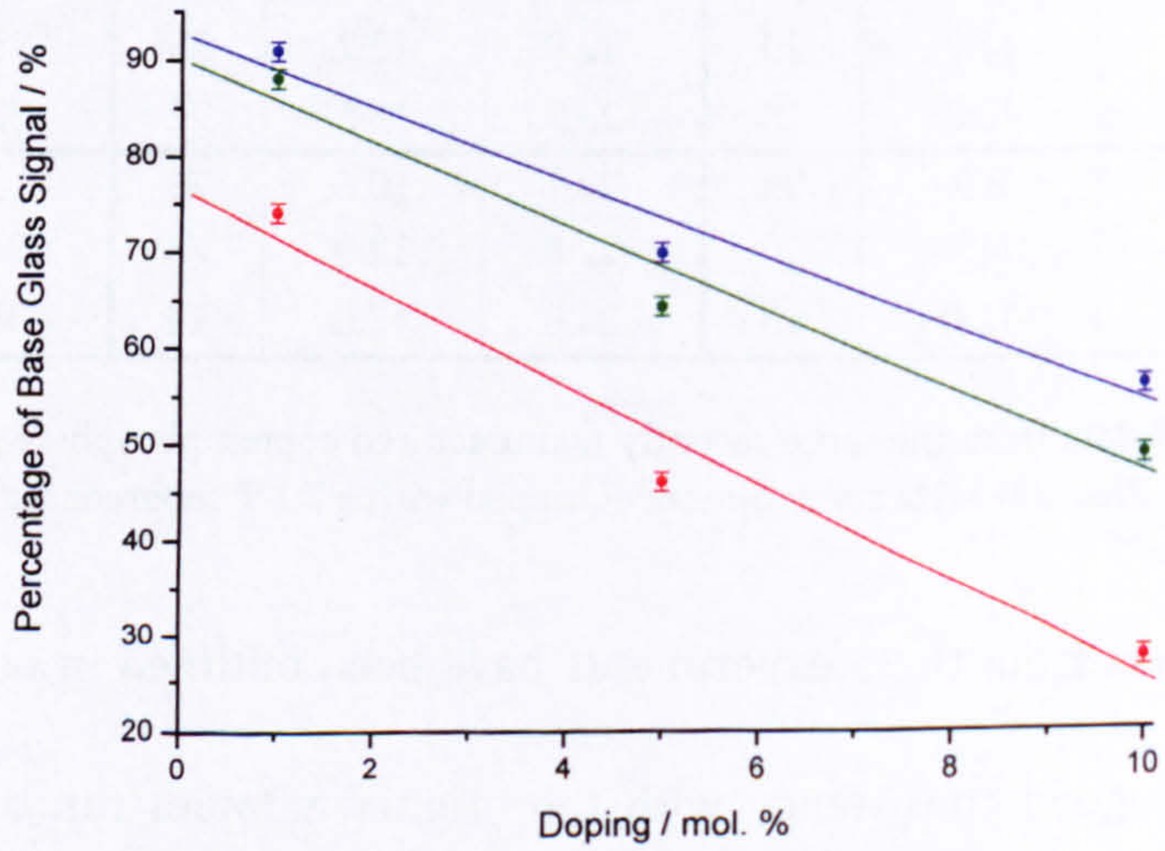

Figure 6.13: Relative change in total ^{31}P NMR signal intensity with increasing copper-doping compared to the base glass signal. CuO (green), $CuO_{0.5}$ (blue) and Cu_2O (red). Note that the lines are guides to the eye only.

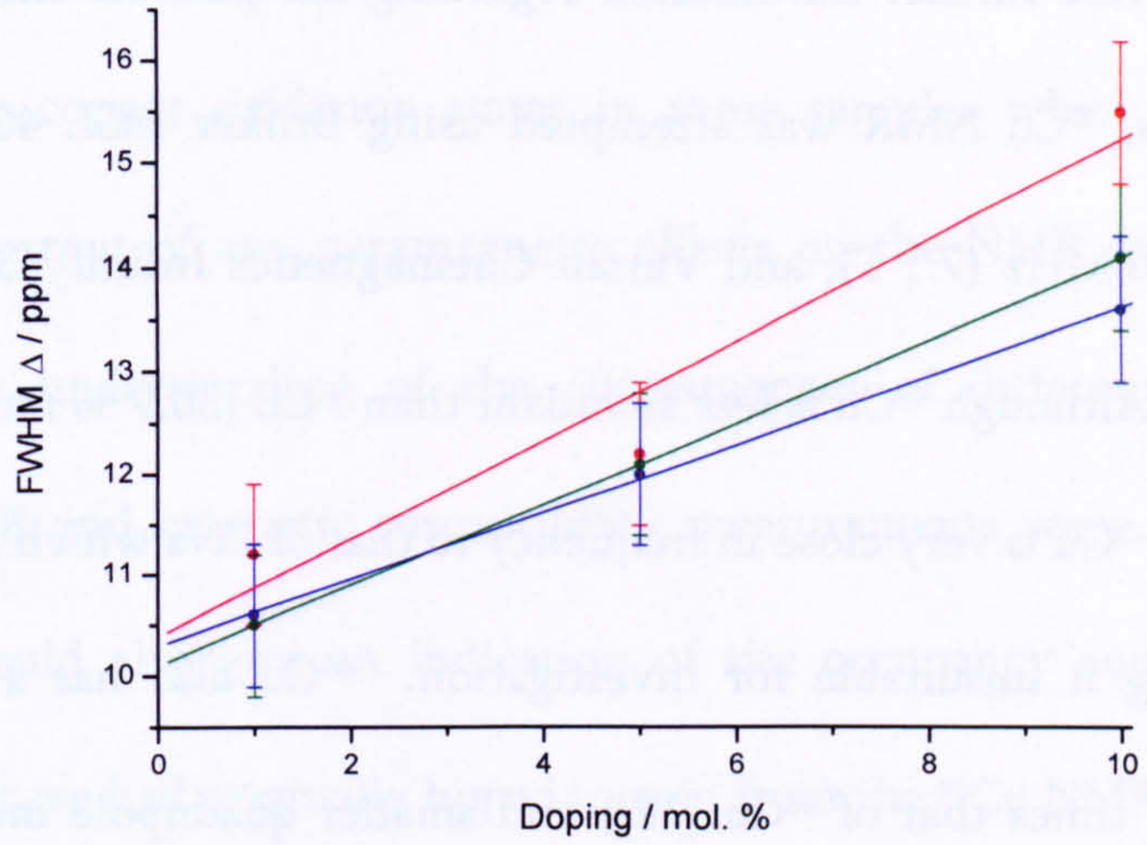

Figure 6.14: FWHM values for the Q^2 ^{31}P NMR peak for the CuO (green), $CuO_{0.5}$ (blue) and Cu_2O (red) doped samples, with change in doping. Note that the lines are guides to the eye only.

The FWHM values (figure 6.14) become greater with increasing copper-doping leading to a reduction in resolution also evident from the original spectra in figures 6.2 to 6.4. This is indicative of paramagnetic broadening, showing that the phosphate tetrahedra that do give rise to an NMR signal are not strongly enough affected by any paramagnetic copper to diminish their entire signal or produce a paramagnetic chemical shift but do undergo some broadening.

The intensity of the sidebands is consistently 20 % of the overall signal and remains unaffected by the quantity of copper-doping which suggests that there is no change in anisotropy of the phosphate environment of those tetrahedra that give rise to an NMR signal.

In order to provide further information regarding the possible site occupancies of the copper ions, ^{65}Cu NMR was attempted using Bruker MSL 400 MHz (9.4 T), Bruker CXP 300 MHz (7.1 T), and Varian-Chemagnetics Infinity 300 MHz (7.1 T) spectrometers. Although ^{65}Cu is less abundant than ^{63}Cu (30.9 % rather than 69.1 % abundant [17]), ^{63}Cu is very close in frequency to that of ^{23}Na which is present in our samples, making it unsuitable for investigation. ^{65}Cu also has a higher Larmor frequency (1.07 times that of ^{63}Cu [17]) and smaller quadupole moment (0.934 of that for ^{63}Cu [17]). This results in greater sensitivity and narrower (by a factor of 1.25 [17]), more easily resolved NMR spectral lines since the first-order quadrupolar broadening is proportional to the quadrupole moment and the second-order quadrupolar broadening is proportional to the square of the quadrupole moment and inversely proportional to the gyromagnetic ratio. All of these experiments however proved unsuccessful in detecting any copper signal at all in any of the samples regardless of initial dopant compound or concentration, suggesting that all or at least the great majority, of the copper present in the samples is in the form of Cu^{2+} even in those of the highest copper-doping levels, as Cu^{2+} ions give rise to no NMR signal due to their paramagnetic nature. It could be however that we are unable to observe the signal from any Cu^{+} ions if they are strongly enough affected by the paramagnetic Cu^{2+} ions for example, thus explaining their detection in the UV-visible spectrophotometry measurements which suggested the presence of mixed valence copper in these glasses, see section 6.2.4. However the likelihood is that if at all present, the Cu^{+} ions are small in quantity.

6.2.6 Cu^{2+} quantification

To confirm the copper oxidation states in these samples which would help in describing the extent of any paramagnetic effects on the NMR spectra as well as giving a better understanding of the consequences of different initial doping compounds, EPR and magnetic susceptibility measurements were employed. The EPR results should also give an indication of site occupancy and environmental information that we had originally hoped to gain from the ^{65}Cu NMR.

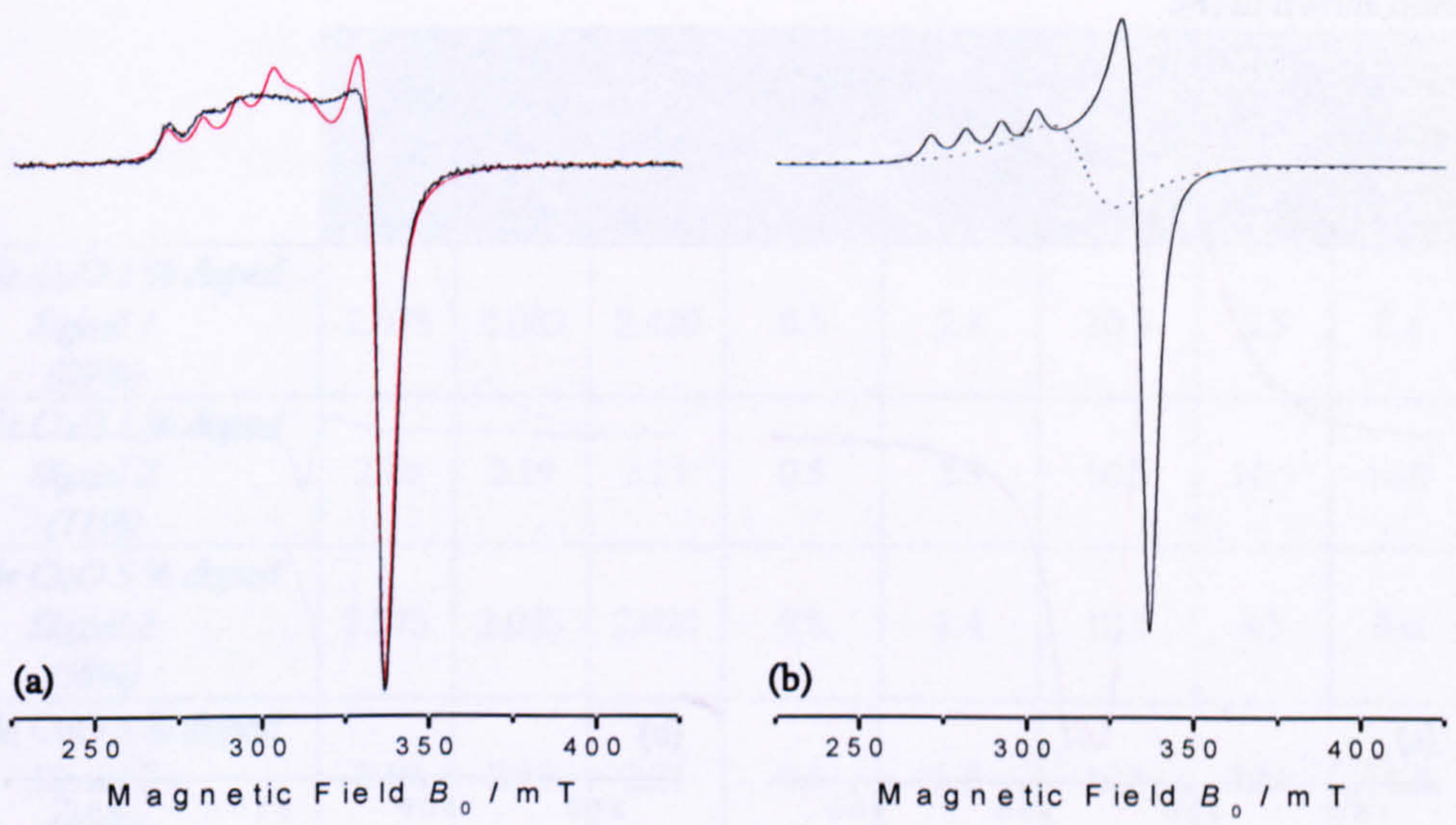

Figure 6.15: (a) The EPR signal received from the CuO 1 % doped sample (in black) and overall simulated spectrum by Kowalczyk (in red), and (b) the two simulated signals comprising the overall spectrum shown in (b).

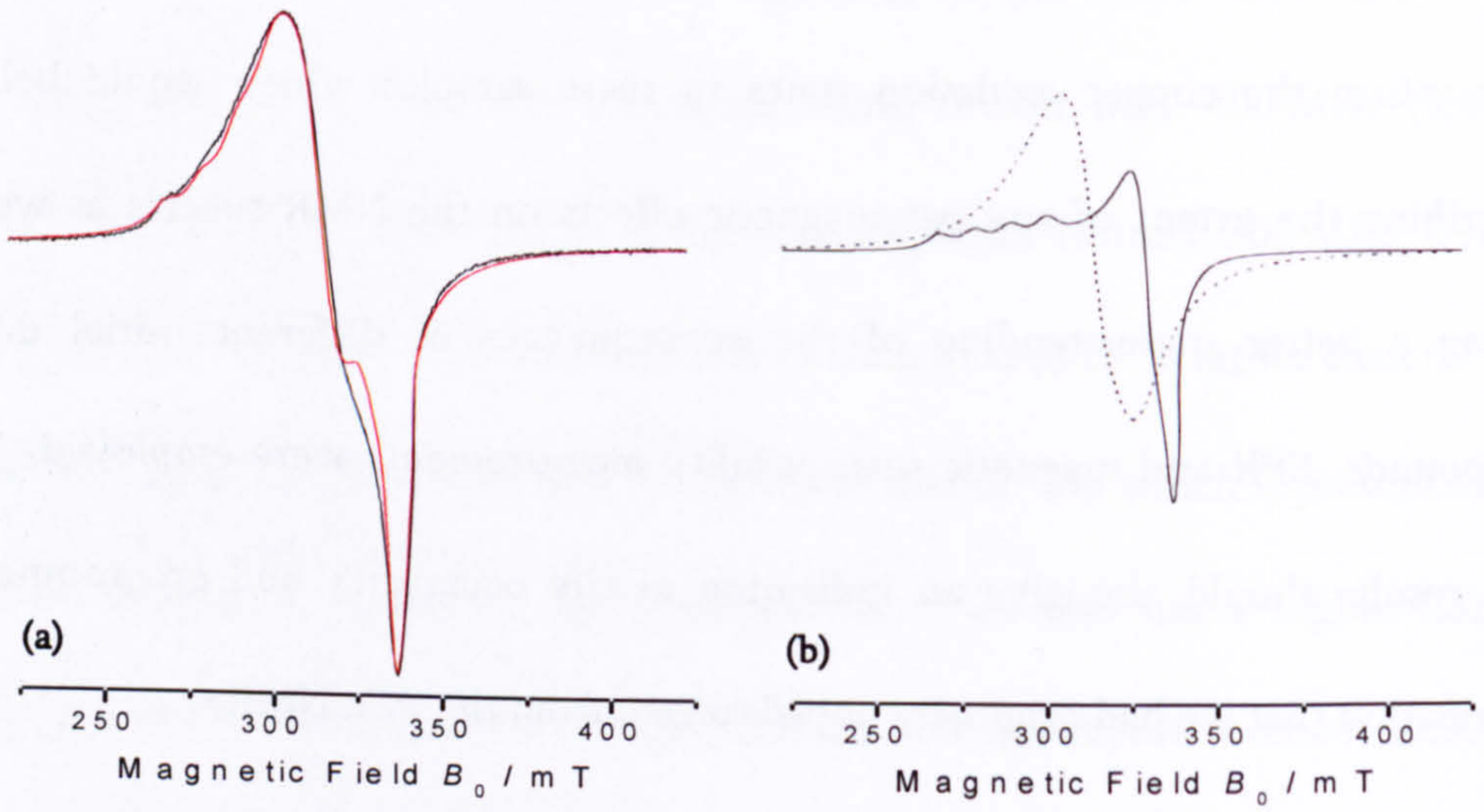

Figure 6.16: (a) The EPR signal arising from the CuO 5 % doped sample (in black) and overall simulated spectrum by Kowalczyk (in red), and (b) the two simulated signals comprising the overall spectrum shown in (b).

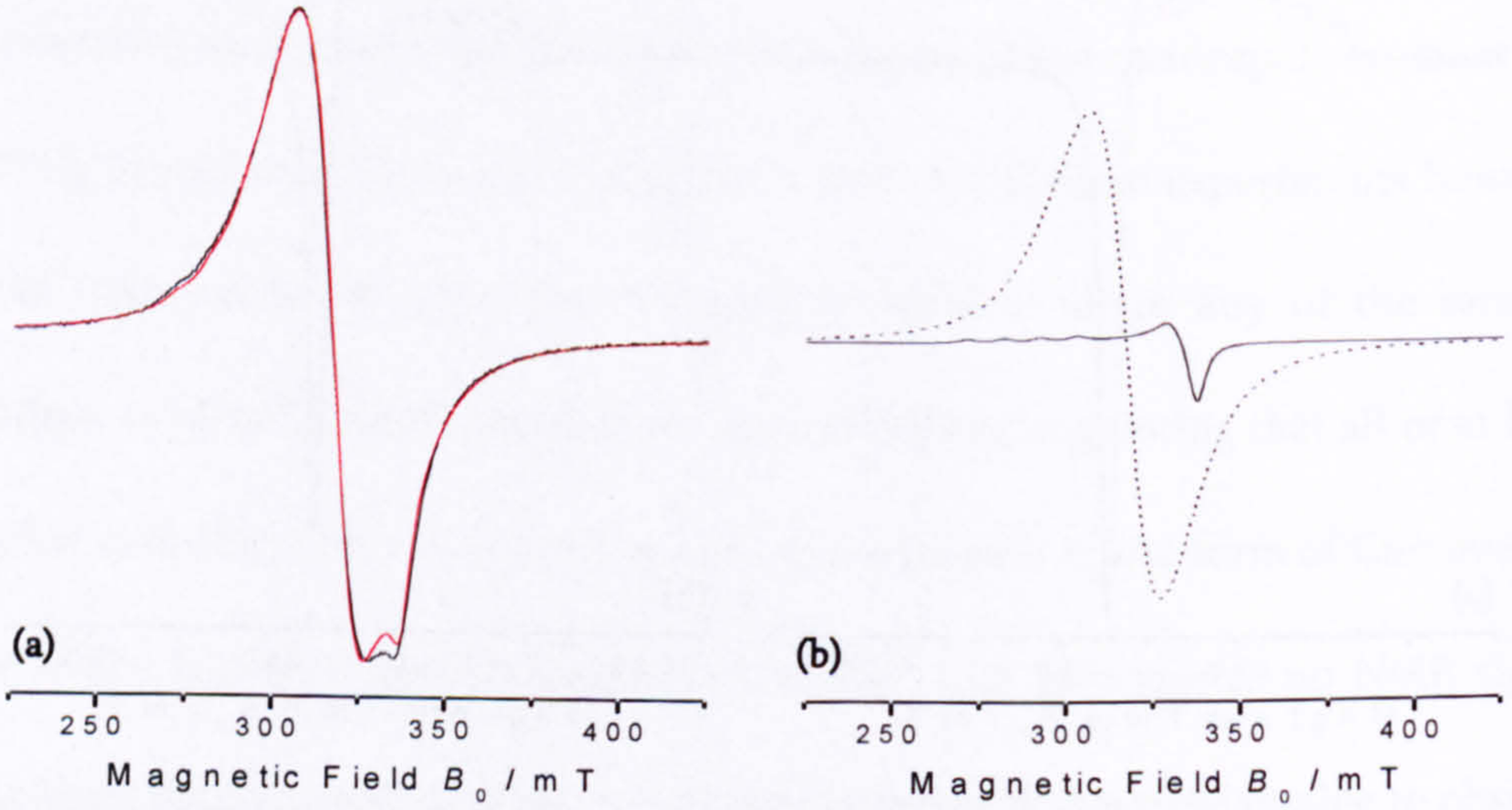

Figure 6.17: (a) The EPR signal received from the CuO 10 % doped sample (in black) and overall simulated spectrum by Kowalczyk (in red), and (b) the two simulated signals comprising the overall spectrum shown in (b).

In the figures 6.15 to 6.17, parts (a) show the Cu^{2+} EPR spectra collected at room temperature and centred on 320 mT with a sweep width of 300 mT, for the CuO 1 %, 5 % and 10 % doped phosphate based glass powder samples. The black lines

show the raw data recorded and the red lines are the powder pattern simulations described by the effective spin Hamiltonian given in equation 6.1 which includes the electronic Zeeman interaction term (where $\boldsymbol{g}$ is the g-tensor), and the hyperfine coupling term between the unpaired electron and nuclear spin of copper (where $\underline{\underline{A}}$ is the hyperfine structure tensor) [18]. The $\boldsymbol{g}$ and $\underline{\underline{A}}$ parameters used in the simulations are listed in table 6.7. and the overall simulated signals are in good agreement with the raw data collected.

$$\mathcal{H} = \mu_B \underline{S} \cdot \underline{\underline{g}} \cdot \underline{B} + \underline{S} \cdot \underline{\underline{A}} \cdot \underline{I} \tag{6.1}$$

	***g*-factor ± 0.001 for signal 1 ± 0.01 for signal 2**			***Hyperfine splitting / mT ± 0.3 mT***			***Linewidths / mT ± 0.5 mT***		
	g_{xx}	g_{yy}	g_{zz}	A_{xx}	A_{yy}	A_{zz}	ΔB_{xx}	ΔB_{yy}	ΔB_{zz}
Sample CuO 1 % doped Signal 1 (89%)	2.073	2.083	2.420	0.5	2.4	10.5	3.5	3.4	3.5
Sample CuO 1 % doped Signal 2 (11%)	2.19	2.19	2.21	0.5	2.5	10.5	10.5	16.0	23.0
Sample CuO 5 % doped Signal 1 (58%)	2.073	2.083	2.420	0.5	2.4	10.5	4.5	5.0	5.0
Sample CuO 5 % doped Signal 2 (42%)	2.19	2.19	2.21	0.5	2.5	10.5	10.5	16.0	23.0
Sample CuO 10 % doped Signal 1 (19%)	2.073	2.083	2.420	0.5	2.4	10.5	3.5	3.2	3.2
Sample CuO 10 % doped Signal 2 (81%)	2.19	2.19	2.21	0.5	2.5	10.5	19.0	19.0	19.0

Table 6.7: The EPR powder pattern simulation parameters by Kowalczyk, used in the effective spin Hamiltonian given in equation 6.1.

Each of the spectra were simulated using two separate signals with the parameters described in the table 6.7 in order to give a good approximation to the overall EPR signals observed. These simulations are shown as signal 1 (the solid line) and signal 2 (the dotted line) in part (b) of figures 6.15 to 6.17. The presence of two signals contributing to the total simulation suggests that the Cu^{2+} ions are present in two different sites within the glass. At low (1 %) doping, signal 1 dominates and is highly characteristic of a typical Cu^{2+} EPR spectrum from distributed, isolated Cu^{2+} impurities [19-23] thus confirming the presence of Cu^{2+} ions in the samples. The effective spin Hamiltonian parameters of Daoudi et al. [19] were used as a starting point for the simulations and were allowed to vary to produce the "best fit" to the experimental powder pattern EPR spectra. The g-factors determined show evidence for environmental anisotropy as $g_{xx} \neq g_{yy} \neq g_{zz}$, which suggests a deviation from axial towards rhombic symmetry for this Cu^{2+} site. This 1 % copper-doped spectrum also presents clear evidence for the occurrence of hyperfine splitting due to interactions between the unpaired electron and the copper nucleus. This hyperfine structure (HFS) is identified by the presence of multiple lines in the first simulated signal, in the form of defined features or shoulders, between 265 and 305 mT and are described by the A_{xx}, A_{yy} and A_{zz} values given in table 6.7.

At this low (1 %) doping concentration signal 2, which is broader ($\Delta B_{\text{}}$ = 10.5 to 23.0 ± 0.5 mT) and approximately isotropic, is overwhelmed by that of signal 1 and shows no clearly resolved spectral features. In simulating this spectrum g was

allowed to vary to produce the best fit when compared to the experimental data but $\underline{A}$ was assumed to be identical to that of signal 1. The g tensor values for signal 2 are typical of those for Cu^{2+} in an axial environment as within the uncertainties $g_{xx} \approx g_{yy} \equiv g_{\perp}$ whilst $g_{xx}, g_{yy} \neq g_{zz} \equiv g_{\parallel}$.

The peak-to-peak linewidths, ΔB, used in the simulations (shown in table 6.7) show that signal 2 is three to five times broader than signal 1 indicating that the Cu^{2+} environments are very different, perhaps suggesting that the Cu^{2+} ions within the second site giving rise to signal 2 are distributed closer together. Both signal 2 and signal 1 have linewidths that are essentially independent of the quantity of copper-doping suggesting that any broadening, for example, dipole-dipole interactions, experienced by the Cu^{2+} ions do not increase with additional copper content. This implies that the strength of the Cu^{2+}-Cu^{2+} interactions is unaltered with doping. However, the relative intensity of signal 2 does increase with the addition of copper such that it is dominant at 10 % doping indicating that the number of ions within this site increases with doping. This may indicate a preference for the Cu^{2+} ions to enter these second, more closely grouped sites at higher doping levels. The possibility of preferential copper-grouping at higher doping is important as this could fit with earlier suggestions of copper nanoclustering or phase separation. However the exact extent and scale of this grouping is unobtainable from the EPR data and the microscopy measurements

previously completed were unsuccessful in observing any copper crystallisation clusters ≥ 5nm in diameter, see section 6.2.3.

The results obtained are consistent with studies by Ardelean et al. [22], as well as those found by Daoudi et al. [19] who performed similar experiments and corresponding simulations on copper polyphosphate glasses of $(50 - x/2)$ % P_2O_5 + $(50 - x/2)$ % Na_2O + x % CuO, where $1 \leq x \leq 30$. The spectra confirm the presence of Cu^{2+} in all of the samples regardless the form or quantity of which copper was introduced into the system (either as bivalent Cu^{2+} ions in copper (II) oxide, CuO doping, or monovalent Cu^{+} ions in copper (I) oxide, Cu_2O doping).

Via comparisons with other studies, specifically those by Daoudi et al. [19] who found similar EPR simulation parameters, it is possible to assume that the Cu^{2+} ions reside in an elongated distorted octahedron where the Cu^{2+} ions charge balance six oxygen ligands. This is consistent with studies by Ardelean et al. [22] and Ezikov and Romanova [23] although the coordination could also be confirmed using Cu K-edge XANES. This octahedral coordination suggests that the Cu^{2+} ions cannot therefore be substituted directly into the tetrahedrally coordinated phosphorus network in a network forming way. This therefore provides evidence for copper ions acting as network modifiers rather than network formers, but does not help to explain the unpredicted Q^3 phosphate speciation from the NMR results. These

results do however only describe the action of the Cu^{2+} ions and the difference between their environments and that of any Cu^{+} ions cannot be stated for certain.

We would expect EPR measurements on isolated dispersed Cu^{2+} impurities to be quantitative such that the integrated signal intensities increase proportionally with the Cu^{2+} content. However, the experimental technique demonstrated great difficulties in achieving reproducible EPR intensities leading to an error of over ~40 % in the estimated concentrations. Factors preventing us from achieving accurate integrated intensities include that the samples were lossy (suffering from dielectric losses from the electric field [24]) and hygroscopic thus could potentially incorporate water, known to affect the signal intensities measured due to absorption of microwaves [24]. However, the samples were oven-dried overnight to prevent the incorporation of water and variations in the signal intensities still arose. The cavity *Q*-factor (section 4.2.2) was very sensitive to the sample positioning and as the small quantities of sample did not entirely fill the active volume of the EPR cavity the concentrations determined could easily vary by a factor of 50 % [24]. Even when supporting the sample tubes at their base using the polytetrafluorethylene (PTFE) Teflon plinth to maintain the sample positioning large variations in intensity still occurred. The consequence of these problems is that we could no longer estimate the concentration of the paramagnetic ions using the reference sample of Cu_2SO_4, so magnetic susceptibility measurements were

subsequently performed in order to quantify the amount of Cu^{2+} ions within each sample.

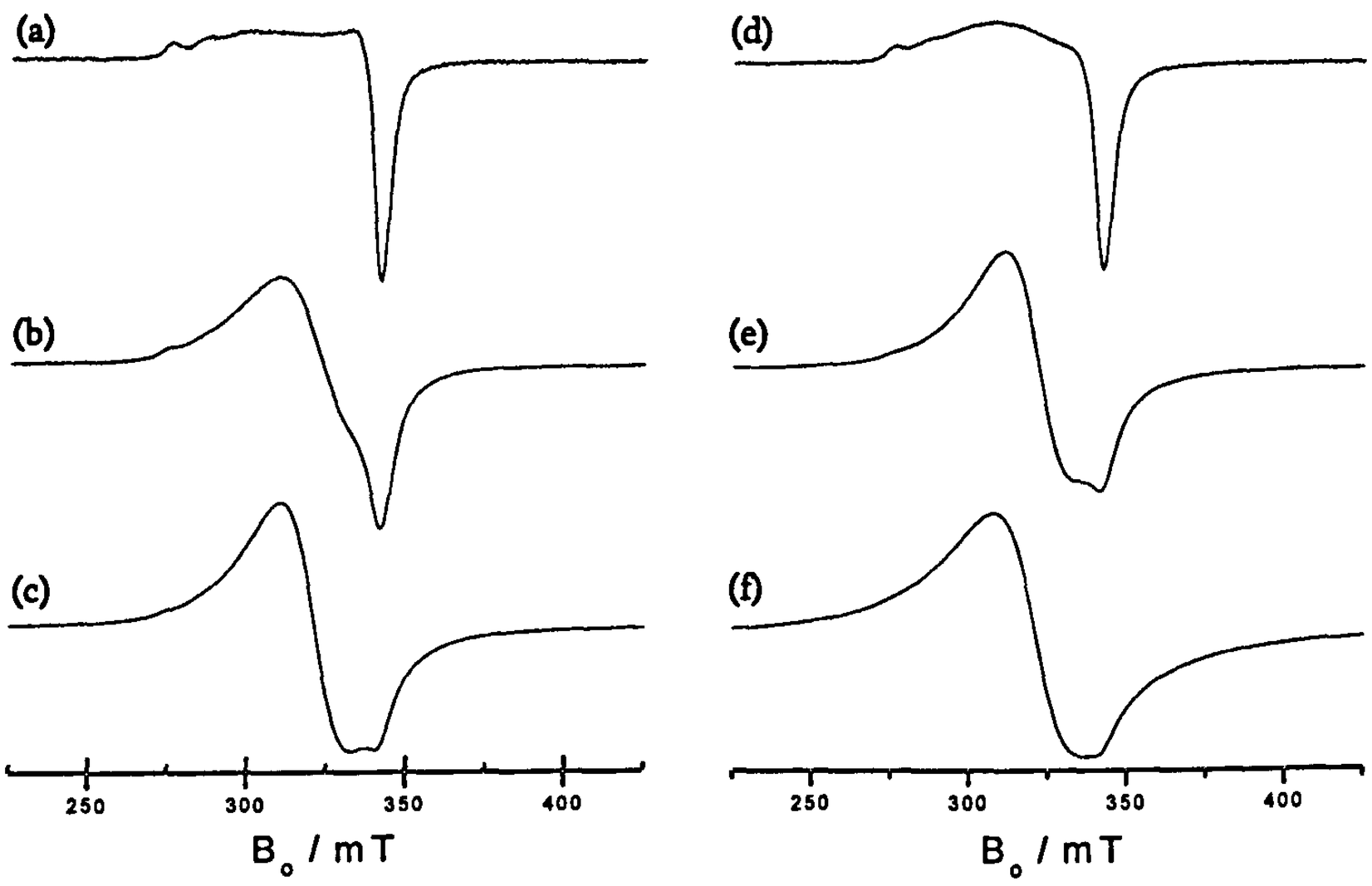

Figure 6.18: The EPR signal collected by Kowalczyk, received from the CuO doped samples where (a), (b) and (c) are from the most recently manufactured samples of 1, 5 and 10 % doping, respectively. (d), (e) and (f) are the older, original samples and contain 1, 5 and 10 % copper-doping, respectively.

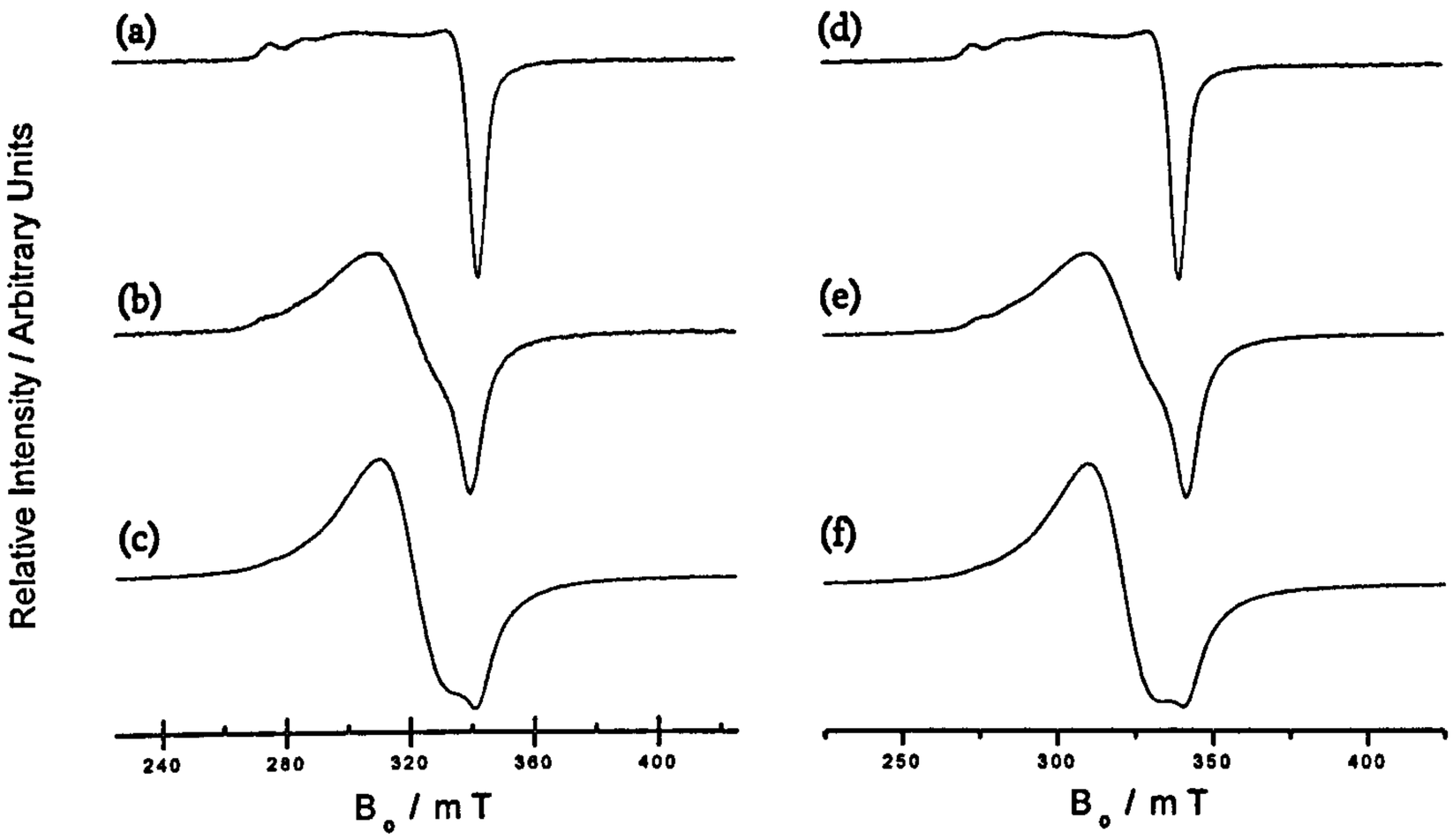

Figure 6.19: The EPR signal received from the $CuO_{0.5}$ doped samples taken by Kowalczyk where (a), (b) and (c) are from the most recently manufactured samples of 1, 5 and 10 % doping, respectively. (d), (e) and (f) are the older, original samples and contain 1, 5 and 10 % copper-doping, respectively.

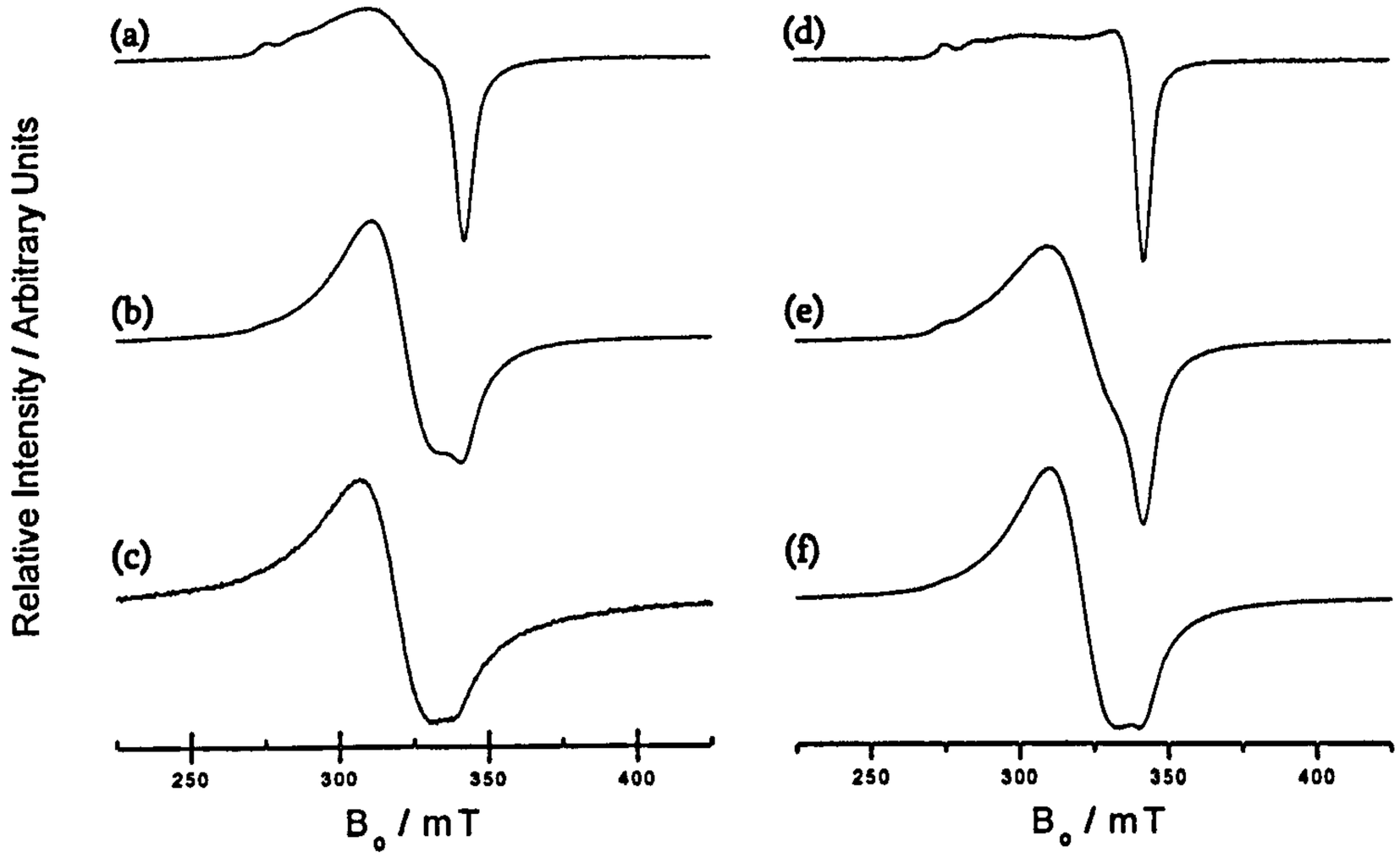

Figure 6.20: The EPR signal received from the Cu_2O doped samples taken by Kowalczyk where (a), (b) and (c) are from the most recently manufactured samples of 1, 5 and 10 % doping, respectively. (d), (e) and (f) are the older, original samples and contain 1, 5 and 10 % copper-doping, respectively.

The spectra collected for each of the samples are shown in figures 6.18 to 6.20 although the intensities are arbitrarily scaled for the reasons described above. The lineshapes clearly show the HFS resolved at 1 % doping for all of the samples and the presence of two signals in samples of > 1 % doping can also be clearly noted. There is however a significant difference in some cases between the EPR experiments performed upon samples of differing ages, specifically see figure 6.18 (b) and (e), and all parts of figure 6.20. This led to concerns over the stability of the phosphate glass structure as it could be that changes occur with sample age possibly due to some exposure to light, air and moisture (although all samples have been kept in a desiccator containing silica gel drying agent). However, these spectra were rerun after overnight drying out of the samples in an oven and there was no change in any of the lineshapes observed, there was also no significant difference between the Cu^{2+} quantities in these samples obtained from the magnetic susceptibility experiments.

As quantitative measurements of the Cu^{2+} ions within the copper phosphate glass samples using EPR were unsuccessful, measurements of magnetic moment with changing temperature were subsequently attempted. The magnetic moments for the samples at each temperature were measured by a SQuID detector. These values were then normalised by the mass of each sample and using their known molecular weights, the net molar magnetisation at each temperature was achieved. By dividing this value through by the magnetic field strength H which was fixed at

1000 Oe the magnetic susceptibility against temperature could be plotted as shown in figures 6.21 to 6.23. In addition to this the values of M versus H/T were also plotted as shown inset into the figures.

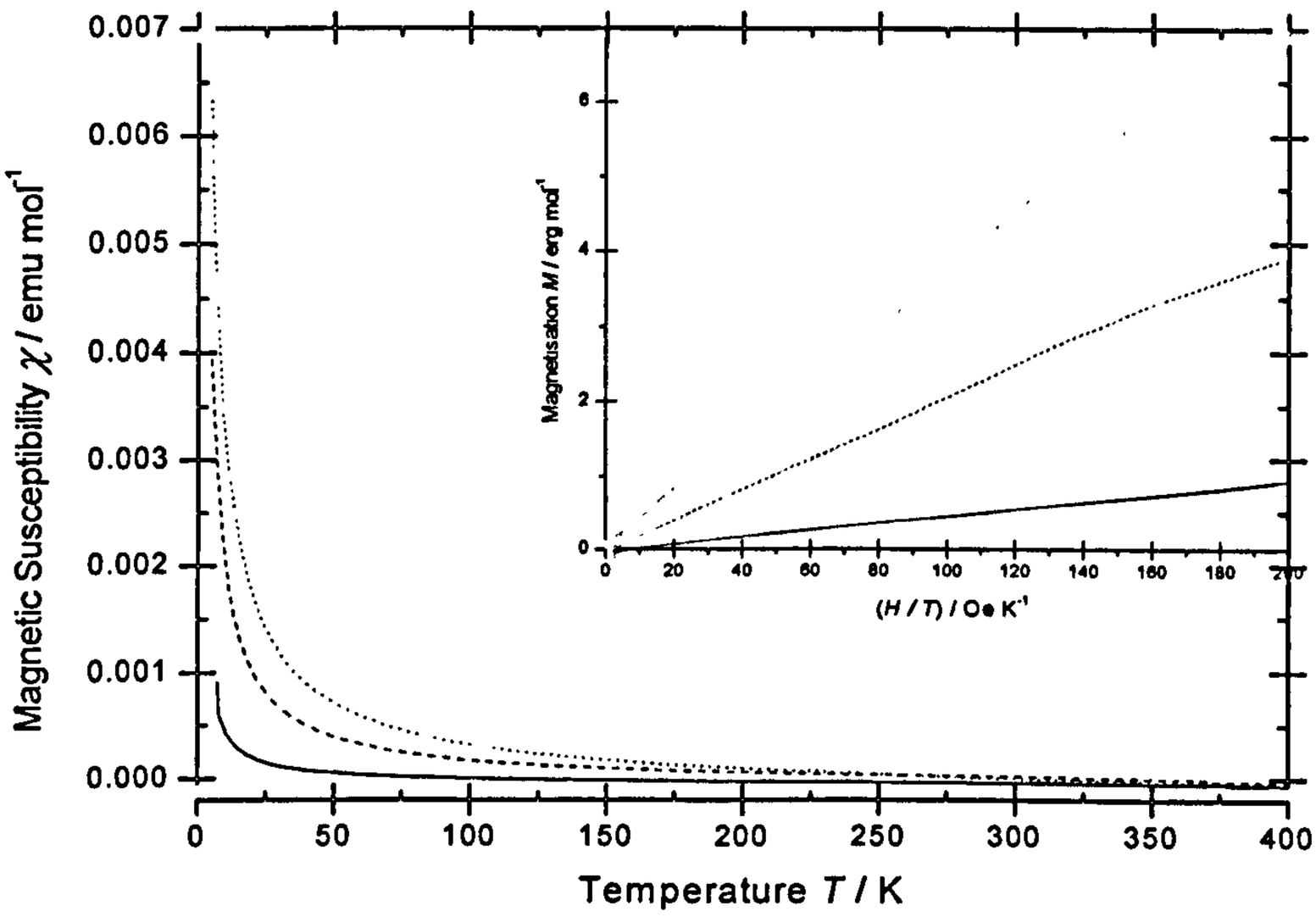

Figure 6.21: The change in magnetic susceptibility with temperature for the 1 % (solid), 5 % (dashed) and 10 % (dotted) CuO doped samples, with the graphs of M versus H/T for the same data inset.

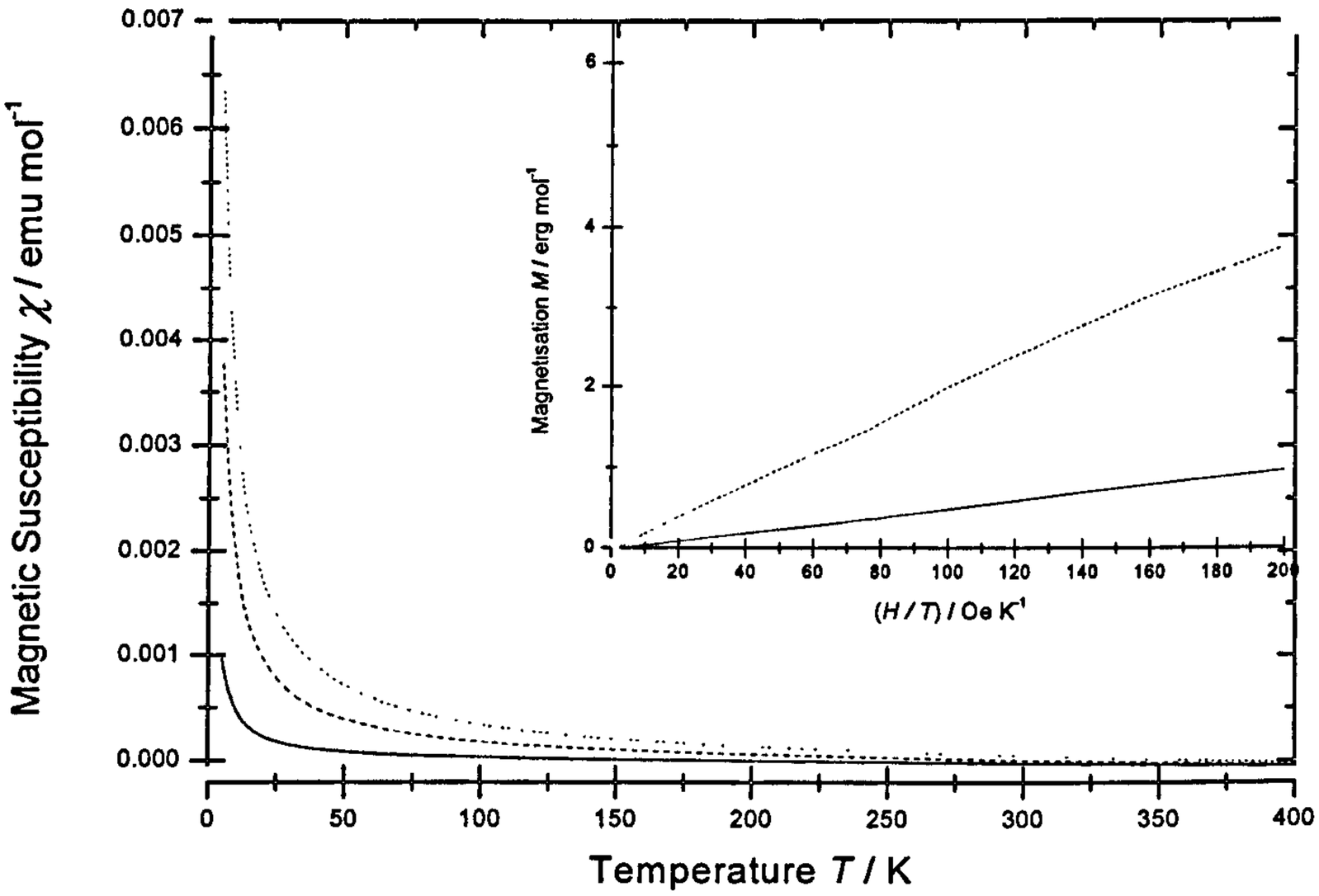

Figure 6.22: The change in magnetic susceptibility with temperature for the 1 % (solid), 5 % (dashed) and 10 % (dotted) $CuO_{0.5}$ doped samples, with the graphs of *M* versus *H* / *T* for the same data inset.

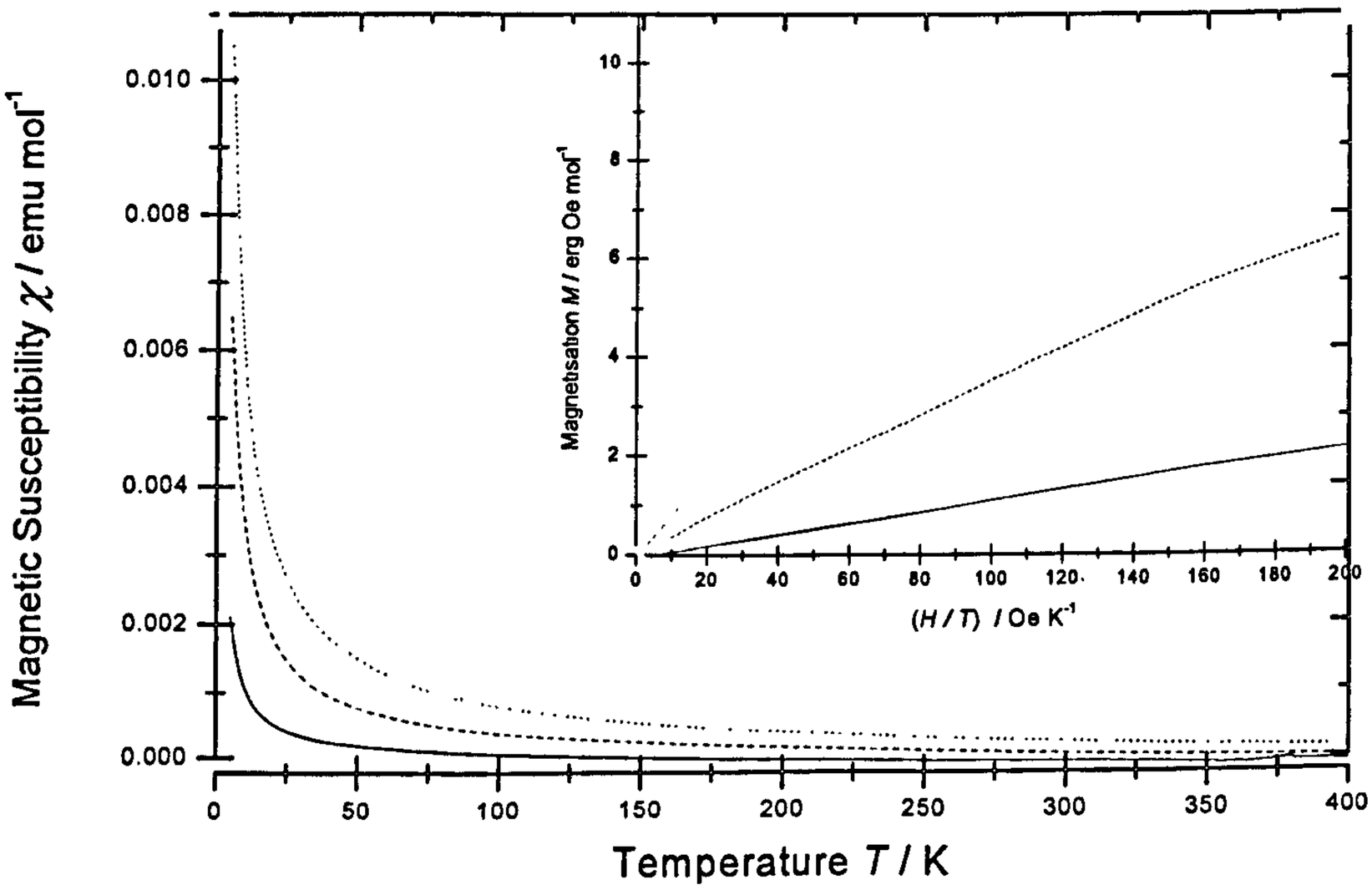

Figure 6.23: The change in magnetic susceptibility with temperature for the 1 % (solid), 5 % (dashed) and 10 % (dotted) Cu_2O doped samples, with the graphs of *M* versus *H* / *T* for the same data inset.

The plots of χ versus T were fitted using the Curie-Weiss expression given below in equation 6.2. This allowed the values for the Curie constant, C, the Weiss constant, θ, and shift, χ_0, to be estimated. This χ_0 term may arise from second-order field effects (van Vleck contributions) or diamagnetism originating from core electrons or the gel capsule sample holder [25]. The results from fitting the magnetic susceptibility curves found χ_0 to be between 2.0 and $8.0 \pm 0.2 \times 10^{-6}$ emu mol^{-1} for this range of samples and the diamagnetic contributions of the constituent nuclei within the samples calculated from the molecular compositions and Pascal constants [25] gave rise to a diamagnetic susceptibility of 4.5 to 4.6×10^{-6} emu mol^{-1} therefore making diamagnetism the most likely source of this shift.

$$\chi = \chi_0 + \frac{C}{T - \theta} \tag{6.2}$$

The first experiment was completed on a reference sample of copper (II) sulphate pentahydrate ($CuSO_4 \cdot 5H_2O$) powder (Fisons Scientific) with a molecular weight of 249.686 g mol^{-1}. In this sample for every mole of copper sulphate there is one mole of Cu^{2+} ions, and thus from equation 4.2, section 4.3.1, page 90, n is equal to 1, allowing the value for μ_{eff} to be calculated as 1.97 ± 0.01. This is in good agreement with that found experimentally by Kittel [26] of 1.9 and is closer to the μ_{eff} term given by $\mu_{eff} = 2[S(S+1)]^{1/2} = 1.73$ where $S = ½$ [26] rather than that calculated by equation 4.3, section 4.3.1, page 90, which gives 3.55 [26] implying that the orbital angular moment contribution, L, to the overall angular momentum, J, is negligible compared to the spin angular momentum, S, and in systems where this is true the

orbital moments are described as quenched [26]. For transition elements such as copper this result was as expected since these are usually spin only systems [26].

Having experimentally calculated the value for μ_{eff}, the molar fraction, n, of paramagnetic centres in each of the powdered glass samples could be calculated which gave the Cu^{2+}/Cu_{Total} percentages given in table 6.8. The experiments were completed on the full set of copper-doped samples including those which were a year older in order to check for any changes that may have occurred due to sample aging by exposure to different environments since the EPR results showed some discrepancies between the samples. The results were found to be consistent for samples of all ages and as such only the results for the most recently manufactured samples are displayed.

Sample doping	*Curie constant C / emu mol.$^{-1}$ ± 0.0001 emu mol.$^{-1}$*	Weiss constant θ / K *± 0.05 K*	*Cu^{2+}/Cu_{Total} / % ± 10 %*
CuO 1 %	0.0054	–0.04	111
CuO 5 %	0.0228	–0.62	94
CuO 10 %	0.0392	–0.60	81
$CuO_{0.5}$ 1 %	0.0061	–1.26	126
$CuO_{0.5}$ 5 %	0.0225	–0.90	93
$CuO_{0.5}$ 10 %	0.0390	–1.13	80
Cu_2O 1 %	0.0125	–0.72	129
Cu_2O 5 %	0.0404	–1.21	83
Cu_2O 10 %	0.0721	–2.04	74

Table 6.8: The Curie and Weiss constants for the copper-doped samples as calculated from the magnetic susceptibility curves, leading to an estimated Cu^{2+}/Cu_{Total} ratio.

The temperature dependence of the magnetisation appears to closely follow the Curie-Weiss law stated in equation 6.2 and the Curie constant clearly increases

linearly with doping (see figure 6.24). For the CuO and $CuO_{0.5}$ doped samples the change in Curie constant is similar showing again that it is the quantity and not starting valence of the copper ions that determines the Cu^{2+} content within the samples. This means that it must be energetically favourable for the copper to reside in this oxidation state as the results show that Cu^{2+} is the dominant state in all of the samples regardless of either the doping concentration or the starting compound (either copper (I) or copper (II) oxide). The higher the copper-doping concentration the smaller the overall Cu^{2+}/Cu_{Total} fraction (see figure 6.25), showing evidence for mixed copper valences, although the results give only a rough estimate of the Cu^{2+}/Cu_{Total} percentages due to uncertainties in the data fitting, difficulties in accurately weighing such small quantities of powdered sample required in these experiments and the estimation of the total amount of copper present. The table of data, 6.8, suggests that at 1 % copper-doping all of the copper is present in the form of Cu^{2+} ions whereas in the UV-visible optical absorption measurements performed on the same samples (see section 6.2.4 and figure 6.11 on page 182) the absorption bands for both redox states were observed suggesting mixed valences even at low doping. As the magnetic susceptibility measurements do not give a measure of Cu^{+} ions it is impossible to confirm the presence of this species, although the high percentage of Cu^{2+}/Cu_{Total} observed means that their presence is unlikely, as does the lack of ^{65}Cu NMR signal from previous measurements.

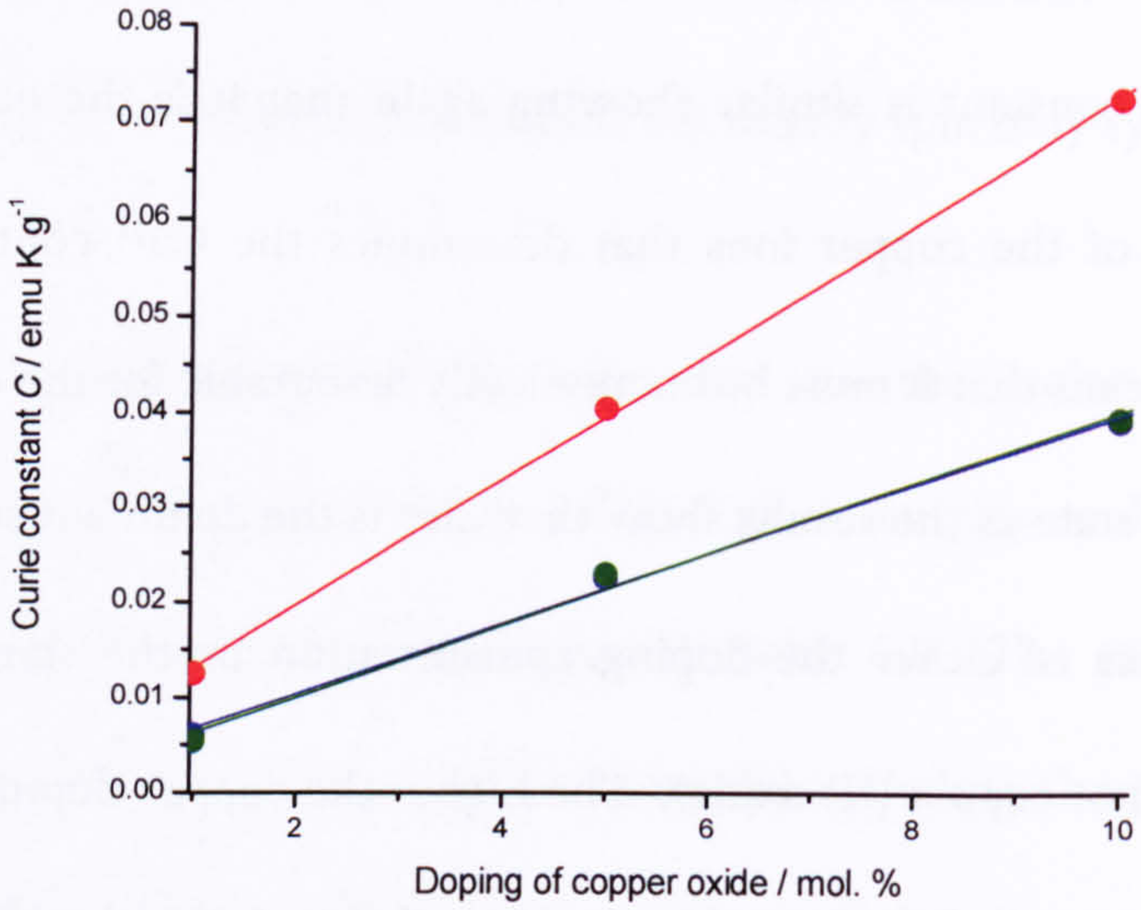

Figure 6.24: The change in Curie constant with doping for the CuO (green), $CuO_{0.5}$ (blue) and Cu_2O (red) doped samples, note that the lines are guides to the eye and the error bars are of the same order of magnitude as the data points. Also note that the CuO and $CuO_{0.5}$ data points and guiding lines are nearly overlapping and therefore hard to distinguish.

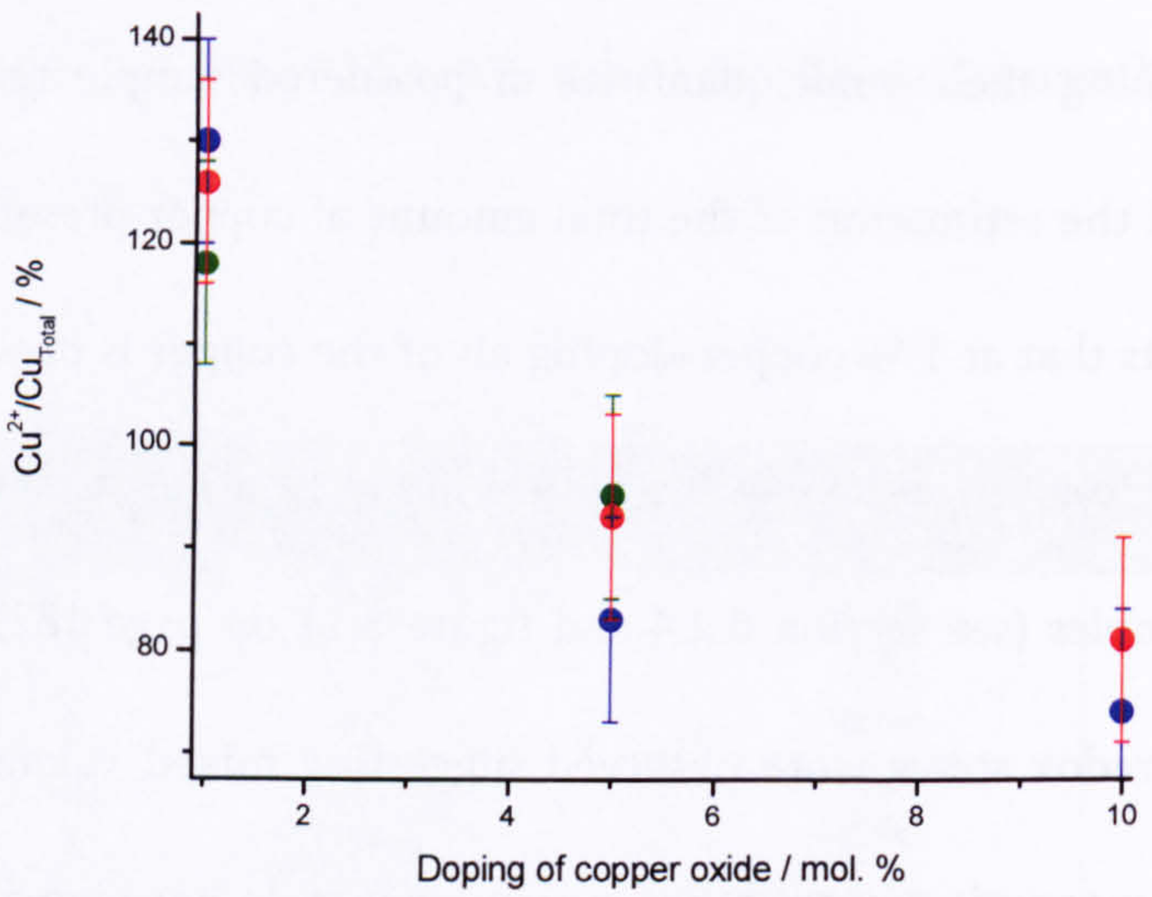

Figure 6.25: The change in Cu^{2+} content relative to the total amount of copper in the phosphate based glass samples as copper-doping increases for the CuO (green), $CuO_{0.5}$ (blue) and Cu_2O (red) doped samples. Note that the CuO and Cu_2O data points are overlapping at 10 mol.% doping and are therefore not distinguishable.

The fitting of the Curie-Weiss behaviour of the samples gave rise to a negative Weiss constant, θ, for all samples and the polarity of this value indicates the nature of the magnetic ordering occurring in the powders as the external field is removed. The

results therefore suggest the presence of some antiferromagnetic (AFM) exchange interactions between the Cu^{2+} ions. However, the size this Weiss constant indicates the strength of these AFM interactions [19] and θ is small (0 K < $\theta \leq$ –2 K) for all of these samples implying that the magnetic moments are only very weakly AFM coupled but that this ordering may occur in the samples at temperatures below ~2 K which may have implications on the VSM results obtained, discussed later.

As the ^{65}Cu NMR experiments could not detect the signal from any Cu^{+} ions at all in these samples suggesting no, or very few Cu^{+} ions in the system, we wanted to confirm the observation of mixed valences calculated here. It is possible that the reduction in Cu^{2+}/Cu_{Total} observed with additional doping may not be an entirely true account of the system as interactions between the copper ions, especially the formation of copper pairs, could potentially create changes in effective magnetic moment, μ_{eff}, therefore affecting the paramagnetic signal generated. The EPR results showed evidence of interactions between the Cu^{2+} ions thereby emphasising our reservations. Additionally any change in the quenching of orbital momentum contributions due to differences in the copper environment could greatly affect μ_{eff}. Experiments on the copper (II) sulphate reference sample found $\mu_{eff} = 1.97 \pm 0.01$, however the Cu^{2+} ions in the glass samples are not necessarily in the same environment to those in the reference sample. This could give rise to a different μ_{eff} value, or it is possible that this μ_{eff} value could change as doping increases if ions occupy different sites within the sample as suggested by the EPR spectra and

simulations. If the system becomes more quenched as doping increases then μ_{eff} could tend to 1.73 [26] using $J = S = ½$, which may account for the drop in Cu^{2+}/Cu_{Total}. To observe the Cu^{2+}/Cu_{Total} values using the theoretical $\mu_{eff} = 1.73$ see table 6.9. It can be seen that this gives closer to the expected 100 % Cu^{2+} percentages for the 10 % doped samples but is too high for < 10 % doping. The EPR results showed two Cu^{2+} sites, one dominant at 1 % doping and the other at 10 % doping. If it were the case that the second, more prominent site at high doping is more quenched than the first, this could account for the discrepancies observed although this cannot be confirmed. It should also be noted that as magnetic susceptibility measurements provide a bulk investigation one cannot distinguish between different Cu^{2+} sites experiencing different environments as in EPR. Consequently the calculations must assume that the system is all the same whereas in reality there could be a mixture of states depending upon the overall doping levels and this again means that the quantities of Cu^{2+} obtained from this method must be treated with caution.

Sample doping	*Cu^{2+}/Cu_{Total} / % Using $\mu_{eff} = 1.73$ ± 10 %*
CuO 1 %	144
CuO 5 %	122
CuO 10 %	105
$CuO_{0.5}$ 1 %	163
$CuO_{0.5}$ 5 %	120
$CuO_{0.5}$ 10 %	104
Cu_2O 1 %	167
Cu_2O 5 %	108
Cu_2O 10 %	96

Table 6.9: Cu^{2+}/Cu_{Total} percentages calculated using the theoretically quenched μ_{eff} value of 1.73 in equation 4.2, section 4.3.2, page 90 [26].

Due to the experimental uncertainties in the results collected using the SQuID magnetometer and the other concerns raised, complementary magnetic measurements were also completed using a VSM system to give a corresponding calculation of the Cu^{2+}/Cu_{Total} ratio. The magnetisation of the samples was measured as the magnetic field was raised from 0 to 10^5 G (0 to 10 T) at a fixed temperature of 1.5 K. From equation 4.5 in section 4.3.1, page 92, the magnetisation per Bohr magneton per mole was plotted against $x = gJ\mu_B B/k_B T \approx \mu_B B/k_B T$ for $J = ½$ and $g \approx 2$. The saturated magnetisation values therefore give the molar fraction of paramagnetic ions in the sample provided that $J = S = ½$. This is shown by running a reference sample of copper (II) sulphate pentahydrate ($CuSO_4 \cdot 5H_2O$) which gave rise to a saturated magnetisation of 0.96 ± 0.10 μ_B on each paramagnetic site suggesting the presence of 96 ± 10 % of copper (II), consistent with expectations. The Cu^{2+}/Cu_{Total} ratios calculated for our glasses using this approach are listed in table 6.10.

Sample doping	*Cu^{2+}/Cu_{Total} / % ± 10 %*
$CuSO_4$ 5H_2O	96
$CuO_{0.5}$ 10 %	72
CuO 10 %	90
Cu_2O 10 %	65

Table 6.10: The Cu^{2+}/Cu_{Total} percentages obtained from the VSM experiments.

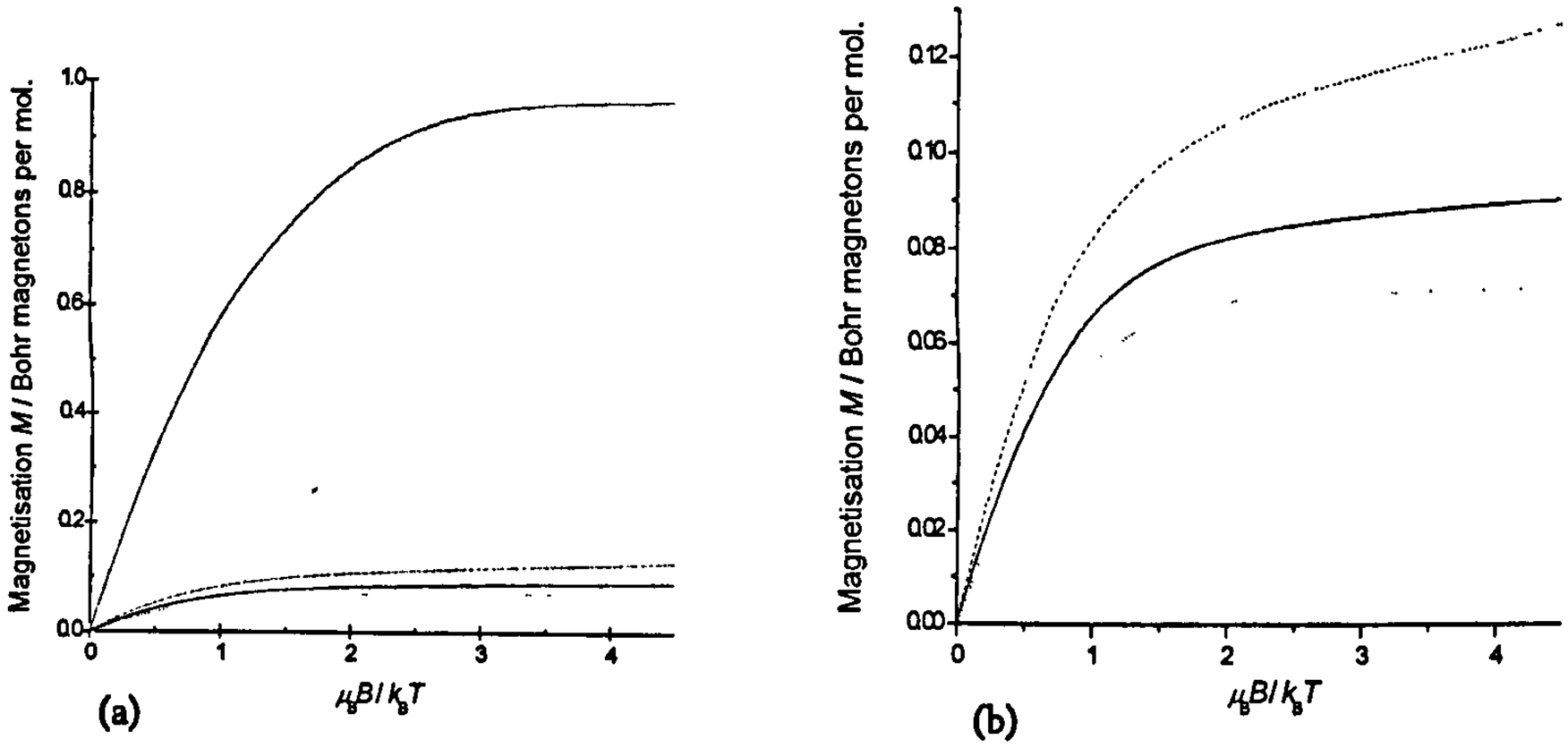

Figure 6.26: The sample magnetisation as a function of $\mu_B B/k_B T$ for (a) the reference sample (dash-dot) and 10 % doped copper samples and (b) rescaled to show more clearly the CuO (solid), $CuO_{0.5}$ (dotted) and Cu_2O (dashed) 10 % doped samples completed by Lees.

These experiments were completed for the samples of 10 % copper-doping only, due to the smaller magnetisations arising from the other samples making the experimental errors larger. Figure 6.26 shows the results collected and includes the measurement taken of the reference sample of copper (II) sulphate. The Cu^{2+}/Cu_{Total} percentages obtained and shown in table 6.10 again show that Cu^{2+} is the dominant copper valence state with mixed copper valences present within the 10 % copper-doped samples which supports the SQuID magnetometer results. However, it is possible that reduced Cu^{2+} quantities are being observed due to the running temperatures used during the VSM experiments as the previous magnetic susceptibility results taken using the SQuID magnetometer showed that the temperature at which any antiferromagnetic correlations could take place is around ≤ 2 K. As the VSM experiments were completed at 1.5 K some AFM ordering of the domains in the sample may occur such that the magnetisation curve obtained from

the measurements may not be representative of a totally paramagnetic system resulting in reduced Cu^{2+}/Cu_{Total} values. The experiments therefore require a trade off between operating at a low enough temperature to achieve magnetic saturation within these field strengths and having the temperature high enough to avoid any low temperature interactions and ordering. The paramagnetic behaviour of the samples was checked by fitting the appropriate Brillouin function from equation 4.6, section 4.3.1, page 92, to the saturation curves. The comparisons between the ideal functions and the raw data are given in figure 6.27. From these it can be seen that the CuO 10 % and the $CuO_{0.5}$ 10 % doped samples approximate closely to a Brillouin function whereas the higher molar copper-containing sample, Cu_2O 10 %, does not. This could be because the higher copper concentration produces stronger AFM correlations at this running temperature such that the sample no longer behaves as a pure paramagnet and does not saturate at the magnetic field strengths employed.

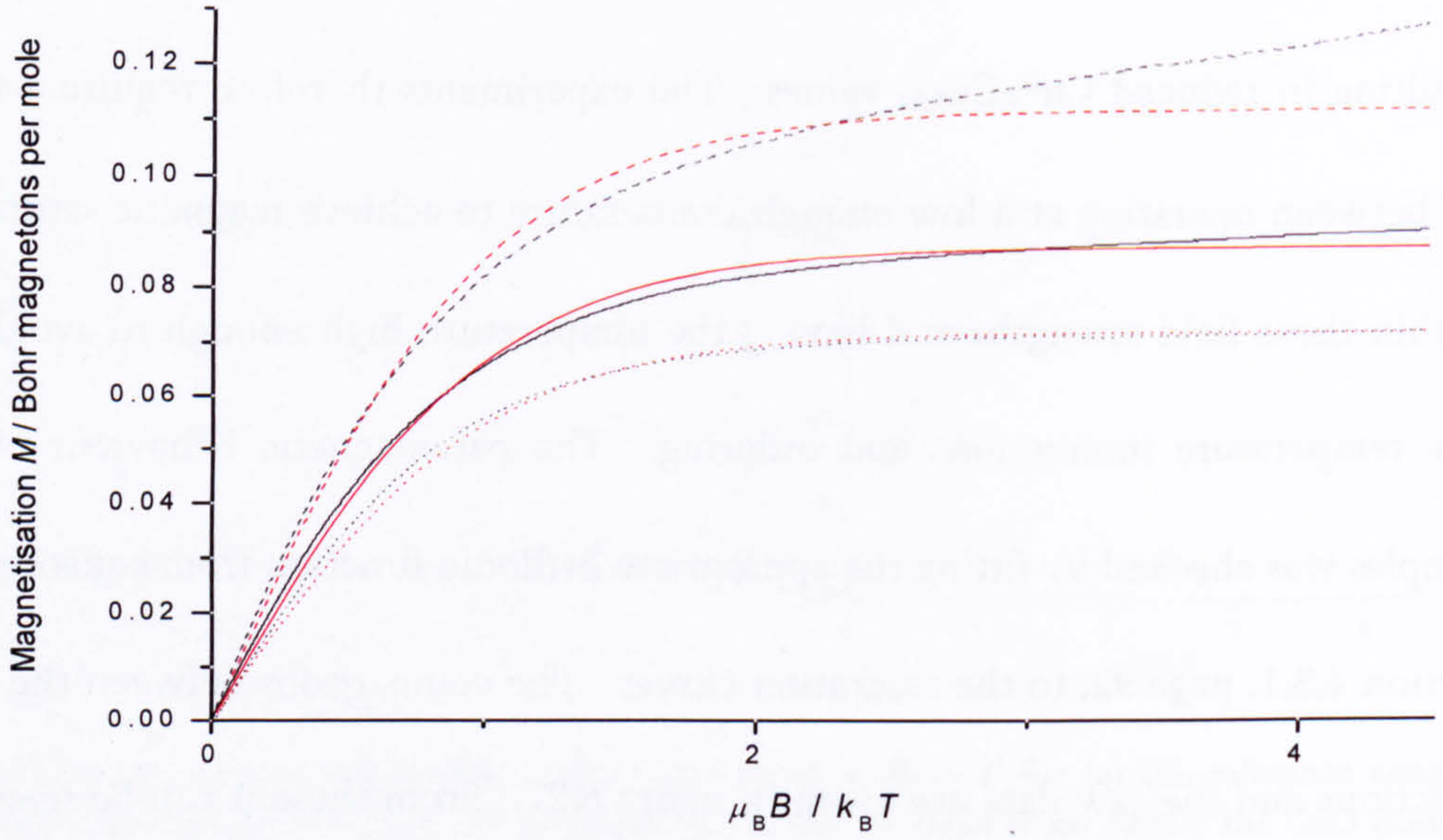

Figure 6.27: The sample magnetisation measured as a function of $\mu_B B / k_B T$ for the CuO (solid), $CuO_{0.5}$ (dotted) and Cu_2O (dashed) 10 % doped samples from figure 6.26, compared to the simulated Brillouin functions (in red) for each sample.

Despite the continuing difficulties in quantification both the EPR and magnetic susceptibility measurements have confirmed the dominating presence of Cu^{2+} ions within the samples and showed that the starting compositions for the copper compounds does not significantly alter the copper valence state once it has been incorporated into the glass itself. The implications of this are that the doping of CuO and $CuO_{0.5}$ results in the same molar concentration of copper as well as the same copper redox state. Different copper oxides in place of Na_2O creates a substitution mostly of Na^+ by Cu^{2+} ions which have twice the charge of Na^+ ions and in the case of Cu_2O doping undergo a direct one-to-one substitution but in the case of CuO and $CuO_{0.5}$ doping two Na^+ ions are replaced by only one Cu^{2+} ion giving a system containing the same charge balancing but half the number of modifying

cations. This suggests that replacement of Na_2O with CuO and $CuO_{0.5}$ doping would have no additional effect on the phosphate network as outlined in section 1.2, whereas Cu_2O doping would in theory depolymerise the network further, reducing the network connectivity since the cations can charge balance more non-bridging oxygen atoms. However any different influences on the phosphate network from these dopants are not observable from the ^{31}P NMR since the loss in signal from paramagnetism results in ambiguous data.

6.2.7 Phosphate coordination, Q^3 speciation and the possibility of network forming

Although it appears likely that the Cu^{2+} within the samples removes the NMR signal for some phosphate tetrahedra, leaving only the remaining unaffected phosphate units only to provide the reduced ^{31}P NMR signal, this still leaves the question of where this Q^3 peak arises from. The information from the ^{63}Cu NMR, EPR and magnetic susceptibility measurements show that the majority (if not all) of the copper within the samples is in the form of Cu^{2+} and as no paramagnetic NMR shift is observed with changing temperature this strongly suggests that the peaks observed in the spectra are in fact most likely due to the presence of different Q species. The fact that more than two Q species are present in some of the samples suggests that these glasses are not as closely determined by the binary model as originally presumed.

We know that these samples contain 45 mol. % of P_2O_5 and that the binary model for this composition would have 78 % of Q^2 and 22 % of Q^1. This translates to 56 % of the oxygen being non-bridging and 44 % being bridging. If a glass of this composition was instead described by a random distribution, the Q^n species present would be 17 % Q^0, 41 % Q^1, 33 % Q^2 and 9 % Q^3 speciation, this therefore shows that the values obtained for these samples, although not an entirely true depiction of the system, do suggest that the glass can still be described more successfully by the binary model than the random model. Part of the discrepancy between the results obtained and the binary model prediction of the Q speciation arises from the occurrence of the process of disproportionation ($2Q^2 \leftrightarrow Q^3 + Q^1$). However, this does not account for the entire discrepancy as if this were the only other process occurring the amount of Q^3 speciation observed would not be as high, implying that some other process is taking place to account for this.

It is observed that as copper is added to the system, the number of oxygen atoms that form bridges between the other atoms in the structure increases leading to an increase in Q^3 phosphate units. The existence of Q^3 species within the samples show that there are higher numbers of bridging oxygen atoms than expected. Furthermore, there is not a high enough percentage of phosphorus atoms in the sample to account for the number of oxygen bridges, thus the effect of some copper could be to become incorporated into the network structure through covalent bonding between the phosphate tetrahedra in addition to, or rather than sitting in

the ionically bonded, charge favourable sites in the glass as first thought. This is referred to as network forming, the possibility of which has also been previously discussed for some ions, such as magnesium and zinc [27], as these may have the ability to sit both within the glass network in place of the phosphorus atoms and next to the oxygen atoms charge balancing them, without becoming part of the actual network. Ions which have this ability to act as both a network modifier and a network former are known as intermediates, as briefly discussed in chapter 2, and these various possible incorporation mechanisms are outlined in figure 6.28. The possibility of network forming in these samples however, assumes that this type of copper incorporation would not lead to complete loss of signal from any paramagnetism or a paramagnetic chemical shift. The occurrence of bridging oxygen atoms in some cases covalently bonding to network forming copper atoms has been suggested by Shih et al. [5]. In their work implementing ^{31}P MAS NMR on CuO doped sodium meta- and polyphosphate glasses they describe the depolymerising effects of the copper ions as they systematically replace the Na_2O up to a doping level of 40 to 50 %. This has also been described by Metwalli et al. [28] using optical studies where this depolymerisation results in reduced Q^2 and increased Q^1 phosphate species. This describes only the network modifying behaviour of copper but in addition to this depolymerising effect, Shih et al. [5] also identified an additional spectral peak in the ^{31}P NMR spectrum which they have assigned as Q^2 species covalently linked to one copper atom, creating a chemical shift due to its effect upon the phosphate tetrahedron's environment i.e. P-O-Cu

linkage which they have compared to the network forming, covalent bonds between aluminium ions in phosphate glass networks, P-O-Al, such as those described by Karabulut et al. [29]. Shih et al. [5] found that although the presence of this peak describes some potential network forming behaviour of the copper ions more prominent in the polyphosphate glasses than the metaphosphates, their dominant effect is still of a network modifying nature. In order to confirm their suspicions of this network forming role for copper they compare this work to their previous studies [30] using XPS to identify P-O-Cu linkage, however although these results do confirm the presence of copper sitting adjacent to some of the terminal oxygen atoms in the glass, the exact nature of the bonding cannot be successfully determined and other studies such as that by Metwalli et al. [28] suggest that copper ions in phosphate glasses reside in octahedral charge balancing sites as expected of modifying cations. It should also be noted that the low field (4.7 T), slow MAS spin rate (3 to 4 kHz) and generally poor NMR spectral resolution obtained in the studies by Shih et al. [5] lead to concerns over the reliability of their peak assignment and the dominance of spinning sidebands upon the NMR spectra make their analysis highly questionable. However, if at all possible, the incorporation of copper atoms in this network forming way could either provide enough network forming ions to increase the phosphate coordination leading to the Q^3 speciation observed in the NMR spectra, or its incorporation could cause a chemical shift in the peak position for the Q^n species as the copper-containing phosphate units will be chemically different than if all of the atoms were phosphorus or oxygen atoms. However, it is

not known quantitatively to what extent this would shift the peaks but this could account for the Q^3 peak observed as it may be a Q^2 peak that has been shifted due to copper covalent bonding which changes their chemical environment similar to the effects suggested by Shih et al. [5]. It is however, unlikely that this shift would be great enough to appear as the signal arising from a different phosphate tetrahedral coordination.

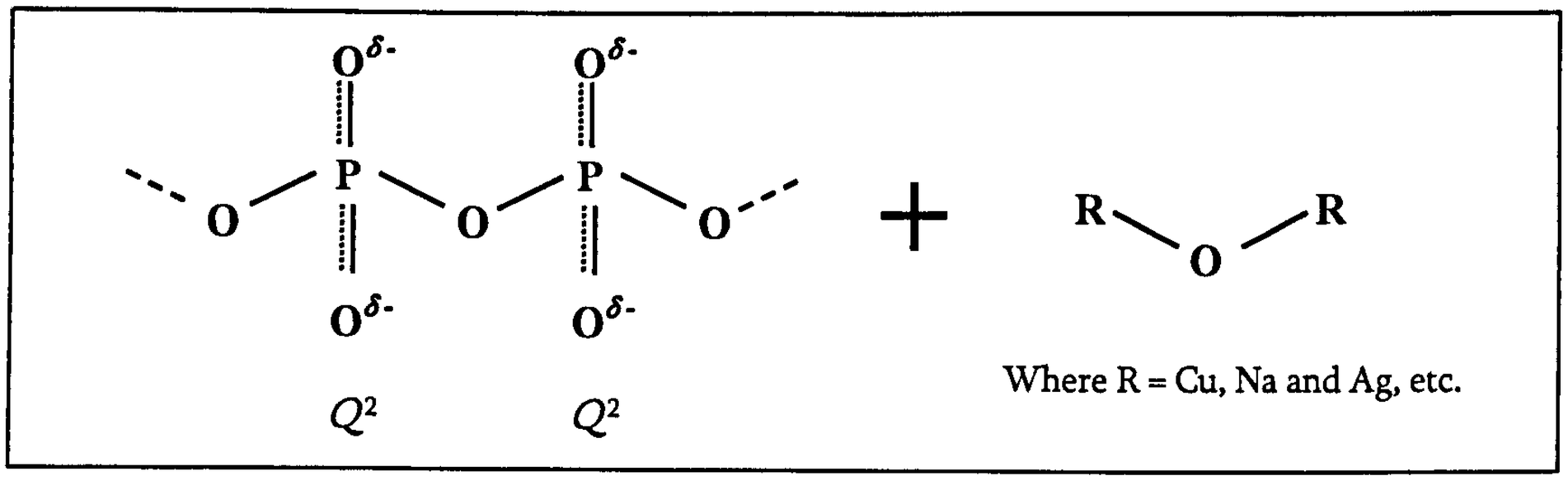

Figure 6.28: The three cation incorporation mechanisms observed.

[i] For the case of the modifying oxide being RO e.g. CuO or CaO:

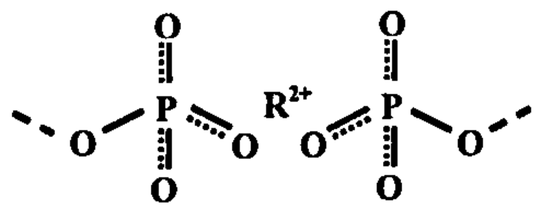

Although both the EPR and spectrophotometry measurements suggest that the Cu^{2+} ions present are octahedrally coordinated and not tetrahedrally coordinated within the phosphate network itself, further experiments were performed for verification due to the claim for network forming copper in the literature [5]. To gain more information on the phosphate coordination and bonding connectivities involved within the sample and to attempt to discover any evidence for this potential P-O-Cu network forming, optical absorption studies were completed in the form of FTIR and Raman spectroscopy. FTIR experiments can give an indication of the subtle changes in phosphate coordination and environment regarding phosphorus chain and P-O bond characteristics not possible from techniques such as NMR. As IR spectroscopy is a linear process in which a photon is absorbed and directly gives rise to a phonon (lattice vibration) one can proportionally relate the change in absorption coefficient of an FTIR spectral line with the number of vibrational modes giving rise to it. The limitation is that a quantitative comparison cannot be made between the intensities of neighbouring absorption peaks in the same spectrum as the relative strengths of the absorption coefficients are not the same for each type of vibration. Thus, twice the intensity of one type of absorption band compared to another, does not imply twice the number of vibrational modes.

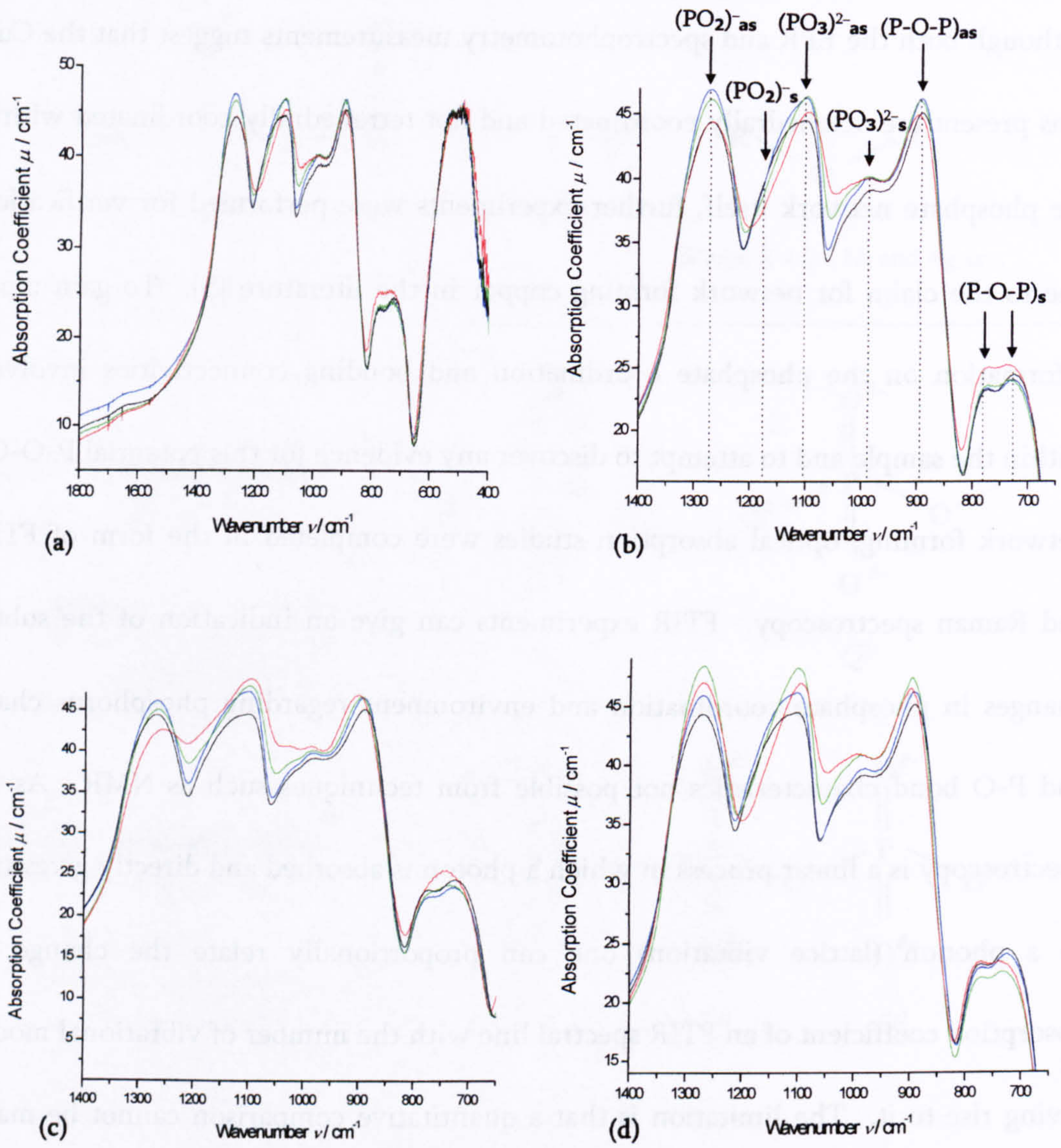

Figure 6.29: The IR absorption spectra of the (a) and (b) CuO doped samples at different scales, (c) the Cu_2O doped samples and (d) the $CuO_{0.5}$ doped samples, where the 0, 1, 5 and 10 % doping concentrations are represented as black, blue, green and red lines, respectively.

The results from the FTIR experiments have been displayed in figure 6.29. As phosphate based glasses have been widely studied in recent years it was possible to identify the various absorption bands present via comparisons with accepted values from previous data [31-36]. The absorption band positions were measured by locating the peak values of each mode present in the spectrum, but as the spectra contained a large number of broad overlapping absorption bands due to the glassy

nature of the material it would have been beneficial to employ a computer simulated deconvolution program, however a suitable model would be needed to achieve this. Using previous studies and literature describing the frequency ranges of relevant vibrational modes [31] the absorption bands were deduced and are clearly listed in table 6.11 as well as labelled in figure 5.29 (b). Diagrammatic representations of the vibrational modes responsible for each absorption peak are also depicted in table 6.11.

Cu content	*Infrared absorption band positions / cm^{-1} ± 2 cm^{-1}*						
	$(PO_4)^{3-}$	$(P\text{-}O\text{-}P)_s^1$	$(P\text{-}O\text{-}P)_s^2$	$(P\text{-}O\text{-}P)_{as}$	$(PO_3)^{2-}{}_s$	$(PO_3)^{2-}{}_{as}$	$(PO_2)^{-}{}_{as}$
0	493-534	725	772	891	988	1108	1274
1 mol. % CuO	493-534	726	774	892	989	1100	1271
5 mol. % CuO	493-534	732	773	894	989	1097	1270
10 mol. % CuO	493-534	731	771	897	990	1093	1271
1 mol. % Cu_2O	493-534	725	771	896	989	1100	1271
5 mol. % Cu_2O	493-534	740	740	897	980	1098	1268
10 mol. % Cu_2O	493-534	741	741	901	989	1094	1262
1 mol. % $CuO_{0.5}$	493-534	725	771	895	982	1098	1269
5 mol. % $CuO_{0.5}$	493-534	731	772	895	985	1097	1270
10 mol. % $CuO_{0.5}$	493-534	733	778	899	994	1092	1271

Vibrational modes			
$(PO_4)^{3-}$	$(P\text{-}O\text{-}P)$	$(PO_3)^{2-}$ $P\text{-}O^{-}$	$(PO_2)^{-}$
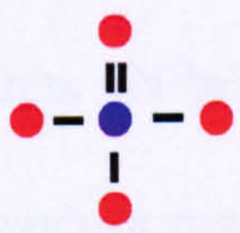	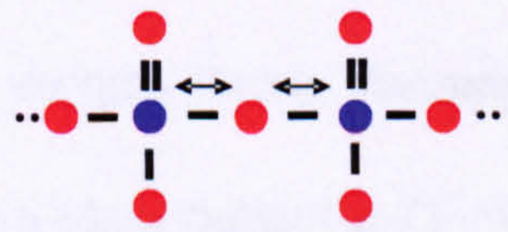	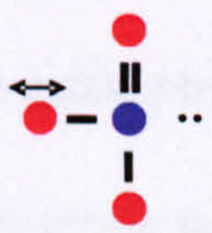	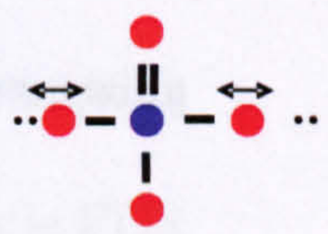
Q^0	$Q^{1/2/3}$	Q^1	Q^2

Table 6.11: IR absorption band positions and descriptions along with a diagrammatic representation of the stretching bond mechanisms giving rise to them.

Each of the spectra obtained have been scaled with sample thickness to give plots of absorption coefficient against wavenumber which is directly proportional to both

the energy and frequency of the vibrational mode. In addition to this scaling for sample thickness, the broad peak observed between 490 and 540 cm^{-1} reported to be the $(PO_4)^{3-}$ Q^0 group deformed (wagging) vibrational mode [5, 32-36] was used to scale the spectra so that each of these peaks matched, as it should remain unaltered throughout the minor changes in composition within this sample set [33 & 34]. Rather than conventional stacked plots, the spectra have been directly overlaid to show plainly the subtle changes occurring with varying doping levels. Note the rather high absorption coefficients of these samples (up to approximately 50 cm^{-1}) characteristic of high Cu^{2+} levels, hence the difficulties arising from performing these experiments on the glass disc samples. It should also be noted at this point that although comparisons here have been made with previous studies involving both glassy and crystalline samples containing higher copper doping percentages which could not be achieved in this investigation without the crystallisation of the copper in the samples, work by Corbridge and Lowe [37 & 38] has shown that there are no observable differences in the FTIR spectra between crystalline and pure glassy phosphate based glasses of this type.

The spectra show a typical phosphate based IR fingerprint, comparable to those observed in numerous other studies on chemically similar glasses [34]. As in previous reports, the vibrational modes arising directly from the phosphate tetrahedra dominate the FTIR spectra with no covalent Cu-O bonding mode visible. This is consistent with other studies such as those by Hogarth and Moridi [34] who

performed experiments on pure crystalline CuO, crystalline P_2O_5 and $(100 - x)\ \%\ P_2O_5 + x\ \%$ CuO (where $0 < x \leq 35$) ultraphosphate crystallised glasses. The FTIR spectrum for the CuO sample in their studies showed one main spectral absorption frequency at 620 cm^{-1} characteristic of the Cu-O stretching mode. However, all of their copper phosphate binary glasses investigated, regardless of the copper-content (up to 35 % CuO), do not exhibit this peak, but are consistent only with the absorption bands found in pure crystalline P_2O_5. Shih et al. [5 & 32] also found no evidence for a Cu-O band developing in the FTIR spectra with even higher CuO doping concentrations up to 50 % which is a result corroborated by other FTIR studies including those by Metwalli et al. [28] and Hogarth and Moridi [34], showing that copper phosphate glass IR spectra appear entirely dominated by their phosphate based glass structural FTIR interpretation unlike other dopants such as lutetium, erbium, and bismuth studied by Ananthamohan et al. [33] and Chahine et al. [35] which contribute resolvable IR active peaks. For this reason, even if copper was entering our phosphate tetrahedral network and covalently bonding with the phosphate units via bridging oxygen atoms that we were unable to confirm using NMR, this may not result in an identifiable Cu-O vibrational mode within the FTIR spectral range observed. However, the FTIR results do still allow deductions to be made regarding the effects of copper-doping on the phosphorus-oxygen bonds already present.

The peaks observed in the FTIR spectra include a peak at ~1270cm^{-1} due to the $(PO_2)_{as}$ asymmetric stretching of the two non-bridging oxygen atoms on the Q^2 phosphate sites [5, 7, 35, 36] (see table 6.11) confirming the clear presence of Q^2 species expected to be the dominant phosphate units in these samples. The symmetric mode of these $(PO_2)_s$ bonds is observed at around 1180 cm^{-1} as reported by Shih et al. [5] and Chahine et al. [35], but is not clearly resolved, so the peak position for this has not been included in the results tables.

The peak at ~1100cm^{-1} has been attributed to the P-O$^-$ asymmetric stretch of the $(PO_3)^{2-}_{as}$ Q^1 chain end groups [5, 33-35] while at 985 ± 2 cm^{-1} the absorption peak relating to the symmetric stretching of these Q^1 end groups is visible [5, 7, 35]. The observation of the $(PO_3)^{2-}$ peaks confirms the existence of Q^1 speciation throughout the entire sample series including the ternary base glass, which supports predictions by the Brow model [4] for this polyphosphate P_2O_5 concentration of 45 % which was also observed in the NMR studies.

The 900 ± 2 cm^{-1} absorption line shows the presence of the $(P\text{-}O\text{-}P)_{as}$ asymmetric stretching mode of the bridging oxygen atoms between the various phosphate units comprising the network [5 & 35]. The equivalent $(P\text{-}O\text{-}P)_s$ symmetric stretch mode gives rise to two peaks at ~725 and ~775 cm^{-1} also observed by Shih et al. [5 & 32], Baia et al. [7], Hogarth and Moridi [34], and Chahine et al. [36]. The composition of these polyphosphate glasses is such that they are dominated by Q^2 tetrahedral units

and thus it can be assumed that these (P-O-P) stretching modes arise from the bridging oxygen atoms between the Q^2 species. However, studies including those by Chahine et al. [35], and Gabelica and Tarte [39] have shown that the (P-O-P) stretching bands for those associated with Q^1 tetrahedra are located in the same frequency range. In the literature reviewed, these (P-O-P) bands could only be assigned to the relevant Q^n species by assuming that they arise from the dominant phosphate units present [35]. The presence of two peaks at different frequencies for the same $(P\text{-}O\text{-}P)_s$ vibrational mode relates to differences in the molecular environments. This could mean that the two peaks arise from the bridging oxygen atoms between two different types of molecular structure for example between:

1) different species i.e. Q^1-Q^1 dimers, Q^1-Q^2 where the Q^1 are the end groups of the Q^2 chains, or between Q^2-Q^2 units in chains.

2) different chain lengths of Q^2 chains, i.e. between phosphate tetrahedral associated with long chains or short chains/rings.

As copper-doping increases, these two $(P\text{-}O\text{-}P)_s$ peaks appear to merge which Chahine et al. [36] also reported for a copper-doping level of ≥ 25 %. Chahine et al. [36] suggested that the two peaks arose from $(P_2O_6)^{2-}$ edge-sharing dimetaphosphate Q^2 ring structures where two phosphate units bridge to each other via two bridging oxygen atoms (i.e. phosphate tetrahedra sharing two corners (known as edge-sharing), so-called cyclo-diphosphate structures), occupying slightly different environments (see figure 6.30). As copper was added, these

dimetaphosphate structures were said to break one of their bridging oxygen atoms producing a Q^1 $(P_2O_7)^{4-}$ dimer giving rise to a single $(P\text{-}O\text{-}P)_s$ peak for higher doping levels [36].

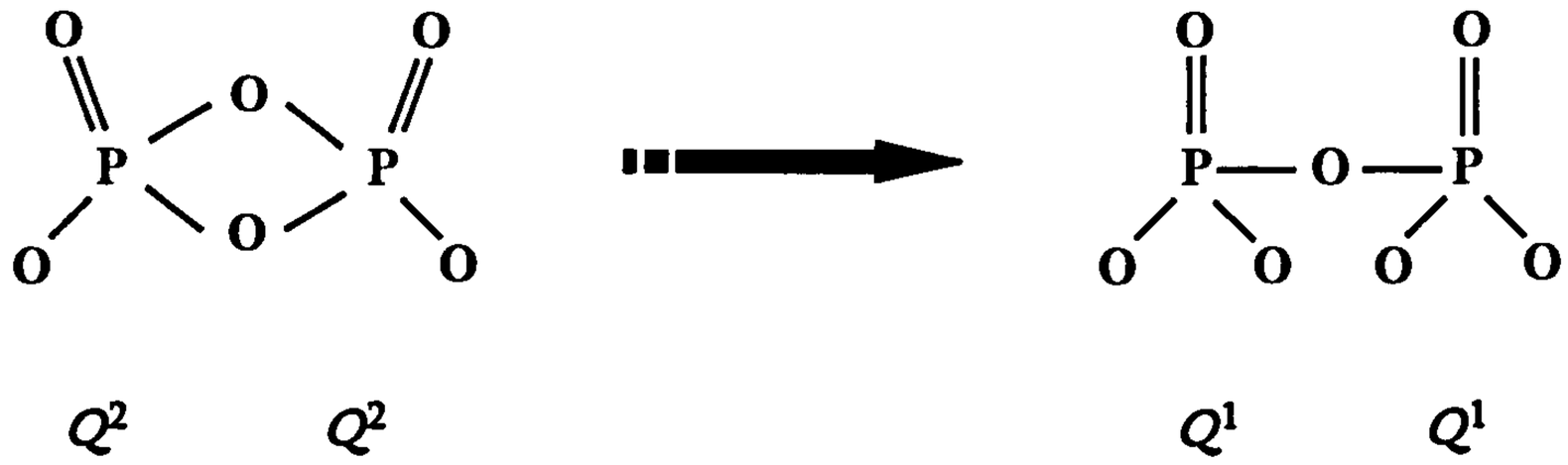

Figure 6.30: Diagrammatic representation of a theoretical edge-sharing dimetaphosphate ring structure converting to a Q^1 $(P_2O_7)^{4-}$ dimer via the breaking of one bridging oxygen atom.

There is not a great deal of information describing this speciation in the literature and no other FTIR studies which have identified two $(P\text{-}O\text{-}P)_s$ peaks have described their occurrence in terms of dimetaphosphate rings so this appears to be an unlikely source of the absorption lines. Van Wazer in 1958 [40] described the lack of evidence of dimetaphosphate existence highlighting some of the Q^2 chain or ring structures that had been incorrectly described as dimetaphosphates at this time including a study by Yost [41]. He did however describe how a compound of this structure could in theory be synthesised and in his paper [42] outlined some other suggested structures. Rashchi and Finch [43] and Lee [44] also describe the $(P_2O_6)^{2-}$ structure and emphasise its lack of verification and the improbability of its occurrence due to the highly strained nature of its edge-sharing (where two phosphate tetrahedra share two oxygen atoms as depicted in figure 6.30) which would also give rise to very different bonding angles to usual Q^2 chains potentially

giving a more shifted expected FTIR absorption line. Most glass synthesis methods also involve temperatures at which reorganisation of structures experiencing considerable strain such as this would occur [40]. In light of this it is believed that the labelling of this structure by Chahine et al. [36] is a misinterpretation, however, it should be noted that if this structure were at all possible then this would give rise to a completely different structure for Q^2 than had originally been considered, which would in turn give rise to very different predicted Q^n speciation percentages, as well as possibly giving rise to a different Q^2 chemical shift value in the NMR spectra. However, it is most likely that the higher frequency (P-O-P)$_s$ absorption line is due to the vibrational mode of short Q^2 chains while the lower frequency ~725 cm^{-1} band arose from longer Q^2 chains as these frequencies are close to those in the literature [7, 32, 34]. Their merger at higher copper-doping levels suggests that the chain lengths possibly become the same. In a purely metaphosphate glass all the Q^2 units should be infinitely long rings $(PO_3)^-_\infty$ and as P_2O_5 is replaced by modifying oxides as in the case of these 45 % P_2O_5 polyphosphate glasses, these infinitely long chains become finite in length and have Q^1 terminating ends. The equation by Van Wazer [40] used to predict the average chain length denoted by the number of phosphate units that it contains, n, depends upon the molar percentages of P_2O_5 and other constituents, where x is the molar fraction of modifier oxide (consisting of CaO, Na_2O and CuO, Cu_2O or $CuO_{0.5}$ for these samples). This gives an average metaphosphate chain length of 9 phosphate units and as the total concentration of modifying oxide does not change in this series of samples, this was

not expected to change unless the copper has additional network modifying or forming effects than those of sodium.

$$n = 2\left(\frac{1-x}{2x-1}\right) \tag{6.3}$$

The absence of absorption peaks at either 1305 cm^{-1} [28 & 34] or 1380 cm^{-1} [28] arising from the P=O double bond in the Q^3 tetrahedra previously observed in studies of ultraphosphate glasses by Metwalli et al. [28] and Hogarth and Moridi [34] suggests an absence of Q^3 speciation in these samples contrary to the NMR results. This may be because the concentration of Q^3 species is not great enough to be prominent in the FTIR spectra as the $1305 \pm 2\ cm^{-1}$ peak could be unresolved beneath the broad $(PO_2)_{as}$ peak at $1270 \pm 2\ cm^{-1}$. The peak observed by Metwalli et al. [28] is not very prominent in their spectra for 50 to 100 % P_2O_5 which should give rise to between 0 and 50 % of Q^3 units and Anathamohan et al. [33] did not observe a Q^3 peak at all with an ultraphosphate sample consisting of 65 % P_2O_5, equivalent to 46 % of Q^3 tetrahedra. It should however be noted that the P=O peak in the study by Hogarth and Moridi [34] is easily identifiable and their samples are closer in composition to ours. This result could raise further doubts as to the Q^3 peak assignment given in the NMR spectra for which the phosphorus content was thought too low unless phase separation of the copper is occurring. If this NMR peak truly arises from Q^3 tetrahedra because of phase separation creating a larger proportion of phosphorus in the remaining glassy network then the remaining bulk glass would need to be the equivalent of an ultraphosphate glass of 54 % P_2O_5 (as

calculated from the 14 % Q^3 intensity observed from the NMR results) which is similar to those samples studied which did give rise to evidence of Q^3 units in FTIR experiments. This again raises the question of what could account for this 'Q^3' NMR peak if it is not in fact due to Q^3 speciation as the possibility of it arising due to Q^2 units shifted by the incorporation of copper into the tetrahedral network has been most likely ruled out by the high temperature experiment performed (see page 184, section 6.2.4). Although unlikely for the reasons discussed above, the effect of the presence of $(P_2O_6)^{2-}$ edge sharing dimetaphosphate ring structures on the NMR spectra are unknown and could lead to a different Q^2 chemical shift in the NMR spectra due to network distortion thus accounting for what has been labelled as the 'Q^3' peak in the NMR results, but this could of course be checked by running ^{31}P MAS NMR experiments on a compound containing this structure to observe the chemical shift values arising. However, it has not been possible to obtain any model samples containing this unit and this again highlights the improbability of this structure occurring in our samples. One could also attempt to implement a computational program to calculate the theoretical chemical shift value.

The FTIR spectra gave rise to clear evidence for Q^0 speciation in the form of a peak between 490 and 540 cm^{-1} suggesting that the Q^1 phosphate units undergo disproportionation $2Q^1 \leftrightarrow Q^2 + Q^0$, producing quantities of Q^0 independent phosphate tetrahedral units which were not observed in the NMR spectra collected. This may be because the quantities of Q^0 are not great enough to be resolved from

the more prominent Q^1 peak, although it has been suggested that NMR is usually more sensitive to the phosphorus speciation within the samples [5 & 34]. In addition to these absorption lines, a number of broad bands were observed at wavenumbers greater than 2000 cm^{-1} and these are most likely to be associated with small amounts of water vapour in the sample chamber.

The changes in absorption spectra that were noted for the spectra of the CuO doped samples (see tables 6.11 and figure 6.29) were similar to those observed for the $CuO_{0.5}$ doped sample series (apart from the unexplained difference in intensity) which is consistent with the changes in phosphate environment having greater dependence upon the copper content of the sample than the oxygen content as these contain the same molar percentage of copper but different quantities of oxygen. Although the intensities of the peaks identified do change, no correlation between intensity and copper concentration was obvious. However the Q^1 peak for samples containing copper is consistently more intense than that in the ternary base glass suggesting that copper is creating more Q^1 species via further depolymerisation of the Q^2 chains as observed by Metwalli et al. [28] although this is contrary to our NMR results. The broad peak between 1060 and 1200 cm^{-1} containing the absorption lines for both the Q^2 $(PO_2)_s$ bond and the $(PO_3)^{2-}{}_{as}$ Q^1 mode becomes less broad as the doping level increases, suggesting that the Q^1 peak is becoming narrower or that the Q^2 shoulder is decreasing. A decrease in this Q^2 peak could suggest a reduction in Q^2 as found in the NMR data which was attributed to the

increase in Q^3. The narrowing of the peaks would suggest that the environment around the molecules responsible for the vibrations at that frequency is becoming more ordered which was unexpected as the ordering of the ^{31}P and ^{23}Na NMR spectra (completed later in section 6.2.9) appears to diminish as demonstrated by the broadening of the NMR peaks present.

The $(PO_3)^{2-}_{as}$ Q^1 peak at 1100 ± 2 cm^{-1} underwent an 8 to 15 ± 2 cm^{-1} decrease in frequency as copper content was increased in all of the samples incorporating CuO and Cu_2O doping. This is shown in figures 6.31 (a), (b) and (c), which have been displaced from their original y-axis values to give a clearer indication of this shift in wavenumber. This reduction in vibrational frequency can be explained in terms of the force constant, k, between the molecules involved as shown in equation 6.4 below, where $\tilde{\nu}$ is the wavenumber, ν is the frequency, c the speed of light, λ the wavelength and m is the reduced mass of the molecules [45].

$$\tilde{\nu} = \nu / c = 1 / \lambda \propto \sqrt{\frac{k}{m}} \tag{6.4}$$

As this $(PO_3)^{2-}_{as}$ vibrational mode involves only phosphorus and oxygen atoms the reduced mass is unaffected and thus the change in frequency must arise from the force constant being influenced by changes in the local environment. If copper enters the glass and directly replaces the sodium ions as charge balancing cations, the field strength of copper ions is greater than that of sodium and thus its interaction via ionic bonding with the non-bridging, terminating oxygen atoms on

these Q^1 chain end phosphates would be greater, hence lengthening and therefore weakening the bond between the oxygen and phosphorus atoms leading to a reduction in wavenumber for the absorption line. In previous studies a copper-doping level of 10 % produced a shift of ~10 cm^{-1} [5 & 34] for this Q^1 peak and in our 10 % doped samples a shift of between 8 and 15 ± 2 cm^{-1} was observed in general agreement with this.

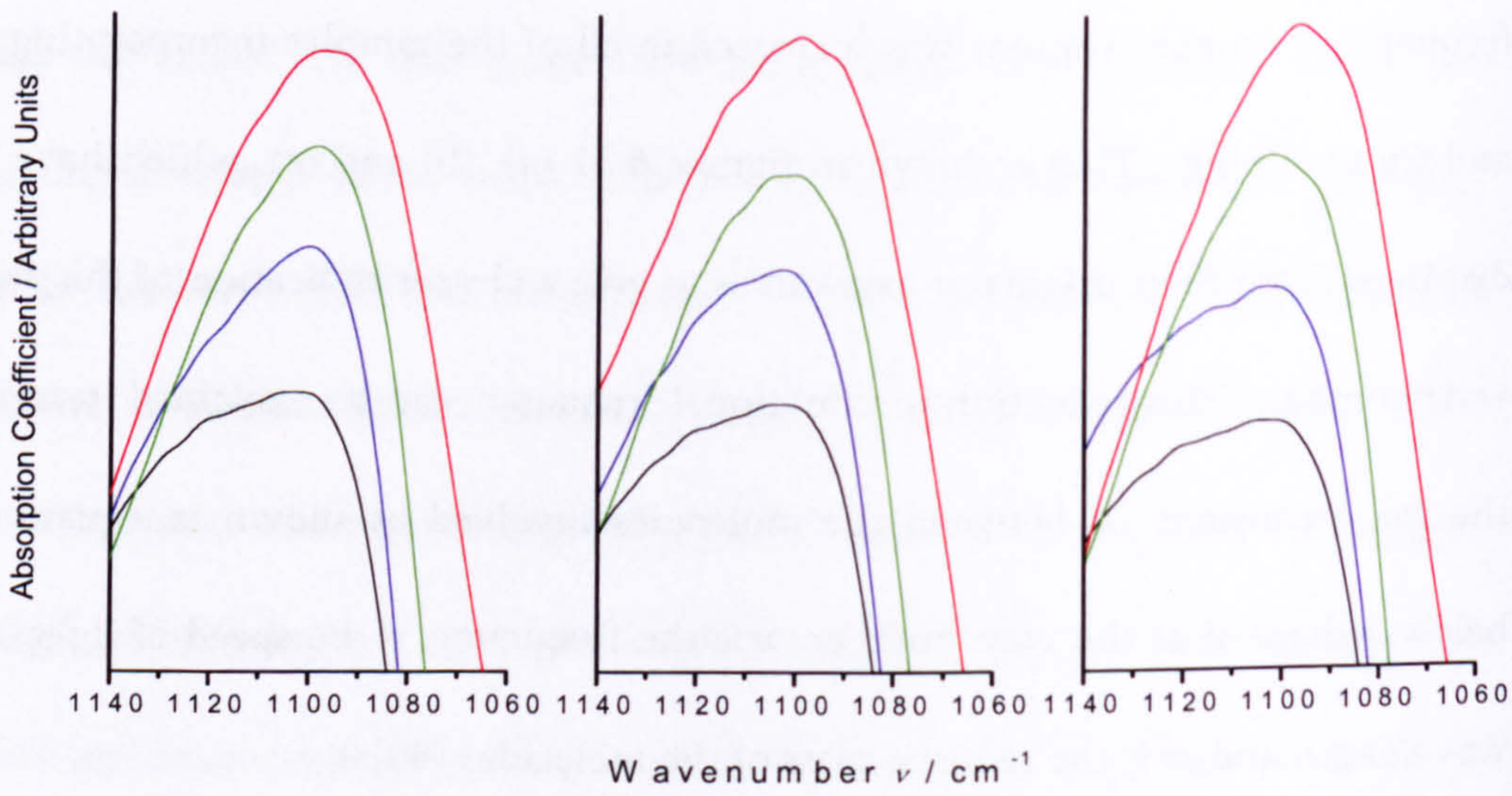

Figure 6.31: The decrease in frequency of the $(PO_3)^{2-}{}_{as}$ Q^1 FTIR absorption peak as copper content was increased in the (a) CuO, (b) Cu_2O and (c) $CuO_{0.5}$ doped samples. The black lines show the FTIR spectrum from the base glass whereas the blue, green and red lines display the spectra for the 1 %, 5 % and 10 % doped samples, respectively. These figures have been displaced from their original y-axis values to give a clearer indication of this shift in wavenumber.

The $(P\text{-}O\text{-}P)_{as}$ band in all of the sample sets moves to higher frequencies as copper is added to the samples which suggests the shortening of phosphate chains and/or a smaller (P-O-P) bond angle [5, 30, 35] due to an increase in the covalent character of the (P-O-P) bonds indicating that the bonds are strengthened as copper is

introduced. This is consistent with the general increase in durability and reduction in dissolution and degradation often achieved in such samples with the addition of metal oxides [30, 32, 46, 47]. We observed a 6 to 10 ± 2 cm^{-1} shift with the greatest shift detected for the Cu_2O doped samples. The same shift in frequency is achieved for 5 % Cu_2O doped sample as the 10% CuO doped sample supporting the predicted dependence of the P-O bonds on the copper molar content. This is also consistent with previous experiments suggesting that the copper-doping in the form of Cu_2O and in CuO has the same redox state within the samples, as the greater field strength of Cu^{2+} would have a greater effect on the bonding angles and lengths than Cu^{+} ions [32 & 48]. Having said this, the overall effect of the Cu_2O doping on the IR spectra does appear to be slightly different than either the $CuO_{0.5}$ or CuO doped samples as is highlighted in the plot of the 10 % $CuO_{0.5}$ and CuO doped samples' spectra compared with the 5 % Cu_2O doped sample as these all contain the same molar percentage of copper (figure 6.32). In the Cu_2O doped samples, the absorption line at 1270 ± 2 cm^{-1} for the (PO_2) Q^2 peak, shifts to lower wavenumbers by 8 ± 2 cm^{-1} for 10 % doping, whereas for the other series of samples there is no significant, discernable change in peak position recognised within the accuracy of the reading. This shift was also observed by Shih et al. [5] in studies on copper-doped calcium phosphates who associated this decrease in the (PO_2) wavenumber with the presence of copper ions charge balancing the two non-bridging oxygen atoms involved in this vibrational mode, as in the case for the shift obtained for the Q^1 non-bridging oxygen atoms. The force constant between the terminal oxygen atoms and the

copper increases as the ionic bonding of copper is stronger than that of sodium and this again alters the bonding between the oxygen and phosphorus atoms.

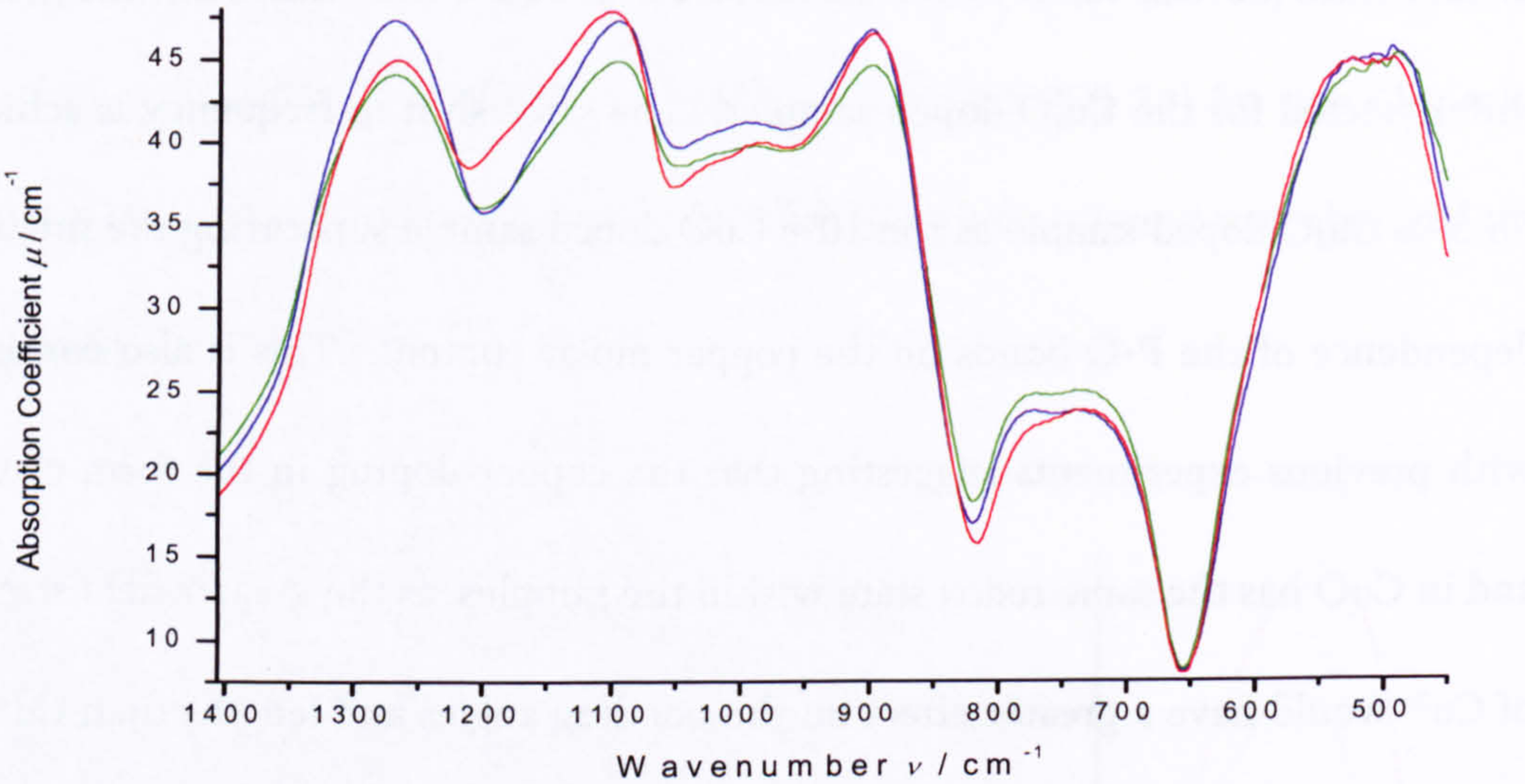

Figure 6.32: A comparison of the FTIR spectra from the 10 % CuO (green) and $CuO_{0.5}$ (blue) doped samples with that of the 5 % Cu_2O doped sample (red) as these all contain the same molar percentage of copper doping.

In the Cu_2O doped samples, unlike the others, the $(PO_2)_s$ Q^2 and $(PO_3)^{2-}{}_{as}$ Q^1 peaks between 1060 and 1200 cm^{-1} become more broad, implying a possible increase in intensity of the Q^2 shoulder or a broadening of one or both of the peaks. The broadening of peaks would indicate disordering or increase in chemical inhomogeniety in the environment surrounding the molecules involved due to the increasing numbers of ionically charge balancing cross-linking copper ions surrounding the terminal oxygen atoms, consistent with that suggested by the NMR.

There has not been any solid evidence for P-O-Cu covalent linkages from the FTIR studies previously performed on copper phosphate samples such as those in this

study or those completed by Hogarth and Moridi [34]. Shih et al. [5] suggested that the P-O-Cu stretching mode would be present at ~1100 cm^{-1} but that its presence could be buried under the broad $P\text{-}O^-$ Q^1 peak at the same frequency. If this P-O-Cu bonding mode was giving rise to a vibrational spectral line at this frequency this could possibly explain the increase in signal observed between 1060 and 1200 cm^{-1} in the spectra of the Cu_2O doped phosphate glass series. In the work by Shih et al. [5] they noted that the FTIR $P\text{-}O^-$ peak at 1100 ± 2 cm^{-1} shifted to 1080 ± 2 cm^{-1} when all sodium had been replaced by copper suggesting that the resulting peak position observed is associated with some sort of bonding between the terminating oxygen atoms and copper. Using this information along with earlier X-ray photoelectron spectroscopy (XPS) experiments of the oxygen 1s binding energies [30] showing the appearance of a new peak between that for the $P\text{-}O^-$ and (P-O-P) peaks with increasing copper content, implies that P-O-Cu bonding is occuring. However, there is not enough evidence provided in their reports to show that this XPS peak and shift in IR frequency arise from covalently bonded tetrahedral copper as these effects could arise even if the copper present was purely charge balancing.

The IR spectroscopy on these glasses has been limited due to the complicated spectra characteristic of glass, but has produced some insight into the changes occurring in the structure due to the change in constituents and has confirmed the presence of different Q^n species. Despite the change in copper-doping it has been found here, as

in other literature [32-36], there are very few changes in the frequencies of the vibrational modes observed and those that were noted suggest only that the copper atoms are sitting in ionic charge balancing sites in place of the sodium ions demonstrated by the shift to lower frequency of the vibrational modes involving non-bridging terminating oxygen atoms such as $P\text{-}O^-$ and $(PO_2)_{as}$ which are influenced by the higher electrostatic field strength of the copper ions. There is no hard evidence of the occurrence of any covalent Cu-O or P-O-Cu peak due to network forming or that any further depolymerisation is occurring with the substitution of sodium for copper. The FTIR spectra for phosphate based glasses using copper-dopants remain highly dependent upon the original phosphate network and are not strongly influenced by the modifying copper cations unlike dopants such as lutetium, erbium, and bismuth which have been reported to have a much more prominent effect on the spectra [33 & 35].

The complementary Raman spectra of the copper-doped phosphate glass samples in the frequency range 400-1300 cm^{-1} are shown in figures 6.33 to 6.36. As numerous studies into phosphate based glasses have employed the Raman technique there is a substantial amount of data available with which to compare the spectral line positions such that they can easily be accounted for. The first figure 6.33 displaying the spectra for the ternary base glass and the 10 % Cu_2O doped quaternary glass is clearly labelled with the vibrational modes that give rise to these Raman lines

described in relevant work by Chahine et al. [36], Koo et al. [49], Swenson et al. [50] and Pemberton et al. [51].

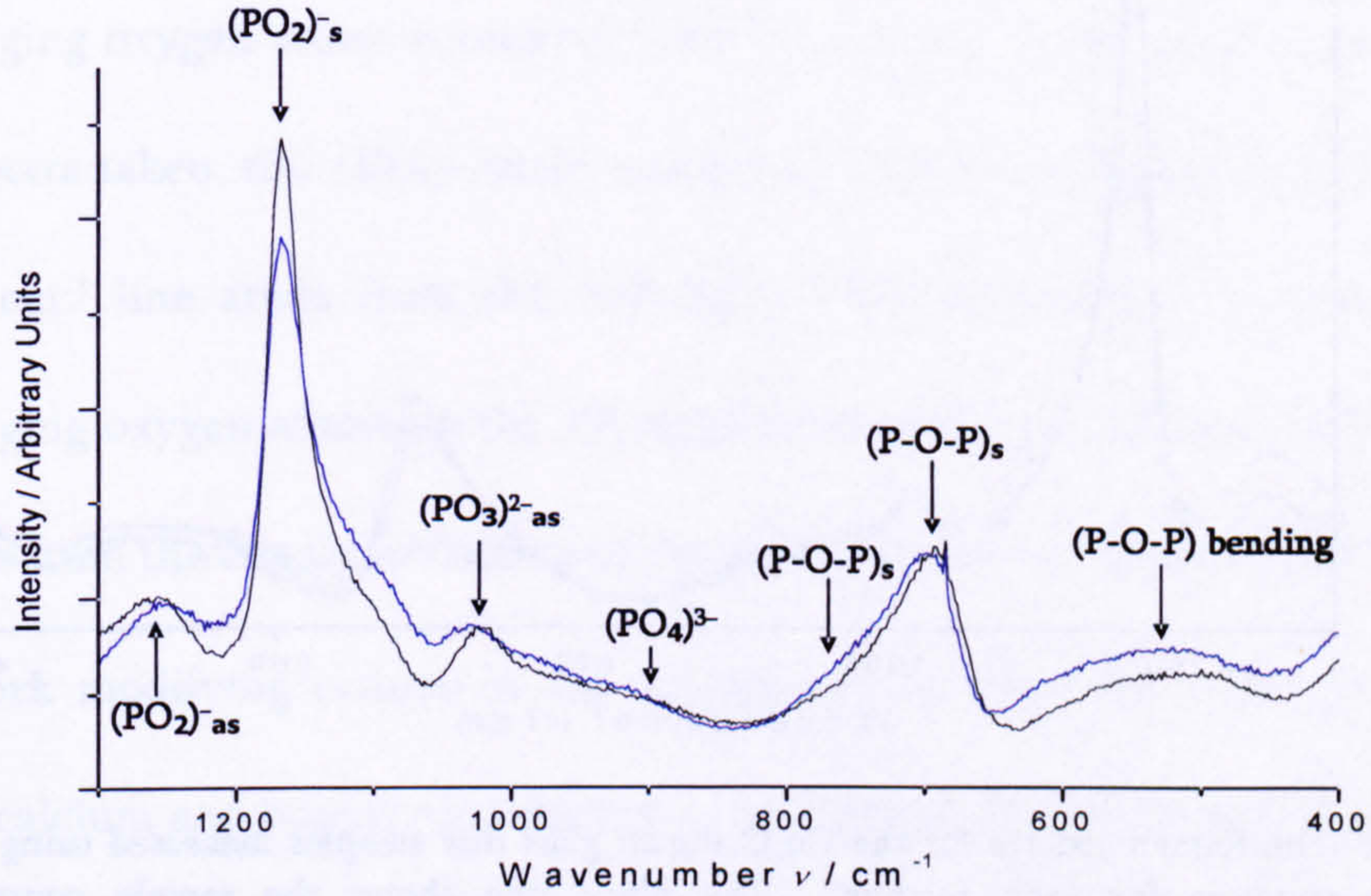

Figure 6.33: The raw Raman spectra and peak associations for the base glass (black) and 10 % Cu_2O doped sample (blue) collected using the same running parameters.

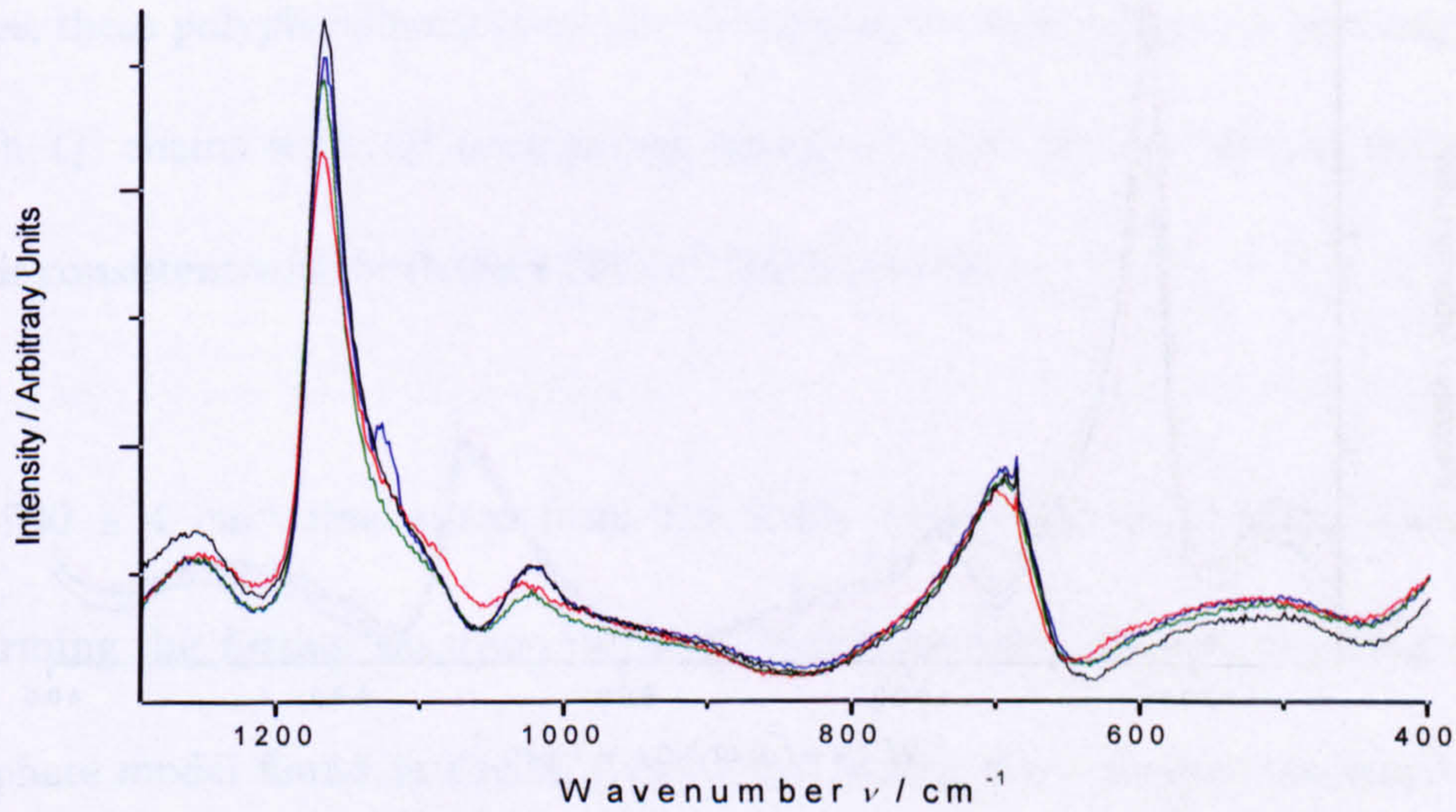

Figure 6.34: The Raman spectra for the CuO doped glass disc samples measured using the same operating parameters for each reading. The black line shows the sample containing no copper-doping while the blue, green and red spectra are those arising from the 1, 5 and 10 % doped samples respectively.

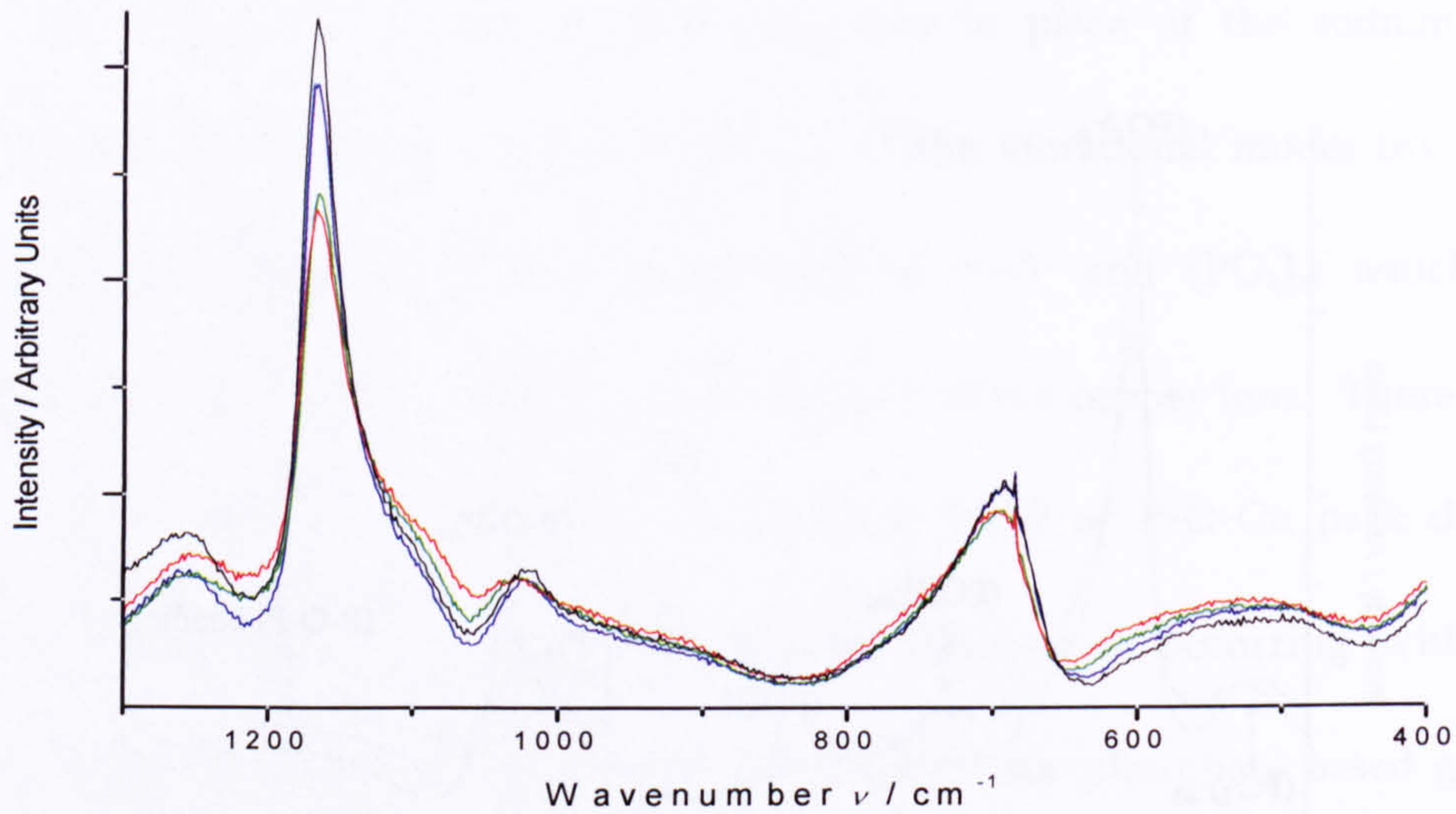

Figure 6.35: The Raman spectra for the Cu_2O doped glass disc samples measured using the same operating parameters for each reading. The black line shows the sample containing no copper-doping while the blue, green and red spectra are those arising from the 1, 5 and 10 % doped samples respectively.

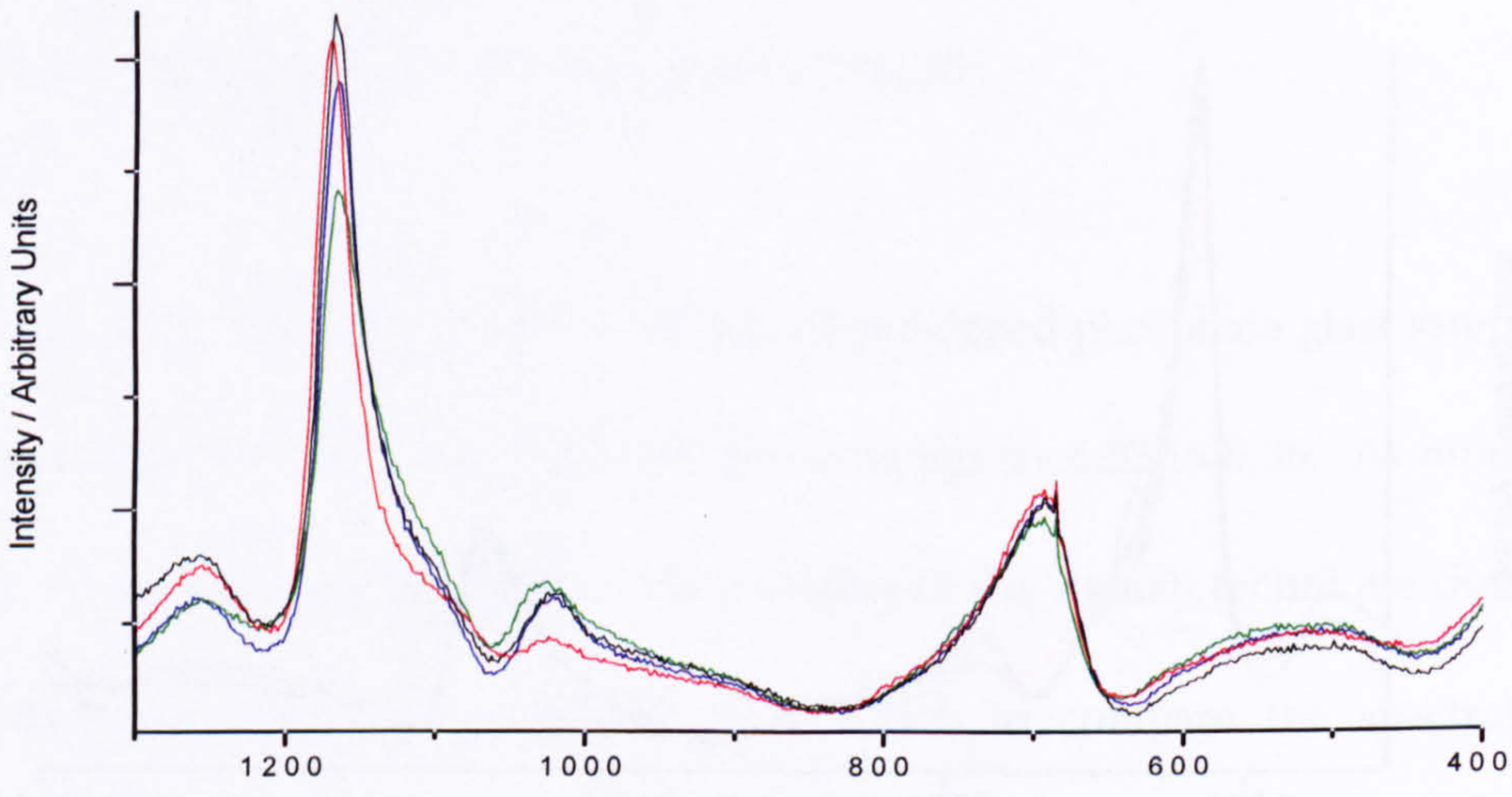

Figure 6.36: The Raman spectra for the $CuO_{0.5}$ doped glass disc samples measured using the same operating parameters for each reading. The black line shows the sample containing no copper-doping while the blue, green and red spectra are those arising from the 1, 5 and 10 % doped samples respectively.

The peaks clearly present in the spectra have been identified as the $(PO_2)_{as}$ asymmetric stretching band of the non-bridging oxygen atoms in the Q^2 tetrahedra at ~1256 cm^{-1}, whilst that of the $(PO_2)_s$ symmetric stretching line of these non-bridging oxygen atoms is observed at 1165 ± 4 cm^{-1}. Although present in the FTIR spectra taken, this $(PO_2)_s$ mode was not as clearly resolved as it is here. The 1020 ± 4 cm^{-1} line arises from the terminal $(PO_3)^{2-}{}_s$ symmetric stretching of the non-bridging oxygen atoms on the Q^1 units terminating the metaphosphate chains and arises from the depolymerisation of the dominant Q^2 species due to the presence of network modifying cations in the polyphosphate structure. The presence of sodium, calcium and copper ions have this depolymerising effect on the phosphate network as this peak is clearly present in all of the spectra showing that unlike the infinitely long Q^2 metaphosphate chains (or rings) expected in metaphosphate glasses, these polyphosphates show the shortening of chain lengths producing finite length Q^2 chains with Q^1 terminating phosphate units at each end of the chain. This is consistent with both the FTIR and NMR results.

The 900 ± 4 cm^{-1} line arises from the from $(PO_4)^{3-}$ Q^0 tetrahedral vibrations, confirming the further disproportionation effects or some random ordering of the phosphate model found in the IR spectra, but which were perhaps too small to be detected in NMR possibly due to the broad and more prominent nature of the other Q^n species present. The peak at 690 ± 4 cm^{-1} has been associated with the (P-O-P)$_s$ symmetric stretching of the bridging oxygen atom between the phosphate

tetrahedra, most likely between the Q^2 species due to its dominance at this composition as shown by the NMR. The spectra also show the possibility of the presence of an additional Raman line at ~795 cm^{-1} within the broad shoulder of the 690 cm^{-1} $(P\text{-}O\text{-}P)_s$ peak which is not intense or resolved enough to validate for certain. Whilst not common in the literature, this peak has been reported by Baia et al. [7] and Hezzat et al. [52] as being an additional $(P\text{-}O\text{-}P)_s$ mode which although not confirmed, may be attributed to the $(P\text{-}O\text{-}P)_s$ stretching of Q^2 chains or rings of much shorter lengths (i.e. consisting of fewer phosphate tetrahedra) [36 & 51]. This is consistent with its higher frequency than the usual $(P\text{-}O\text{-}P)_s$ peak observed at 690 ± 4 cm^{-1}, which is known to be characteristic of shorter chain sizes. This also supports the assignment of the two peaks found for the same mode in the FTIR results. It should be noted however, that Metwalli et al. [28] and Hudgens et al. [53] have reported this Raman shift arising from the asymmetric $(P\text{-}O\text{-}P)_{as}$ stretching mode rather than an additional symmetric stretch. The broad peak at 480 to 570 cm^{-1} has been identified in very few spectra in the literature but suggestions [7 & 52] include that it is due to a P-O-P bending mode, however there is not enough previous evidence to confirm this.

The intensities of each spectrum have not been scaled relative to each other as there is a possibility that all of the peaks present could change with composition leaving no constant peak to scale against. For this reason the spectra have been displayed as collected, using the same running parameters for each measurement. Thus a direct

comparison between changes in intensity cannot be made, however the intensity of the $(PO_2)_s$ Q^2 peak associated with the 1165 cm^{-1} associated Raman shift does appear to decrease in intensity relative to the $(PO_3)^{2-}_{as}$ Q^1 1020 cm^{-1} line, possibly suggesting a reduction of Q^2 speciation which is also observed in the NMR. Unfortunately there is no indication of the consequence of this reduction in Q^2 as the P=O double bond absorption line from the Q^3 species expected at approximately 1380 to 1390 cm^{-1} [28 & 53] is outside of the experimental frequency range used here, so the presence of any Q^3 units cannot be verified.

Unlike other Raman studies involving phosphate glasses with addition of cations [35, 36, 50-53], no shift of the Raman peaks to higher frequencies were found which usually suggests shortening of phosphate chain lengths as depolymerisation occurs. This may be because the copper is network forming and did not lead to further depolymerisation, but instead gave rise to a growth in Q^3 species as observed in the NMR results, although the Q^3 species could not be identified here. However, the sensitivity of the Raman technique to these changes in composition appears not as good as the FTIR technique, perhaps as it is not a linear process as described in section 4.5.

Even though no additional modes to those found in the FTIR studies were found, these experimental measurements did result in further evidence confirming the phosphate speciation present within the samples. The Raman spectra also showed

no evidence of either P-O-Cu or Cu-O bonds, although no other literature reviewed on similar copper-doped phosphate glasses had identified these either.

6.2.8 Thermal analysis and crystallisation of the samples

The powdered glass samples were thermally analysed using the Setaram differential thermal analyser described in section 5.2.2. The DTA traces obtained provided us with the glass transition temperatures, T_g, crystallisation temperatures, T_c, and melting temperatures, T_m, of each sample, given in table 6.12. Having determined T_c, the glass disc samples could then be annealed at the appropriate crystallisation temperatures for two hours to give rise to information regarding any phases becoming present. As discussed in section 5.2.2, an understanding of these effects are important as the heat treatment methods used during prosthesis coating could result in the crystallisation of the glass.

Cu content	T_g / °C ± 4 °C	T_c / °C ± 4 °C		T_m / °C ± 4 °C	
		Peak 1	*Peak 2*[1]	*Peak 1*	*Peak 2*
0	377	512		731	
1 mol. % CuO	387	525		731	
5 mol. % CuO	388	533		707	
10 mol. % CuO	403	579		693	724
1 mol. % Cu_2O	379	497	523	724	
5 mol. % Cu_2O	387	548		703	
10 mol. % Cu_2O	401	581		695	845
1 mol. % $CuO_{0.5}$	405	578		692	730
5 mol. % $CuO_{0.5}$	390	540		708	
10 mol. % $CuO_{0.5}$	403	564		696	731

Table 6.12: DTA measurements for the copper-doped glass samples showing no distinctive correlation between doping and temperature of significant events.

[1] Where some DTA traces show more than one crystallisation or melting event.

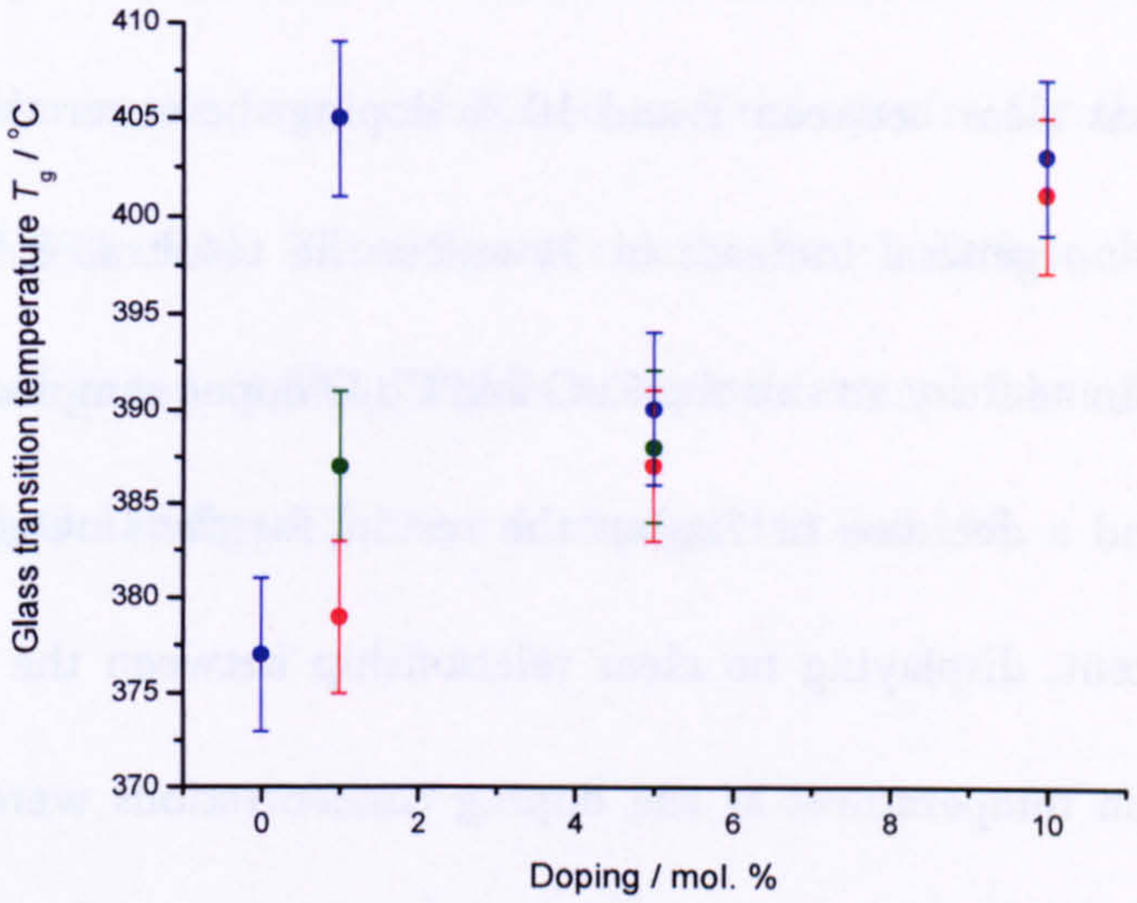

Figure 6.37: The changes in glass transition temperature, T_g, with copper-doping concentration for the CuO (green), Cu_2O (red) and $CuO_{0.5}$ (blue) doped samples.

From previous studies by Chahine et al. [35 & 36], Metwalli et al. [28] and Shih et al. [5], the effect of adding copper in the form of CuO to their phosphate based glass samples was to enhance the chemical durability of the samples, leading to an increase in the glass transition temperature. This was due to copper ions having stronger cross-links between the phosphate chains therefore reinforcing the overall glass structure since they suggest that the copper ions have greater ionic bonds than sodium so the phosphate tetrahedra interact more strongly with the copper. This is consistent with our FTIR data displaying the changes in P-O bonding due to the stronger cross-linking effect of the copper ions as they replace the sodium (section 6.2.7). From the DTA measurements which give an indication of T_g which is loosely related to sample durability (see figure 6.37), our CuO doped samples showed an increase in the glass transition temperature (with a change of 16 ± 4 °C between 1 and 10 % doping) although the minor increase between 1 and 5 % doping means

that the increase was not a linear one. For the Cu_2O doped samples a 24 ± 4 °C increase in T_g was clear between 1 and 10 % doping, however the $CuO_{0.5}$ doped samples showed no general increase in T_g unless the result at 1 % doping is an anomalous one. In addition to this the CuO and Cu_2O doped samples show a general increase in T_c and a decrease in T_m, but the results for the $CuO_{0.5}$ doped samples remain inconsistent, displaying no clear relationship between the glass transition and crystallisation temperatures as the doping concentrations were increased, see table 6.12 and figure 6.37. An example of the thermal analysis traces for the copper-doped samples is given in figure 6.38. It would be beneficial to complete dissolution experiments and Vickers hardness testing to observe how these properties change with increasing copper-doping as the dissolution is predicted to reduce while the hardness increases [1, 5, 46, 47] and this could perhaps give a clearer indication of the changes in durability with copper content.

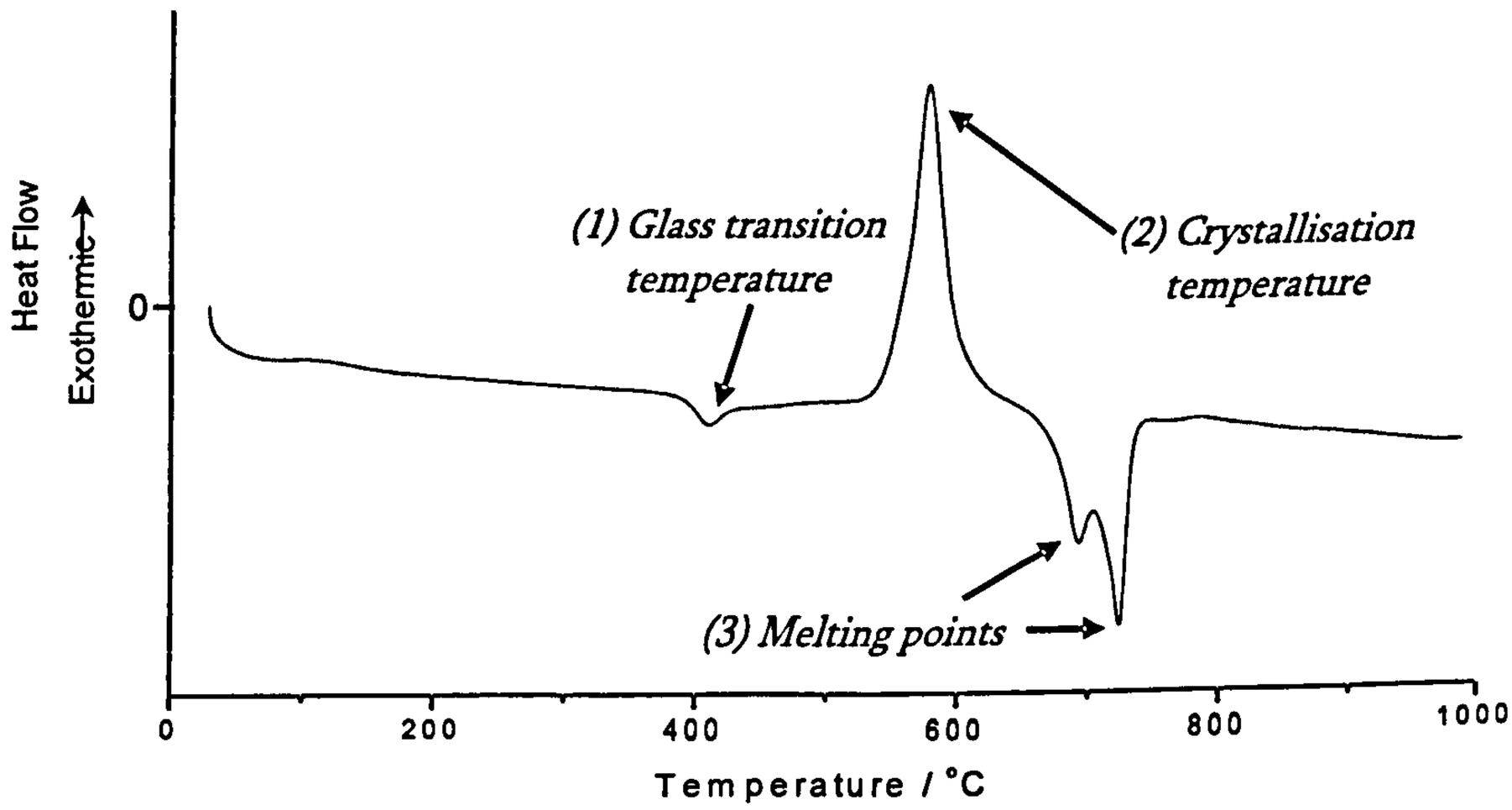

Figure 6.38: DTA for the 10 mol. % CuO doped phosphate glass sample, against a reference sample of alumina.

After heating the samples to their crystallisation temperatures for two hours ^{31}P MAS NMR measurements were conducted and the spectra for these samples are given in figures 6.39 to 6.41. These figures clearly show a distinct change in spectral features when compared to the ^{31}P NMR experiments performed on the purely glassy samples, shown in figure 6.2 to 6.4 on pages 165 and 166.

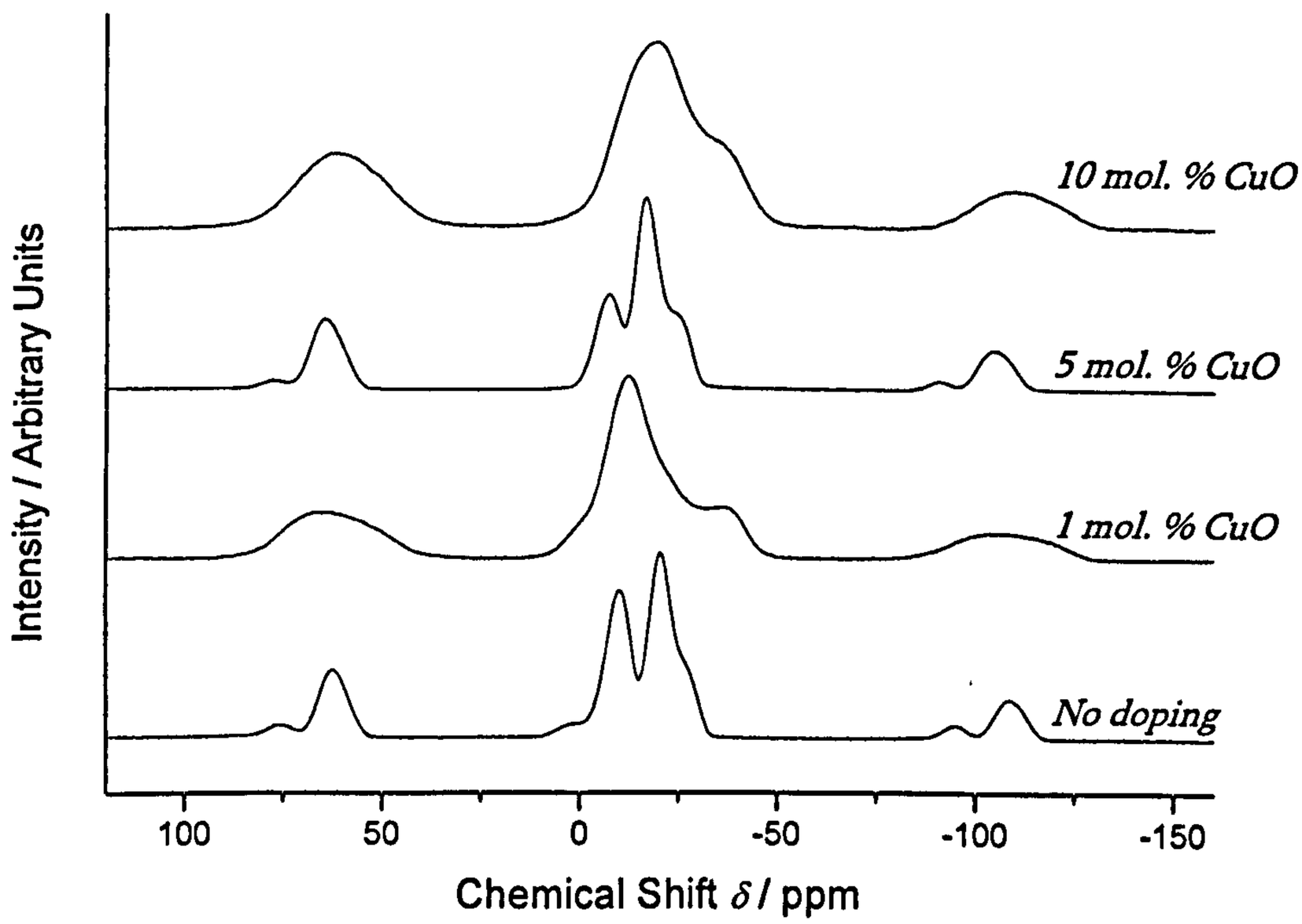

Figure 6.39: The ^{31}P MAS NMR spectra for the partially crystallised CuO doped glasses at a magnetic field of 8.45 T, spinning at ~12 kHz.

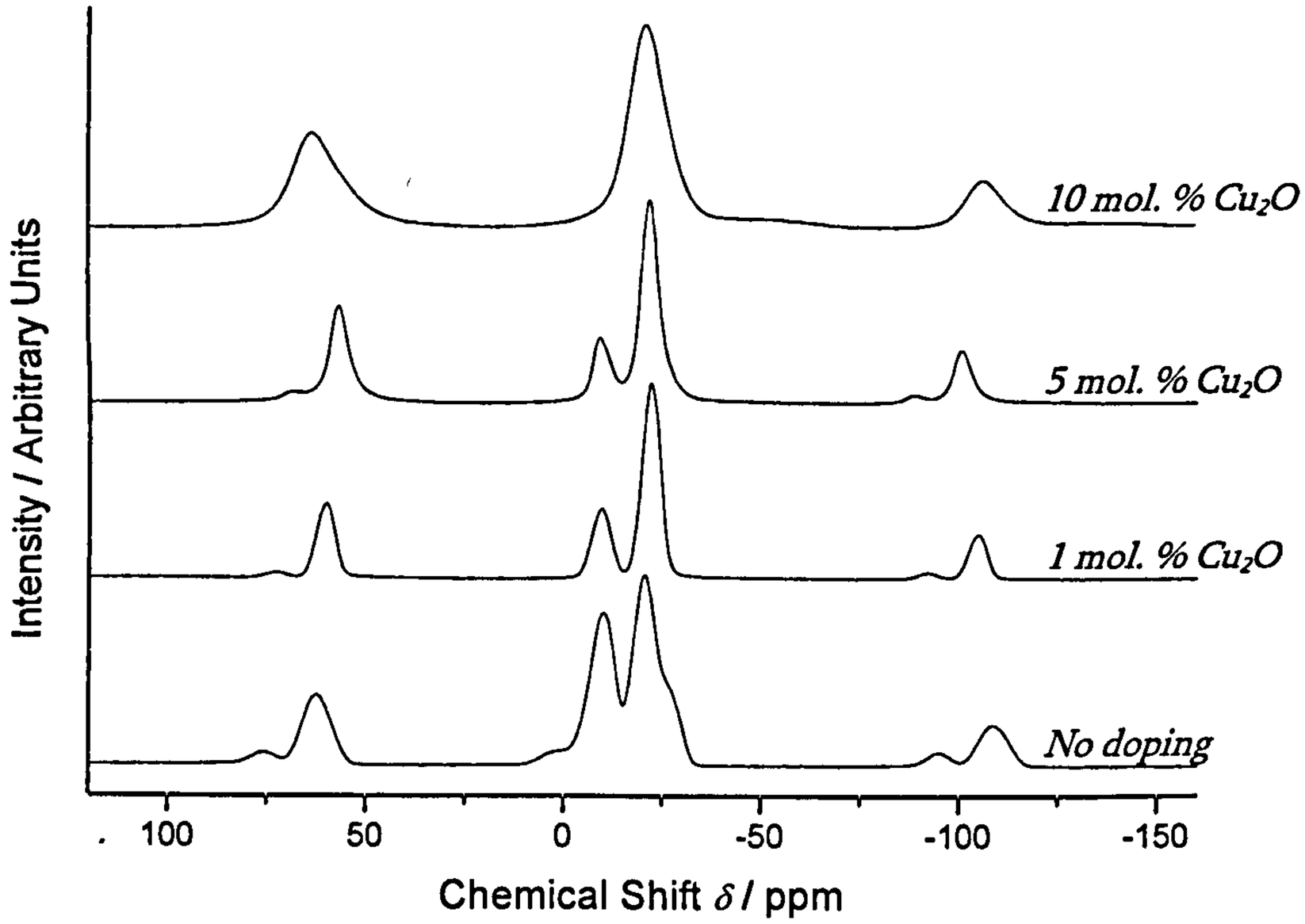

Figure 6.40: The ^{31}P MAS NMR spectra for the partially crystallised Cu_2O doped glasses at a magnetic field of 8.45 T, spinning at ~12 kHz.

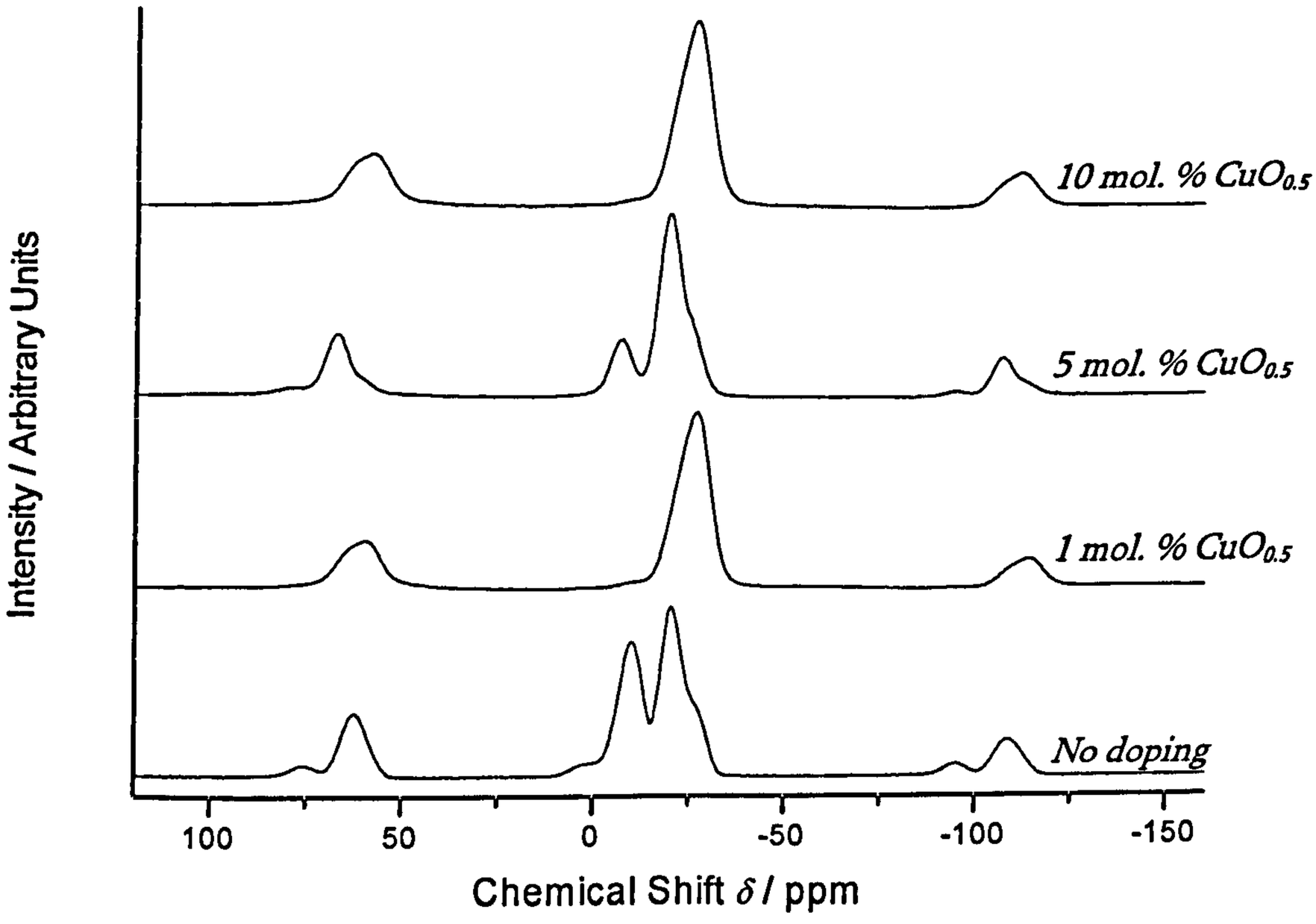

Figure 6.41: The ^{31}P MAS NMR spectra for the partially crystallised $CuO_{0.5}$ doped glasses at a magnetic field of 8.45 T, spinning at ~12 kHz.

Although displaying some increase in ordering expected after crystallisation, characterised by the slight reduction in FWHM specifically apparent from comparing the Cu_2O doped samples, these crystallised samples still demonstrate anisotropic environments, as the peaks clearly present give rise to characteristic spinning sidebands.

The dominant peaks in all of the spectra arise from Q^1 tetrahedral units (between –7 and –10 ppm) and Q^2 units (between –16 and –27 ppm), although the peak positions and intensities do appear to vary significantly between the spectra and show little consistency with the doping concentration which must arise from different phases crystallising out.

A distribution of different environments is clearly visible from the breadth of some of the peaks, for example that of the CuO 10 % doped sample, and is also portrayed by the appearance of some shoulders or smaller peaks adjacent to those that are more prominent. The small shoulder sometimes visible around –36 ppm could be evidence for some Q^3 units also occurring within these crystallised samples although further investigation would be required to confirm this as the crystalline phases have not yet been identified when compared with the data from previous experimentation by Duncan [54] and Brow [55].

6.2.9 ^{23}Na NMR

To add to this study the sodium environments in the glass samples were also investigated to give an indication of the effects of copper substitution. An example of the ^{23}Na NMR spectra collected is given in figure 6.42 so that the improved resolution and chemical shift values at increasing operating field can be observed.

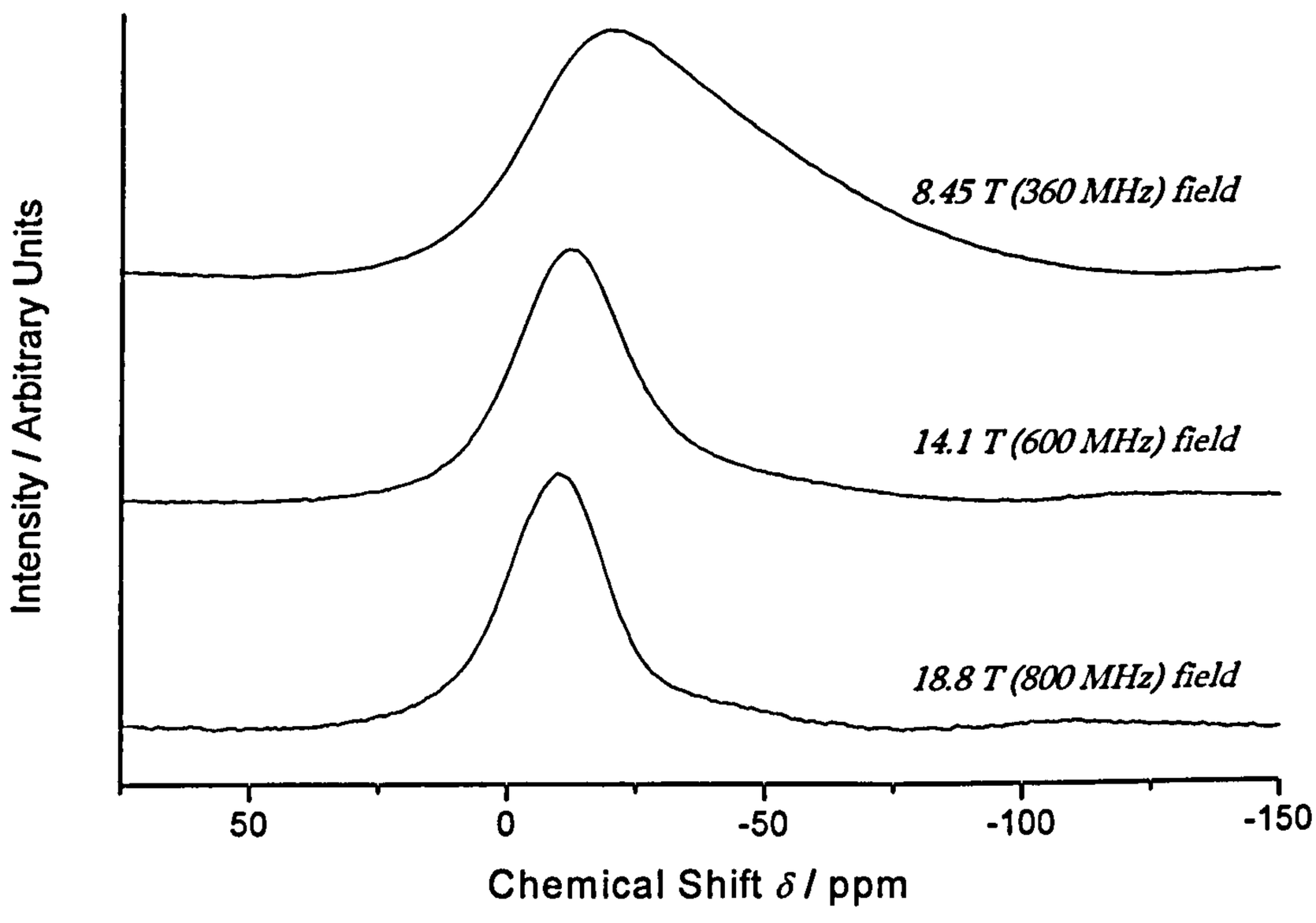

Figure 6.42: The ^{23}Na MAS NMR spectra for the 10 mol. % Cu_2O doped glass sample showing the improved resolution at higher magnetic fields.

Unlike the silver-doped phosphate glass samples, the results for the ^{23}Na NMR experiments shown in table 6.13 and figures 6.43 to 6.45, clearly show a tendency towards a more disordered and distorted state as doping concentrations are increased, although the associated uncertainties in the data fitting are still rather substantial. This implies that the copper atoms disrupt the sodium environments as

they are added to the system. In the observation of the sidebands from the ^{31}P NMR signals (section 6.2.2 and 6.2.5) their relative intensities were not found to change with copper-doping, suggesting no increase in anisotropy of the phosphate environment which might be expected if the copper ions were network forming and covalently bonding to the phosphate tetrahedra via their oxygen atoms. This shows that the copper is more strongly affecting the homogeneity of the sodium environment than that of the phosphorus. These two results in conjunction potentially support suggestions that the copper ions occupy the charge balancing sites similar to the sodium ions, rather than entering the phosphate tetrahedral network, therefore altering the sodium surroundings. Nonetheless the effect upon the sodium ions of copper network forming and entering the tetrahedral phosphate network is uncertain.

The more prominent changes in disorder and distortion observed for the copper-doped samples when compared to the silver-doping in section 5.2.3, pages 146 to 149, may arise from the differences between Cu^{2+} and Ag^{+} ions when compared to Na^{+}. The larger charge on the Cu^{2+} ions may affect the sodium environment more strongly than replacement by Ag^{+}, and due to differences in ionic size for example, these ions could also occupy different charge balancing sites outside of the phosphate tetrahedra which change the extent of their effects upon the sodium ions, especially as the EPR results have shown evidence for two separate Cu^{2+} sites. The presence of two copper sites could also give rise to more disorder of

the sodium surroundings and may explain the disordering as higher doping concentrations are used. Cu^{2+} paramagnetism could also affect the ^{23}Na NMR signals but as multiple fields have been used to constrain the fitting parameters and the quadrupolar distributions have successfully been determined by manipulating their field dependence, any significant paramagnetic broadening effects can be ruled out. No significant differences between the ^{23}Na results for the range of copper-doped samples have been identified as figures 6.43 to 6.45 each display a similar relationship with increasing doping concentration which was slightly unexpected as the Cu_2O doped samples contribute a higher molar percentage of Cu^{2+} ions to the system.

Cu content	δ_{iso} / *ppm* ± *2 ppm*	χ_Q / *MHz* ± *0.3 MHz*	$\Delta\chi_Q$ / *MHz* ± *0.2 MHz*
0	–7	2.4	2.2
1 mol. % CuO	–6	2.4	2.1
5 mol. % CuO	–6	2.7	2.4
10 mol. % CuO	–6	3.0	2.9
1 mol. % Cu_2O	–6	2.6	2.0
5 mol. % Cu_2O	–7	2.4	2.1
10 mol. % Cu_2O	–4	3.2	2.4
1 mol. % $CuO_{0.5}$	–7	2.5	2.1
5 mol. % $CuO_{0.5}$	–7	2.6	2.4
10 mol. % $CuO_{0.5}$	–5	3.0	2.6

Table 6.13: ^{23}Na NMR data obtained for the copper-doped phosphate glass samples.

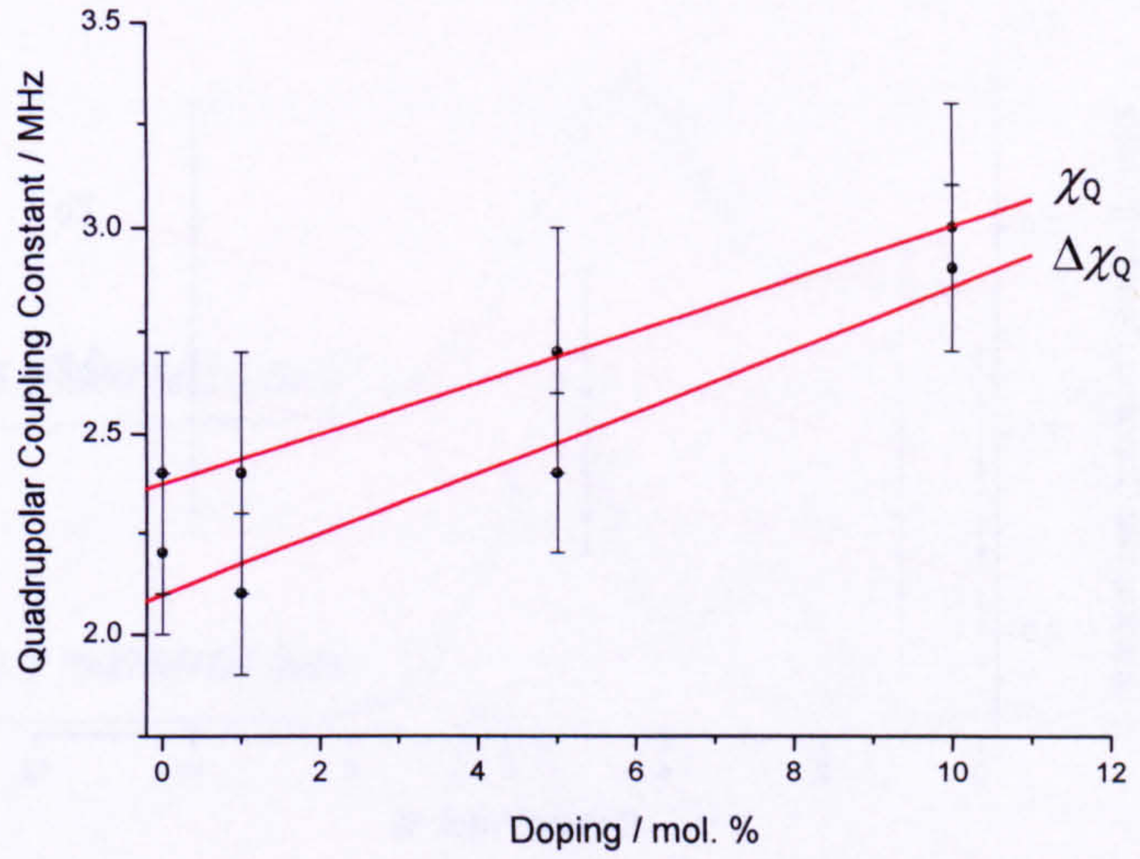

Figure 6.43: The ^{23}Na NMR quadrupolar coupling constant and quadrupolar distribution as a function of doping concentration for the CuO doped glass samples, including lines of best fit.

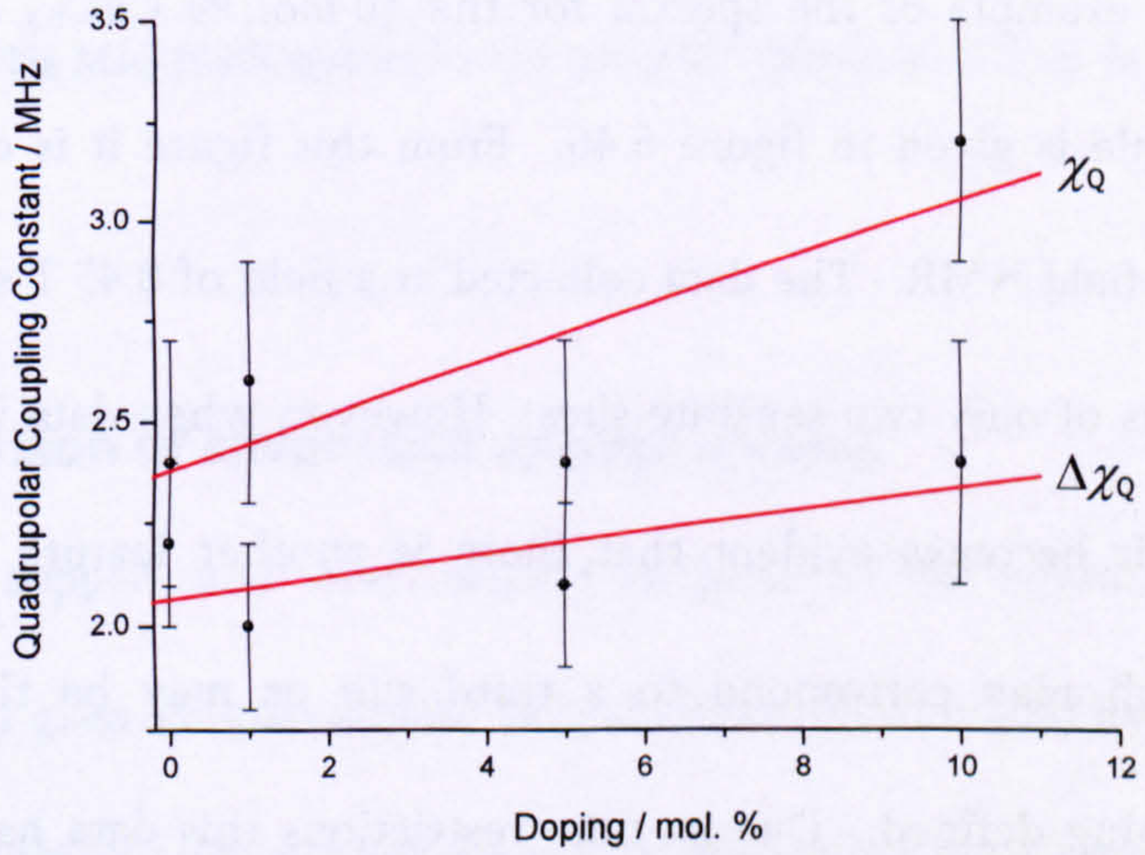

Figure 6.44: The ^{23}Na NMR quadrupolar coupling constant and quadrupolar distribution as a function of doping concentration for the Cu_2O doped glass samples.

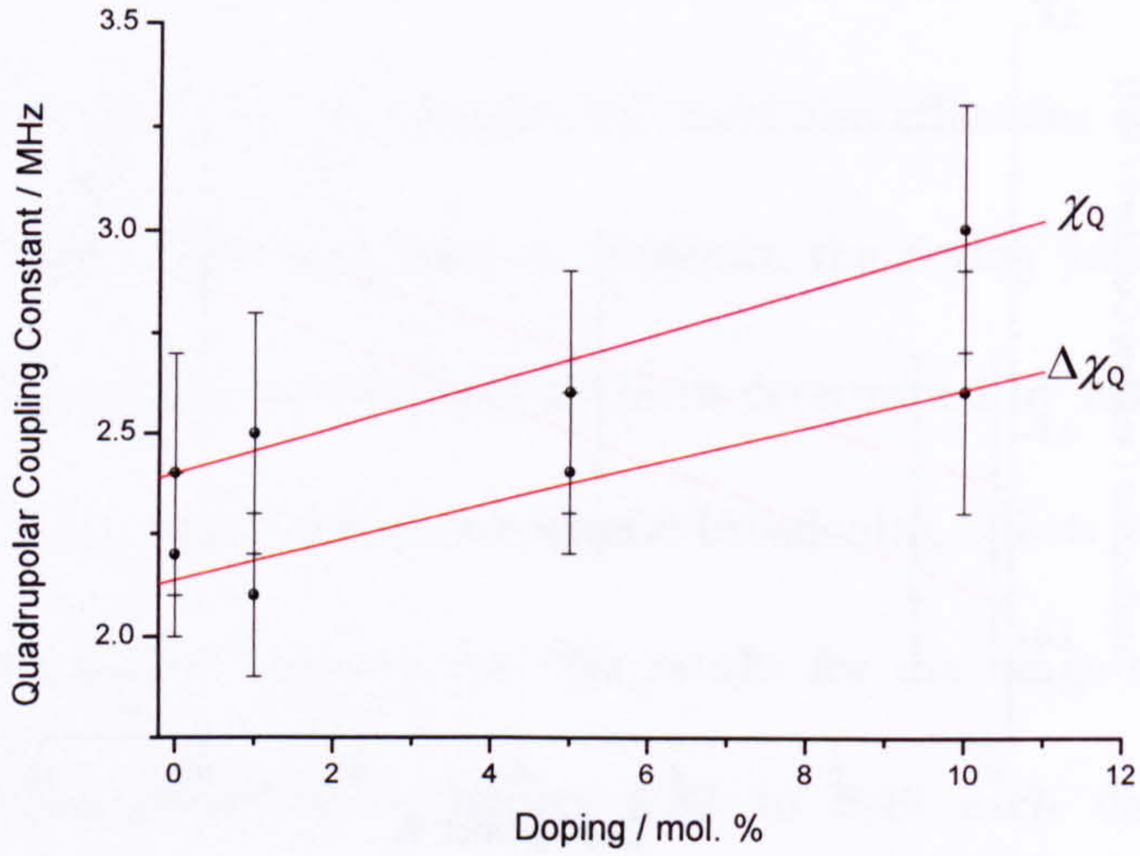

Figure 6.45: The ^{23}Na NMR quadrupolar coupling constant and quadrupolar distribution as a function of doping concentration for the $CuO_{0.5}$ doped glass samples.

The ^{23}Na NMR experiments were also carried out on the partially crystallised samples and an example of the spectra for the 10 mol. % $CuO_{0.5}$ doped partially crystallised sample is given in figure 6.46. From this figure it is clear to see the benefits of high field NMR. The data collected at a field of 8.45 T suggest that the spectrum consists of only two separate sites. However, when data is collected at a field of 18.8 T it becomes evident that there is another feature not previously observable which may correspond to a third site or may be the quadrupolar lineshape becoming defined. Due to time restrictions this data has not yet been fitted so information from the partially crystallised samples remains inconclusive.

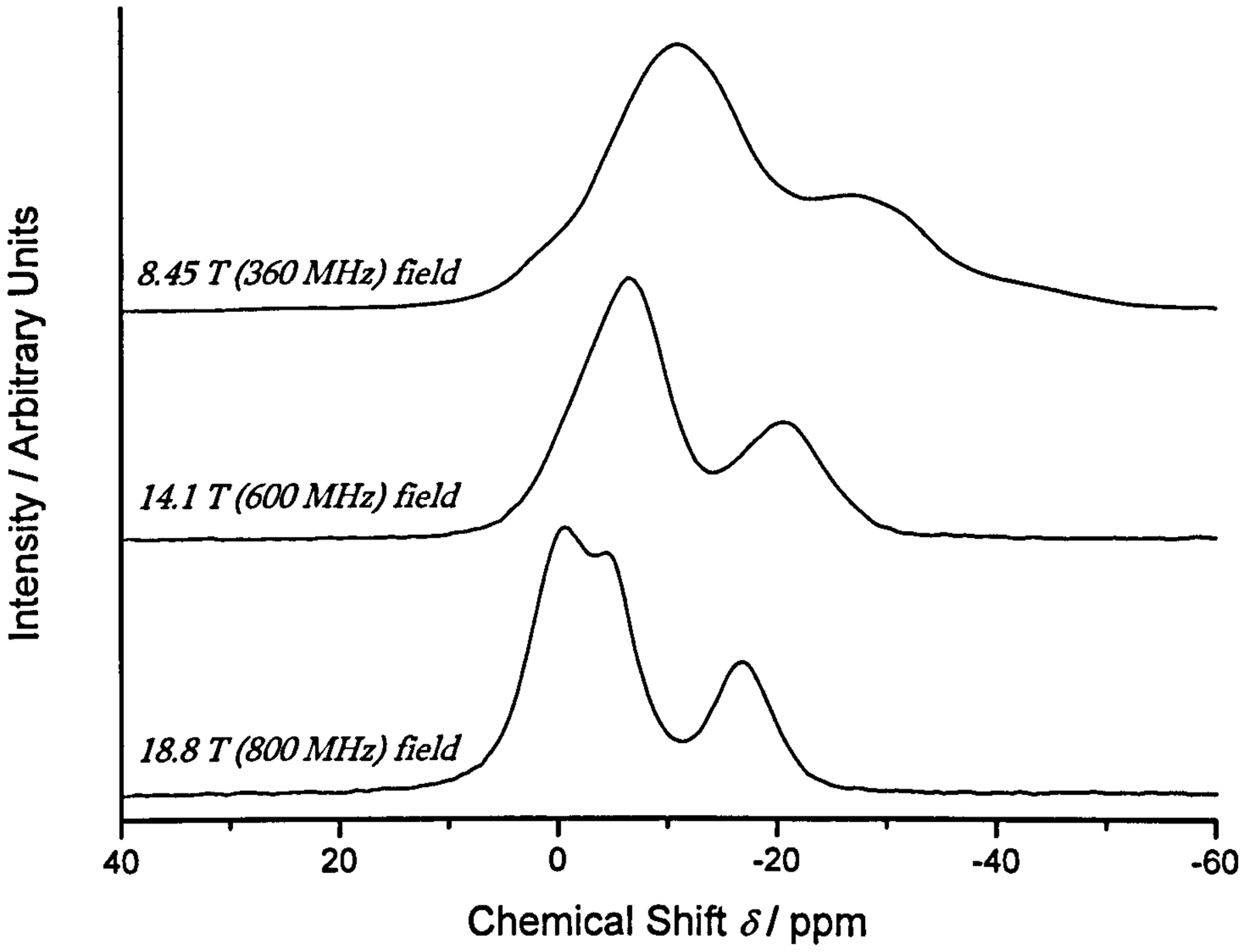

Figure 6.46: The ^{23}Na MAS NMR spectra for the partially crystallised 10 mol. % $CuO_{0.5}$ doped glass at three fields.

6.3 A comparison of silver- and copper-doping

The effects of copper- and silver-doping in place of the sodium ions in these phosphate based glass samples appear very different from expectations in that both of these samples show a distinct deviation from the binary model predictions of their phosphate networks. The replacement of sodium with silver and copper in both cases, resulted in the formation of Q^3 phosphate units although the copper-doped samples displayed the presence of Q^3 units at much lower (≥ 5 %) doping concentrations than for silver (≥ 12.5 %) except for the disproportionation observed, even though the copper-doped samples contained a smaller proportion of

phosphorus. Both ions were found to occupy octahedrally coordinated cross-linking sites between the non-bridging oxygen atoms of the phosphate tetrahedra and although the copper ions have twice the charge than the silver or sodium ions, this does not account for the considerable differences observed. It is most probable that these differences arise due to a combination of the different ionic sizes, electronic configuration and magnetic properties of the two ions. However, it would be interesting to understand more about the role of sodium in these glasses in order to make a more informed deduction about the effects of its substitution for copper or silver.

From our studies into the silver-doped quaternary phosphate glasses, at low doping concentrations small quantities of Q^1 and Q^3 tetrahedra were present and are most likely due to disproportionation of the Q^2 species present, however at higher doping levels the continual increase in Q^3 tetrahedra exceeding that of Q^1 tetrahedra suggests that the silver may be phase separating as there is no evidence for network forming silver. Although the copper-doped samples showed a greater increase in Q^3 speciation for smaller doping concentrations, the NMR measurements performed on these glasses showed no evidence for disproportionation to either Q^0, Q^1 or Q^3 species although the optical studies did allow us to identify Q^0 and Q^1 species. A recent study [5] has claimed that copper ions may be considered as intermediate cations which can network form in addition to modifying, which could account for

the Q^3 speciations observed, however the experimental work conducted in this investigation has not supported these claims for the copper in our samples.

Although the presence of Q^3 phosphate units within both sets of samples have no confirmed cause, it is most likely that this phosphate coordination arises from phase separation of the metals from the glass. This phenomenon has not yet been detected through the presence of crystallised clusters or metallic particles in the copper-containing samples, but this does not entirely rule out the possibility. Furthermore the silver-doped samples do exhibit some evidence of silver-containing clusters but we cannot accurately determine their composition or the time at which these clusters formed. The results, however inconclusive, have been interesting as it is now known that it is not just the ratio of modifying oxide to P_2O_5 concentration that is needed to understand the phosphate network structure but it is also important to know the type of modifying oxide incorporated as this has additional influences upon the network during incorporation.

6.4 Conclusions and further work

The previously determined antibacterial properties of the copper ions within these samples have been checked using CLSM imaging and the properties of phosphate glasses such as their ability to accommodate high concentrations of transition metals [28], controlled dissolution rates and chemical similarity to bone structure make

them an ideal ion host for these novel health care applications. To achieve a greater understanding of the effects of the quantity and form of copper-doping upon the structural characteristics of the glass, the ^{31}P NMR studies were performed and showed the presence of Q^1 and Q^2 phosphate units for doping levels of < 5 % and Q^1, Q^2 and Q^3 phosphate speciation for higher doping concentrations. This was highly unexpected as the presence of modifying oxide dopants should depolymerise the phosphate network leading to a generally lower Q^n speciation [4], in this case giving 78 % of Q^2 and 22 % of Q^1 units. In these samples the overall modifier content remained constant while the type of modifying cations changed as sodium was replaced by copper and as such the Q^1 and Q^2 quantities should have remained unaltered, but this was not the case. However, we were unable to gain an insight into the absolute Q^n percentages present within the samples due to the loss of signal created by the paramagnetic nature of the copper ions.

A previous study [5] has suggested that copper ions can act not only as network modifiers, like modifying ions such as sodium and calcium, but can also be network forming. Apart from the appearance of an unexpected Q^3 NMR peak this study has shown no other evidence supporting copper becoming part of the tetrahedral glass network via covalent linkages with the oxygen ligands from the phosphate units. However, a summary of the possible explanations for the observed Q^3 speciation is given below in table 6.14 along with the corresponding corroborative or contradicting experimental evidence. It would be preferable to perform Cu K-edge

XANES in order to verify the copper environment which could confirm or rule out this possibility of network forming more conclusively.

Possible explanations for the presence of Q^3 phosphate speciation	***Supporting evidence***	***Contradictory evidence***
Incorrectly assigned chemical composition.		SEM-EDX and TEM measurements confirm expected composition.
Copper phase separation.	EPR possibly suggests copper grouping.	XRD, SEM-EDX, TEM and UV-visible spectrophotometry show no evidence for metallic or crystalline copper.
Paramagnetic shift of Q^2 signal.	Presence of Cu^{2+} ions confirmed using ^{65}Cu NMR, EPR, UV-visible spectrophotometry and magnetic susceptibility measurements.	High temperature NMR rules out any temperature dependent chemical shift positioning.
Copper network forming increasing coordination or creating a chemical shift of other Q^n species.	The observation of some Q^3 species in the ^{31}P NMR data.	FTIR and Raman spectroscopy provide no evidence for P-O-Cu bonding, UV-visible spectrophotometry and EPR suggest copper octahedrally coordinated. Chemical shift for Q^3 assigned peak is larger than expected for a Q^2 peak simply chemically shifted due to its different environment.
Paramagnetic copper removing the NMR signal leading to misinterpretation of results.	Confirmed using quantitative NMR experiments, presence of Cu^{2+} also confirmed (see above). As the ^{31}P NMR spectra showed no change in anisotropy with added copper, this suggests that the signal received is not a good indication of the network affected by the copper.	
Dimetaphosphate ring structures.		Background literature suggests this is a highly unlikely scenario.

Table 6.14: A summary of the possible explanations for the unexpected Q^3 phosphate coordination displayed by these samples and the experiments performed during this study.

From this evidence it is most likely that the Cu^{2+} ions present in the sample diminish the ^{31}P NMR signal substantially and if the Cu^{2+} ions have a preferential occupancy within the sample then this would account for the deviation of phosphate speciation

from expectations. Although this could explain the changes in the intensities of the Q^1 and Q^2 units observed as well as the quantitative reduction in ^{31}P NMR signal received, this would still however, not account for the presence of Q^3 phosphate units. The most probable explanation for the existence of Q^3 tetrahedral units is that some phase separation (copper clustering) is occurring to leave a glass network consisting of a higher overall proportion of P_2O_5, accounting for this higher network coordination. However as we do not know the quantitative effects of the paramagnetic removal of NMR signal on the relative intensities of the Q species present within the NMR spectra we cannot say how much Q^3 is actually present within the sample as a whole and therefore cannot calculate the quantity of copper that would have to phase separate. For this reason the occurrence of phase separation in any form remains purely speculative.

As in the case of the silver-doped glass investigation, to extend this study it would be valuable to resolve the different oxygen bridges in the samples using ^{17}O multiple quantum NMR of ^{17}O enriched glasses [56 & 57]. A distinction between bridging and non-bridging oxygen atoms could help to confirm the phosphate speciation observed and the construction of an ^{17}O enrichment furnace is already underway. To gain further insight into the connectivity between different Q^n species present two-dimensional MAS NMR must be used or double-resonance experiments which should provide increased resolution. It would also be helpful to complete sodium K-edge XANES measurements to describe the sodium environment so that

comparisons can be made between the cross-linking behaviour of the sodium and copper ions, however the low (~1 keV) beam energies involved in these measurements make the experiments challenging to perform as the low energy photoelectrons can be problematic to detect [58].

An interesting extension to this study would be an investigation into the oxidation states of the copper. Shih and Chin [32] manufactured copper phosphate glasses under varying melting conditions to control the Cu^{2+}/Cu_{Total} ratio and it is possible that the effect of Cu^{2+} ions upon the glass structure could be different to that of Cu^{+} ions which would be intriguing to study as well as observing any differences in their antibacterial effects.

It would also be desirable to perform degradation and dissolution measurements for the copper-doped samples as the change in these properties could then be related to the structural changes and P-O bonding characteristics observed since the variation of the DTA features with doping was somewhat inconclusive.

No significant differences between the phosphate structures from the ^{31}P NMR results for the range of copper-doped samples have been identified as they each display similar structural relationships and properties with increasing doping concentration. This is surprising as the Cu_2O doped samples contain double the molar concentration of copper than the CuO or $CuO_{0.5}$ doped samples and has only

been found to have more pronounced effects on the signal intensity reduction obtained from the ^{31}P NMR and the shifts in absorption frequencies discovered from the FTIR results. It would however, be preferable to experiment on a greater range of samples with both intermediate doping concentrations and higher doping levels than the samples currently available. Unfortunately at present it has not been possible to manufacture these glasses with higher copper concentrations without them undergoing crystallisation.

References

[1] A. M. Mulligan, M. Wilson and J. C. Knowles, *The effect of increasing copper content in phosphate-based glasses on bioflims of Streptococcus sanguis,* Biomaterials, **24** (2003), 1797-1807.

[2] S. P. Valappil, D. M. Pickup, D. L. Carroll, C. K. Hope, J. Pratten, R. J. Newport, M. E. Smith, M. Wilson and J. C. Knowles, *Effect of silver content on the structure and antibacterial activity of silver-doped phosphate-based glasses,* Antimicrobial Agents and Chemotherapy, **51**:12 (2007), 4453–4461.

[3] C. J. R. Sheppard and D. M. Shotton, *Confocal laser scanning microscopy,* Bios Scientific Publishers Ltd., Oxford, UK (1997).

[4] R. K. Brow, *Review: the structure of simple phosphate glasses,* Journal of Non-Crystalline Solids, **263** & **4** (2000), 1-28.

[5] P. Y. Shih, J. Y. Ding and S. Y. Lee, *^{31}P MAS-NMR and FTIR analyses on the structure of CuO-containing sodium poly- and meta-phosphate glasses*, Materials Chemistry and Physics, **80** (2003), 391-396.

[6] P. J. Goodhew, J. Humphreys and R. Beanland, *Electron microscopy and analysis*, 3rd Ed., Taylor and Francis, London, UK (2001).

[7] L. Baia, M. Baia, W. Kiefer, J. Popp and S. Simon, *Structural and morphological properties of silver nanoparticles – phosphate glass composites*, Chemical Physics, **327** (2006), 63-69.

[8] A. A. Kutub, A. E. Mohamed and C. A. Hogarth, *Some studies of the optical properties of copper phosphate glasses containing praseodymium*, Journal of Materials Science, **21** (1986), 3517-3520.

[9] B-S. Bae and M. C. Weinberg, *Optical absorption of copper phosphate glasses in the visible spectrum*, Journal of Non-Crystalline Solids, **168** (1994), 223-231.

[10] B-S. Bae and M. C. Weinberg, *Ultraviolet optical absorptions of semiconducting copper phosphate glasses*, Journal of Applied Physics, **73**:11 (1993), 7760-7766.

[11] R. Debnath, *On the excitation of the ^3E luminescent state of Cu^+ ions in glass*, Journal of Luminescence, **43** (1989), 375-377.

[12] K. Uchida, S. Kaneko, S. Omi, C. Hata, H. Tanji, Y. Asahara, A. J. Ikushima, T. Tokizaki and A. Nakamura, *Optical nonlinearities of a high concentration of small metal particles dispersed in glass: copper and silver particles*, Journal of the Optical Society of America B, **11**:7 (1994), 1236-1243.

[13] S-H. Wu and D-H. Chen, *Synthesis of high-concentration Cu nanoparticles in aqueous CTAB solutions*, Journal of Colloid and Interface Science, **273** (2004), 165-169.

[14] I. Lisiecki, F. Billoudet and M. P. Pileni, *Control of the shape and size of copper metallic particles*, Journal of Physical Chemistry, **100** (1996), 4160-4166.

[15] A. P. Guimarães, *Magnetism and magnetic resonance in solids*, John Wiley and Sons Inc., New York, USA (1998).

[16] J. F. Stebbins, *Nuclear magnetic resonance spectroscopy of silicates and oxides in geochemistry and geophysics*, Mineral Physics and Crystallography: A Handbook of Physical Constants, American Geophysical Union (1995), 303-331.

[17] K. J. D. MacKenzie and M. E. Smith, *Multinuclear solid state NMR of inorganic materials*, Pergamon Press, London (2002).

[18] W. Gordy, *Theory and applications of electron spin resonance*, John Wiley & Sons Inc., New York, USA (1980).

[19] S. Daoudi, L. Bejjit, M. Haddad, M. E. Archidi, A. Chahine, M. Et-Tabirou and P. Molinié, *EPR and magnetic susceptibility of Na_2O-CuO-P_2O_5 glasses*, Spectroscopy Letters, **40**:5 (2007), 785-795.

[20] R. V. S. S. N. Ravikumar, V. Rajagopal Reddy, A. V. Chandrasekhar, B. J. Reddy, Y. P. Reddy and P. S. Rao, *Tetragonal site of transition metal ions doped sodium phosphate glasses*, Journal of Alloys and Compounds, **337** (2002), 272-276.

[21] A. Kraiewski, A. Ravaglioli and C. B. Azzoni, *Thermal expansion in a CuO-doped silico-phosphate glass*, Journal of Materials Science Letters, **4** (1985), 1-5.

[22] I. Ardelean, R. Cieco-Lucacel and S. Filip, *EPR and magnetic investigations of copper ions in $2B_2O_3$-As_2O_3 glass matrix*, Journal of Magnetism and Magnetic Materials, **272-276** (2004), 337-338.

[23] V. I. Ezikov and D. V. Ramonova, *Valence and coordination of copper ions in semiconducting copper calcium phosphate glasses*, Glass Physics and Chemisty, **28**:1 (2002), 33-35.

[24] M. Mazúr and M. Valko, *Error sources in quantitative EPR spectroscopy*, EPR newsletter, **13**:1-2 (2003), 27.

[25] F. E. Mabbs and D. J. Machin, *Magnetism and transition metal complexes*, Chapman and Hall, London, UK (1973).

[26] C. Kittel, *Introduction to solid state physics*, 7th Ed., John Wiley and Sons Inc., New York, USA (1996).

[27] U. Hoppe, *A structural model for phosphate glasses*, Journal of Non-Crystalline Solids, **195** (1996), 138-147.

[28] E. Metwalli, M. Karabulut, D. L. Sidebotton, M. M. Morsi and R. K. Brow, *Properties and structure of copper ultraphosphate glasses*, Journal of Non-Crystalline Solids, **344** (2004), 128-134.

[29] M. Karabulut, E. Metwalli and R. K. Brow, *Structure and properties of lanthanum-aluminium-phosphate glasses*, Journal of Non-Crystalline Solids, **283** (2001), 211-219.

[30] P. Y. Shih, S. W. Yung and T. S. Chin, *Thermal and corrosion behaviour of P_2O_5-Na_2O-CuO glasses*, Journal of Non-Crystalline Solids, **224** (1998), 143-152.

[31] K. Nakamoto, *Infrared and Raman spectra of inorganic and coordination compounds*, 2nd Ed., John Wiley and Sons Inc., Chichester, UK (1986).

[32] P. Y. Shih and T. S. Chin, *Effect of redox state of copper on the properties of P_2O_5-Na_2O-CuO glasses*, Materials Chemistry and Physics, **60** (1999), 50-57.

[33] C. Ananthamohan, C. A. Hogarth, C. R. Theocharis and D. Yeates, *Investigation of infrared absorption spectra of copper phosphate glasses containing some rare earth oxides*, Journal of Materials Science, **25** (1990), 3956-3959.

[34] C. A. Hogarth and G. R. Moridi, *Infrared spectra of copper-calcium-phosphate glasses*, Journal of Materials Science Letters, **3** (1984), 481-483.

[35] A. Chahine, M. Et-Tabirou and J. L. Pascal, *FTIR and Raman spectra of the Na_2O-CuO-Bi_2O_3-P_2O_5 glasses*, Materials Letters, **58** (2004), 2776-2780.

[36] A. Chahine, M. Et-Tabirou, M. Elbenaissi, M. Haddad and J. L. Pascal, *Effect of CuO on the structure and properties of $(50 - x/2)Na_2O$-xCuO-$(50 - x/2)P_2O_5$ glasses*, Materials Chemistry and Physics, **84** (2004), 341-347.

[37] D. E. C. Corbridge and E. J. Lowe, *The infra-red spectra of some inorganic phosphorus compounds*, Journal of the Chemical Society, (1953), 493-502.

[38] D. E. C. Corbridge and E. J. Lowe, *The infra-red spectra of inorganic phosphorus compounds Part II: Some salts of phosphorus oxy-acids*, Journal of the Chemical Society, (1954), 4555-4564.

[39] M. Gabelica-Robert and P. Tarte, *Infrared spectrum of crystalline and glassy phosphates: preservation of the pyrophosphate group in the glassy structure*, Journal of Molecular Structure, **79** (1982), 251-254.

[40] J. R. Van Wazer, *Phosphorus and its compounds: Volume 1*, Interscience Publishers, New York, USA (1958).

[41] D. M. Yost and H. Russell, *Systematic inorganic chemistry of the fifth-and-sixth-group nonmetallic elements*, Oxford University Press, London, UK (1946).

[42] J. R. Van Wazer and E. J. Griffith, *Structure and properties of the condensed phosphates: General structural theory*, Journal of the American Chemical Society, **77** (1955), 6140-6144.

[43] F. Raschi and J. A. Finch, *Polyphosphates: A review - Their chemistry and application with particular reference to mineral processing*, Minerals Engineering, **13**:10-11 (2000), 1019-1035.

[44] K.-S. Lee, *Hidden nature of the high-temperature phase transitions in crystals of KH_2PO_4-type: Is it a physical change?*, Journal of Physics and Chemistry of Solids, **57**:3 (1996), 333-342.

[45] A. D. Cross and R. A. Jones, *An introduction to practical infra-red spectroscopy*, 3rd Ed., Butterworth & Co. Publishers Ltd., London, UK (1969).

[46] H. S. Gao, T. E. Tan and D. Wang, *Effect of composition on the release kinetics of phosphate controlled release glasses in aqueous medium*, Journal of Controlled Release, **96** (2004) 21– 28.

[47] H.S. Gao, T. E. Tan, D. Wang, *Dissolution mechanism and release kinetics of phosphate controlled release glasses in aqueous medium*, Journal of Controlled Release, **96** (2004) 29– 36.

[48] B. Kumar and S. Lin, *Redox state of iron and its related effects in the CaO-P_2O_5-Fe_2O_5 glasses*, Journal of the American Ceramic Society, **74**:1 (1991), 226-228.

[49] J. Koo, B-S. Bae and H-K. Na, *Raman spectroscopy of copper phosphate glasses*, Journal of Non-Crystalline Solids, **212** (1997), 173-179.

[50] J. Swenson, A. Matic, A. Brodin, L. Börjesson and W. S. Howells, *Structure of mixed alkali phosphate glasses by neutron diffraction and Raman spectroscopy*, Physical Review B, **58** (17) (1998), 11331-11337.

[51] J. E. Pemberton, L. Latifzadeh, J. P. Fletcher and S. Risbud, *Raman spectroscopy of calcium phosphate glasses with varying CaO modifier concentrations*, Chemistry of Materials, **3** (1991), 195-200.

[52] M. El Hezzat, M. Et-Tabirou, L. Montagne, E. Bekart, G. Palavit, A. Mazzah and P. Dhamelincourt, *Structure and ac conductivity of sodium-lead-cadmium metaphosphate glasses*, Materials Letters, **58** (2003), 60-66.

[53] J. J. Hudgens, R. K. Brow, D. R. Tallent and S. W. Martin, *Raman spectroscopy study of the structure of lithium and sodium ultraphosphate glasses*, Journal of Non-Crystalline Solids, **223** (1998), 21-31.

[54] T. M. Duncan, *A complication of chemical shift anisotropies*, Farragut Press, Chicago (1990), 5-25.

[55] R. K. Brow, C. C. Phifer, G. L. Turner and R. J. Kirkpatrick, *Cation effects on ^{31}P NMR chemical shifts of metaphosphate glasses*, Journal of the American Ceramics Society, **74**:6 (1991), 1287-1290.

[56] A. Flambard, L. Montagne and L. Delevoye, *A new ^{17}O-isotopic enrichment method for the NMR characterisation of phosphate compounds*, Chemical Communications, **32** (2006), 3426-3428.

[57] C. Jäger, P. Hartmann, R. Witter and M. Braun, *New 2D NMR experiments for determining the structure of phosphate glasses: a review*, Journal of Non-Crystalline Solids, **263** & **4** (2000), 61-72.

[58] *Handbook of X-ray spectrometry (practical spectroscopy)*, Eds: R. E. Van Grieken and A. A. Markowicz, 2nd Ed., Marcel Dekker Inc., New York, USA (2002).

Chapter 7

Rare-Earth Doping In Phosphate Glass

7.1 Introduction

The phosphate glass samples investigated in this chapter incorporate doping in the form of aluminium, which is often used to enhance the durability of such glasses, and yttrium to represent small rare-earth ions (~0.09 nm ionic radius within a 6-fold coordinated environment [1]) commonly used as impurity ions in lasing media. The samples in which aluminium and yttrium are substituted directly in place of each other aim to resolve any differences in effect upon the phosphate glass structure arising from the two types of trivalent cations. These results can also be compared

to those by Karabulut et al. [2] who completed similar experiments upon phosphate glasses in which lanthanum, which is representative of the large rare-earth lasing dopants (radius of 0.1032 nm in a 6-fold coordinated environment [1]), was substituted in place of the aluminium (ionic radius of 0.0535 nm in the form of AlO_6 [1]). Observing any variations between the network changes occurring when using lanthanum or yttrium as the rare-earth dopant are hoped to lead to a better understanding of how the differences in properties of the two cations, such as their different ionic size, can influence the glass structure. Previous studies such as those by Graia et al. [3], Milligan et al. [4] and others [5-7] have shown that these ions can each occupy different environments within phosphate based glasses. The mechanisms driving their different site occupancies and how this influences the phosphate network and in turn the glass properties, were explored in our investigation using multinuclear MAS NMR, differential scanning calorimetry (DSC) and Vickers hardness testing. Some aluminophosphate glass samples were also prepared in which both lanthanum and yttrium were incorporated in different quantities so that their influences upon an aluminosilicate glass network could also be investigated.

7.2 Results and discussion

In the first series of aluminophosphate samples, yttrium had been systematically substituted in place of the aluminium whilst keeping the molar fraction of P_2O_5 at an

approximately constant value of 70 ± 4 %. The EPMA measured sample compositions can be found in table 1.1 (page 18), but were intended to be (25 – x) % (Al_2O_3) + x % (Y_2O_3) + 75 % (P_2O_5). The discrepancy between the desired and obtained compositions emphasises the importance of chemical analysis post-glass manufacture as a very small difference in composition can lead to a significant change in the expected network coordination.

The ^{27}Al NMR measurements on these samples showed the presence of 4-, 5- and 6-fold coordinated aluminium, denoted by AlO_4, AlO_5 and AlO_6 respectively as the nearest neighbour atoms are oxygen ligands. These aluminium species gave rise to the clearly resolved spectral peaks shown in figure 7.1 and an example of the peak fitting at two fields (using 600 and 800 MHz NMR spectrometers) is shown in figure 7.2. The experiments were run at two fields so that the peaks present could be resolved more clearly and to give more precise data fitting since the fit parameters could be constrained by multiple field analysis using QuadFit [8], section 3.7. There is no evidence of Al-O-Al (aluminium next nearest neighbours) bonding as this would give rise to additional peaks in the ^{27}Al NMR spectrum [9] and the peaks observed have been attributed to aluminium in 4-, 5- and 6-fold environments with phosphorus next nearest neighbours. This is consistent with the low (≤ 34 %) aluminium quantities incorporated which would be expected to result in a statistically dispersed aluminium distribution, unless there was any preferential clustering of aluminium which the ^{27}Al NMR appears to have ruled out.

The absence of Al-O-Al bonding was of significance as previous studies by Karabulut et al. [2], Hoppe et al. [10] and Brow et al. [11] have suggested that the incorporation of rare-earth cations such as lanthanum in phosphate based glasses, display evidence for lanthanum-to-oxygen coordinations greater than expected from the number of non-bridging oxygen atoms available to coordinate to each charge balancing La^{3+} ion which leads to the occurrence of La-O-La configurations. The formation of La-O-La linkages means that clustering of lanthanum-to-oxygen polyhedra occurs (referred to as rare-earth clustering) and it is interesting to observe whether similar effects are occurring with the aluminium and yttrium trivalent cations incorporated within our samples which appears not to be the case for the aluminium. However, as an extension to this work it would be highly desirable to complete ^{89}Y NMR or Y K-edge XANES to further investigate the possibility of rare-earth clustering.

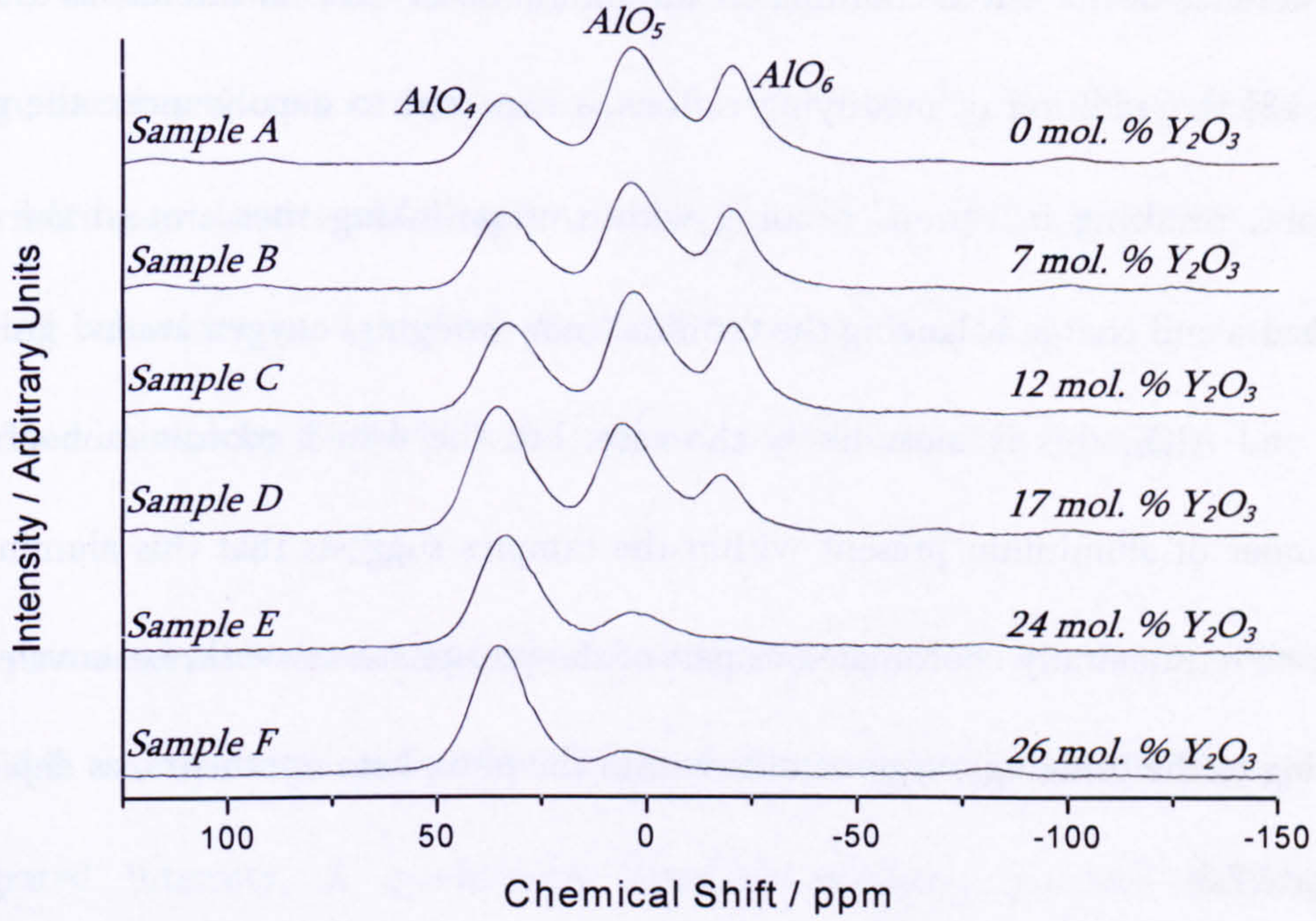

Figure 7.1: ^{27}Al spectra for the yttrium-doped aluminophosphate samples, $(25 - x)$ % Al_2O_3 + x % Y_2O_3 + 75 % P_2O_5 taken using the 600 MHz spectrometer at a field of 14.1 T and spin rate of ~20 kHz.

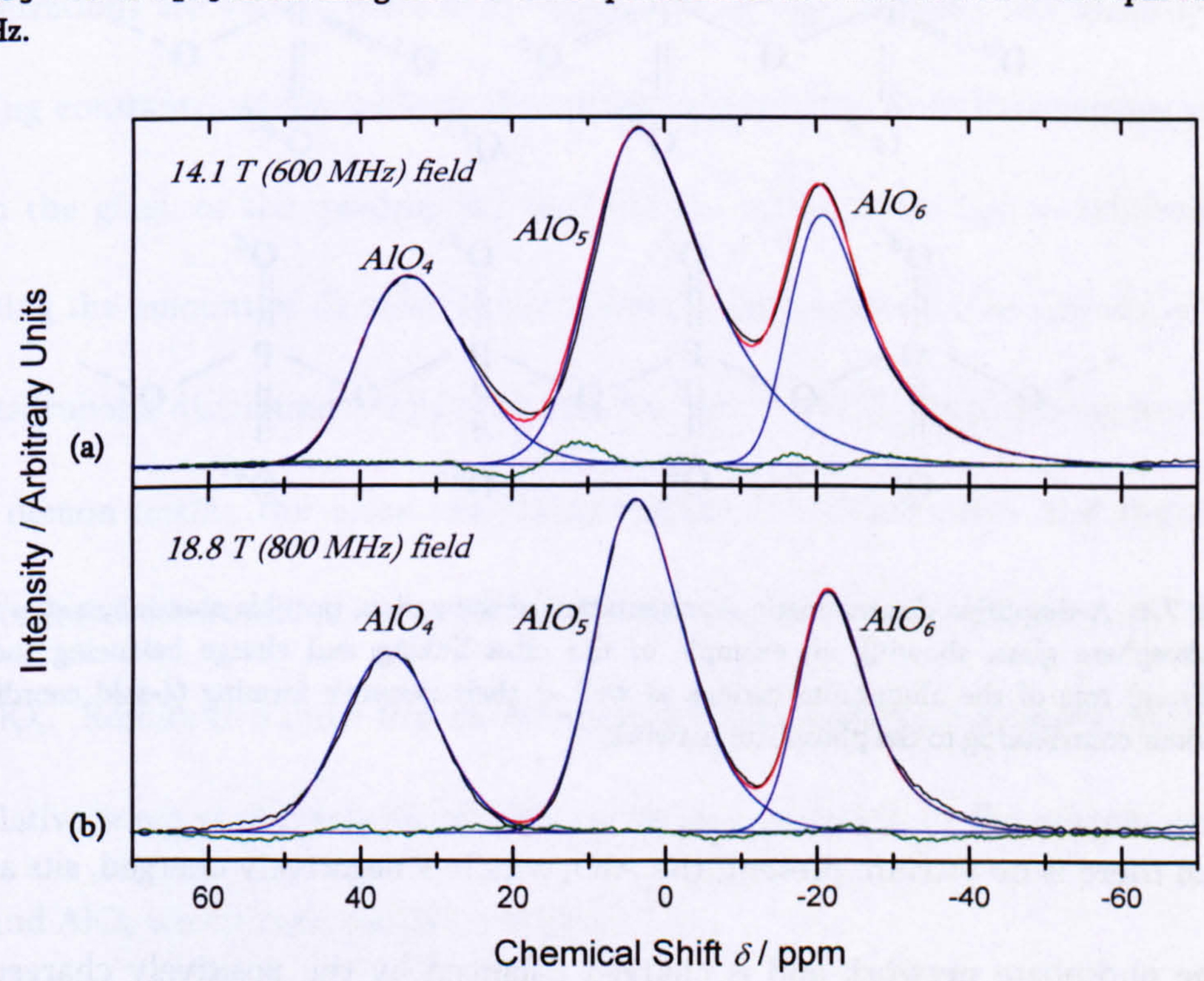

Figure 7.2: The deconvolution of the ^{27}Al MAS NMR spectra for sample A taken at two fields (a) 18.8 T (800 MHz) and (b) 14.1 T (600 MHz). The fitted peaks are shown in blue, the overall fit in red, the original spectrum in black and the difference between the fit and the raw data in green.

The presence of the 4-fold coordinated aluminium observed is of interest as usually [12 & 13] the addition of modifying cations is expected to depolymerise the glass network, resulting in cations residing within cross-linking sites around the PO_4 tetrahedra and charge balancing the terminal (non-bridging) oxygen atoms. For the AlO_5 and AlO_6, this is most likely the case, but the 4-fold coordination of the remainder of aluminium present within the samples suggests that this aluminium could be tetrahedrally coordinated as part of the phosphate network, i.e. covalently bonding to the bridging oxygen atoms within the phosphate tetrahedra, as depicted in figure 7.3.

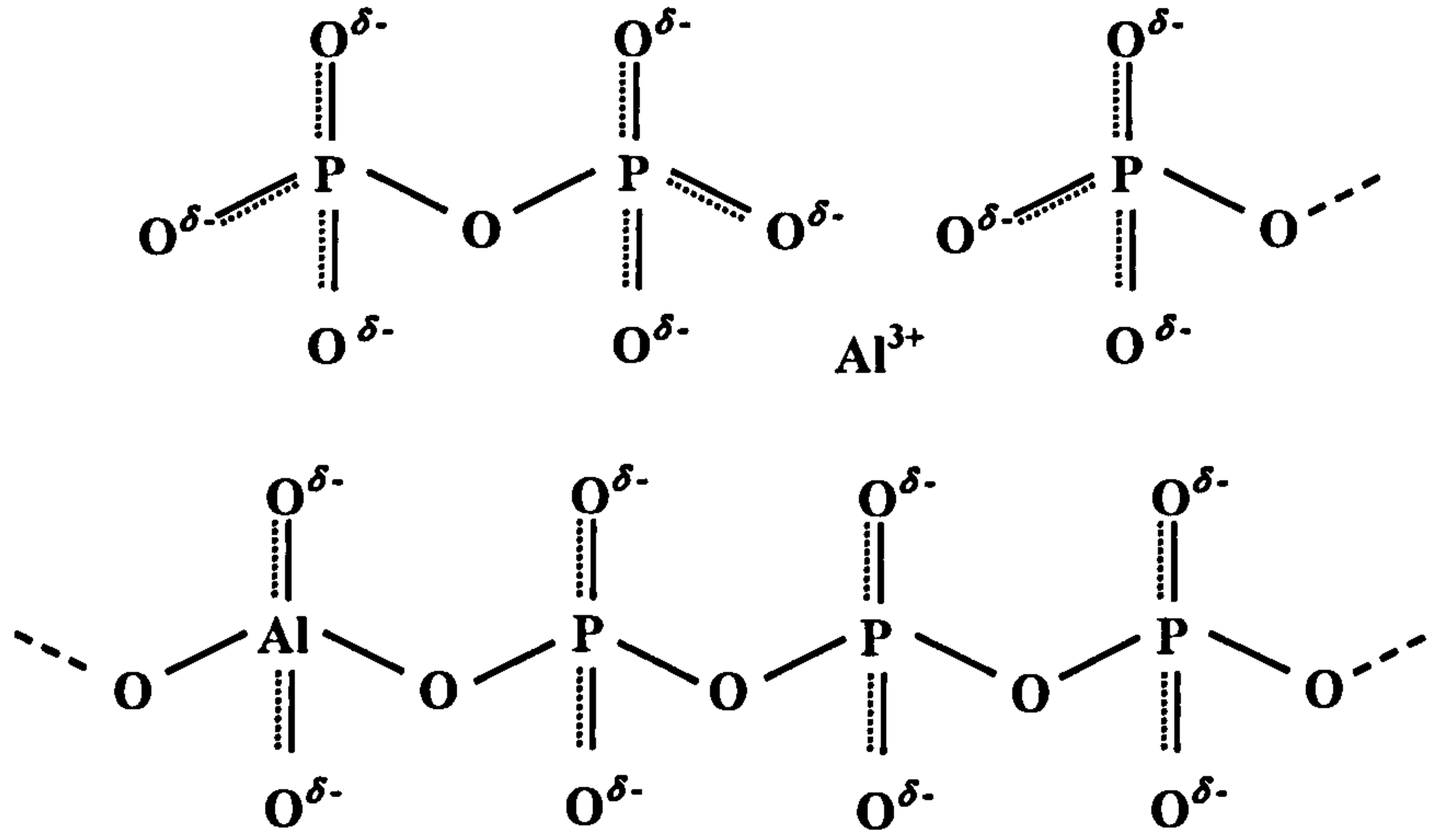

Figure 7.3: A simplified diagrammatic representation of the various possible aluminium sites within the phosphate glass, showing an example of the cross-linking and charge balancing (network modifying) role of the aluminium cations as well as their network forming (4-fold coordinated) behaviour contributing to the phosphate network.

When there is no yttrium present, the AlO_4 which is negatively charged, sits as part of the phosphate network and is charged balanced by the positively charged Al^{3+} cations which remain outside the network and are 5- or 6-fold coordinated. This implies that aluminium behaves as what is commonly termed an 'intermediate'

cation, which means that Al^{3+} may act not only as a depolymerising modifying cation, but may also act as a network former, repolymerising the glass structure and contributing to the overall phosphate network. The possibility of similar network forming behaviour has also been discussed for magnesium and zinc ions which is described in work by Hoppe [14] although these studies remain ongoing.

The parameters obtained from the fitted ^{27}Al MAS NMR spectra are shown in table 7.1 and give an indication of the isotropic chemical shift, δ_{iso}, relative integrated intensity, *I*, quadrupolar coupling constant, χ_Q, and quadrupolar distribution, $\Delta\chi_Q$, for each aluminium site. For each aluminium site, as the doping concentrations are varied, there is no significant change in either the quadrupolar coupling constants, which indicate the extent of distortion of the aluminium units within the glass, or the quadrupolar distribution, which gives rise to information regarding the amount of disorder in the system. The results do however show that the quadrupolar distribution, $\Delta\chi_Q$, is smaller for the ^{27}Al NMR signal arising from the AlO_4, demonstrating the more constrained range of environments and therefore more ordered environments in which these Al^{3+} ions reside compared to the AlO_5 and AlO_6. Results also show that as the amount of yttrium in the samples increases, the relative integrated intensity of AlO_4 increases in relation to the percentages of AlO_5 and AlO_6 which both decline, see figure 7.4.

Sample	AlO_4				AlO_5				AlO_6			
	δ_{iso} / ppm ± 3 ppm[i]	χ_Q / MHz ± 0.5 MHz	$\Delta\chi_Q$ / MHz ± 0.5 MHz	I / % ± 3 %	δ_{iso} / ppm ± 3 ppm	χ_Q / MHz ± 0.5 MHz	$\Delta\chi_Q$ / MHz ± 0.5 MHz	I / % ± 3 %	δ_{iso} / ppm ± 3 ppm	χ_Q / MHz ± 0.5 MHz	$\Delta\chi_Q$ / MHz ± 0.5 MHz	I / % ± 3 %
A	41	6.0	1.9	25	9	6.4	3.9	48	-17	5.6	5.0	27
B	40	5.4	1.6	32 ± 4	10	6.4	3.9	46 ± 4	-17	5.6	4.7	22 ± 4
C	40	5.8	2.2	33	9	6.5	3.9	45	-18	5.3	4.8	22
D	41	5.5	1.9	46	10	6.4	4.1	41	-16	4.9	4.0	13
E	41	6.0	2.1	69	7	6.0	5.0	28	-18	4 ± 1	3 ± 1	3
F	42	5.8	2.2	81	9	6.2	4.8	17	-16	6 ± 1	2 ± 1	2

Table 7.1: ^{27}Al NMR results for the yttrium-doped aluminophosphate glass series.

[i]These errors are correct for all of the tabulated data unless otherwise stated adjacent to the corresponding value.

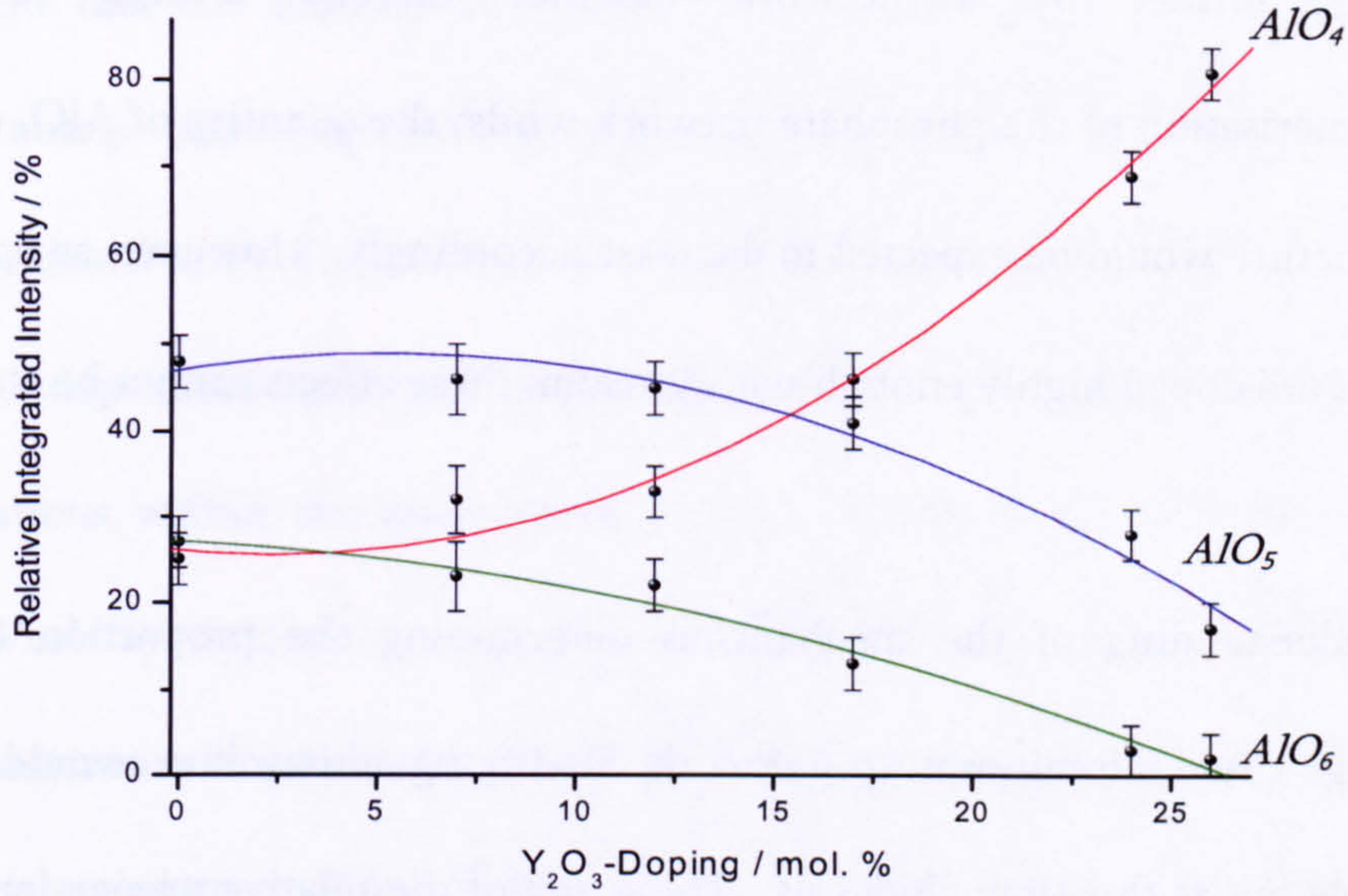

Figure 7.4: The change in content of different aluminium coordination with increasing yttrium-doping. Note that the lines are guides to the eye.

It appears as though yttrium preferentially replaces the 6- and 5-fold coordinated aluminium and the fraction of AlO_6 was found to become negligible for glasses containing large molar percentages (> 17 %) of yttrium. An interesting question yet to be resolved would involve the effects of adding further quantities of yttrium which exceed the amount of AlO_5 and AlO_6 present. Although yttrium has the same valence as aluminium, it has a different ionic radius, electronic configuration and is known to occupy different environmental coordinations in some phosphate structures as shown in work by Shannon [1], Graia et al. [3], Milligan et al. [4] and others [5 & 6]. There is no evidence for YO_4 suggesting that yttrium cannot become a network former and enter the phosphate tetrahedral network in the same manner as some aluminium. Therefore if further increased in quantity to replace the 4-fold, network forming aluminium, the addition of yttrium would be a replacement of a

network former by a network modifier thereby leading to increased depolymerisation of the phosphate network whilst the quantity of AlO_4 observed in the structure would be expected to decrease accordingly. However, as none of these samples are doped highly enough with yttrium, these effects cannot be studied here.

An understanding of the mechanisms determining the proportion of network forming 4-fold aluminium to network modifying aluminium would be highly desirable but at this time eludes us. The graph of the relative proportion of AlO_4 to AlO_6 + AlO_5, versus total aluminium in figure 7.5 appears to show an exponential decrease of the relative AlO_4 concentration with aluminium-doping at this P_2O_5 composition of ~70 ± 4 %, although the influences of additional modifiers present within the sample, in this case yttrium, and sample manufacturing conditions upon the aluminium coordination are unknown.

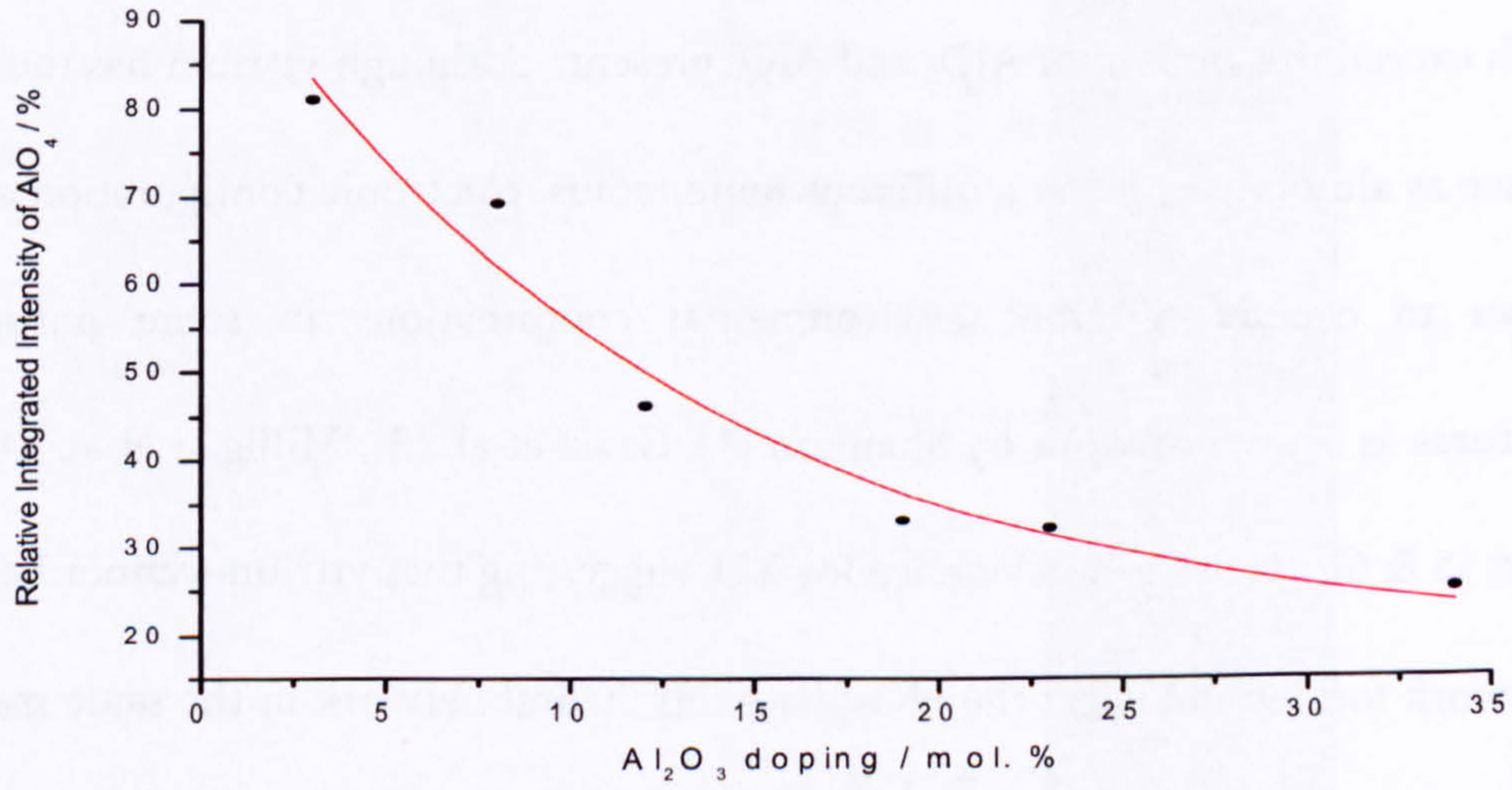

Figure 7.5: The change in relative amount of 4-fold aluminium with respect to the total aluminium incorporated, as the total amount of Al_2O_3 doping increases.

It is thought that the aluminium coordination is most likely governed by the number of charge balancing terminal oxygen atoms present within the phosphate glass to coordinate with. The number of non-bridging oxygen atoms available to the aluminium is dependent upon both the phosphate content and the type and quantity of other cations within the glass already charge balancing the terminal oxygen present. Work by Karabulut et al. [2] which describes the rare-earth clustering effects of lanthanum in an aluminophosphate glass network goes onto explain what they call 'aluminium avoidance' behaviour. This is where the aluminium coordination observed, changes with the addition of aluminium to avoid any formation of Al-O-Al linkages (around the terminal oxygen atoms) by replacing octahedral (AlO_6) with tetrahedral (AlO_4) aluminium [11 & 15]. So long as the quantity of P_2O_5 remains constant, there should be a constant number of non-bridging oxygen atoms within the sample which means that as more Al^{3+} ions enter the glass system and charge balance these terminal oxygen atoms, fewer non-bridging oxygen atoms will be available to each Al^{3+} ion. Therefore a point will be reached where the oxygen atoms will become charge balanced by more than one Al^{3+} cation and when this occurs Al-O-Al configurations will be formed. However, since some of the aluminium becomes tetrahedrally coordinated thus not allowing this configuration to be reached, the excess Al^{3+} ions become part of the phosphate network, preventing an excess of charge balancing aluminium ions from residing within the cross-linking sites. This is supported by figure 7.6 which displays the actual AlO_4 content increasing in each sample as the total amount of aluminium is

increased. The total AlO_4 content was calculated using the integrated AlO_4 intensity obtained from the ^{27}Al NMR data (table 7.1) in conjunction with the total quantity of aluminium determined from the EPMA results (table 1.1). Conversely, as more rare-earth ions (lanthanum or yttrium) are added, these charge balance the terminal oxygen atoms leaving fewer available to coordinate with the Al^{3+} ions forcing the Al^{3+} into 4-fold coordinated sites and therefore reducing the aluminium coordination [2]. This also means that in glasses with lower phosphate contents (and therefore more non-bridging oxygen atoms) a higher aluminium content could be reached before the formation of AlO_4 so long as the rare-earth composition remains constant.

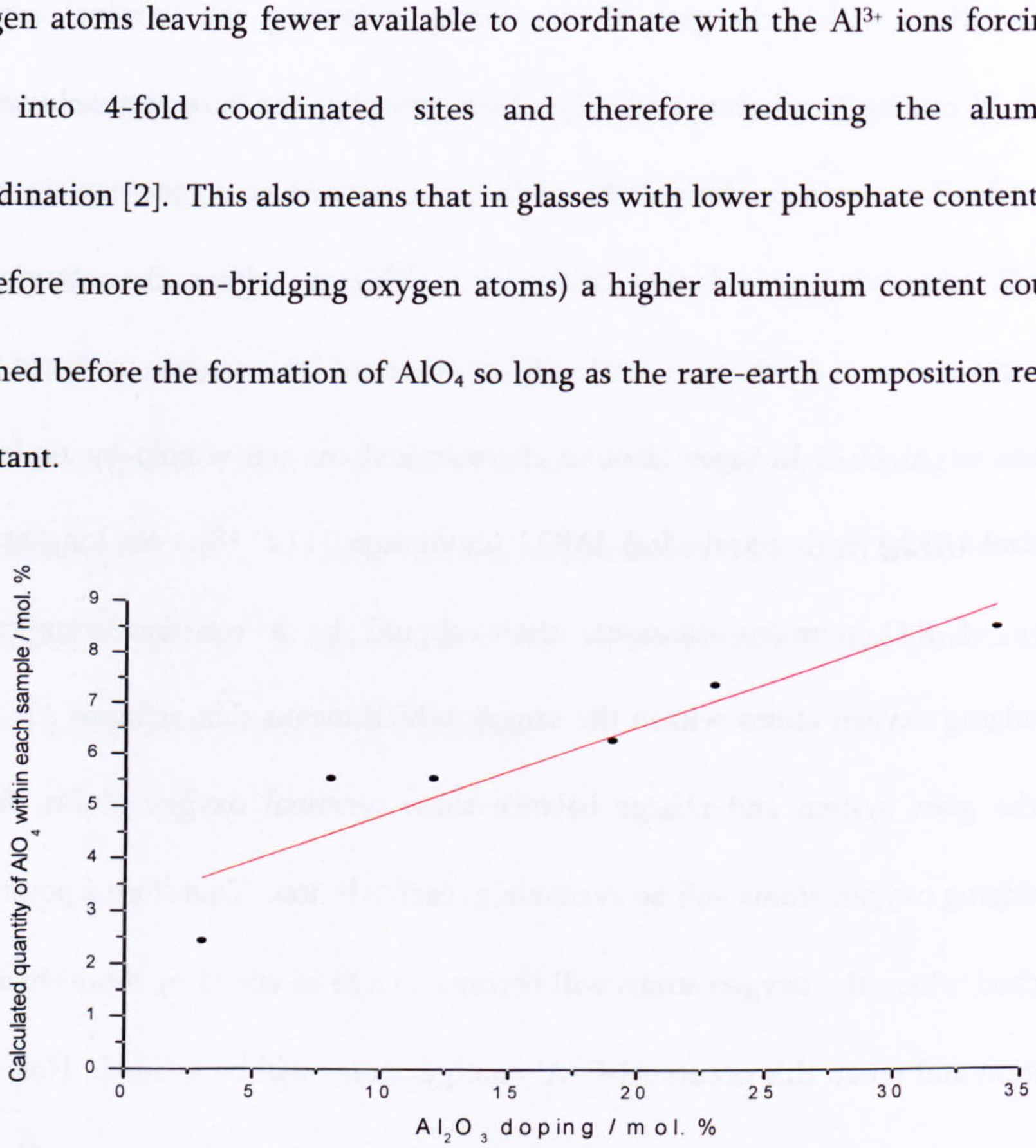

Figure 7.6: The change in actual AlO_4 quantity as the total aluminium-doping increases.

The ^{31}P NMR results for these samples displayed in figures 7.7, 7.8 and summarised in table 7.2, reveal three separate sites and their changes with aluminium content, but due to the incorporation of aluminium it becomes difficult to associate these

peaks to specific Q^n species as the presence of aluminium ions in the glass network can create substantial chemical shifts [12, 13, 16]. The results obtained were compared with work done by Zhang and Eckert in 2004 and 2006 [17 & 18] in which the shift of the Q^0 tetrahedral units is given as the tetrahedra become associated with growing numbers of aluminium next nearest neighbours. On the basis of this data, the speculative, but consistent assignment of the peaks at approximately –14 ppm, –28 ppm and –42 ppm were identified as Q^1 (1Al), Q^2 (1Al) and Q^3 (1Al) respectively, i.e. each tetrahedron has one aluminium next nearest neighbour associated with it, causing this shift in the measured signal. This assignment of one aluminium next nearest neighbour per phosphate tetrahedron is consistent with the low molar percentage of aluminium (and more specifically, AlO_4) present in the samples (between 3 and 34 %), however these Q^n speciation assignments could be verified more accurately by performing 2D NMR experiments in the future.

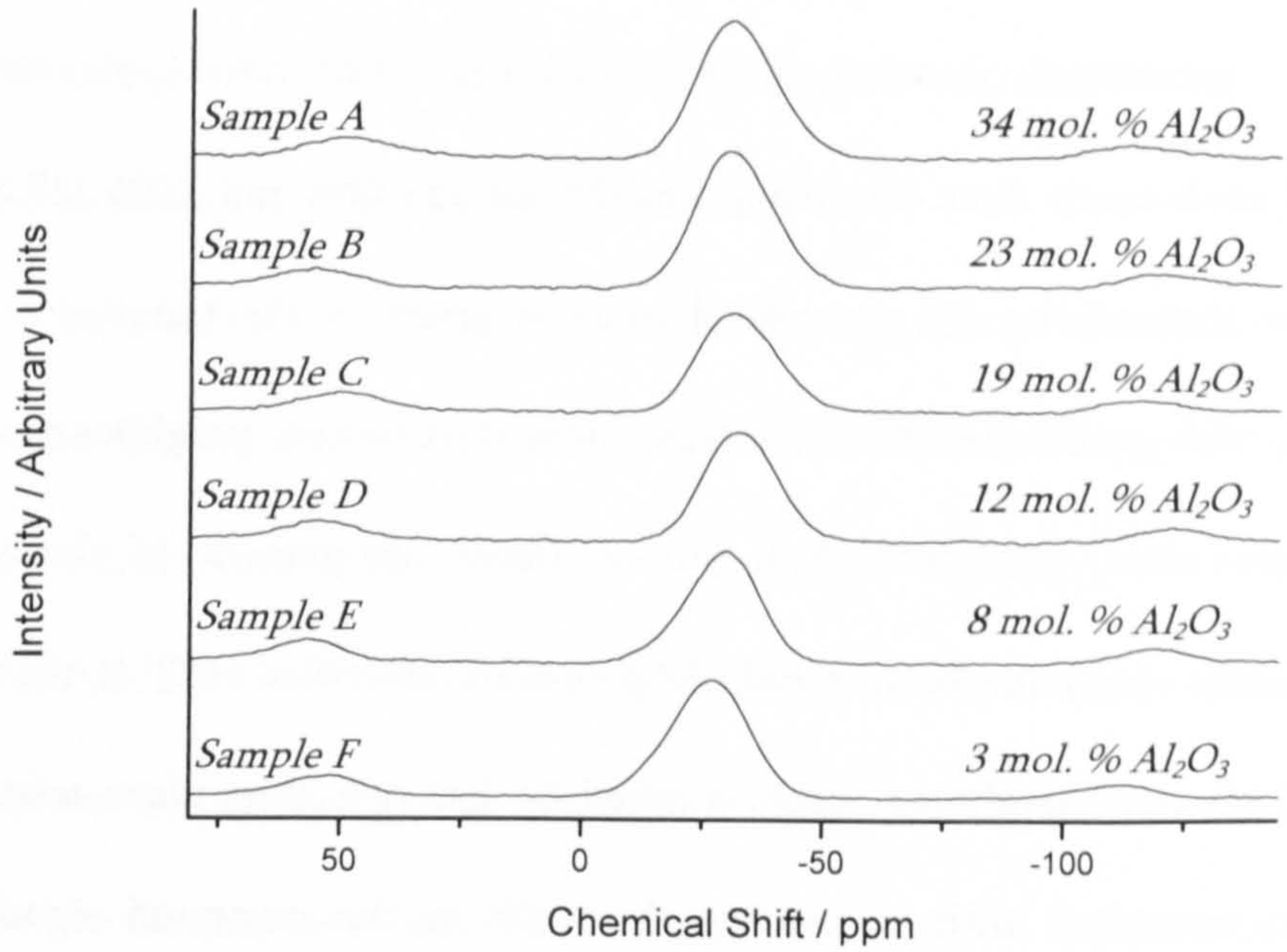

Figure 7.7: The ^{31}P MAS NMR spectra for the yttrium-doped aluminophosphate glasses at a magnetic field of 8.45 T, spinning at ~12 kHz.

Sample	*$^{31}P\ Q^1$ (1Al)*			*$^{31}P\ Q^2$ (1Al)*			*$^{31}P\ Q^3$ (1Al)*		
	δ_{iso} / ppm ± 1 ppm	*Δ / ppm ± 1 ppm*	*I / % ± 1 %*	*δ_{iso} / ppm ± 1 ppm*	*Δ / ppm ± 1 ppm*	*I / % ± 1 %*	*δ_{iso} / ppm ± 1 ppm*	*Δ / ppm ± 1 ppm*	*I / % ± 1 %*
A (34 % Al_2O_3)				–30	16	91	–43	13	9
B (23 % Al_2O_3)				–29	17	90	–41	12	10
C (19 % Al_2O_3)				–30	17	88	–42	12	12
D (12 % Al_2O_3)				–31	18	100			
E (8 % Al_2O_3)	–16	14	10	–29	16	90			
F (3 % Al_2O_3)	–13	13	9	–26	18	91			

Table 7.2: Table of ^{31}P NMR data for the yttrium-doped aluminophosphates reporting the isotropic chemical shift, δ_{iso}, FWHM, Δ, and relative integrated intensity, *I*, for each of the phosphate sites observed in the NMR spectra.

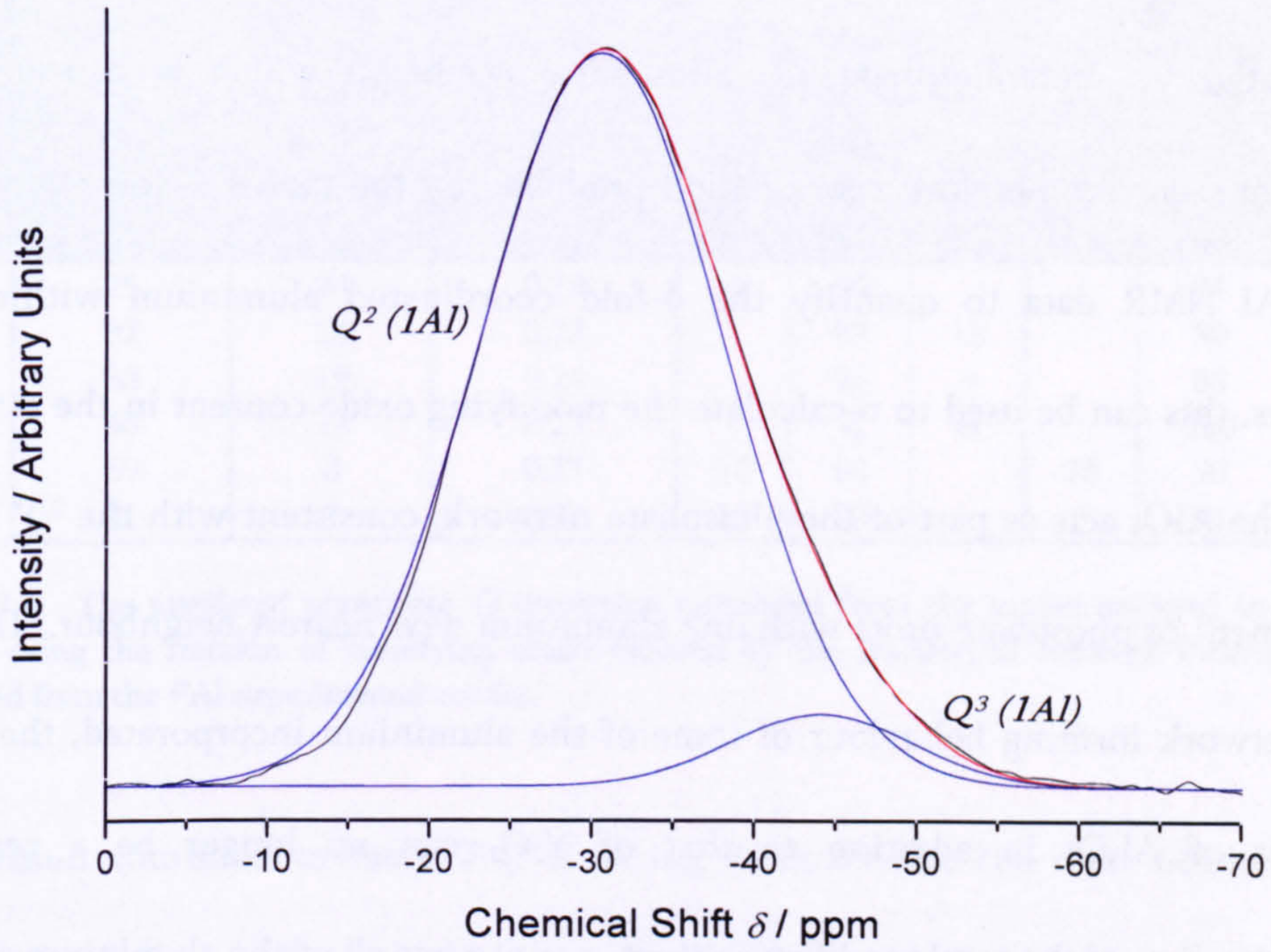

Figure 7.8: The ^{31}P NMR spectrum (black) with the fitted peaks (in blue) for sample A of the yttrium-doped aluminophosphate glass series. The red line shows the overall fit.

In a polyphosphate glass such as this where $P_2O_5 \approx 70$ %, using equations 1.10 and 1.11, for $0.25 < x < 0.40$, where x is the molar fraction of $Al_2O_3 + Y_2O_3$ modifying oxide, the predicted phosphate speciation from the model gives rise to those calculated in table 7.3.

Sample	x	*Predicted ^{31}P Q speciation / % ± 0.1 %*			*Experimentally Observed ^{31}P Q speciation Intensities / % ± 1 %*		
		Q^1 (1Al)	*Q^2 (1Al)*	*Q^3 (1Al)*	*Q^1 (1Al)*	*Q^2 (1Al)*	*Q^3 (1Al)*
A (34 % Al_2O_3)	0.343	56.6	43.4			91	9
B (23 % Al_2O_3)	0.300	28.6	71.4			90	10
C (19 % Al_2O_3)	0.305	31.8	68.2			88	12
D (12 % Al_2O_3)	0.291	23.1	76.9			100	
E (8 % Al_2O_3)	0.325	44.7	55.3		10	90	
F (3 % Al_2O_3)	0.289	21.9	78.1		9	91	

Table 7.3: The predicted Q speciation quantities of the phosphate coordination using the model outlined in section 1.2.2.1, compared to the experimental results.

The experimental results observed here show that the phosphate network is entirely dominated by metaphosphate Q^2 phosphate tetrahedra which is considerably different from the network coordination predicted by the model. However, using the ^{27}Al NMR data to quantify the 4-fold coordinated aluminium within the samples, this can be used to recalculate the modifying oxide content in the samples since the AlO_4 acts as part of the phosphate network, consistent with the ^{31}P NMR assignment of phosphate units with one aluminium next nearest neighbour. Due to this network forming behaviour of some of the aluminium incorporated, the total amount of Al_2O_3 in addition to that of Y_2O_3 can no longer be a realistic representation of the total modifier content, x, since not all of the aluminium acts in this modifying and depolymerising way. By reducing the total modifier fraction x, by the amount of 4-fold aluminium quantified from the ^{27}Al NMR as described in table 7.4 below, the adjusted x^* value could then be used to calculate the predicted phosphate Q^n species from the model. These calculations shown in table 7.4 give rise to phosphate coordinations consistent with those observed experimentally, within the allocated uncertainties which arise from the associated errors in the aluminium quantification from the previous NMR experiments and the uncertainties in the chemical analysis. Any other differences may arise from the uncertainties in the data processing and fitting. Any disproportionation effects are not considered as no evidence for this was found in the NMR data.

Sample	Relative percentage of AlO_4 / % ± 1 %	Total Al_2O_3 / % ± 1 %	Total fraction of modifying oxide neglecting the fraction of AlO_4, x* ± 0.02	Predicted ^{31}P Q speciation / % ± 10 %			Experimentally observed ^{31}P Q speciation intensities / % ± 1 %		
				Q^1 (1Al)	Q^2 (1Al)	Q^3 (1Al)	Q^1 (1Al)	Q^2 (1Al)	Q^3 (1Al)
A	25	34	0.26	4	96			91	9
B	32	23	0.23		87	13		90	10
C	33	19	0.24		96	4		88	12
D	46	12	0.23		92	8		100	
E	69	8	0.27	10	90		10	90	
F	81	3	0.27	10	90		9	91	

Table 7.4: The predicted phosphate *Q* speciation calculated from the model outlined in section 1.2.2.1 using the fraction of modifying oxide reduced by the fraction of network forming AlO_4 obtained from the ^{27}Al experimental results.

This result (outlined in table 7.4) is strong evidence for the dual behaviour of aluminium cations and their ability to act as both network formers and modifiers in a role described as 'intermediate' cation behaviour. However, the factors influencing which role the aluminium ions perform are not yet understood.

The experiments performed here on yttrium-doped aluminophosphate glass samples can be easily compared to those performed on lanthanum-doped aluminophosphate glasses investigated by Karabulut et al. [2]. These samples are close in elemental composition to our samples and were also manufactured by first melting the oxide powders in air using alumina crucibles, therefore allowing the incorporation of atmospheric water and some aluminium contamination. The ^{27}Al results were collected at a frequency of 94.67 MHz on a 360 MHz spectrometer equipped with 8.45 T magnetic, using a MAS spin rate of 10 kHz. Although we make a comparison with this lower field data, it needs to be realised that this low field data is likely to

be in significant error due to the large second-order quadrupole effect at such a low field. The samples analysed consisted of two batches, the compositions of which were as follows:

- $(25 - x)$ % La_2O_3 + x % Al_2O_3 + 75 % P_2O_5
- $(30 - x)$ % La_2O_3 + x % Al_2O_3 + 70 % P_2O_5

In their study a selection of the sample compositions were checked using EDX and were found to be within ± 7 % of those intended [2]. The ^{27}Al NMR results adapted from this work [2] are shown in figures 7.9, 7.10 and table 7.5 [2], from which it can be seen that three peaks are observed near +33 ppm, +4 ppm and –20 ppm that have been assigned as AlO_4, AlO_5 and AlO_6 respectively, with phosphorus next nearest neighbours [2].

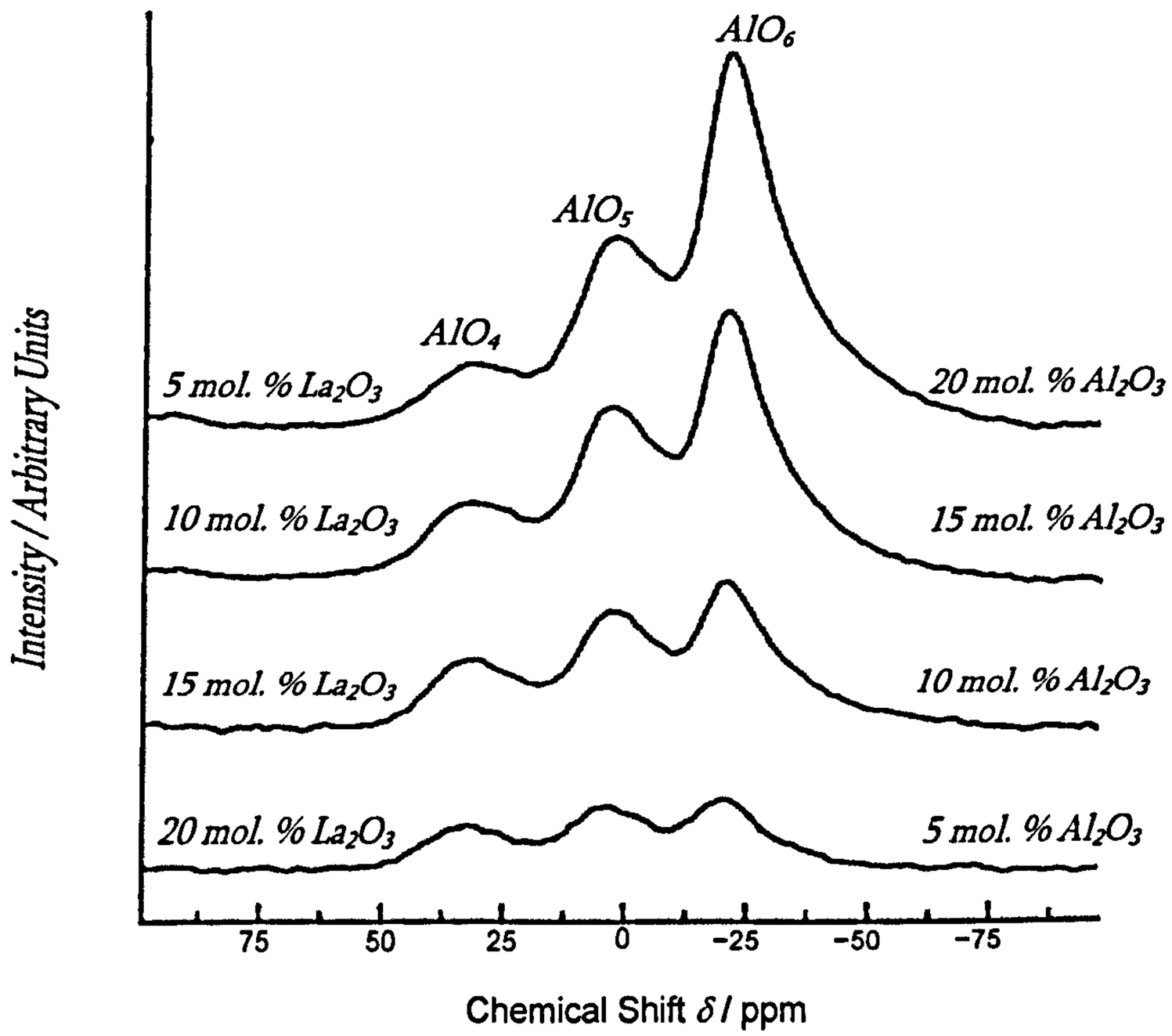

Figure 7.9: ^{27}Al NMR spectra for the $(25 - x)$ % La_2O_3 + x % Al_2O_3 + 75 % P_2O_5 glasses, reproduced from [2] where the x-axis scale has been reversed for convenience.

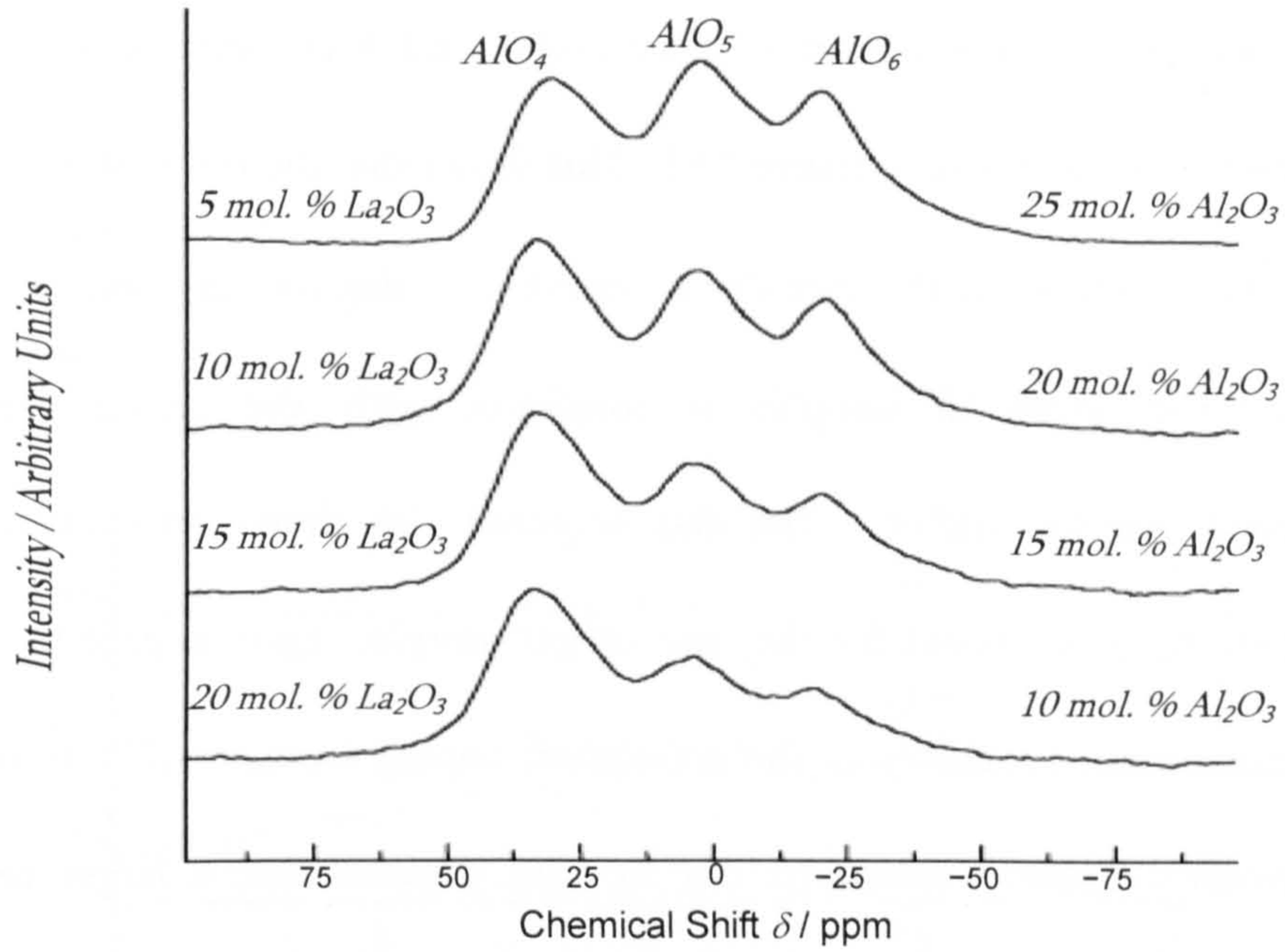

Figure 7.10: ^{27}Al NMR spectra for the $(30 - x)$ % La_2O_3 + x % Al_2O_3 + 70 % P_2O_5 glasses, reproduced from [2] where the x-axis scale has been reversed due to convention.

Sample Composition / mol. % ± 7 %			*AlO_4*		*AlO_5*		*AlO_6*	
La_2O_3	*Al_2O_3*	*P_2O_5*	*δ_{iso} / ppm*	*I / %*	*δ_{iso} / ppm*	*I / %*	*δ_{iso} / ppm*	*I / %*
25	0	75						
20	5	75	33.7	25	4.3	32	–20.3	43
15	10	75	32.7	22	2.5	31	–21.0	47
10	15	75	32.3	17	3.0	31	–21.3	52
5	20	75	32.3	11	3.0	26	–21.3	63
0	25	75	32.3	9	2.2	30	–21.5	61
30	0	70						
20	10	70	33.7	48	4.8	31	–18.1	21
15	15	70	33.2	43	3.5	33	–20.0	24
10	20	70	33.2	38	3.5	35	–20.8	27
5	25	70	31.1	32	3.0	36	–20.3	32
0	30	70	32.0	22	2.0	36	–22.0	42

Table 7.5: ^{27}Al NMR data for the lanthanum-doped aluminophosphate glasses, adapted from [2].

In the first series of samples with 75 mol. % P_2O_5, the spectra were found to be dominated by AlO_6 with the relative intensity of this peak decreasing as the aluminium in the system is replaced by lanthanum, see figure 7.11. In the second series of samples with 70 mol. % of P_2O_5 the spectra are dominated by tetrahedral

aluminium and the relative quantities of both AlO_5 and AlO_6 decrease as La_2O_3 is added to the system as shown in figure 7.12. This shows that the trend of increasing relative AlO_4 content with increasing rare-earth doping in both of the lanthanum-doped series of samples is consistent with the results for our yttrium-doped samples studied. The data acquired also shows no evidence for Al-O-Al bonding as discussed for the case of our samples, again supporting their theory of aluminium avoidance as the aluminium-doping increases [2]. However, the aluminium avoidance behaviour put forward suggests that a larger relative intensity of AlO_4 should be observed for the higher phosphorus pentoxide containing sample series (75 % P_2O_5) due to the fewer terminal oxygen atoms available for the AlO_5 and AlO_6 to coordinate with, but this is inconsistent with results by Karabulut et al. [2]. These contradictions may arise from the loss of ^{27}Al NMR signal which has been reported in a number of studies for certain cases where experiments have been attempted at relatively low fields (< 9.4 T) [19]. Although this cannot be confirmed, it does however emphasise the virtue of multiple-field NMR and it would be an interesting future task for us to repeat these measurements ourselves on similar samples. It is important to note that we also do not know how the quantification in the study by Karabulut et al. [2] was conducted as their method for extracting the intensity measurements from the NMR data has not been made clear in their descriptions.

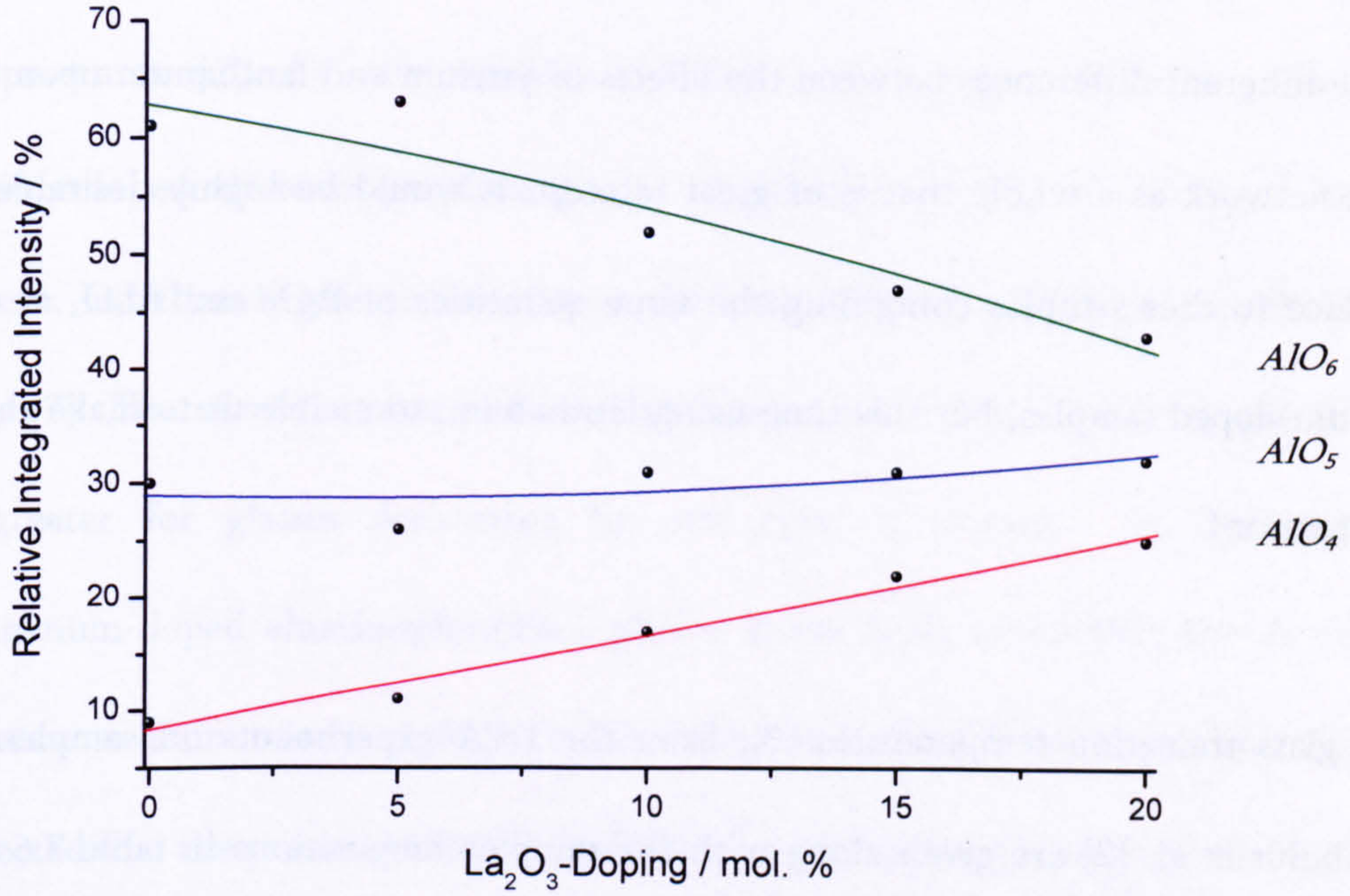

Figure 7.11: The change in relative integrated intensities of AlO_4, AlO_5 and AlO_6 with increasing lanthanum-doping for the $(25 - x)$ % La_2O_3 + x % Al_2O_3 + 75 % P_2O_5 samples, based on data from [2]. Note that the coloured lines are guides to the eye.

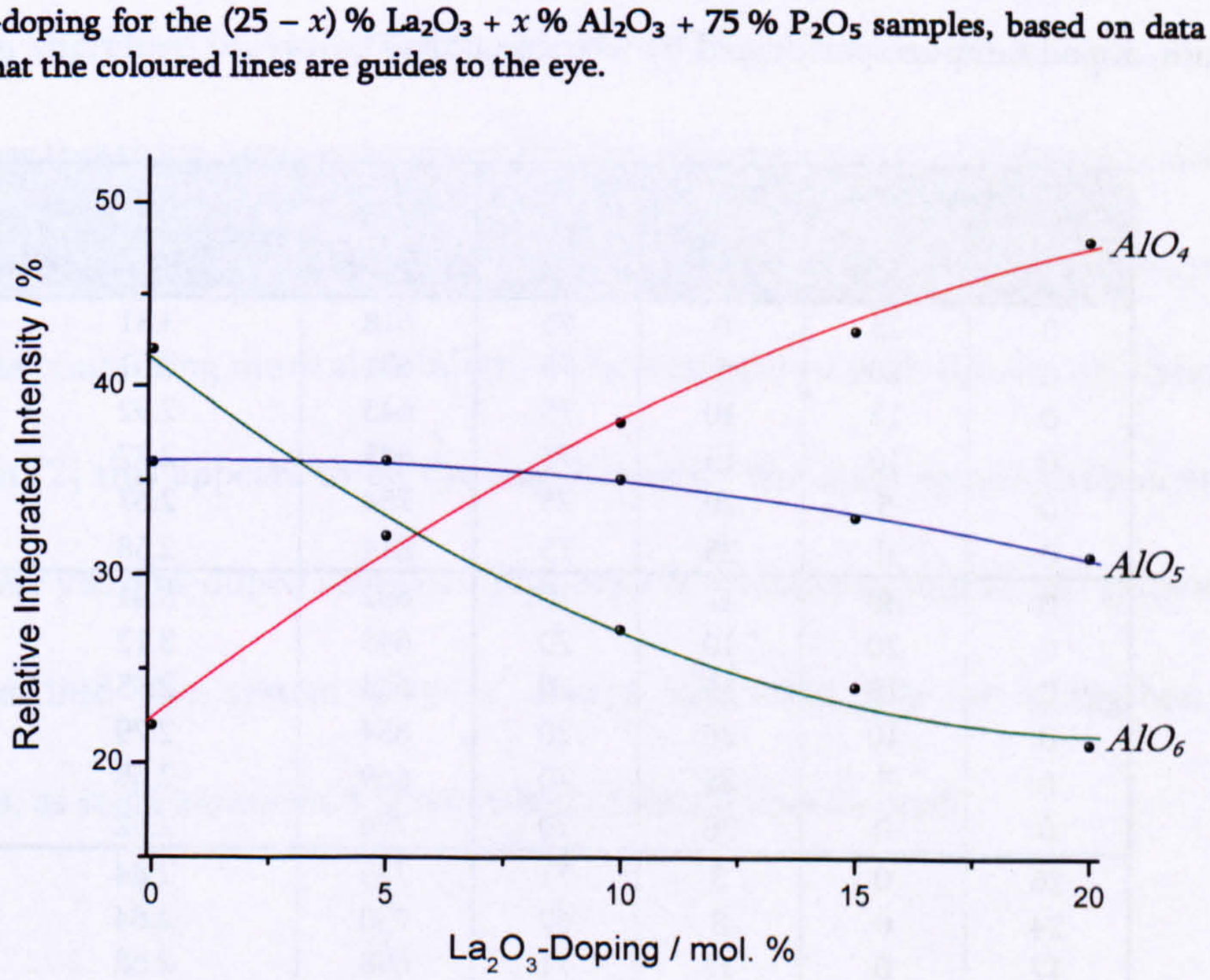

Figure 7.12: The change in content of different aluminium coordination with increasing lanthanum-doping in the $(30 - x)$ % La_2O_3 + x % Al_2O_3 + 70 % P_2O_5 samples, based on data from [2]. Note that the lines are guides to the eye.

Unfortunately these studies did not include any ^{31}P NMR investigations and since it is the inherent differences between the effects of yttrium and lanthanum upon the glass network as a whole that is of great interest, it would be highly desirable to produce further samples containing the same quantities of P_2O_5 and Al_2O_3 as our yttrium-doped samples, but this time using lanthanum, to enable us to make these comparisons.

The glass transition temperatures, T_g, from the DTA experiments on samples by Karabulut et al. [2] are given along with the sample compositions in table 7.6 [2], where these have been compared to those from DSC experiments on our yttrium-doped samples, performed by Martin et al. [7].

Sample composition / mol. %				*T_g / °C ± 3 °C*	*Density ρ / g cm^{-1} ± 0.01 g cm^{-1}*
Y_2O_3	*La_2O_3*	*Al_2O_3*	*P_2O_5*		
0	25	0	75	618	3.31
0	20	5	75	631	3.01
0	15	10	75	643	2.92
0	10	15	75	685	2.77
0	5	20	75	754	2.67
0	0	25	75	814	2.58
0	30	0	70	632	3.42
0	20	10	70	645	3.12
0	15	15	70	644	2.95
0	10	20	70	654	2.79
0	5	25	70	669	2.65
0	0	30	70	754	2.52
26	0	3	71	735	2.84
24	0	8	67	730	2.84
17	0	12	71	698	2.68
12	0	19	69	707	2.62
7	0	23	70	704	2.55
0	0	34	66	742	2.53

Table 7.6: Sample composition and corresponding T_g and density results for the lanthanum- [2] and yttrium-doped aluminophosphate glasses [7]. Data adapted from [2] and in the case of the yttrium-doped samples, measurements conducted by Martin [7].

These results have uncovered prominent differences between the glass transition temperatures (T_g) for the lanthanum- and yttrium-doped samples. For the yttrium-doped aluminophosphate glasses T_g decreases as yttrium is added to the system, but then begins to increase as the percentage of yttrium gets sufficiently large [7]. Therefore the intermediate doped glasses have the lowest T_g values, and T_g is greater for glasses dominated by one type of dopant. In the case of lanthanum-doped aluminophosphate glasses it has been found that the T_g values decrease as aluminium is replaced by the rare-earth ions [7], see figure 7.13. It was expected that the presence of Al_2O_3 within these phosphate glasses would strengthen the glass network as aluminium has stronger ionic bonding than that of lanthanum or yttrium therefore providing stronger cross-linking between the PO_4 tetrahedra. As the glass transition temperature to a first approximation can be directly related to the strength and chemical durability of the glass, this was also expected to be greater for samples containing more aluminium. When compared with the incorporation of lanthanum [2] this appears to be the case however, the same relationship does not exist for our yttrium-doped samples. This may be because not all of the aluminium introduced into the system plays a charge balancing role to strengthen the cross-links, as some aluminium become tetrahedrally coordinated.

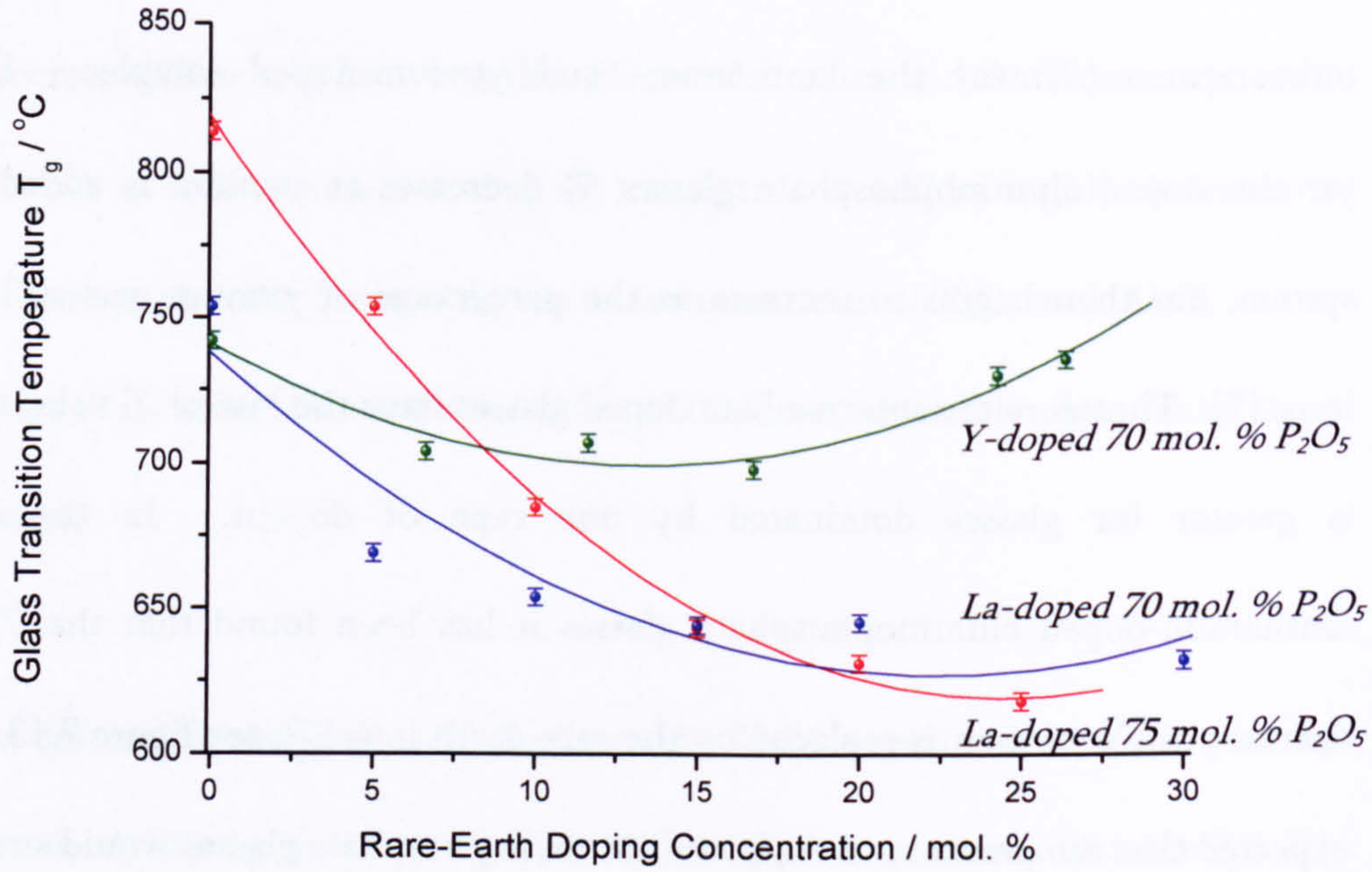

Figure 7.13: The change in glass transition temperature with increasing doping for the lanthanum- and yttrium-doped aluminophosphate glasses, taken from [2] and [7]. Note that the lines are guides to the eye.

The densities of the glasses were also measured and are reported in table 7.6. These measurements were achieved using Archimedes' method by immersing the samples in fluids of differing density such as air, water, acetone [7], or kerosene [2], and measuring the mass of the samples using an electronic balance [20]. Each measurement was repeated to provide a more precise average reading and the temperature of the immersion fluids was also recorded to allow more accurate densities to be calculated using equation 7.1 where ρ_S and ρ_F are the mass densities of the sample and fluid respectively, and W_A and W_F are the weight of the sample in air and the fluid respectively [20].

$$\rho_S = \rho_F \frac{W_A}{W_A - W_F} \tag{7.1}$$

The results show a consistent decrease in density as the rare-earth oxides are replaced by Al_2O_3 in all of the three series of samples which was expected since the rare-earth cations, yttrium and lanthanum are exchanged for the lighter aluminium ions [21].

The Vickers hardness, H_v, of our yttrium-doped glass samples was also measured using a Leco Microhardness testing machine [7]. This is a standard method for measuring the 'hardness' of a material by quantifying its resistance to plastic deformation when pressure is applied from a pyramid shaped diamond for a set length of time. The indentation created in the sample's surface is measured under a microscope and the Vickers Hardness value also known as the Vickers Pyramid Number, H_v, is related to the applied mass, m, and diagonal length of the resulting indentation, l, by $H_v = 1.854\ m/l$ [20 & 22]. The results are displayed in figure 7.14 and show that as the aluminium content increases (and correspondingly that of the yttrium decreases) the Vickers hardness increases, consistent with the strengthening behaviour expected of the aluminium inclusion, thus confirming the reason that Al_2O_3 is often incorporated into phosphate glasses.

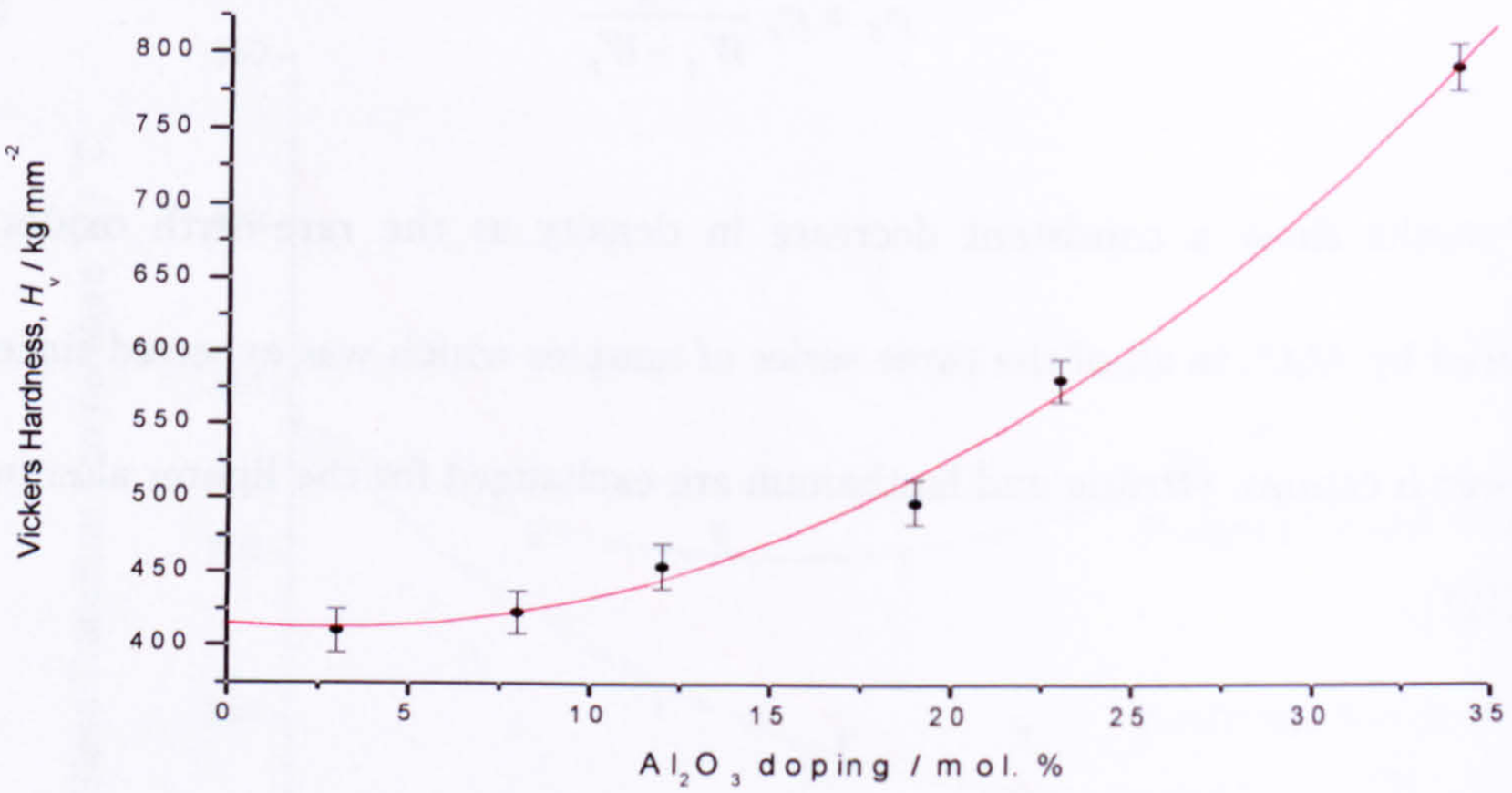

Figure 7.14: Vickers Hardness values of the yttrium-doped phosphate glass samples from measurements taken by Martin [7].

The phosphorus data collected in figure 7.15 and table 7.7 assigned using [17], for the mixed dopant samples containing both lanthanum and yttrium, but in different relative amounts (see section 1.2.2.1 for the exact compositions) show a negligible difference between the phosphorus network of the two samples. This leads to the conclusion that the different ionic sizes of these two cations do not give rise to a distinguishable difference in the phosphate network for these samples because the dopants are not incorporated directly into the phosphate tetrahedral network but instead sit within charge balancing sites outside the glass network where they do not have an observable effect on the phosphorus NMR signal. It would however be beneficial to examine a greater range of samples containing different concentrations of mixed rare-earth ion doping and would be useful to explore other properties of these quaternary-based La_2O_3-Al_2O_3-Y_2O_3-P_2O_5 samples to compare with those containing only one rare-earth species described previously.

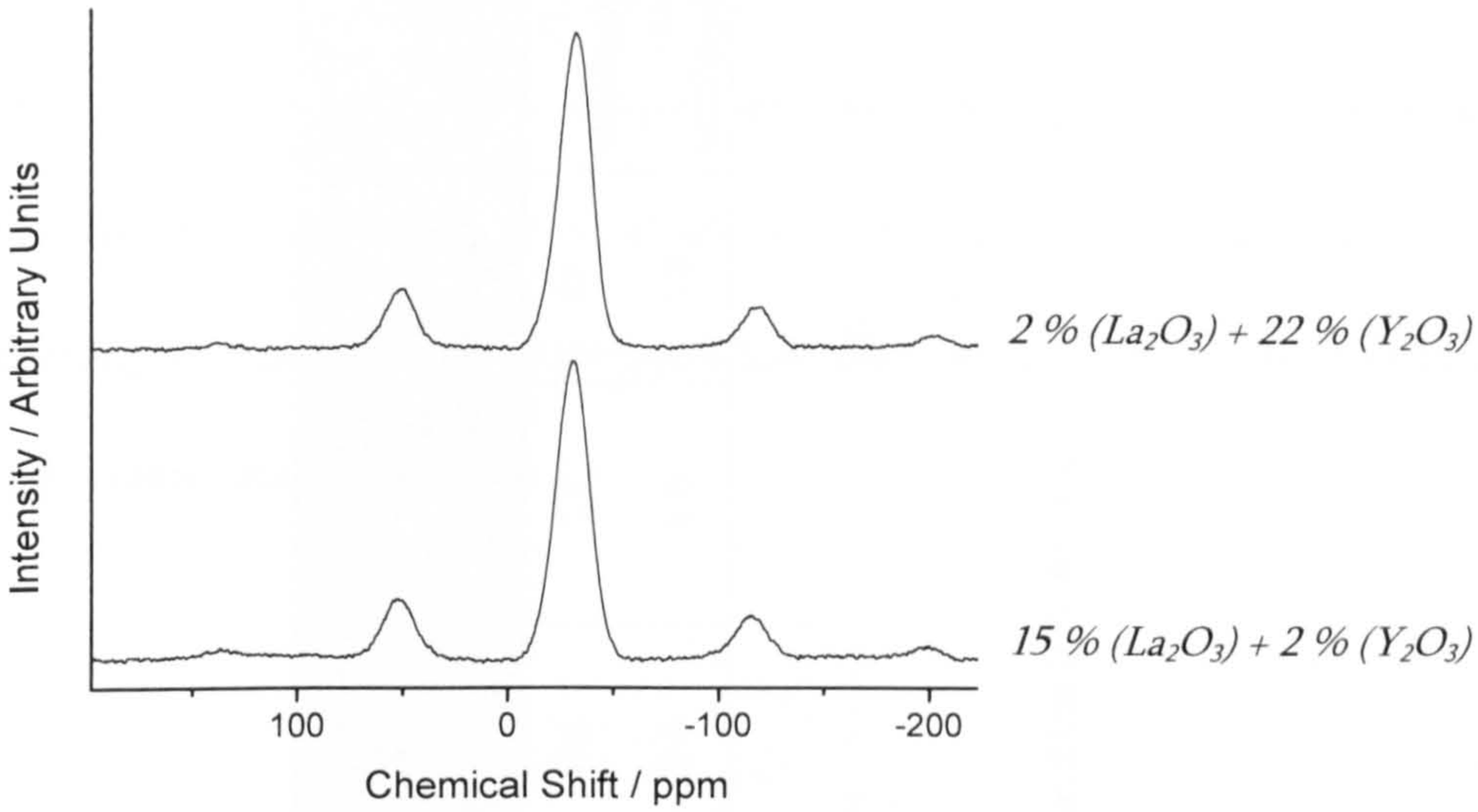

Figure 7.15: The ^{31}P MAS NMR spectra for the lanthanum-yttrium-doped aluminophosphate glasses at a magnetic field of 8.45 T, spinning at ~12 kHz.

Sample	*^{31}P Q^1 (1Al)*			*^{31}P Q^2 (1Al)*		
	δ_{iso} / ppm ± 1 ppm	*Δ / ppm ± 1 ppm*	*I / % ± 1 %*	*δ_{iso} / ppm ± 1 ppm*	*Δ / ppm ± 1 ppm*	*I / % ± 1 %*
2 % (La_2O_3) + 22 % (Y_2O_3) aluminophosphate	–18	12	6	–31	16	94
15 % (La_2O_3) + 2 % (Y_2O_3) aluminophosphate	–16	12	4	–30	18	96

Table 7.7: The ^{31}P NMR fitted data for the lanthanum-yttrium-doped samples.

In our investigation into the aluminosilicate samples it was found that when the 15 % (La_2O_3) + 35 % (Al_2O_3) + 50 % (SiO_2) and 16 % (Y_2O_3) + 33 % (Al_2O_3) + 51 % (SiO_2) samples were compared, the ^{27}Al NMR in figure 7.16 (a) also showed three aluminium coordinations present. These were AlO_4, AlO_5 and AlO_6, the data of which is given in table 7.8, where the 4-, 5- and 6-fold chemical shift values are different from that of the aluminophosphate samples due to the presence of silicon in place of the phosphorus as the next nearest neighbour.

Sample	AlO_4				AlO_5				AlO_6			
	δ_{iso} / ppm ± 6 ppm	$\Delta\chi_Q$ / MHz ± 0.5 MHz	χ_Q / MHz ± 0.5 MHz	I / % ± 8 %	δ_{iso} / ppm ± 6 ppm	$\Delta\chi_Q$ / MHz ± 0.5 MHz	χ_Q / MHz ± 0.5 MHz	I / % ± 4 %	δ_{iso} / ppm ± 6 ppm	$\Delta\chi_Q$ / MHz ± 0.5 MHz	χ_Q / MHz ± 0.5 MHz	I / % ± 6 %
Y-aluminosilicate	68	5.2	9.5	68	38	6.7	9.4	26	7	5.0	7.9	6
La-aluminosilicate	67	6.3	8.9	84	38	6.4	8.9	14	9	6.3	8.9	2

Table 7.8: ^{27}Al NMR results comparing the yttrium- and lanthanum-doped aluminosilicate glass samples.

The ^{29}Si MAS NMR for these lanthanum- and yttrium-doped aluminosilicates, in figure 7.16 (b), shows that the samples have only tetrahedral silicon atoms giving rise to an NMR signal at an isotropic chemical shift value characteristic of a completely connected (Q^4) aluminosilicate glass network with no non-bridging oxygen atoms present, see table 7.9.

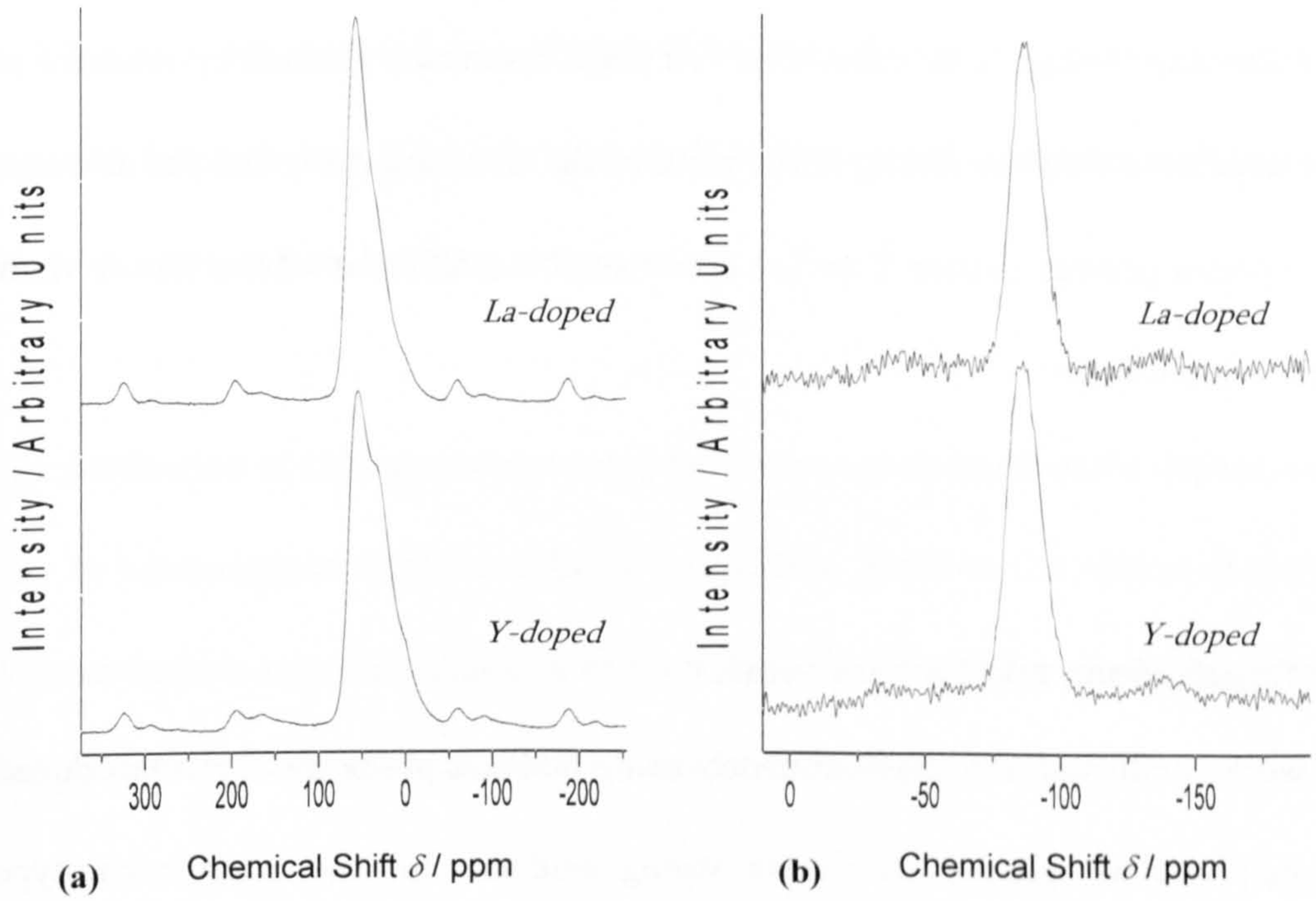

Figure 7.16 (a) and (b): (a) The ^{27}Al (14.1 T) and (b) the ^{29}Si (8.45 T) spectra for the lanthanum- and yttrium-doped aluminosilicate glasses.

Sample	*Si Q^4 speciation*	
	δ_{iso} / ppm ± 0.4 ppm	*Δ / ppm ± 1 ppm*
Y-aluminosilicate	–85.5	15
La-aluminosilicate	–86.3	13

Table 7.9: The ^{29}Si NMR data of the peaks fitted.

The two samples show very little difference in their silicon environments and yet the lanthanum-doped sample was found to contain a larger relative percentage of AlO_4 compared to the corresponding yttrium-doped sample. This shows that the silicate network is unaltered by the presence of yttrium and lanthanum as these ions sit purely in place of the AlO_5 and AlO_6. The two rare-earth ions do not become incorporated into the network itself as they have no tendency towards this behaviour due to their ionic sizes. The ^{27}Al NMR results are affected by presence of these dopants as they are sitting in the place of the AlO_5 and AlO_6, and the different ionic species present (either Y or La) also contribute different effects due to their different ionic sizes.

7.3 Conclusions and further work

The work conducted here predominantly using NMR to probe some yttrium-doped aluminophosphate glasses has shown strong evidence for the intermediate-type behaviour of aluminium as a modifying cation. The Al^{3+} ions were shown to have the ability to network modify via depolymerisation, as well as network form. This was detected by the distribution between different coordinations for aluminium in these different roles, as the network forming aluminium ions were tetrahedrally coordinated within the phosphate network. By considering this behaviour of the aluminium cations, it was possible to use the structural model outlined in section 1.2.2.1 to give excellent consistency with the experimentally obtained glass network

coordination deduced from the ^{31}P NMR measurements. This helped to confirm that the tetrahedral aluminium was indeed becoming part of the phosphate network.

Results also showed that Y^{3+} cations remain within the cross-linking sites, charge balancing the terminal oxygen atoms, although it would be of great benefit to attempt ^{89}Y NMR or Y K-edge XANES. This could confirm the yttrium coordination and hence check for evidence of Y-O-Y linkages due to rare-earth clustering as reported for lanthanum [2] as the rare-earth dopant content increases such that they must 'share' their non-bridging oxygen atoms.

The production of similar samples using lanthanum as the rare-earth dopant would also be advantageous to allow a direct comparison between the effects of the two dopants and observe the influences of their ionic sizes upon the phosphate network not possible from the comparisons with work by Karabulut et al. [2].

Although some theories have been briefly discussed regarding the influences over the aluminium coordination within these types of glasses, this has yet to be fully understood and is an area in which much more thorough investigations could and should be attempted.

References

[1] R. D. Shannon, *Revised Effective Ionic Radii and Systematic Studies of Interatomic Distances in Halides and Chaleogenides*, Acta Crystallographica Section A: Foundations of Crystallography, **32** (1976), 751-767.

[2] M. Karabulut, E. Metwalli and R. K. Brow, *Structure and properties of lanthanum-aluminium-phosphate glasses*, Journal of Non-Crystalline Solids, **283** (2001), 211-219.

[3] M. Graia, A. Driss and T. Jouini, *Crystal structure of three polymorphs of* $Y(PO_3)_3$, Solid State Sciences, **5** (2003), 393–402.

[4] W. 0. Milligan, D. F. Mullica, *G.* W. Beall and L. A. Boatner, *Structural Investigations of YPO,* $ScPO_4$, *and* $LuPO_4$, Inorganica Chimica Acta, **60** (1982), 39-43.

[5] J. Matuszewski, J. Kropiwnicka and T. Znamierowska, *The Crystal Structure of Lanthanum Metaphosphate* $LaPsO_9$, Journal of Solid State Chemistry, **75** (1988), 285-290.

[6] D. F. Mullica, W. 0. Milligan, D. A. Grossie, G. W. Beall and L. A. Boatner, *Ninefold Coordination in* $LaPO_4$*: Pentagonal Interpenetrating Tetrahedral Polyhedron*, Inorgania Chimica Acta, **95** (1984), 231-236.

[7] R. A. Martin, P. S. Salmon, D. L. Carroll, M. E. Smith and A. C. Hannon, *Structure and thermal properties of yttrium alumino-phosphate glasses*, Journal of Physics: Condensed Matter, **20** (2008), 115204.

[8] T. F. Kemp, *High field solid state ^{27}Al NMR of ceramics and glasses*, Masters Thesis, University of Warwick, UK (2004).

[9] J. F. Stebbins, S. K. Lee and J. V. O'Glesby, *Al-O-Al oxygen sites in crystalline aluminates and aluminosilicate glasses: High-resolution oxygen-17 NMR results*, American Mineralogist, **84** (1999), 983-986.

[10] U. Hoppe, R. Kranold, D. Stachel, A. Barz and A. C. Hannon, *A neutron and X-ray diffraction stuffy of the structure of the LaP_3O_9 glass*, Journal of Non-Crystalline Solids, **232** & **234** (1998), 44-50.

[11] R. K. Brow, C. A. Click and T. M. Alam, *Modifier coordination and phosphate glass networks*, Journal of Non-Crystalline Solids, **274** (2000), 9-16.

[12] R. K. Brow, *Review: the structure of simple phosphate glasses*, Journal of Non-Crystalline Solids, **263** & **264** (2000), 1-28.

[13] J. R. Van Wazer, *Phosphorus and its compounds: Volume 1*, Interscience Publishers, New York, USA (1958).

[14] U. Hoppe, *A structural model for phosphate glasses*, Journal of Non-Crystalline Solids, **195** (1996), 138-147.

[15] P. Hartmann, J. Vogel, U. Friedrich and C. Jäger, *Nuclear magnetic resonance investigations of aluminum containing phosphate glass-ceramics*, Journal of Non-Crystalline Solids, **263** & **264** (2000), 94-100.

[16] K. J. D. MacKenzie and M. E. Smith, *Multinuclear solid state NMR of inorganic materials*, Pergamon Press, London, UK (2002).

[17] L. Zhang and H. Eckert, *Sol-gel synthesis of Al_2O_3-P_2O_5 glasses: Mechanistic studies by solution and solid state NMR*, Journal of Materials Chemistry, **14** (2004), 1605-1615.

[18] L. Zhang and H. Eckert, *Short- and medium-range order in sodium aluminophosphate glasses: New insights from high-resolution dipolar solid-state NMR spectroscopy*, Journal of Physical Chemistry B, **110** (2006), 8946-8958.

[19] M. E. Smith, *Application of ^{27}Al NMR techniques to structure determinations in solids*, Applied Magnetic Resonance, **4** (1993), 1-64.

[20] R. A. Martin, *Properties of rare earth phosphate glasses and rare earth halide liquids*, PhD Thesis, University of Bath, UK (2002).

[21] G. W. C. Kaye and T. H. Laby, *Tables of physical and chemical constants*, 86th Ed., Longman, Harlow, UK (1995).

[22] W. F. Smith, *Principles of materials science and engineering*, 2nd Ed., McGraw-Hill Publishing, London, UK (1990).

Chapter 8

Sulphur-Doped Silicate Glass

8.1 Introduction

Sulphur-bearing silicate and aluminosilicate glasses were studied to aid understanding of how the formation conditions of magma, a natural aluminosilicate, influence the speciation of sulphur which can lead to a greater understanding of volcanic outgassing. The experimental results obtained in this section of the investigation represent an important milestone in the use of ^{33}S NMR as it is well known that these are difficult experiments to perform since the sensitivity is incredibly low as ^{33}S is a low-γ nucleus, refer to section 3.3.2, page 63. The papers

published on the subject of ^{33}S NMR to date are scarce and for this reason, the results collected here have already produced interest despite the poor signal-to-noise ratio in comparison to other higher γ nuclei.

8.2 Results and discussion

The sample preparation conditions have been listed in table 8.1 in order to make a comparison between these and the spectra collected, shown in figure 8.1. The sample compositions have already been stated in table 1.2, on page 25.

Sample number	*Formation conditions*			
	Temperature / °C	*Heating time / Days*	*Pressure / GPa*	*Oxygen fugacity description*
1	900	2	2.0	high
2	1000	1	0.2	low
3	1000	1	0.2	high
4	850	3	0.2	high
5	850	2	0.2	high
6	850	2	0.2	high

Table 8.1: The sulphur-doped silicate glass sample preparation conditions.

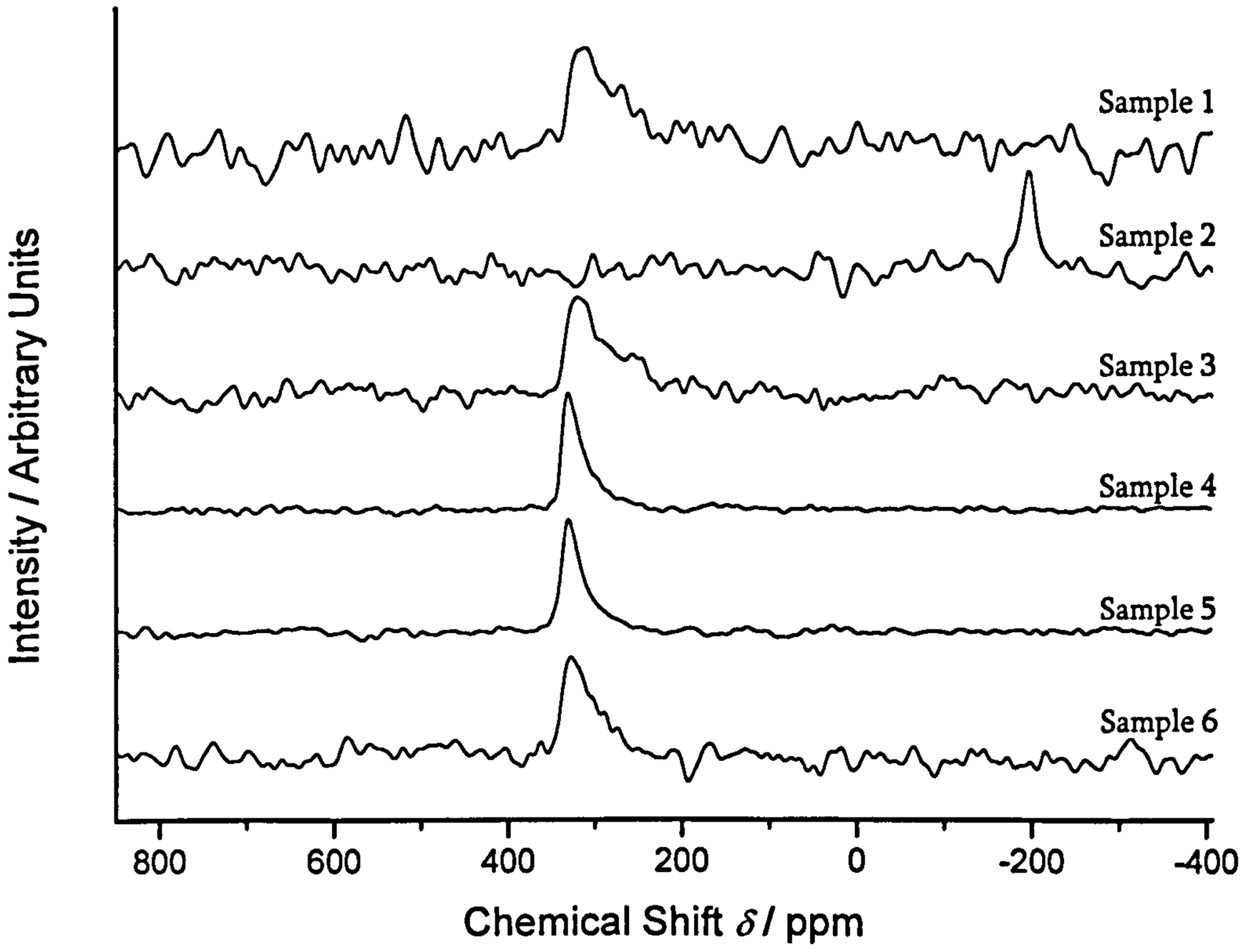

Figure 8.1: ^{33}S MAS NMR spectrum for each of the sulphur-doped aluminosilicate glass samples, labelled 1 to 6, whose compositions can be found in table 1.2, page 25.

The ^{33}S NMR spectra shown in figure 8.1 display a significant difference between the chemical shift of the NMR peak arising from sample 2 with respect to each of the other spectra. This was the only sample to have been prepared under reducing conditions with a very low oxygen partial pressure and has an albite-type rock composition ($NaAlSi_3O_8$) [1]. The position of this peak is −198 ± 1 ppm and there is only a single site present. Using previous literature in this area summarised by MacKenzie and Smith [2] this peak position suggests that the site relates to a sulphide component. Each of the other samples were created under more oxidising conditions and the chemical shifts, details of which are given in table 8.2, relate to

sulphate sites. There are however, two separate sites present in samples 1 and 3 which correspond to two sulphate species with very similar chemical shift values. It may also be possible that sample 6 contains two sites as the FWHM is wider than that of samples 4 and 5, and this could be confirmed in future extensions to this work by attempting methods such as satellite transition MAS (STMAS) NMR [3], which may be able to resolve the peaks. It may however, simply be the case that this spectral line is just wider than that of samples 4 and 5 as the principal difference between them is the number of modifying alkali cations present in the sample. Sample 6 contains both Na^+ and Ca^{2+} ions whereas sample 4 contains Na^+ and sample 5 contains K^+ ions. This may also explain the two sites observed for samples 1 and 3 which consist of three cations in the form of Ca^{2+}, Na^+ and K^+ and have very similar spectra and compositions to each other which fall into the rock category of trondjemite, also known as haplogranitic rock [1] with compositions listed in table 1.2, page 25.

Sample number	*Chemical shift δ_{iso} / ppm ± 1 ppm*	*FWHM / ppm ± 3 ppm*
1	+314	74
2	−198	20
3	+319	52
4	+330	26
5	+330	26
6	+328	41

Table 8.2: Peak positions and full width at half maximum height measurements from the ^{33}S NMR spectra.

^{27}Al NMR experiments were also performed on the first three samples, the results of which are shown in figure 8.2. Due to time restrictions it was not possible to collect data at two fields, therefore limiting the accuracy at which this data could be fitted, so no fits are reported here. The results do however show that there is only one type of aluminium coordination present in these samples corresponding to AlO_4 [2].

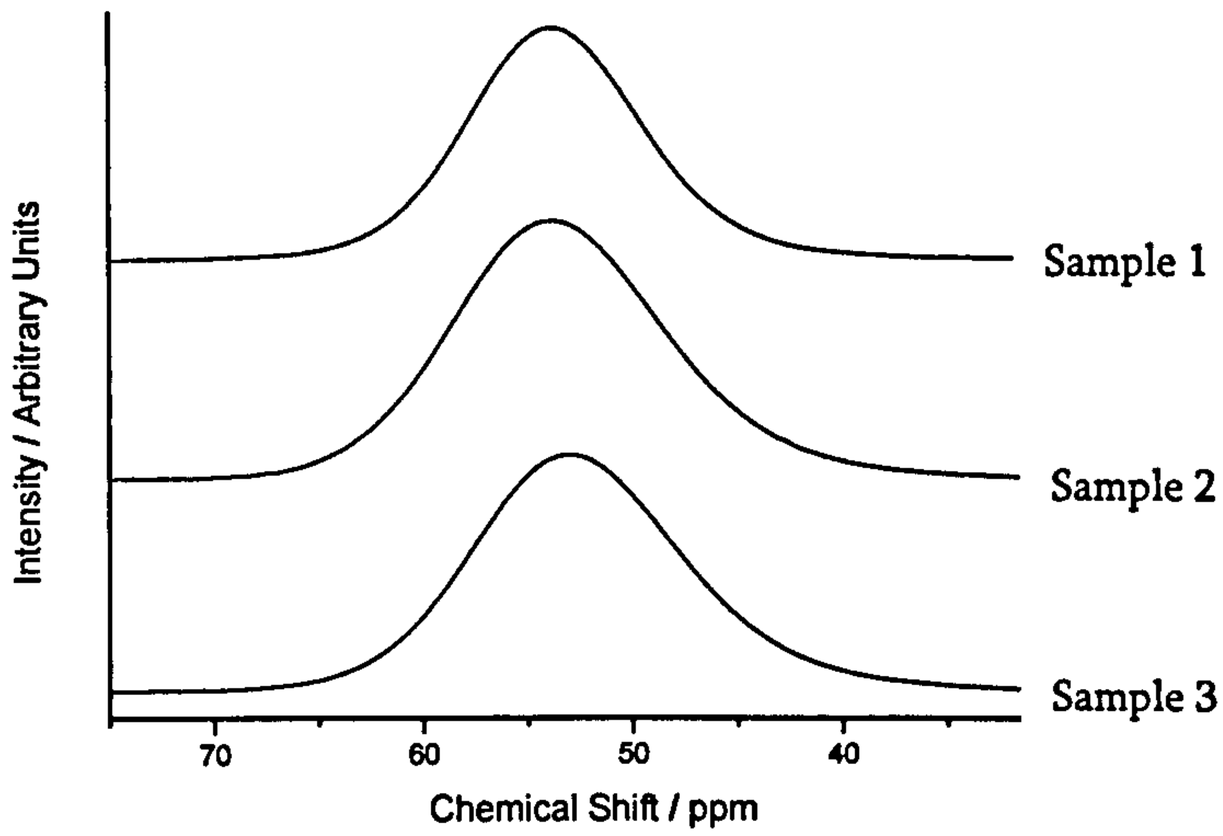

Figure 8.2: Aluminium MAS NMR spectra for samples 1, 2 and 3.

The results obtained from the solid-state NMR technique are of virtue as they not only confirm the expected sulphur speciation as there are very few previously published results in this area of research, but can also make an important comparison with the various other studies performed by Klimm and Kohn at the Department of Earth Sciences at the University of Bristol who provided these samples. The SO_2 solubility results performed on these samples have shown that there is a definite change in the sulphur solubility levels with modification of composition and formation conditions although the table of results is not reported here. In previous studies performed by Brooker et al. [4] the structural dependence

of the solubility of CO_2 in silicate melts was investigated and a strong correlation between the carbon solubility and the non-bridging oxygen content of the melts were found. For a long-term plan, if further sulphur-doped samples are studied then enough data should be accumulated for a similar relationship to be sought for the SO_2 solubility levels in the not too distant future. Importantly, one must note that the sulphur solubility studies have been performed on over-saturated sulphur samples, i.e. glasses containing precipitated sulphur, whereas the NMR was performed on samples where the sulphur was contained only within the glass network itself and not allowed to precipitate out due to over-saturation. This may affect the accuracy of any comparisons made.

8.3 Conclusions

The experiments performed here showed a different number of sites present in the NMR spectra for sulphur silicate samples consisting of more than one type of cation species. This will be of interest as more samples are investigated and can be compared to this data. The results presented here also provided a clear distinction between the chemical shift of the reduced and oxidised samples as the former condition gives rise to a sulphide rather than a sulphate species. At present the most common technique for the determination of the oxidation state of sulphur-containing samples is to measure the S$K\alpha$ X-ray wavelength shifts emitted from the sample due to the incident electron beam using an electron microprobe. In

numerous experiments, including those performed by Carroll and Rutherford in 1988 [5] and Wallace and Carmichael in 1994 [6], this technique has shown a great deal of success in distinguishing between these species. However, in more recent, ongoing studies by Klimm and Kohn, this technique has produced very little detectable shift in the peak values between some sulphide- and sulphate-bearing samples[i]. This leads to the conclusion that NMR may prove useful in making this distinction a clearer and more definite one. Clearly it is necessary for additional samples to be run to make a comparison between samples of the same composition, but formed under both reduced and oxidised conditions, in order to test this method more thoroughly, but the results here are extremely promising. With further work in this area, this could potentially lead to a very reliable method for determining the magma formation conditions from natural magma samples via the sulphur speciation.

References

[1] K. Klimm, S. C. Kohn and M. E. Smith, *Sulphur oxidation state and speciation in silicate glasses: EPMA, XANES and NMR studies*, 11th International Conference on Experimental Mineralogy, Petrology and Geochemistry (EMPGXI), Bristol, UK (2006).

[i] This information has been collected via personal communication with Kohn and Klimm at the Department of Earth Sciences, University of Bristol.

[2] K. J. D. MacKenzie and M. E. Smith, *Multinuclear solid state NMR of inorganic materials*, Pergamon Press, London, UK (2002).

[3] S. E. Ashbrook and S. Wimperis, *High-resolution NMR of quadrupolar nuclei in solids: the satellite-transition magic angle spinning (STMAS) experiment*, Progress in Nuclear Magnetic Resonance Spectroscopy, **45** (2004), 53-108.

[4] R. A. Brooker, S. C. Kohn, J. R. Holloway and P. F. McMillan, *Structural controls on the solubility of CO_2 in silicate melts. Part 1: Bulk solubility data*, Chemical Geology, **174** (2001), 225-239.

[5] M. R. Carroll and M. J. Rutherford, *Sulphur speciation in hydrous experimental glass of varying oxidation state: Results from measured wavelength shifts of sulphur X-rays*, American Mineralogist, **73** (1988), 845-849.

[6] P. J. Wallace and I. S. E. Carmichael, *S speciation in submarine basaltic glasses as determined by measurements of SKa X-ray wavelength shifts*, American Mineralogist, **79** (1994), 161-167.

Chapter 9

SUMMARY

Having explored numerous types of glass composition with the addition of modifying oxides, this study has clearly brought to light some of the various structural reconfigurations occurring during dopant incorporation. The NMR technique has proved invaluable in probing the structural network of the samples investigated, without which the various dopant behaviour and incorporation mechanisms within the glasses would have remained elusive.

The predominant samples studied were phosphate based glasses where one type of modifying oxide was replaced by another to observe the influences of different modifying cation species upon the structural network. In each case the effects of the cations on the phosphate network were found to be more complicated than initially predicted using the simple binary phosphate glass model approximation.

Both the silver- and copper-doped mixed alkali phosphates exhibited unexpected phosphate network coordination at high doping concentrations, displaying the presence of Q^3 tetrahedral units. We were unable to conclusively confirm the cause of these phosphate units due to some apparently contradictory experimental results and concerns over the stability of the samples throughout the duration of the investigation. It is however, most likely that in both cases, the occurrence of some phase separation leads to a heterogeneous chemical composition where the bulk of the sample differs from expectations. This could explain the deviations from the predicted model although the form of this possible phase separation is in question due to the absence of unequivocal evidence. However, at this time any other explanations for the glass structure observed are inconclusive. It should also be noted that the presence of paramagnetic copper confirmed in all of the copper-containing glass series has severely limited the structural information and reliability of the data obtained.

The properties of the silver- and copper-doped phosphate glasses were also explored and in both cases we were able to verify their antibacterial effectiveness along with their modifiable dissolution rates, although further studies in this area are required for the copper-doped samples. For the silver-containing samples, it was also found that whilst there was a distinct change in the desired properties with low doping concentrations up to 5 mol. %, there were not yet any observable structural differences until much higher doping concentrations were achieved. This information may prove helpful as it is now known that to achieve changes in the material properties of the glass such as the degradation rates and antimicrobial efficiency, the atomic structure does not need to be changed significantly which means that the behaviour of the glasses may be more predictable.

It would be interesting to investigate in more depth, the differences between Ag^{+}, Cu^{2+} and Na^{+} cations to understand the reasons for the differences in glass structure and properties observed. Perhaps an initial step towards achieving this would be to perform sodium and copper K-edge XANES.

The yttrium-doped aluminophosphate samples demonstrated strong evidence for aluminium's ability to both cross-link between the non-bridging oxygen atoms of the PO_4 units, as well as residing within 4-fold coordinated sites as part of the phosphate tetrahedral network, contributing to the overall structure. This was confirmed by not only the ^{27}Al MAS NMR which displayed the signals arising from

AlO_4, AlO_5 and AlO_6 but also by the ^{31}P NMR which confirmed that the connectivity between the phosphate units present are those expected from the model so long as this network forming AlO_4 is considered as part of the phosphate network rather than as a network modifier. The amount of network forming AlO_4 appears to be influenced by the amount of available non-bridging oxygen atoms to coordinate with and as no evidence for Al-O-Al linkages was found this supports aluminium avoidance mechanisms. Although the number of terminal oxygen atoms available to the aluminium is dependent upon the concentration of other charge balancing cations (in this case yttrium), it is also dependent upon the P_2O_5 content in the sample and it would be beneficial for further studies to include samples of different P_2O_5 to modifier ratios.

Yttrium has been found to only remain in charge balancing sites outside the phosphate tetrahedral network and although some comparison with lanthanum was attempted, additional experiments could supplement the work already completed by offering an insight into their different impacts upon glass structure. This work could also include yttrium and lanthanum XANES and NMR.

Research undertaken on the aluminosilicates was more limited due to the small selection of samples available, although this work is ongoing at the University of Bath.

The investigations into the sulphur-doped model magma samples has already generated interest as ^{33}S NMR is not a commonly used technique and the results showed a different number of sites present in the NMR spectra for samples consisting of more than one type of cation species as well as displaying a clear distinction between the sample that was created in reduced conditions compared with those prepared in more oxidising environments. This demonstrates the potential for using ^{33}S MAS NMR to determine magma formation conditions although it is necessary to investigate additional samples in order to test this method more thoroughly, as those investigated here did not form an ideal systematic sample series.

List Of Abbreviations

AFC	Automatic frequency controller	*EDX*	Energy dispersive X-ray
AFM	Antiferromagnetic	*EMF*	Electromotive force
CLSM	Confocal laser scanning microscopy	*EPMA*	Electron probe microanalysis
CSA	Chemical shift anisotropy	*EPR*	Electron paramagnetic resonance
CSPV	Coldseal pressure vessel	*FEG*	Field emission gun
CW	Continuous wave	*FID*	Free induction decay
DSC	Differential scanning calorimetry	*FFT*	Fast Fourier transform
DTA	Differential thermal analysis	*FM*	Ferromagnetic
DTGS	Deuterated triglycine sulphate	*FTIR*	Fourier transform infrared spectroscopy
		FWHM	Full width at half maximum

HFS	Hyperfine structure
ICP-MS	Inductively coupled plasma mass spectroscopy
IHPV	Inner heated pressure vessel
IR	Infrared
LASER	Light amplification by stimulated emission of radiation
MAS	Magic angle spinning
MCA	Multichannel analyser
MRSA	Methicillin-resistant *Staphylococcus aureus* (MRSA)
NBO	Non-bridging oxygen
ND	Neutron diffraction
NDIS	Neutron diffraction with isotopic enrichment
NMR	Nuclear magnetic resonance
NNO	Nickel-nickel oxide
PEEK	Polyaryletheretherketone
PTFE	Polytetrafluorethylene
QFM	Quartz-fayalite-magnetite
r.f.	Radio frequency
SEM	Scanning electron microscope
SQuID	Superconducting quantum interference device
SRS	Synchrotron radiation source
STMAS	Satellite transition magic angle spinning
UHV	Ultra-high vacuum
UV	Ultraviolet
VP	Variable pressure
VSM	Vibrating sample magnetometer
WD	Working distance
XANES	*X-ray absorption near edge structure*
XPS	X-ray photoelectron spectroscopy
XRD	X-ray diffraction
YAG	Yttrium aluminium garnet

PAGE/PAGES EXCLUDED UNDER INSTRUCTION FROM UNIVERSITY